

# Implications of inviscid hydrodynamics and its variants for turbulence and statistical physics

A Thesis

Submitted to the  
Tata Institute of Fundamental Research, Mumbai,  
for the degree of  
Doctor of Philosophy  
in Physics

by

**Sugan Durai Murugan Velazhagan**

International Centre for Theoretical Sciences,  
Tata Institute of Fundamental Research,  
Bangalore, India  
November, 2023



# DECLARATION

This thesis is a presentation of my original research work. Wherever contributions of others are involved, every effort is made to indicate this clearly, with due reference to the literature, and acknowledgement of collaborative research and discussions.

The work was done under the guidance of Professor Samriddhi Sankar Ray, at the International Centre for Theoretical Sciences, Tata Institute of Fundamental Research, Bangalore, India.



**Sugan Durai Murugan Velazhagan**

In my capacity as supervisor of the candidate's thesis, I certify that the above statements are true to the best of my knowledge.



Samriddhi Sankar Ray

Date: 21 November, 2023

# ACKNOWLEDGEMENTS

I extend my heartfelt gratitude to my esteemed advisor, *Professor Samriddhi Sankar Ray*, whose exceptional guidance, unyielding support, patience, and understanding have been the cornerstones of my success throughout the course of my PhD journey. Prof. Ray's commitment to my academic growth has always been a constant source of inspiration and motivation and has been instrumental in shaping my understanding of the subject matter. I consider myself incredibly fortunate and truly gifted to have been under the mentorship of Professor Ray for my PhD.

My sincere appreciation goes out to the following list of individuals with whom I was fortunate to have collaborated, or at the very least interacted with, who were instrumental to my research work: Beginning with the esteemed mathematical physicist *Professor Uriel Frisch* (Côte d'Azur Observatory), followed by Professors *Subhro Bhattacharjee* (ICTS-TIFR), *Rama Govindarajan* (ICTS-TIFR), *Rahul Pandit* (IISc), *Vishal Vasan* (ICTS-TIFR), *Sergey Nazarenko* (University of Warwick), *Nicolas Besse* (Côte d'Azur Observatory), *Dario Vincenzi* (Université Côte d'Azur), and *Giorgio Krstulovic* (Université Côte d'Azur), post-doctorates at ICTS: *Siddhartha Mukherjee* and *Jason Ryan Picardo*, and students: *Rahul Singh* (ICTS-TIFR), *Dheeraj Kumar* (Sorbonne Université) and *Ritwik Mukherjee* (ICTS-TIFR). It is only equitable that I take this occasion to acknowledge Siddhartha and Ritwik for their exceptional contributions in our collaboration concerning the turbulence multifractality research work, which is described in Chapter 5 in this thesis. Their intellectual insights and dedication played vital

---

role in identifying and interpreting our study's most intriguing findings. I would also like to make a special mention to my thesis monitoring committee *Prof. Rahul* and *Prof. Rama* , for their invaluable mentoring during my PhD.

I am deeply grateful to *Prof. Dario* for his inspiring support and guidance during my project visit at Côte d'Azur University, Nice, France. I extend my sincere gratitude to all the esteemed professors for cultivating an enriching and inspiring academic environment at ICTS, as well as at IISc during my coursework. Your unwavering commitment to academic excellence has set a remarkable standard that I am proud to have been a part of. Especially to Professors *Abhishek Dhar* (ICTS-TIFR), *Loganayagam* (ICTS-TIFR), *Diptiman Sen* (IISc) , *Rama Govindarajan* and *Aninda Sinha* (IISc) for the inspiring teaching and the passion you provided for the subject. Your teaching style goes beyond the dissemination of information; it is a true art of sparking curiosity and fostering a love for learning. Your ability to make complex concepts accessible and your enthusiasm for the subject have not only enhanced my academic experience but have also motivated me to explore further and delve deeper into the field.

I am truly thankful to all my colleagues for their support, collaborative spirit, teaching, and assistance. In particular, I have been profoundly enriched by my colleague *Srikanth B. Pai*, who was an invaluable wellspring of knowledge and a beacon of enlightening perspectives during my coursework at ICTS. I have been truly inspired by *Pronobesh Maity* for his intelligence, indomitable willpower and relentless pursuit of goals. Amongst many who have been an integral part of my academic journey, I would like to thank my batchmates: *Bhavik, Aswin, Arnab, Pinak, Prashant, Shashank, Monica, Basudeb, Junaid, Chandramouli, Divya and Srashti* and *Soumyadip*, my seniors and juniors: *Santhosh, Akhil, Joydeep, Adithya, Saurav, Saumav, Saikat, Jitendra, Omkar, Banukiran and Rajashri*. The camaraderie and sense of community that we have shared have fostered an environment of mutual learning and growth. Your contributions, whether through brainstorming sessions, constructive critiques, or fruitful discussions, have enriched the quality of my work and made this journey all the more rewarding. The dedication

---

and assistance of the ICTS staff members from various departments (lab, library, academic, administrative and IT) have been instrumental in the smooth progress of my research. Particular mentions to *Mr. Hemanta* for his support in the cluster simulations.

In a symphony of gratitude, I extend my deepest appreciation to my wife, *Kavitha*, for her endless support and constant motivation for my academic career. I am indebted to my father, *Velazhagan*, my sister, *Thanga Tamizh Amudhu*, close friends (*Amit, Poison, Buobsy, Pushkar, Niloy and Varghese*), and my in-laws (*Kural, Aswin, Kavitha's family*) for their support, encouragement, and belief in my abilities. My family and friends's love and encouragement have provided the emotional strength needed to overcome challenges and persevere in this demanding journey. My seven-month-old son, *Aran Ilamugil Aazhiyan*, has unfurled a new tapestry of responsibility within me, weaving threads of purpose and commitment that have greatly influenced the completion of this thesis. I found solace and rejuvenation in the playful antics of my devoted canine companions, *Kay* and *Maya*. I express profound gratitude to my stalwart laptop (*Jarvice*), desktop (*Vulcan*), and the formidable computing clusters, *Mario* and *Mowgli* at ICTS for its computational prowess.

Amidst this journey, I carry with me the unwavering spirit of my late mother, *Vasuki*, who instilled in me the values of perseverance and determination. Her love and guidance continue to shape my path, infusing my efforts with a profound sense of purpose. This thesis is a tribute to her enduring legacy, a testament to the strength she embedded within me, and a reflection of the boundless inspiration she continues to provide from beyond.

I wish to extend my heartfelt appreciation to my esteemed institution, ICTS-TIFR, for the invaluable opportunity of pursuing my PhD, and I am profoundly grateful to the Department of Atomic Energy, Government of India, for the stipend, a beacon of financial support that empowers research scholars. This thesis stands as a testament to the collective effort, encouragement, and guidance of

---

all those who have been a part of my academic and personal journey. I am profoundly grateful for their contributions, and I look forward to continuing to build upon the foundation they have helped me establish.

*Dedicated to my loving mother,*



Vasuki Kaliyaperumal, M.E.,  
Polytechnic Lecturer,  
1965–2017.

# List of publications

1. Suppressing thermalization and constructing weak solutions in truncated inviscid equations of hydrodynamics: Lessons from the Burgers equation, **Sugan Durai Murugan**, U. Frisch, S. Nazarenko, N. Besse, and S. S. Ray. [Phys. Rev. Research 2, 033202\(2020\)](#).
2. Many-body Chaos in Thermalised Fluids, **Sugan Durai Murugan**, D. Kumar, S. Bhattacharjee, and S. S. Ray. [Phys. Rev. Lett. 127, 124501\(2021\)](#).
3. Genesis of thermalization in the three-dimensional, incompressible, Galerkin-truncated Euler equation, **Sugan Durai Murugan** and S. S. Ray. [Phys. Rev. Fluids 8, 084605\(2023\)](#).
4. Turbulent flows are not uniformly multifractal, S. Mukherjee, **Sugan Durai Murugan**, R. Mukherjee, and S. S. Ray. [arXiv:2307.06074](#)

# List of Figures

1.1	Tracing singularity in the inviscid Burgers equation . . . . .	6
1.2	Thermalization in the Galerkin-truncated Euler equation . . . . .	11
1.3	Onset of thermalization in the Galerkin-truncated Burgers equation . . . . .	13
1.4	Energy cascade picture in turbulent flows . . . . .	17
1.5	Extreme events in fully-developed turbulence . . . . .	19
1.6	Energy spectrum of turbulent flows . . . . .	23
1.7	Structure function exponents $\zeta_p$ : From models and data . . . . .	23
1.8	Features of K41 in the EDQNM model . . . . .	26
2.1	Illustration of thermalization <i>via</i> energy spectrum and strain field . . . . .	34
2.2	Visual clues of thermalization in vorticity field isosurfaces . . . . .	36
2.3	Perturbed vortex sheets showing onset of thermalization . . . . .	39
2.4	Perturbed vortex sheets (with a variation) showing onset of thermalization . . . . .	42
2.5	Vortex sheets disturbed by Taylor-Green flow, showing onset of thermalization . . . . .	44
2.6	Perturbed vortex filament showing onset of thermalization . . . . .	45
3.1	Shock formation in the Burgers equation . . . . .	51
3.2	Entropy solution: Dissipating through shocks . . . . .	56
3.3	Galerkin-truncated vs Entropy solutions for the Burgers equation . . . . .	57
3.4	Birth of <i>Tygers</i> for $\sin(x)$ initial condition . . . . .	59
3.5	Galerkin-truncated vs Entropy vs Purged solutions for the Burgers equation . . . . .	66
3.6	Energy in the boundary layer during the <i>Tyger</i> purging . . . . .	70
3.7	Convergence of the Purged solution to the Entropy solution . . . . .	71
3.8	Suppression of oscillations in GT Euler equation . . . . .	76

4.1	Thermalized solution to the GT Burgers equation . . . . .	85
4.2	PDF of velocity in the thermalized solutions . . . . .	86
4.3	Section of the difference field . . . . .	89
4.4	Growth of the decorrelator . . . . .	95
4.5	PDF of direction cosines of the difference field . . . . .	97
4.6	Error between linearized and actual decorrelator . . . . .	97
4.7	Lyapunov exponents of thermalized fluid . . . . .	99
4.8	Saturation of the decorrelator . . . . .	100
4.9	Spatial spread of the decorrelator . . . . .	101
4.10	Autocorrelation function in a thermalized fluid . . . . .	102
5.1	Multifractal nature of the dissipation field . . . . .	107
5.2	Local partition function . . . . .	110
5.3	Correlation dimension field . . . . .	111
5.4	Aspects of local multifractality and correlation with dissipation . . .	113
5.5	Multifractal spectrum for a non-intermittent turbulent flow . . . . .	115
6.1	Map of statistical theories and closure models . . . . .	121
6.2	Area of integration for the spectral transfer term . . . . .	129
6.3	Pseudo-color plot of Dynamo effect for various dimensions . . . . .	140
6.4	Growth of a magnetic energy: Dynamo—No-dynamo . . . . .	141
6.5	Nature of transfer terms for the dynamo effect . . . . .	142
6.6	Transfer <i>vs</i> Diffusion terms for the dynamo effect . . . . .	143
6.7	Magnetic energy spectrum in the model . . . . .	145
A.1	Local vs Global characterisation of multifractality in Curdling model	150

# Contents

<b>List of publications</b>	<b>viii</b>
<b>List of figures</b>	<b>ix</b>
<b>Abstract</b>	<b>xiii</b>
<b>1 Introduction</b>	<b>1</b>
1.1 Preamble . . . . .	1
1.2 The Euler Equation for <i>Ideal</i> Fluids . . . . .	3
1.3 Fully-developed Turbulence: The Navier-Stokes equation . . . . .	15
1.4 An Overview of the Thesis . . . . .	27
<b>2 Genesis of Thermalization in the 3D Galerkin-truncated Euler equation</b>	<b>31</b>
2.1 Thermalization for a <i>Generic</i> flow . . . . .	33
2.2 The Onset of Thermalization: What <i>Model Flows</i> Tell Us? . . . . .	37
2.3 The Phenomenological Picture . . . . .	46
<b>3 Dissipative solutions from Galerkin-truncated Inviscid Hydrodynamics</b>	<b>49</b>
3.1 Entropy <i>vs</i> Thermalizing solutions . . . . .	50
3.2 Suppressing Thermalization in the Galerkin-truncated Burgers equation . . . . .	61
3.3 Suppression of Oscillations in the Galerkin-truncated Euler solution . . . . .	75
<b>4 Many-body Chaos in Thermalized fluids</b>	<b>79</b>
4.1 Fundamental Questions in Statistical Physics . . . . .	79
4.2 Decorrelators in Thermalized fluid . . . . .	85

4.3	Thermal Bound of Lyapunov exponents . . . . .	91
<b>5</b>	<b>Local Nature of Multifractality in Turbulence</b>	<b>105</b>
5.1	Coarse-grained Local Measurement . . . . .	107
5.2	Correlation with Dissipation . . . . .	112
<b>6</b>	<b>Dynamo Problem in the EDQNM -MHD Closure Model</b>	<b>118</b>
6.1	Introduction to the Dynamo Problem . . . . .	118
6.2	EDQNM-MHD Closure model . . . . .	121
6.3	Dynamo Problem in the EDQNM-MHD Framework . . . . .	137
<b>7</b>	<b>Conclusion</b>	<b>146</b>
<b>A</b>	<b>Multifractal analysis of Curdling model</b>	<b>149</b>
A.1	Localized Multifractality Dominating the Global Analysis . . . . .	149
<b>B</b>	<b>EDQNM-MHD model</b>	<b>152</b>
B.1	Isotropic Quasi-Normal equations . . . . .	152
B.2	$d$ -dimensional Integral . . . . .	155
B.3	Conserved quantities in the Quasi-Normal model . . . . .	156
B.4	Numerical Simulation of EDQNM-MHD . . . . .	159
	<b>References</b>	<b>162</b>

# Abstract

Finite-dimensional inviscid hydrodynamical equations have solutions that eventually thermalize with a Gibbsian distribution and energy equilibrium across Fourier modes. We examine the route to thermalization in the Galerkin-truncated three-dimensional Euler equation and show how this phenomenon can be effectively reduced to a one-dimensional problem. We also discuss strategies to prevent thermalization, which are essential but elusive so far, to numerically obtain dissipative (weak) solutions and discuss their importance for conjectures on the blow-up problem. We then show how thermalized fluids are an ideal candidate to study classical many-body chaos, and in particular, by using decorrelators, we show that the Lyapunov exponent scales as the square root of the temperature, consistent with recent studies and conjectures from other condensed matter systems.

In the end, we present a local multifractal characterization of turbulent structures and a novel attempt to study the dynamo problem in the framework of the EDQNM closure model.

# Chapter 1

## Introduction

### 1.1 Preamble

Slow moving and highly viscous classical fluids move in a *laminar* and orderly fashion. This is true, for example, when we look at the typical motion of oil or honey. However, for fluids such as atmospheric winds which small enough *viscosities* or high speeds leading to large enough *Reynolds* numbers, the flow quickly becomes chaotic, out-of-equilibrium, irreversible and intermittent. In short, they are *turbulent*. Indeed, most flows are turbulent [1].

These range from the astrophysical to the terrestrial scales and beyond. In astrophysics, for example, turbulence is central to a diverse set of phenomena such as the generation of large scale magnetic fields (the dynamo problem), the formation of protoplanets and the dynamics of solar winds [2–4]. Going down in scale, atmospheric flows are nearly always turbulent and their role in determining how quickly rain droplets form in warm clouds or how ice crystals orient in cold clouds has gained attention in recent years [5, 6]. At more terrestrial scales, turbulent flows determine to a large extent how pollutants disperse or even the distribution of volcanic ash in air [7]. Marine turbulence is just as ubiquitous and affect not just the

energy balance of our oceans but also a key component in nutrient mixing and the motion of small and large organisms [8]. Beyond such *natural* settings, turbulence remains a most vital component in several important applications. These range, to name a few, from the boundary layers which form over the wings of aircrafts, the laminar-to-turbulent transitions in pipe flows, or the complex motion whenever there is flow past obstacles [9].

All of this suggests that while turbulence is often labelled as “*the last great unsolved problem of the classical physics*” [1], in reality what one deals with is a large set of different problems all of which pose significant challenges in various branches of the natural sciences. Thus while the key questions for mathematicians may well be in proofs of smoothness or not in solutions of the underlying equations of fluid mechanics, for the fluid dynamicist the most interesting aspects could lie in questions of instabilities and transition. Similarly the astrophysicist and plasma scientist may worry primarily about questions of the fate of magnetic fields in highly turbulent plasmas whereas the geophysicist and climate scientist are increasingly concerned about how the fundamental properties of turbulence relate to the health and future of our oceans and weather. An engineering perspective is often one which is pinned to the issue of how turbulence can be characterized or controlled: This is as much true for flows in channels as it is for aerodynamic stability of automobiles, trains and aeroplanes.

While it is hard to have a precise definition of turbulence, it is fair to say that turbulence is the solution of the Navier-Stokes equation (or flows in nature or in the laboratory) in the limit of very large Reynolds numbers [10, 11]. Typically, such flows remain in a non-equilibrium steady state where the energy injected is, on average, balanced by the energy lost through viscous dissipation. In practice, there are three essential ingredients which make flows turbulent. The first of these is *viscosity*—akin to a frictional force between fluid elements resisting motion or shear—and commonly understood as the *thickness* of the fluid which sets honey apart from water. The viscous effects, as we shall see subsequently, are essentially dominant at the small scales of a flow. The second ingredient is the drive or the

energy injection which actually makes a fluid move by stirring it up. As in most, especially three-dimensional flows, this is a large-scale effect and we inject energy in fluids routinely when we stir a cup of tea or switch on a fan. Finally, boundaries determine the precise finer details of a turbulent flow and indeed can even determine whether a flow remains laminar or turbulent. Indeed the flow past a puckered golf ball will have a different spatio-temporal structure than that past a smooth cricket ball. Thus, some of the most important problems in engineering, especially in efficient transportation, involves understanding the role of boundaries.

In this Thesis, our approach is primarily at the interface of statistical physics and applied mathematics. The canonical setting for such questions is rooted in the notion of statistically homogeneous, isotropic flows which, as we shall see, in some cases, are not necessarily turbulent. Such flows are of course routinely realised—for example, the flow at the center of a wind tunnel or indeed in the core of a cloud—where the precise nature of surfaces become somewhat irrelevant and the results more *universal*. What this essentially means is that the third ingredient, namely the question of boundaries, no longer play a role by essentially assuming an infinite domain of the fluid or, more precisely, periodic boundary conditions.

Historically, however, the primitive equations of motion for a fluid with velocity  $\mathbf{u}(\mathbf{x}, t)$  at position  $\mathbf{x}$  and time  $t$  was first given by Leonard Euler in the mid 18<sup>th</sup> century for an *ideal* fluid with no viscosity. Our starting point for this Thesis is also the eponymous—and much celebrated—Euler equation and its variant.

## 1.2 The Euler Equation for *Ideal* Fluids

Three-dimensional flows (3D) ideal, incompressible fluids, with the scalar pressure field  $P$ , satisfy the Euler equation,

$$\frac{\partial \mathbf{u}}{\partial t} + \mathbf{u} \cdot \nabla \mathbf{u} = -\nabla P \tag{1.1}$$

augmented by the constraint  $\nabla \cdot \mathbf{u} = 0$  and initial conditions  $\mathbf{u}_0$ .

Amongst the very instances of partial differential equations (PDEs), Euler had presented this description of the motion of an ideal or non-viscous fluid to the Berlin Academy in 1752 and eventually published in its memoirs as “*Principes généraux du mouvement des fluides*” in 1757 [12]. Today, even after 250 years this equation stands as one of the most fundamental in both physics and mathematics [13, 14]. By assuming suitable “smoothness” and decay of the velocity field (sufficiently rapidly) at infinity, it is possible to show that the 3D Euler equation has several conserved quantities [15], globally in time, such as the total energy  $E = \frac{1}{2} \int_{\mathbb{R}^3} |\mathbf{u}|^2$ , helicity  $H = \int_{\mathbb{R}^3} \mathbf{u} \cdot \boldsymbol{\omega}$ , momentum  $M = \int_{\mathbb{R}^3} \mathbf{u}$ , angular momentum  $C = \int_{\mathbb{R}^3} \mathbf{x} \times \mathbf{u}$ , and net vorticity  $\Omega = \int_{\mathbb{R}^3} \boldsymbol{\omega}$ .

However, weak solutions of the 3D Euler equations need not conserve energy [16] which makes such solutions particularly appealing for understanding (*dissipative*) turbulence from the point of view of statistical physics. In fact, Onsager’s pioneering work [17, 18] was a way to construct a mathematical framework in which the limit of infinite Reynolds number (Re) turbulence may be the manifestation of weak solutions of the inviscid Euler equation and hence the energy dissipation in real turbulence may reach a non-vanishing limit as  $Re \rightarrow \infty$ . This conjecture, which has gained subsequent support from numerical simulations and experimental measurements, is known as *dissipative anomaly* [19]. Briefly stated, non-conservation of energy, in either the infinite Reynolds number limit of *real turbulence* or in the sense of weak solutions of the inviscid Euler equations, is guaranteed not through an explicit viscous dissipation but the lack of *sufficient* smoothness of the velocity field itself. The latter is often defined by the Hölder exponent  $h$  that satisfies:

$$\langle |\mathbf{u}(\mathbf{x} + \mathbf{r}) - \mathbf{u}(\mathbf{x})| \rangle \sim r^h \tag{1.2}$$

Precisely formulated, weak solutions of the Euler equation admit anomalous dissipation when the Hölder exponent  $h < 1/3$  and remain energy

conserving for  $h \geq 1/3$ . However the proof of this still remains one of the most significant open questions in mathematics [20].

These ideas are of course intimately connected to the notion of whether there is a finite-time blow-up in the solutions of the 3D Euler equation itself. In other words, starting with sufficiently smooth initial data, could the solution to the three-dimensional Euler equation develop singularities in a finite time? This is recognised—along with its counterpart for the Navier-Stokes equation—as single most fundamental question at the interface of fluid dynamics and analysis, while providing a tantalising prospect of understanding the onset of turbulence as a manifestation of the appearance of such singular solutions.

While the question remains an open one still, its analogue for the analytically more tractable one-dimensional (1D) inviscid Burgers equation [21, 22]

$$\frac{\partial u}{\partial t} + u \frac{\partial u}{\partial x} = 0 \tag{1.3}$$

is solved and provides a way to make sense of this question. By assuming the initial data  $u(x, 0) = u_0(x)$  to be analytic—such as trigonometric functions—with the complex singularity sitting at infinity, it is possible to predict if and when the solution to equation (1.3) would develop a singularity. The simplest approach to this would be construct the Lagrangian map:

$$a \mapsto x(a) = a + tu_0(a). \tag{1.4}$$

The solution to the Burgers equation turns singular when the Jacobian  $\partial x/\partial a$  of this map vanishes. Trivially, the corresponding time  $t^*$  for a blow-up is just

$$t^* = \left( \max \left| \frac{du_0(x)}{dx} \right| \right)^{-1}. \tag{1.5}$$

For simplicity, for  $u_0(x) = \sin(x)$ , then the time of blow-up  $t^* = 1$  is finite. Such an approach also allows us to easily detect the position, in both Eulerian and Lagrangian coordinates, of the *position* of the singularity. In fact, for  $0 \leq t \leq t^*$ , we

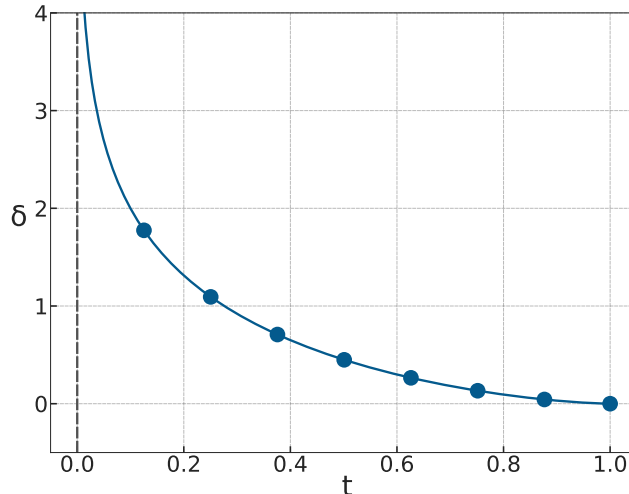


Figure 1.1: Tracing the imaginary part of the complex singularity position,  $\delta(t)$ , as in Eq. (1.6), for the initial condition  $u_0(x) = \sin(x)$ . Starting from  $\delta(0) = -\infty$ , reaches the real axis in a finite time,  $\delta(t^* = 1) = 0$ .

can locate the position of the singularity (using equation (1.5)) as:

$$x^*(t) = i \left[ \cosh^{-1} \left( \frac{1}{t} \right) - t \sinh \left( \cosh^{-1} \left( \frac{1}{t} \right) \right) \right] \quad (1.6)$$

If we denote the imaginary part of the singularity as  $\text{Im}\{x^*(t)\} = \delta(t)$ , then for such an initial condition, the singularity at  $t = 0$  is at infinity on the imaginary line, and hits the real axis ( $\delta = 0$ ) at  $t^* = 1$ , as shown in figure 1.1. However, since there is a finite-time blow-up as we saw above, at time  $t \lesssim t^*$ , the (pole) singularity ought to be close to the real line. Hence, to leading order  $\mathcal{O}(t^* - t)$ , the singularity closest to the real line can be obtained by expanding  $\sin(a)$  up to cubic order:

$$x = (t^* - t)a + \frac{a^3}{6}; \quad \frac{\partial x}{\partial a} = t^* - t + \frac{a^2}{2}. \quad (1.7)$$

This inevitably leads to  $a^*(t) = \pm i\sqrt{2(t^* - t)}$  and, in Eulerian coordinates,  $x^*(t) = \pm \frac{2\sqrt{2}}{3}i(t^* - t)^{3/2}$ . Physically, the finite-time singularities manifest themselves as “shocks” in the solution of the 1D Burgers equation.

Unfortunately, such simple formulations do not exist for the 3D Euler equation to definitively prove the existence of a finite  $t^*$  for a blow-up. Nevertheless, several mathematically rigorous criterion exist that can be used to rule out or rule

in finite-time singularities in the Euler equation. Perhaps the one which makes the strongest contact with our physical intuition of turbulence owes itself to the work of Beale, Kato and Majda [23, 24] (BKM theorem). The theorem states, if a smooth solution of the three-dimensional Euler equation can be continued till  $t^*$ , and  $t^*$  is the first such time that the solution satisfies for the vorticity field  $\boldsymbol{\omega} = \nabla \times \mathbf{u}$ ,

$$\int_0^{t^*} dt \|\boldsymbol{\omega}(t)\|_{L^\infty} = \infty \quad (1.8)$$

then the solution becomes singular at  $t^*$ . While a detailed review of the many important works on the regularity of the 3D Euler equation and its connections to turbulence—beginning with seminal 1934 work of Leray [25, 26]—is well beyond the scope of this Thesis, it is perhaps worth looking at one such approach in some detail since it makes an obvious connection with spectral methods of simulations on one hand and the fundamental limitations of the same in practice. This is the so-called *analyticity* strip method [27] which, in principle, seems most compatible with numerical simulations as a tool for probing regularity.

### 1.2.1 The Question of Finite-Time Blow-Up: Analyticity Strip Method

Assuming analyticity of the velocity field (at least up to some time  $T$ ) guarantees that potential singularities are always in the imaginary domain. To simplify our analysis, we assume at some time  $t \leq T$  the velocity field  $\mathbf{u}$  to have one or more complex pole singularities at positions  $z_i = x_i + i\delta_i$ . The expansion of complex function  $u(z)$  about a pole at  $z^*$  is

$$u(z) = (z - z^*)^\mu \sum_{s=0}^{\infty} c_s (z - z^*)^s, \quad \text{Re}\{\mu\} \geq 1 \quad (1.9)$$

How does the Fourier transform of such a velocity field  $\hat{u}_k = \int_{-\infty}^{\infty} dz e^{ikz} u(z)$  behave? The contribution from  $z^*$ , that has its imaginary part  $\delta = \text{Im}\{z^*\}$  closest to the real axis, is dominant to the integral. One can show it in

the asymptotic limit [28]

$$\approx -\frac{2 \sin(\pi\mu)}{k^{\mu+1}} \exp\left(i\left[kz^* - \frac{\pi}{2}\mu\right]\right) \sum_{s=0}^{\infty} k^{-s} c_s \Gamma(\mu + s + 1)$$

for  $k \gg 1$ ,  $\hat{u}_k \sim k^{-(\mu+1)} e^{-\delta k}$  (1.10)

To summarize, the analyticity strip method suggests that an obvious way to conjecture for or against a finite-time singularity is to numerically solve the Euler equation and measure the width of the analyticity strip, that is  $\delta$ , the distance to the real domain of the nearest complex singularity. By assuming analyticity, at least up to a hypothetical time of blow-up  $t^*$ , this procedure thus reduces to measuring the Fourier modes of the velocity field  $\hat{u}_k \sim \exp\{-\delta(t)k\}$  (ignoring vectors for convenience), for large wavenumbers  $k$ , and thence,  $\delta$  as a function of time  $t$ . Therefore, a numerically compelling *proof* for a finite-time blow-up is to show  $\delta(t) \rightarrow 0$  in a finite time.

Simple as it sounds, such an approach unfortunately runs into a severe problem in its implementation. This is because spectral accuracy demands that what we actually solve is the Galerkin-truncated Euler equation, with finite degrees of freedom, and not quite the PDE (1.1). While this may seem a small detail, in reality it leads to very different physics as we explain below.

## 1.2.2 The Galerkin-truncated Euler Equation: Absolute Equilibria

The Galerkin-truncated three-dimensional Euler equation is written as

$$\frac{\partial \mathbf{v}(\mathbf{k}, t)}{\partial t} = -\mathbb{P}_{k_G}[\mathbf{v} \cdot \nabla \mathbf{v} + \nabla P], \quad \mathbf{v}(\mathbf{k}) \cdot \mathbf{k} = 0 \quad (1.11)$$

where  $\mathbb{P}_{k_G}$  is a low-pass Galerkin projector which sets the velocity modes with wavenumbers  $|\mathbf{k}| \geq k_G$  equal to 0, where  $k_G$  is a positive (large) integer. Thus,

for  $2\pi$  periodic functions, the Galerkin-projection ensures

$$\mathbb{P}_{k_G} \mathbf{v}(\mathbf{x}) = \sum_{|\mathbf{k}| \leq k_G} e^{i\mathbf{k}\cdot\mathbf{x}} \hat{\mathbf{v}}(\mathbf{k}) \quad (1.12)$$

This modification, while preserving the nonlinear structure of this equation, ensures a strict conservation of energy and phase space as we will see below. Of course, the initial conditions are projected likewise:  $\mathbf{v}_0 = \mathbb{P}_{k_G} \mathbf{u}_0$ .

For what follows in this Thesis, it's useful to actually write the Galerkin-truncated (GT) equation (1.11) in Fourier space. Written in component-form for the Fourier modes  $\hat{v}_\alpha(\mathbf{k})$ , this reduces to

$$\frac{\partial \hat{v}_\alpha(\mathbf{k})}{\partial t} = -\frac{i}{2} \mathcal{P}_{\alpha\beta\gamma} \sum_{\mathbf{q}} \hat{v}_\beta(\mathbf{q}) \hat{v}_\gamma(\mathbf{k} - \mathbf{q}) \quad (1.13)$$

where the convolution (as well as the initial conditions) is projected on the Fourier subspace defined by the truncation wavenumber  $k_G$ , that is  $|\mathbf{k}|, |\mathbf{q}|, |\mathbf{k} - \mathbf{q}| \leq k_G$ . The additional coefficient  $\mathcal{P}_{\alpha\beta\gamma}^{(k)} = k_\beta \mathbb{P}_{\alpha\gamma}^{(k)} + k_\gamma \mathbb{P}_{\alpha\beta}^{(k)}$ , where  $\mathbb{P}_{\alpha\beta}^{(k)} = \delta_{\alpha\beta} - k_\alpha k_\beta / k^2$  (with  $\delta_{\alpha\beta}$  is the Kronecker delta) arises from the pressure gradient and ensures incompressibility  $\mathbf{k} \cdot \mathbf{v}(\mathbf{k}) = 0$ .

The Fourier space version of the Galerkin-truncated Euler equation is explicitly of the form of a finite-dimensional, non-dissipative, dynamical system [29, 30] defined as

$$\frac{dy_a}{dt} = \sum_{b,c=1}^N A_{abc} y_b y_c \quad (1.14)$$

where the constant coefficients  $A_{abc}$  have the properties,

$$A_{abc} = A_{acb}, \quad A_{aab} = 0 \quad \text{and} \quad A_{abc} + A_{bca} + A_{cab} = 0 \quad (1.15)$$

This implies the global energy conservation

$$\frac{d}{dt} \sum_{a=1}^N |y_a|^2 = 0 \quad (1.16)$$

and the incompressibility of the phase space flow with the generalized velocity field  $\frac{dy_a}{dt}$ :

$$\sum_a \frac{\partial}{\partial y_a} \left( \frac{dy_a}{dt} \right) = 0 \quad (1.17)$$

With a collection of systems with a prescribed density  $\rho(y_a, t)$ , the generalized continuity equation is

$$\frac{\partial \rho}{\partial t} + \sum_a \frac{\partial}{\partial y} (\rho \dot{y}_a) = 0 \quad (1.18)$$

when combined with equation (1.17) gives

$$\frac{d\rho}{dt} = \frac{\partial \rho}{\partial t} + \sum_a \dot{y}_a \frac{\partial \rho}{\partial y_a} = 0. \quad (1.19)$$

This is the Liouville's theorem for our dynamical system conserving the phase-space density  $\rho$  along its trajectory. Hence from Liouville's theorem [31], the *a priori* probability of finding this system in any region of this phase space is proportional to the volume of this region. By looking for equilibrium solutions to the equation (1.19), that is  $\frac{\partial \rho}{\partial t} = 0$ , we use an analogy with statistical thermodynamics. The conservation of energy allows the particular Boltzmann-Gibbs equilibrium [31]:

$$\mathcal{P}(y_a) = \frac{1}{\mathbb{Z}} \exp\left(-\beta \sum_a y_a^2\right) \quad (1.20)$$

where  $\mathbb{Z}$  is the partition function of the system. From this point of view of canonical ensemble, we expect the system to reach this distribution, and the mean energy of  $y_a$  will be

$$\langle y_a^2 \rangle \sim \frac{1}{\beta} \quad (1.21)$$

which is independent of 'a'. Thus statistically every mode of the Fourier components of velocity must be in energy equipartition, with a Gibbsian probability distribution [29]. Therefore the energy spectrum, at suitably long times, behave in three dimensions as

$$E(k) = \begin{cases} \sim k^2 & \text{for } k \leq k_G \\ 0 & \text{for } k > k_G \end{cases} \quad (1.22)$$

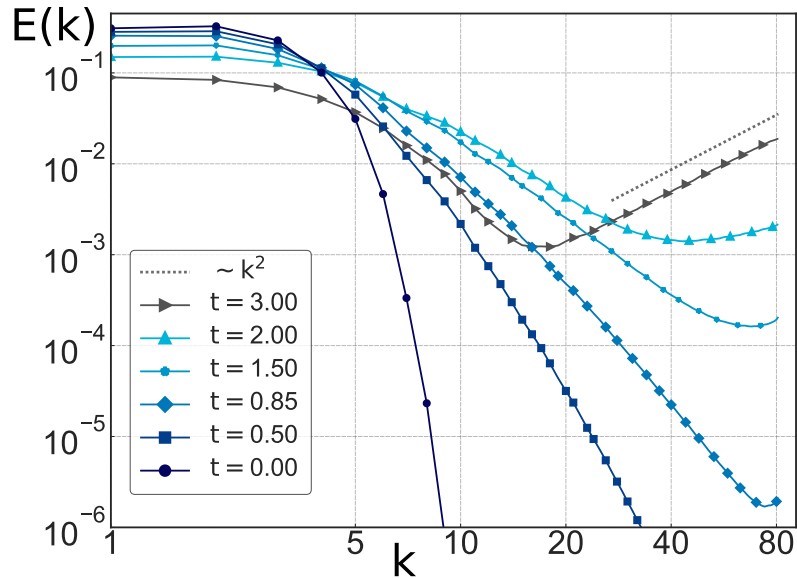


Figure 1.2: Energy spectrum for the incompressible GT Euler equation, taken from DNS with  $N^3 = 256$  grid points, illustrating the transient stages—thermalization beginning from the largest (active) wavenumbers—with a growing  $k^2$  spectrum at the tail of the spectrum.

The  $E(k) \sim k^2$  (or in  $d$ -dimension,  $E(k) \sim k^{d-1}$ ) is essentially a statement of energy equipartition in a fluid which is *thermalized* or in *absolute equilibrium*. A passing familiarity with turbulence would suggest that the emergent thermalized flow of the Galerkin-truncated equation has little in common with turbulent flows or indeed solutions of the Navier-Stokes equation for large enough Reynolds numbers. For starters, the energy spectrum for turbulence  $E(k) \sim k^{-5/3}$  is in stark contrast to the equipartition spectrum. Nevertheless, it is worth recalling that theoretically such approaches have been used historically, with varying successes, not only to *understand* turbulence—the works of T. D. Lee, E. Hopf [32, 33] and somewhat later by R. H. Kraichnan [34] to understand the dual cascade in two dimensions—but also generalised more recently for models of decimated turbulence to investigate the origins of intermittency and *critical* dimensions [35] where the Kolmogorov picture coincided with the absolute equilibrium solution.

While the fact that Galerkin-truncated equation ought to thermalize is obvious, it was *only* in 2005 that Cichowlas *et al.* [36] showed numerically the existence of such thermalized solution and, in the process, the long-lived transients

like in the Navier-Stokes equation. Indeed at intermediate times, it was shown that a given wavenumber  $k_{\text{th}}(t)$  separates the two regimes:

$$E(k) \sim \begin{cases} k^{-5/3} & \text{for } k \leq k_{\text{th}} \\ k^2 & \text{for } k \geq k_{\text{th}} \end{cases} \quad (1.23)$$

Discussing the decreasing behaviour of  $k_{\text{th}}(t)$ , starting from  $k_{\text{th}}(0) = k_{\text{G}}$  as a form of effective dissipation of fluid, modes having  $|\mathbf{k}| < k_{\text{th}}$ , into the thermal bath governed by modes  $|\mathbf{k}| \geq k_{\text{th}}$ . This transient regime is what was described earlier, as the state of the ideal fluid model in the far-from-equilibrium regime, has a  $k^{-5/3}$  spectrum for  $k < k_{\text{th}}(t)$ . Figure 1.2 shows the energy spectrum  $E(k)$  for the Galerkin-truncated Euler equation at different times, starting with a large scale initial condition, showing the emergence of  $k^2$  behaviour (grey line at  $t = 3$ ). The small-scale thermalized modes act as a fictitious microworld providing an effective viscosity to the large-scale modes. Further, if the rate at which the thermalized modes gain energy, equivalent to the dissipation of energy from the turbulent modes ( $k < k_{\text{th}}(t)$ ), it agrees well with a typical case seen in a Navier-Stokes flow. This depicts a *relevance* as at least in the transient regime, the truncated Euler equation has some form of turbulence, which needs further investigation. Such emergence was also seen in an inviscid EDQNM model by Bos and Bertoglio [37]. In reference. [38], Krstulovic and Brachet presented a phenomenological two-fluid model for what is observed in a spectral-truncated three-dimensional Euler equation.

The underlying mechanisms which lead to absolute equilibria states in three dimensions however remained unanswered and was *only* solved in 2011 for the one-dimensional Burgers equation [39]. The same prescription for Galerkin-truncation of course extends *mutatis mutandis* to the Burgers equation (with  $2\pi$  periodic boundary conditions allowing for a simple Fourier expansion) in one dimension, with a compact  $k_{\text{G}}$  support in Fourier space:

$$\frac{\partial \hat{v}_k}{\partial t} = -\frac{ik}{2} \sum_q \hat{v}_q \hat{v}_{k-q}, \quad \text{all } |k|, |q|, |k-q| \leq k_{\text{G}} \quad (1.24)$$

In a nutshell, beginning with simple initial conditions (such as  $v_0 = \sin(x)$ ),

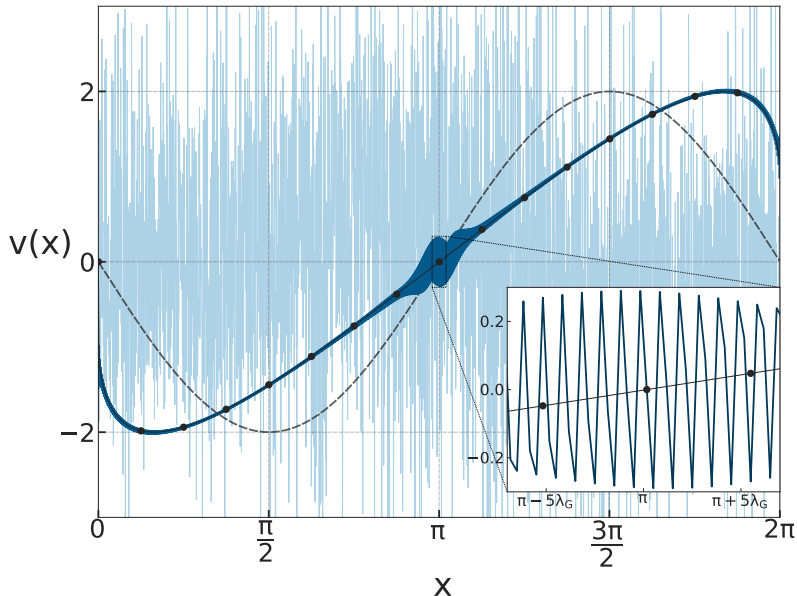


Figure 1.3: Illustrating onset of thermalization in the GT Burgers equation: For the initial condition,  $u_0(x) = -2\sin(x)$  (*dashed black*), solution at  $t \gtrsim t^* = 0.5$  (*dark blue*) shows oscillation (see Ref. [39]) appearing around the resonance point  $x = \pi$ , contrasted with the Entropy solution (*black circles*). *Inset* showing a zoomed in plot around  $x = \pi$ , showing the  $\lambda_G = 2\pi/k_G$ -wavelength oscillations. At later times ( $t \approx 4.0$ ), the GT solution (*light blue*) is seen fully thermalized.

the Galerkin-truncation results in, within a finite time, triggering of oscillations in *prescribed* locations that onsets the thermalization in the system [39]. These localized oscillations, with a wavelength  $\lambda_G = 2\pi/k_G$ , being the manifestation of the energy pumped into the shocks, soon grows rapidly in amplitude and with a positive strain stretching them far in real space, interacts back with the system to spread its extent of thermalization to nearby wavenumbers, eventually converging to the solution with Gibbsian statistics [40–43].

Nevertheless, these Hamiltonian flows have other reasons for studying them, mainly from the fact that when these solutions to the truncated Euler equations are in the far-from-equilibrium regime then their equilibrating dynamics should resemble that of the turbulent flows, after all the non-linear structure remains essentially the same for both. To see it more clearly, consider the truncated Euler equations with an initial condition having a finite but non-zero energy per unit mass that has reached an energy spectrum as given by the equation (1.22). Now, if the  $k_G$  is modified, and taken to the limit of  $k_G \rightarrow \infty$ , it would take forever and a state

of statistical equilibrium will never be attained as the velocity field evolves in time according to the Euler equation. This inability to reach equilibrium in the ultraviolet regime is one of the main characteristics of turbulence. This limit of  $k_G \rightarrow \infty$  in the Galerkin-truncated Euler equations cannot be interchanged with singular limit of  $\nu \rightarrow 0$  in the Navier-Stokes equation, because of the so-called dissipative anomaly in the latter. But the key observation would be that, the net enstrophy will diverge in the limit for the former, establishing the transfer of energy to smaller scales (building higher velocity gradients) in the transient stages (in the equilibration). Interestingly, the Galerkin-truncation on the spectral space has other advantages when equipped correctly.

In the last couple of decades or so, since the work of L'vov *et al.* [44], and subsequently Frisch *et al.* [35], the generalization of the idea of Galerkin-truncation to fine-tune triadic interactions has led to a narrowing of the gap between equilibrium statistical physics and turbulence. This, in particular, has been used most importantly in deepening of our understanding of central questions in 3D turbulence such as intermittency [35, 45–49] and the issue of bottlenecks [50–52] in the energy spectrum.

Further such equilibrium classical and quantum many-body systems have been used recently to address the question of relating the measure of chaos, such as the Lyapunov exponent  $\lambda$ , butterfly speed  $v_B$  [53, 54] to the thermodynamical variables like the temperature  $T$ . In the context of a dynamical system displaying chaos, if an initial disturbance  $\delta \mathbf{x}_0$  grows to  $\delta \mathbf{x}$  at time  $t$ , then the *sensitivity* to the initial condition is commonly characterized by the *leading* Lyapunov exponent of the system defined by

$$\lambda := \lim_{t \rightarrow \infty} \frac{1}{t} \lim_{|\delta \mathbf{x}_0| \rightarrow 0} \ln \left( \frac{|\delta \mathbf{x}(t)|}{|\delta \mathbf{x}_0|} \right) \quad (1.25)$$

The butterfly velocity  $v_B$  is defined for spatially extended system [55] as the velocity with which the perturbation propagates. Quantities such as

cross-correlators and decorrelators are constructed in classical systems [55–57] to quantify their sensitivity to initial conditions ( $\lambda$  and  $v_B$ ) from their spatio-temporal variation, while the out-of-time-ordered commutators (OTOC) [58] are the leading diagnostic in studying the scrambling of information for the quantum systems [59, 60]. Thermalized fluids resulting from these Galerkin-truncated systems, such as the 1D Burgers equation and the 3D Euler equation are remarkable many-body systems that exhibit intrinsic chaos, with hydrodynamical nature of interactions. Thus these are apt models to probe fundamental questions in statistical physics relating thermalization, equilibration and ergodicity [40, 61]. Most recently, the possibilities of small-scale thermalization in real flows [62] have provided further impetus to studying the interplay of equilibrium statistical physics and turbulence, often in dimensions that are not necessarily integer [63, 64].

Fully-developed turbulence, of course, is dissipative. It took several decades since Euler’s work on inviscid, ideal flows for Claude Navier and Gabriel Stokes to (independently) construct the mathematical framework—the Navier-Stokes equation—to understand *real* classical, Newtonian fluids by incorporating the effects of (kinematic) viscosity.

### 1.3 Fully-developed Turbulence: The Navier-Stokes equation

By using the same unit-density formulation as before, the three-dimensional Navier-Stokes equation is

$$\frac{\partial \mathbf{u}}{\partial t} + \mathbf{u} \cdot \nabla \mathbf{u} = -\nabla P + \nu \nabla^2 \mathbf{u} + \mathbf{f} \quad (1.26)$$

augmented, as before, by the constraint  $\nabla \cdot \mathbf{u} = \mathbf{0}$  to ensure incompressibility, and initial conditions  $\mathbf{u}_0(\mathbf{x})$ . The crucial difference from the Euler equation are the inclusion of the viscous dissipation term, with  $\nu$ , the coefficient of kinematic

viscosity, and an external force  $\mathbf{f}$  (stochastic or deterministic) is *often* used to drive the solution to a statistically steady state, where, on average, the energy injected  $\langle \mathbf{f} \cdot \mathbf{u} \rangle$  is balanced by the energy dissipated  $\epsilon$  through viscosity. For any characteristic scale  $L$  (and we later discuss a more specific and useful notion of what should be the characteristic scale), the Reynolds number of the flow—which is a measure of the inertial to viscous forces—is defined as  $\text{Re} \equiv UL/\nu$  [65], where the velocity  $U$  is the one associated with scale  $L$ . Flows are turbulent, when the Reynolds number is *very* large.

While the mathematical questions related to the existence of smooth and meaningful solutions of the Navier-Stokes equation remains an outstanding question—it is in fact one of the remaining unsolved Millennium Problems of the Clay Institute [66]—several aspects of fully-developed turbulence is now reasonably well understood. While we cannot do justice in this short Chapter to all the many building blocks in our understanding [9, 30, 67, 68], it is important to summarize the central results which form the underpinnings of a statistical physics perspective of full-developed turbulence.

Three-dimensional turbulence is *sustained*—non-equilibrium steady states—by the effects of energy injection  $\epsilon_{\text{inj}} = \int \mathbf{f} \cdot \mathbf{u}$  at large length scales  $L$  and viscous dissipation  $\epsilon = \int \nu(\nabla\mathbf{u})^2$  at small length scales  $\eta = \nu^{3/4}/\epsilon^{1/4}$ , and it is reasonable to assume that the physics ought to be non-universal and involve the details of the system at scales  $r \gtrsim L$  and  $r \lesssim \eta$ .

An intuitive, but, instructive way to imagine the process by which the injected energy from the large length scales are transferred to scales  $\sim \eta$  where viscous effects become dominant is the cascade picture due, originally, to Richardson [69]. This assumes that the large energy containing eddies of scale  $L$  (where the injection happens) break-up into subsequent sequences of daughter eddies of a smaller scale which in turn break-up in to yet smaller daughter eddies while retaining, in sum, the total energy input at the first generation. Given the structure of the dissipative term, energy dissipation via viscosity is minimal as long as the

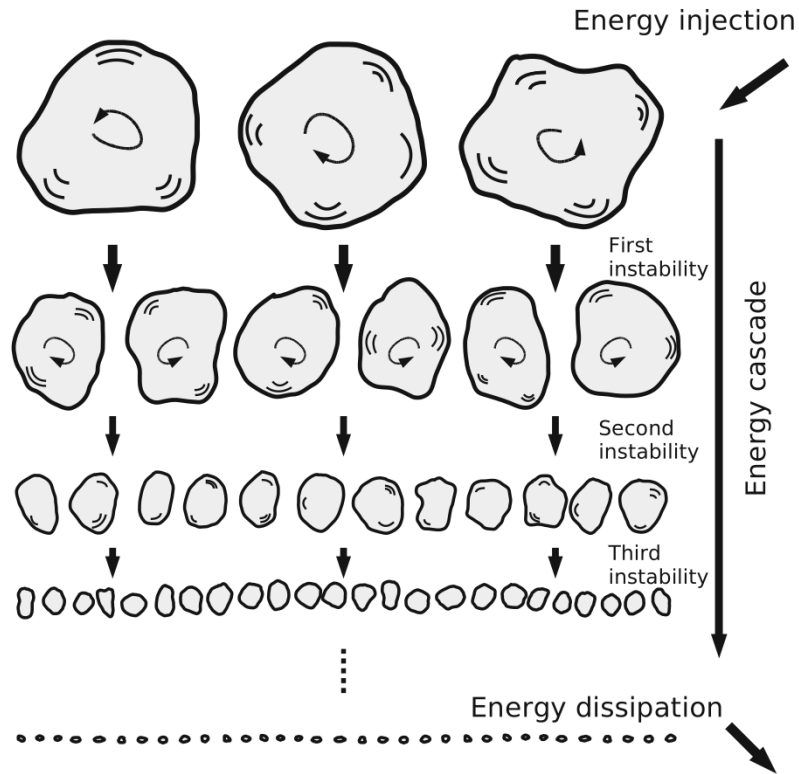


Figure 1.4: Energy cascade picture in turbulent flows, according to Richardson [69] and Kolmogorov [70]. Figure adapted from Ref. [71]

scales are large enough (or wavenumbers small enough). Eventually this *forward cascade* of the energy flux, say  $\Pi$ , yields eddies of size  $\eta$  where viscous effects are no longer negligible and energy dissipates at a rate  $\epsilon$ . This phenomenological explanation is best visualized in figure 1.4, as illustrated in [67]. Thus this cascade picture suggests that on average  $\epsilon_{\text{inj}} = \Pi = \epsilon$  with the so-called inertial range of scales—where we have a constant energy flux  $\Pi$ —affected neither by the precise forcing mechanism nor the kind of fluid  $\nu$  being used. Within the framework of homogeneous, isotropic turbulence, it is then reasonable to expect that the inertial range of scales  $r$  (with  $L \gg r \gg \eta$ ) should display some degree of universality in its behaviour.

A more precise formulation of this can be seen in the scale-by-scale energy budget analysis of the Navier-Stokes equation which we summarize here (see Ref. [67] for details). Consider a low-pass filtering operator  $\mathbb{P}_k : f(\mathbf{x}) \mapsto f^<(\mathbf{x}) =$

$\sum_{|\mathbf{q}| < k} \hat{f}(\mathbf{q}) e^{i\mathbf{q}\cdot\mathbf{x}}$ , applying this to the Navier-Stokes equation:

$$\begin{aligned} \frac{\partial \mathbf{u}^<}{\partial t} + \mathbb{P}_k(\mathbf{u}^< + \mathbf{u}^>) \cdot (\nabla \mathbf{u}^< + \mathbf{u}^>) &= -\nabla P^< + \mathbf{f}^< + \nu \nabla^2 \mathbf{u}^< \\ \nabla \cdot \mathbf{u}^< &= 0 \end{aligned} \quad (1.27)$$

The cumulative kinetic energy upto scale  $k$  is defined as  $\mathcal{E}_k = \frac{1}{2} \langle |\mathbf{u}^<|^2 \rangle = \frac{1}{2} \sum_{|\mathbf{q}| \leq k} |\hat{u}(\mathbf{q})|^2$ . Now taking the scalar product of equation (1.27), and averaging over the system domain, that is  $\langle \cdot \rangle = \int d\mathbf{x} \cdot$ , to obtain the *scale-by-scale* energy budget equation for the cumulative energy  $\mathcal{E}_k$

$$\frac{\partial \mathcal{E}_k}{\partial t} + \Pi_k = -2\nu \Omega_k + \mathcal{F}_k \quad (1.28)$$

where  $\Omega_k = \frac{1}{2} \langle |\boldsymbol{\omega}^<|^2 \rangle$  and  $\mathcal{F}_k = \langle \mathbf{f}^< \cdot \mathbf{u}^< \rangle$  are cumulative enstrophy and energy injection respectively. The energy flux  $\Pi_k$  from scales larger than  $l \sim k^{-1}$  to smaller scales due to non-linear interactions is given by

$$\Pi_k = \langle \mathbf{u}^< \cdot (\mathbf{u}^< \cdot \nabla \mathbf{u}^>) \rangle + \langle \mathbf{u}^< \cdot (\mathbf{u}^> \cdot \nabla \mathbf{u}^>) \rangle \quad (1.29)$$

Turbulent flows are of course dissipative, out of equilibrium and the equalities discussed above are only in the sense of averages. Indeed, a measurement of, for example, the velocity field at a single point  $\mathbf{x}$  in time, shows strong fluctuations about a *mean* which makes a statistical approach to understanding the properties of the velocity field all the more important. Furthermore, turbulence is chaotic and intermittent [67, 72–74]. An example of the latter is most strikingly seen in a time-series (or indeed a spatial distribution, as seen in Fig. 1.5a) the kinetic energy dissipation rate  $\epsilon(\mathbf{x}) = 2\nu(\partial_j u_i)^2$ , which shows intermittent high spikes punctuated by quiescent periods [67]. This spiky distribution of the mean energy dissipation rate shows up as a log-normal distribution in  $\epsilon(\mathbf{x})$  and, perhaps more crucially, in the non-Gaussian, large tails of the probability distributions of almost every observable such as velocity increments (in the inertial range), velocity gradients or even acceleration (see Fig. 1.5b).

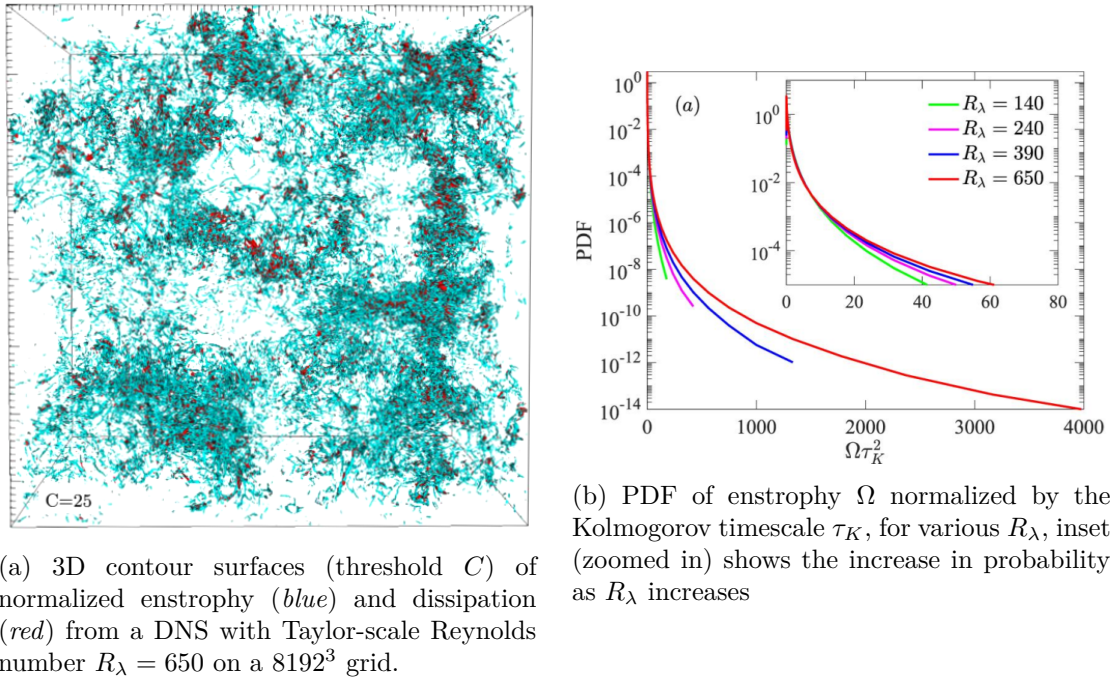


Figure 1.5: Extremity of events in a turbulent flow, studied through DNS. Figure adapted from Buaria *et al.* [75]

A starting point in understanding the statistics of fully-developed turbulence—at least from the point of view of universality—is of course the nature of the two-point correlation functions [76]. These are most conveniently done in terms of the correlation functions of the velocity increments over a scale  $r$  which lies in the inertial range. These correlation functions, historically [77] called as *longitudinal structure functions* and defined precisely via:

$$S_p(r) = \langle |(\mathbf{u}(\mathbf{x} + \mathbf{r}) - \mathbf{u}(\mathbf{x}) \cdot \hat{\mathbf{r}})|^p \rangle \quad (1.30)$$

It is assumed to have a scaling form,

$$S_p(r) \sim r^{\zeta_p} \quad (1.31)$$

within the inertial range of scales. The angular brackets  $\langle \cdot \rangle$  in the definition imply either a time average over the nonequilibrium statistical steady state (when the turbulence is driven) or an average over ensembles of initial conditions.

The *notorious* quadratic non-linearity of the Navier-Stokes equation dispels

chances of calculating the exponents  $\zeta_p$  from a microscopic theory beginning with the equations of motion except for the case of  $p = 3$ . Indeed  $\zeta_3 = 1$  is perhaps the only *exact* result in turbulence which is a direct consequence of the Navier-Stokes equation.

$$S_3(r) = \langle (\delta \mathbf{u}_{\parallel}^3(r)) \rangle = -\frac{4}{5}\epsilon r + 6\nu \frac{d}{dr} \langle (\delta \mathbf{u}_{\parallel}(r))^2 \rangle \quad (1.32)$$

The fact that  $\zeta_3 = 1$  suggests, trivially, that a possible formula for the equal-time scaling exponents should be  $\zeta_p = p/3$ . We now know very well that such simple scaling relations do not hold in turbulence. Nevertheless, the measured values of the second-order structure function  $\zeta_2 \approx 2/3$  or indeed its Fourier counterpart, the energy spectrum  $E(k) = 4\pi k^2 \langle |\tilde{\mathbf{u}}(\mathbf{k})|^2 \rangle \sim k^{-5/3}$  (where the tilde denotes the Fourier transform,  $k = |\mathbf{k}|$ ,  $\mathbf{k}$  is the wave vector) shows that for lower order statistics the dimensional prediction is not *grossly* incorrect.

Despite the lack of validity of  $\zeta_p = p/3$ , this result is a direct outcome of perhaps the single most important phenomenological work in turbulence in the 20<sup>th</sup> century which still forms the backbone of our understanding of this subject.

### 1.3.1 The Kolmogorov Phenomenology

In 1941, A. N. Kolmogorov wrote three deeply profound papers [70, 78–80] which forms the basis of the modern theory of fully developed turbulence. These papers built around the following hypothesis (so-called as the K41 theory) that had laid an universal characterization of fully-developed turbulence using theoretical and phenomenological arguments [81, 82]:

1. The small-scale components are approximately in statistical equilibrium, determined completely by the dissipation rate of the system  $\epsilon = \nu \|\nabla \mathbf{u}\|_2^2$ , in the vanishing viscosity limit,  $\nu \rightarrow 0$  ( $\text{Re} = \infty$ ). The second order structure

function would then scale as

$$\langle |\delta \mathbf{u}(\mathbf{r})|^2 \rangle = \langle |\mathbf{u}(\mathbf{r} + \mathbf{x}) - \mathbf{u}(\mathbf{r})|^2 \rangle \sim \epsilon^{2/3} r^{2/3} \quad (1.33)$$

2. The small-scale flow is self-similar, with a unique scaling exponent ‘ $h$ ’ in the scaling of the structure function.

$$\langle \delta \mathbf{u}(\Gamma \mathbf{r}) \rangle \simeq \Gamma^h \langle \delta \mathbf{u}(\mathbf{r}) \rangle \quad (1.34)$$

Using the universality (1.33) and the self-similarity (1.34) together, naturally leads to  $h = 1/3$ , equivalently the Kolmogorov energy spectrum:

$$E(k) = C_K \epsilon^{2/3} k^{-5/3} \quad (1.35)$$

Data from various experiments and direct numerical simulations over years for the kinetic energy spectrum of turbulent flows, shown in figure 1.6, agrees well with K41 phenomenology, only later to be found with corrections due to the *intermittency* [67].

### 1.3.2 Intermittency and the Multifractal Formalism

A key and central assumption that beholds the K41 theory is the self-similarity of the velocity-field signals, as in equation (1.34), at the inertial range scales. Both experimental and numerical investigation of the structure function of order  $p$ , suggested deviations from  $\zeta_p = p/3$  (as seen in Fig. 1.7, also see Refs. [67, 74, 83]), the effect usually known as the “intermittency”, characterizing the breakdown of self-similarity or global invariance assumed in K41 with one unique scaling exponent  $h = 1/3$ . The heavy tails in the probability distribution of the velocity gradients is another indicator of presence of intermittency. With no exact results on the intermittency, our understanding of intermittency is from phenomenological and dynamic modeling of turbulence. Kolmogorov and Obhukov

presented their log-normal model in 1962 [84], followed by She-Lévêque model [85], random  $\beta$ -model [86], to include the intermittency corrections in the higher-order structure functions, assuming a certain distribution for the energy dissipation. Considerably a more general one was by Parisi and Frisch, known as the Multi-fractal model of turbulence [87], where a local-scale invariance is assumed with a continuous spectrum of exponents, each of which belonging to a given fractal set. In the inertial range,  $\delta u(\mathbf{x}, r) \sim r^h$  if  $\mathbf{x} \in S_h$ , and  $S_h$  is a fractal set with dimension  $D(h)$  and  $h \in (h_{\min}, h_{\max})$ . Here a probabilistic description of finding an exponent  $h$  at scale  $r$  with a probability  $P_r(h) \sim r^{3-D(h)}$  is considered, predicting a structure function

$$S_p(r) = \langle |\delta u(r)|^p \rangle \sim \int_{h_{\min}}^{h_{\max}} dh r^{hp} r^{3-D(h)} \sim r^{\zeta_p} \quad (1.36)$$

In the  $r \lll L$  limit, a Legendre transformation between  $\zeta_p$  and  $D(h)$  is attained by the steepest descent estimation

$$\zeta_p = \min_h \{hp + 3 - D(h)\} \quad (1.37)$$

Given that knowing  $D(h)$  or equivalently  $\zeta_p$  from Navier-Stokes equation is not possible, only experimental and numerical data can provide us with it. The relevance and success of the multi-fractal model lies in its capability to test and predict the non-trivial statistical features in fully-developed turbulent flows. Figure 1.7 shows the  $\zeta_p$  obtained from other models and from experiments.

### 1.3.3 Closure Models

The strong coupling between the wide range of scales arising from the non-linear interactions presents the so-called *closure* problem in turbulence. For example, if the velocity field  $\mathbf{u}$  is decomposed into mean  $\bar{\mathbf{u}}$  and fluctuation  $\mathbf{u}'$  as  $\mathbf{u}(\mathbf{x}, t) = \bar{\mathbf{u}}(\mathbf{x}, t) + \mathbf{u}'(\mathbf{x}, t)$ , called as Reynolds decomposition [93]. Then the Reynolds averaged Navier-Stokes equation for the mean field  $\bar{\mathbf{u}}$  would contain a non-trivial unknown term, the Reynolds stress  $\overline{u'_i u'_j}$ , in determining the evolution of the mean

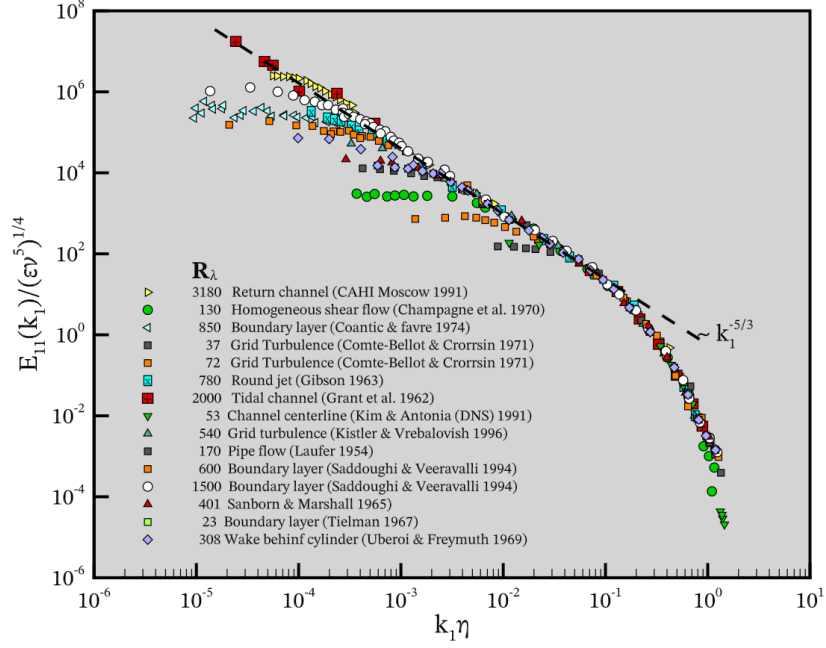


Figure 1.6: Compensated one-dimensional spectrum  $E_{11}(k_1)/(\epsilon\nu^5)^{1/4}$ , made from data collected from Chapman [88] and Veeravalli [89]. Figure adapted from Ref. [90]

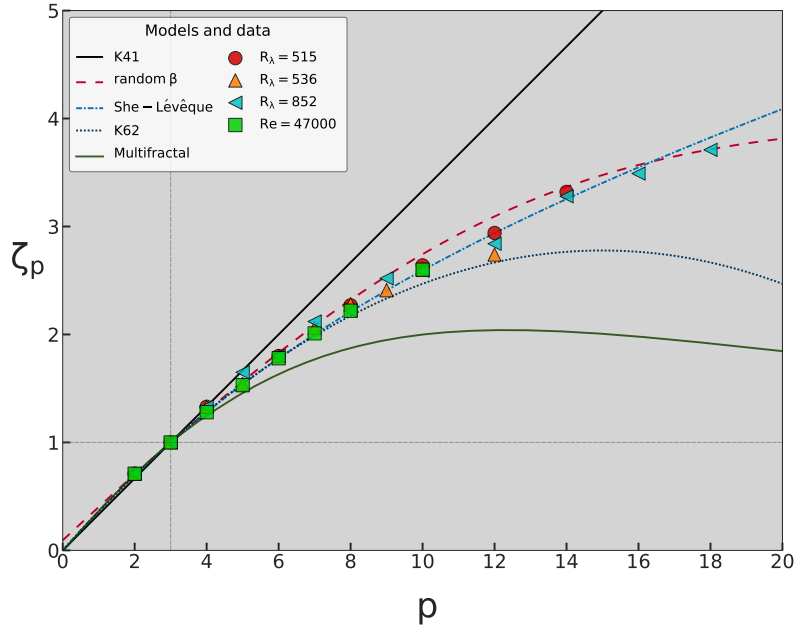


Figure 1.7: Structure function scaling exponent  $\zeta_p$  (as in Eqs. (1.30) & (1.31)) taken from experimental data (*symbols*) from Refs. [74, 83] and prediction from models (*lines*) presented in Refs. [67, 84–87, 91, 92]

field  $\bar{\mathbf{u}}$ .

$$\frac{\partial \bar{u}_i}{\partial t} + \bar{u}_j \cdot \partial_j \bar{u}_i = -\partial_i \bar{p} + \nu \partial_{jj}^2 \bar{u}_i - \partial_j \overline{u'_i u'_j} \quad (1.38)$$

This closure problem stated in other words, translates to a infinite unclosed set of statistical moment equations obtained from the Navier-Stokes equation. Every  $n^{\text{th}}$  order moment would have an unknown moment of order  $n + 1$  in its evolution equation, written symbolically as:

$$\begin{aligned} \left[ \frac{d}{dt} + 2\nu k^2 \right] \langle \hat{u}\hat{u} \rangle &= c_1 \langle \hat{u}\hat{u}\hat{u} \rangle, \\ \left[ \frac{d}{dt} + \nu(k^2 + q^2 + p^2) \right] \langle \hat{u}\hat{u}\hat{u} \rangle &= c_2 \langle \hat{u}\hat{u}\hat{u}\hat{u} \rangle, \\ &\dots = \dots \end{aligned} \tag{1.39}$$

where  $\langle \cdot \rangle$  is a statistical average. Consequently, in the absence of separate information to determine the additional statistics, statistical reparametrization or stochastic modelling is often done to substitute for the unknown, to tackle the closure problem. We discuss briefly a *famous* two-point closure model known as the Eddy-Damped Quasi-Normal Markovian (EDQNM) model, that has been widely studied and used (see Refs. [10, 30, 94] for more details).

The EDQNM model has an underlying assumption that turbulence is close to Gaussianity at higher order moments. Despite the strong departures from Gaussianity, in terms of PDF's of velocity gradient, it is not totally unphysical to model turbulent flow using Brownian-type particles. In the hierarchy of evolution equation (1.39), the first hypothesis, Quasi-Normal (QN), where the fourth-order cumulant for the velocity field is assumed to be zero ( $\langle \hat{u}\hat{u}\hat{u}\hat{u} \rangle_c = 0$ ). The evolution equation of the triple correlations then becomes:

$$\left[ \frac{d}{dt} + \nu(k^2 + q^2 + p^2) \right] \langle \hat{u}\hat{u}\hat{u} \rangle = \sum \langle \hat{u}\hat{u} \rangle \langle \hat{u}\hat{u} \rangle \tag{1.40}$$

Further revisions were added to the QN model by Orszag, accounting for the overcompensation of the gaussian assumption of the fourth-moment. The QN model is added with an additional linear damping term  $\mu_k$  (along with the viscous damping:  $\nu k^2$ ) for the third-moment [95]. Frisch proposed the eddy-damping timescale of the form:

$$\mu_k = a \left( \int_0^k dq q^2 E(q, t) \right)^{1/2} \tag{1.41}$$

Thus yielding an Eddy-Damped Quasi-Normal model where the closed set of equations for the third and second moment now are

$$\begin{aligned} \left[ \frac{d}{dt} + \nu(k^2 + q^2 + p^2) + \mu_{kqp} \right] \langle \hat{u}\hat{u}\hat{u} \rangle &= \sum \langle \hat{u}\hat{u} \rangle \langle \hat{u}\hat{u} \rangle, \quad \mu_{kqp} = \mu_k + \mu_q + \mu_p \\ \left[ \frac{d}{dt} + 2\nu k^2 \right] \langle \hat{u}\hat{u} \rangle &= \int \int d\mathbf{q} d\mathbf{p} \theta_{kqp}(t) \sum \langle \hat{u}\hat{u} \rangle \langle \hat{u}\hat{u} \rangle \\ \theta_{kqp}(t) &= \int_0^t d\tau \exp\left(-[\mu_{kqp} + \nu(k^2 + q^2 + p^2)](t - \tau)\right) \end{aligned} \quad (1.42)$$

The second hypothesis (Markovianization) is that the relaxation time of the triple correlations is small compared with the relaxation time of the double correlations. Hence an approximation:

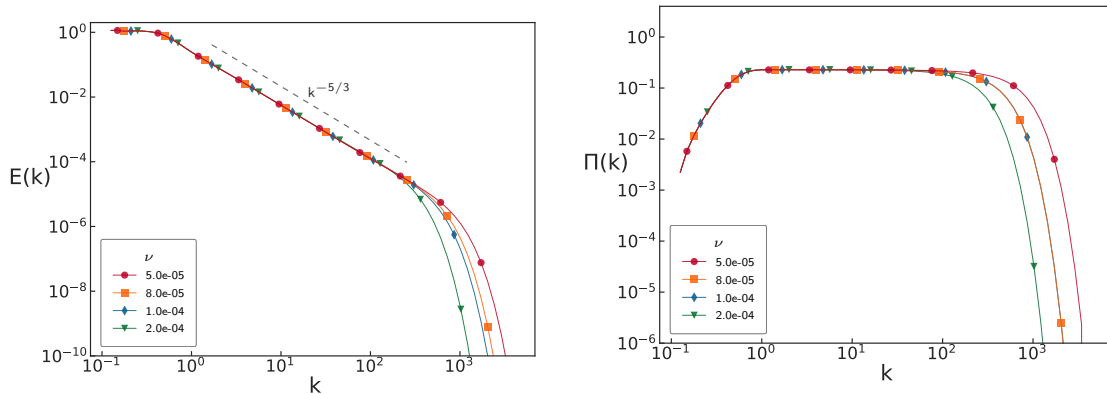
$$\theta_{kqp} = \frac{1 - e^{-(\mu_{kqp} + \nu(k^2 + q^2 + p^2))t}}{(\mu_{kqp} + \nu(k^2 + q^2 + p^2))} \quad (1.43)$$

The final EDQNM equation for the energy spectrum  $E(k)$  for the three-dimensional isotropic turbulence without helicity, is

$$\left[ \frac{d}{dt} + 2\nu k^2 \right] E(k, t) = \int_{\Delta_k} dp dq \theta_{kqp} \frac{k}{qp} b_{kqp} [k^2 E(p, t) - p^2 E(k, t)] E(q, t) \quad (1.44)$$

Here the integral  $\int_{\Delta_k} dp dq$  involves points in the  $q - p$  plane that allows the possibility of forming a triangle with sides  $k, q, p$ . The  $b_{kqp}$  is a geometric coefficient, that depends on the geometry of the triangle formed. In figure 1.8, results from numerical simulation of equation (1.44) is presented, consistent with K41 phenomenology.

Amongst several closure models (see Chap.7 in Ref [30] for a brief review), for an isotropic turbulent flows, the EDQNM model is an excellent tool to predict the energy transfers between various modes and the high Reynolds number behaviours, at relatively low numerical cost compared with direct numerical simulations of the Navier-Stokes equation. Nevertheless, the EDQNM model has its own limitations, as it cannot model intermittent effects that are seen in real turbulent flows. With a K41 energy spectrum  $E(k) \sim k^{-5/3}$  (see Fig. 1.8a), it shows a singular behaviour,



(a) Energy spectrum of an EDQNM model following the *famous* K41 power law:  $E(k) \sim k^{-5/3}$ .

(b) Flux  $\Pi = \int_k^\infty dq T(q)$  of an EDQNM model, shown to be constant in the inertial range.

Figure 1.8: Numerical results at a stationary steady state (obtained by forcing), from simulation of Eq. (1.44), showing the features of a K41 theory. Results are shown for different viscosities.

as the enstrophy blows up  $Z = \int_0^\infty dk k^2 E(k) \rightarrow \infty$  in the vanishing viscosity limit ( $\nu \rightarrow 0$ ).

The EDQNM closure phenomenology is adopted for other hydrodynamical equations as well. Over the years, it has been explored in two-dimensional turbulence [96, 97] to examine the inverse cascade, in passive scalar advection in turbulent flows, helical turbulent flows [98] to address the double cascade, thermalization of truncated inviscid equations [37], bottleneck effects in turbulence [50] and magnetohydrodynamics (MHD).

It is computationally quite expensive—even seemingly impossible—to run a DNS for the MHD equations to simulate astrophysical conditions. Hence, the EDQNM model was extended naturally to the MHD equations [99] allowing one to investigate both theoretically and numerically the various effects that are in play [100–102] including the multifaceted dynamo problem [103, 104].

## 1.4 An Overview of the Thesis

The question of thermalization of classical systems with many degrees of freedom is a fundamentally important one in statistical physics. There are several examples of such systems, with explicitly broken integrability, which thermalize. While we often *know* that such systems ought to thermalize, the precise mechanisms and time-scales at which they do still remain unresolved in many cases. As we have discussed in an earlier Section, a slightly different class of such systems which are even less understood are the finite-dimensional (Galerkin-truncated) equations of ideal hydrodynamics. The long time solutions of these equations are expected to thermalize by virtue of a phase-space and energy conservation; however, the precise mechanisms, in physical space, which trigger such states has only been discovered recently for the relatively simpler one-dimensional Burgers equation [39]. Thus while the existence and importance of thermalized solutions—characterized by a Gibbs distribution of the velocity field and kinetic energy equipartition amongst its (finite) Fourier modes—of the truncated Euler equations have been known, how such solutions are achieved remained an open question.

In Chapter 2, we show through detailed numerical simulations, the early stage triggers for the inevitable thermalization in physical space. Furthermore, some aspects of this process are shown to be reduced to an effective one-dimensional problem, making comparisons with the more studied Burgers equation feasible. Finally, we discuss how our understanding of the mechanism of thermalization can be exploited to numerically obtain dissipative solutions of the Euler equations which, through more systematic study, could pave the way for finding evidence for or against finite-time blow-up in computer simulations.

As we have discussed before, one of a way to conjecture for or against a finite-time singularity is to numerically solve the Euler equation and measure the width of the analyticity strip  $\delta$ , that is, the distance to the real domain of the nearest complex singularity. By assuming analyticity, at least up to a hypothetical time of

blow-up  $t^*$ , this procedure reduces to measuring the Fourier modes of the velocity field  $\hat{u}_k \sim \exp\{-\delta(t)k\}$  (ignoring vectors for convenience), for large wavenumbers  $k$ , and thence,  $\delta$  as a function of time  $t$ . Therefore, a numerically compelling *proof* for a finite-time blow-up is to show  $\delta(t) \rightarrow 0$  in a finite time.

Simple as it sounds, such an approach unfortunately runs into a severe problem in its implementation. To solve such equations on the computer, one has to make them finite-dimensional through a Galerkin-truncation which of course thermalize, beginning at small scales. Hence, asymptotically at large wavenumbers the Fourier modes of the velocity field grow as a power law  $\hat{u}_k \sim k^{d-1}$  (energy equipartition), where  $d$  is the spatial dimension, and not fall-off exponentially from which the width of the analyticity strip can be extracted. Hence, the measurement of  $\delta(t)$  becomes unreliable *soon enough* to prevent us from making a reasonable conjecture of if and when  $\delta(t)$  might vanish. Therefore, in order to have a more reliable measurement of  $\delta(t)$  for times long enough to conjecture on whether there is a finite-time blow-up of, example, the three-dimensional, incompressible, Euler equation, it is vital to have a (numerical) prescription—without resorting to viscous damping—which prevents the solutions from thermalizing. In Chapter 3, based on the more tractable Burgers equation, we propose a novel method to prevent thermalization in such systems *without* resorting to viscous damping. It thus allows us to recover dissipative (*weak*) solutions as well as provide a fairly simple method to conjecture (numerically) on the possibilities of finite-time blow-up in the Euler equation.

While Chapters 2 and 3 deal with the onset and control of thermalization, in Chapter 4, we make explicit use of thermalized fluids to address a very important and contemporary question in statistical physics which rests on the notions of thermalization and equilibration. These are facilitated by many-body chaos intrinsic to such systems. However there are equally ubiquitous examples of many-body systems—turbulent flows being one which first springs to mind—where the role of chaos is anything but equilibrating. To use the analogy of the butterfly effect, while the amplification of the wingbeat can lead to unpredictability in many

driven-dissipative systems, the same amplification also lead to a loss of memory of initial conditions, resulting in ergodic behaviour and eventual thermalization or equilibration, in Hamiltonian many-body systems.

In Chapter 4, we reconcile these two seemingly disparate roles and radically different fallouts of chaos and show the universal nature of what bridges ideas of many-body chaos with the foundational principles of statistical physics. Our work is based on cross-correlators or out-of-time-ordered-correlators (OTOCs) which provide a general framework to understand chaos in classical and quantum many-body systems by linking equilibrium and dynamical aspects through rigorous estimates of the temperature-dependence of the degree of chaos (Lyapunov exponent). We use the chaotic and thermalized solutions of the 3D Euler equation (Chapter 2) and the 1D Burgers equation (Chapter 3) to show, through state-of-the-art simulations and analytical calculations, that the Lyapunov exponent grows as the square root of temperature and linearly with the degrees of freedom. This underlines the universal aspects of many-body chaos and its fundamental connection to equilibrium properties (temperature). This emergent universality, ranging from frustrated spin to glassy systems, strongly coupled quantum field theories to black holes, is central to understanding the dynamics of strongly coupled many-body systems without an apparent (weakly interacting) quasi-particle description and hence a kinetic theory.

In Chapter 5, we turn to the problem of fully developed turbulence by using the 3D Navier-Stokes equation and revisit the question of multifractality. As we discussed before, the Frisch-Parisi multifractal formalism remains the most compelling rationalisation for anomalous scaling in fully developed turbulence. We now show that this formalism can be adapted locally to investigate the spatial distribution of how multifractal the energy dissipation field is. In particular, we show that most regions of the flow are close to being mono-fractal interspersed with islands of multifractality corresponding to the most singular structures in the flow. By defining a suitable measure of the degree of multifractality spatially, we show that this grows logarithmically with the local strength of the energy dissipation.

These results suggest ways to understand how singularities could arise in disparate regions of a flow and provide new directions in understanding anomalous dissipation and intermittency. We then employ the same technique to a non-intermittent, model turbulent flow—so called “decimated” turbulence—to check the robustness of our conclusions.

Finally, in Chapter 6 we construct and solve an Eddy-Damped Quasi-Normal Markovian (EDQNM) model for magnetohydrodynamic (MHD) turbulence in arbitrary dimensions. In particular, our detailed numerical simulations (for a given Prandtl number and magnetic Reynolds number) show the existence of an *upper*  $d_U$  and *lower*  $d_L$  dimensions such that only for  $d_L \leq d_U$  dynamo action is possible. Curiously, the no-dynamo regime is shown to exist up to dimensions  $d_L \gtrsim 2$ —coincident with the *critical* dimension up to which an inverse cascade in fluid turbulence persists [63]. This is of course slightly larger than  $d = 2.0$  for which the anti-dynamo theorems exist. We rationalise our phase diagram of the dynamo–no-dynamo transition in terms of the competing effects of the effective *forcing*, through non-linearities, and magnetic diffusion.

## Chapter 2

# Genesis of Thermalization in the 3D Galerkin-truncated Euler equation

We saw earlier in Chapter 1, that inviscid equations of hydrodynamics which are constrained to have a finite number of Fourier modes leads to thermalized flows which are distinctly different from our more accustomed viscous fluids. This is because the projection of the inviscid equations on a finite set of Fourier modes leads to a phase-space conserving dynamical system (Hamiltonian flow [105]), and at long times reaches a stationary distribution, an inevitable thermalized, absolute equilibrium Gibbs state [32, 96, 98, 106]. Consequently, this is accompanied by an equipartition of kinetic energy across Fourier modes  $\mathbf{k}$  [36, 38, 107], quite unlike the celebrated Kolmogorov scaling  $\sim k^{-5/3}$  associated with turbulence in three dimensions (3D) or the  $k^{-2}$  scaling of the entropy solution in the one-dimensional (1D) Burgers problem [108]. Therefore, such thermalized fluids are amenable to well-established theories of equilibrium statistical physics while being intrinsically chaotic.

From the more specific vantage point of turbulence and fluid dynamics,

the relevance of such systems is more subtle and less immediately obvious. This is particularly so for 3D turbulence where several fundamental questions remain unanswered. Hence, in the absence of the many theoretical tools available for studying the 1D Burgers equation [21], it is tempting to exploit the advantages of a 3D Galerkin-truncated incompressible Euler equation to make sense of real turbulent flows. Of course, superficially, such equilibrium solutions are in stark contrast to those obtained in (driven-dissipative) turbulence or in numerical solutions of the viscous Navier-Stokes equation. And yet the truncated equation retains the same nonlinear triadic structure as the parent inviscid partial differential equations, or indeed, in three dimensions, the viscous Navier-Stokes equation, which models turbulent flow. Thus, in many ways, the 3D Galerkin-truncated incompressible Euler equation is a compelling link between ideas of statistical physics for a Hamiltonian system with conserved dynamics [29, 95] and those which describe the behavior of out-of-equilibrium, driven-dissipative, viscous turbulent flows [67, 109, 110].

There is another important reason why the Galerkin-truncated equation merits attention. One of the outstanding questions at the interface of physics and mathematics is the existence of weak or dissipative solutions [17, 26, 111] and the possibility of a finite-time blow-up for the 3D Euler equation [112–114]. While a review of this subject goes well beyond the scope of the present paper, suffice to say that probing the blow-up problem numerically is a monumental challenge [107, 115–139]. Indeed, conjectures remain speculative at best despite well-formulated criteria [16, 23, 24, 140–144] which, in principle, should be easily detectable in well-resolved direct numerical simulations (DNSs) [145]. The obstacle to this, however, is that simulations are necessarily finite-dimensional: The commonly used spectral simulations [146, 147] solve the Galerkin-truncated and *not* the infinite-dimensional partial differential equations of inviscid flows. Hence, in finite times, which may well precede the time of blow-up (as is the case for the inviscid one-dimensional Burgers equation [39, 41]), the solutions thermalize (starting with the smallest scales), making methods for singularity detection, such as the analyticity strip approach [27], arduous [137, 148]. Hence, for finite resolutions, in the absence of convergence of such truncated solutions (which thermalize) to the

actual (weak) solutions of the Euler equations themselves, conjectures on blow-ups from DNSs [23, 140, 144, 149] will remain unsettled until mechanisms to circumvent Gibbs states in mathematically self-consistent ways are discovered. The discovery of such methods is, of course, contingent on knowing how truncated equations thermalize in the first place. It is useful to recall that such methods have been discovered for the more academic 1D Burgers problem [43, 150–153] owing to our thorough understanding of how the one-dimensional equation thermalizes.

Thus, the long-time chaotic Gibbs solutions [61] of the Galerkin-truncated Euler equations play contrasting roles in studies of fundamental problems in turbulence. On the one hand, they allow us to connect ideas from statistical physics to turbulence, and on the other, they remain a stumbling block in numerical methods for studying questions of blow-up and dissipative solutions. This makes understanding how such 3D flows thermalize particularly essential. As a result, in recent years, since the pioneering work of Cichowlas *et al.* [107], a reasonably complete picture of how energy equipartition happens in Fourier space has emerged [36–38, 154–156]. However, unlike the case of the 1D Burgers equation [39–41, 150], not much is known of the origins of thermalization in physical space for the 3D problem.

## 2.1 Thermalization for a *Generic* flow

With this in mind, we perform detailed DNSs of the unit-density, three-dimensional, Galerkin-truncated, incompressible ( $\nabla \cdot \mathbf{u} = 0$ ) Euler equation

$$\frac{\partial \mathbf{u}}{\partial t} = -\mathbb{P}_{k_G}[\mathbf{u} \cdot \nabla \mathbf{u} + \nabla p]. \quad (2.1)$$

The low-pass Galerkin projector  $\mathbb{P}_{k_G}$  sets to zero all modes of the velocity field with wavenumbers larger than the prescribed Galerkin-truncation wavenumber  $k_G$ , that is  $\mathbb{P}_{k_G} \mathbf{u}(\mathbf{x}) = \sum_{|\mathbf{k}| \leq k_G} e^{i\mathbf{k} \cdot \mathbf{x}} \hat{\mathbf{u}}_{\mathbf{k}}$ .

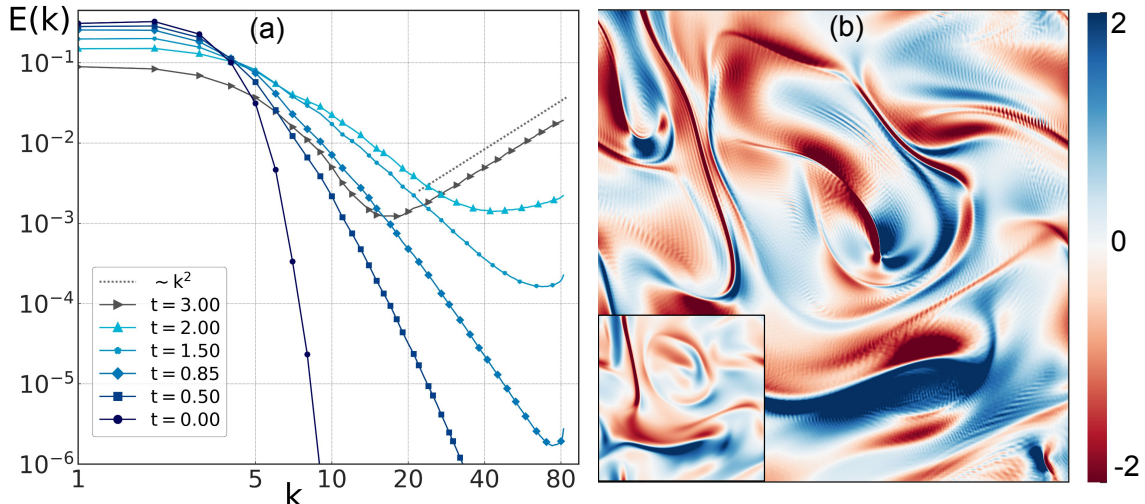


Figure 2.1: (a) Log-log plots of the kinetic energy spectrum at different times from a DNS ( $N = 256$ ) of the Galerkin-truncated Euler equation with generic, large-scale initial conditions. (b) Pseudo-color plots of the strain field component  $S_{yz}$  ( $N = 512$ ) in the  $XY$  plane at time  $t = 1.8$ , where thermalization is triggered in the flow (*inset* at an earlier time  $t = 1.2$ ). While oscillatory structures are conspicuous by their absence for the former (*inset*), coherent streaks of oscillations with wavelengths  $\lambda_G$  are clearly visible for the latter. See Ref. [157] for an animation of the evolution of  $S_{yz}$  from a non-thermalized to a *fully* thermalized state.

Our DNSs use a pseudo-spectral method with a fourth-order Runge-Kutta scheme for time integration on  $2\pi$  periodic domains with  $N^3$  collocation points ( $N = 256$  and  $512$ ) and truncation wavenumber  $k_G = N/3$ . We have checked that our results and conclusions are consistent across simulations and choice of collocation points. We choose initial conditions (also projected on the compact Fourier domain) which has a energy spectrum of the form  $E(k) \sim k^2 \exp(-k^4/k_t^4)$  to ensure that the initial energy is concentrated in the largest scales, that is  $k_t \sim \mathcal{O}(1)$ . Galerkin-truncation ensures that the kinetic energy and phase space remain conserved for all times, which, coupled with the finite-dimensionality imposed by the cut-off wavenumber  $k_G$ , eventually leads to a thermalized fluid with kinetic energy equipartitioned across all Fourier modes.

Given the choice of initial conditions that confines kinetic energy at large scales, the excitement of the largest wavenumbers requires some time. In figure 2.1(a), we show the evolution of the kinetic energy spectrum,  $E(k) \equiv \frac{1}{2} \sum_{q=k-1/2}^{k+1/2} |\hat{\mathbf{u}}(\mathbf{q})|^2$ , through representative log-log plots at various instances of time.

Similar evolutions of the spectrum have been reported in the first study of this kind by Cichowlas *et al.* [107].

While a long-time thermalized fluid, through Liouville’s theorem, with Gibbs statistics [61] is obvious, the transition from a smooth initial condition that behaves like a “viscous” fluid for finite times to one that is thermalized and essentially devoid of structure is far from obvious. A clue may be found in plots of the isosurfaces of the vorticity fields, as they evolve in time. In figure 2.2(a), we show a plot of the vorticity ( $\boldsymbol{\omega} = \nabla \times \mathbf{u}$ ) isosurface for  $\sigma \leq |\boldsymbol{\omega}|^2 - \|\boldsymbol{\omega}\|_2^2 \leq 2\sigma$ , where  $\sigma(t)$  is the standard deviation of the enstrophy field, at early times ( $t = 0.5$ ) when the largest available wavenumbers are still not fully excited. When seen in the energy spectrum (figure 2.1(a)) at the same time, there is no sign of thermalization. These enstrophy isosurfaces are smooth and indistinguishable—as indeed the kinetic energy spectrum at such times—from what one would expect from an extremely high Reynolds number Navier-Stokes simulations with similar initial conditions and at similar times. At slightly later times, ( $t \gtrsim 0.85$ ) however, isosurfaces show minute but detectable oscillatory structures (see Fig. 2.2(b)) with wavelengths  $\lambda_G = 2\pi/k_G$ , reminiscent of what is seen for the corresponding problem in the one-dimensional Burgers equation [39, 41, 42]. We recall that a similar phenomenon was seen recently in simulations of the 3D, Galerkin-truncated *axisymmetric* incompressible Euler equation [137]. These initially localized (in both physical and Fourier space) oscillations rapidly spread through the domain, with increasing amplitudes, whilst becoming non-monochromatic. A snapshot of these fully thermalized states (figure 2.2(c)) looks noisy [153] and bears no resemblance to the well-formed isosurfaces that characterize *fully*-developed turbulence or indeed solutions of the truncated equation before the onset of thermalization (figure 2.2(a)). Consequently, the energy spectrum at such times and beyond converges to an equipartition [107] with  $E(k) \sim k^2$  (figure 2.1(a)).

While the signatures of thermalization are fairly obvious in plots such as those shown in figure 2.2, the incipient thermalized phase is best captured in visualisations of the velocity gradient. In figure 2.1(b), we show two-dimensional

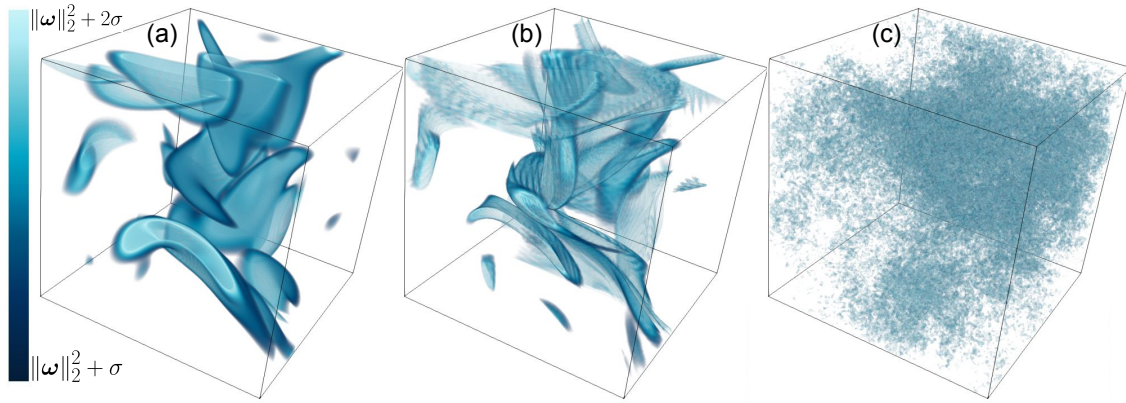


Figure 2.2: Isosurfaces of the vorticity field from DNS ( $N = 256$ ) for  $\sigma \leq |\boldsymbol{\omega}|^2 - \|\boldsymbol{\omega}\|_2^2 \leq 2\sigma$  at (a)  $t = 0.5$ , (b)  $t = 0.85$ , and (c)  $t = 2.5$ . See Ref. [158] for an animation of the evolution of these isosurfaces from a non-thermalized to a fully thermalized state.

(XY plane) cuts of the strain field ( $S_{ij} \equiv 0.5(\partial_j u_i + \partial_i u_j)$ ) that, at times when the effects of truncation are felt, show clear, organized oscillatory structures (panel (b)), which were absent at earlier times (*inset* in panel (a)). We recall that in the one-dimensional (1D) inviscid Galerkin-truncated Burgers problem, the oscillatory structures that trigger thermalization are initially localized at point(s) co-moving with the shock(s) through a resonance effect [39]. The flow we study now is fundamentally different: it is three-dimensional and incompressible. So how does thermalization onsets (Figs. 2.2(b) and 2.1(b)) in the 3D Euler equations and is there an analog of resonance points or do the oscillations appear *out of the blue*?

The answer to this is delicate and figure 2.1(b) is suggestive. Starting from initial conditions (such as the ones we have) that concentrate energy at large scales, the nonlinearity of the systems generates smaller and smaller scales in time and generates structures ranging from vortex sheets to tubes. As smaller and smaller scales get excited, many of these structures can sharpen (as thin sheets or tubes) [129, 132, 159] with a characteristic length scale  $\sim k_G^{-1}$ . Such sharp structures, analogous to pre-shocks in the 1D Burgers equation, act as a source of *truncation waves* of wavelength  $\lambda_G$ —indeed the Fourier transform of the projection operator *has* a wave with wavenumber  $k_G$ —which travel along the directions in which such structures are compressed. The oscillations, of course, ensure the conservation of total kinetic energy that is a constraint in this Galerkin-truncated system. In the

representative snapshot shown in figure 2.1(b), the oscillations of varying amplitudes appear not all over but in specific regions of the flow with wave vectors that, for this realization of the flow, are quite often, but not always, normal to the intense structures seen in the domain. Of course, whether such oscillations amplify or rapidly diminish in space and time is determined by the nature of the strain field locally, as we illustrate below. For oscillations that do survive, the nonlinearity allows other modes to get rapidly excited and the nonlocality of the incompressible equation allows a rapid spread of these complex oscillations across the whole domain. This eventually leads to a chaotic, thermalized fluid bereft of structure and an equipartition of kinetic energy across Fourier modes, as illustrated in figure 2.2(c).

This phenomenological picture, though compelling, is difficult to *prove* in numerical simulations with the generic initial conditions that we use: The complexity of the spatial structures generated does not allow an easy way to test the different ingredients that go into the argument constructed above. In order to substantiate our theory on the genesis of oscillations in the first place, we resort to DNSs which are controlled in a way to isolate the two different effects at play: The sharpening of velocity gradients  $\nabla u \sim k_G^{-1}$  and the consequent onset of thermalization along specific directions relative to such intense structures.

## 2.2 The Onset of Thermalization: What *Model Flows* Tell Us?

Among the many candidate flows—such as isolated vortex tubes and sheets—we choose to work with an initial condition consisting of two separated, opposite-signed vortex sheets (parallel to the YZ plane), located symmetrically at  $x = x_1$  and  $x = -x_1$ , in a periodic box  $[-\pi, \pi]^3$ . Furthermore, these sheets have a localized perturbing flow at their centers to disturb the sheet from equilibrium. Such

a flow configuration is generated by the following initial condition: For  $0 \leq x \leq \pi$ :

$$u_x = \mathcal{P}_\perp \left[ u_0 k_\beta (x - x_1) \exp \left( -\frac{1}{2} k_\beta^2 ((x - x_1)^2 + y^2 + z^2) \right) \right] \quad (2.2a)$$

$$u_y = \sqrt{2} \tanh [\gamma k_G (x - x_1)] \quad (2.2b)$$

$$u_z = \mathcal{P}_\perp \left[ u_0 k_\beta z \exp \left( -\frac{1}{2} k_\beta^2 ((x - x_1)^2 + y^2 + z^2) \right) \right]. \quad (2.2c)$$

To ensure periodicity in  $u_y$  ( $u_x, u_z$  are localized within  $k_\beta^{-1}$ ), for  $-\pi \leq x \leq 0$  the velocity field is chosen with the symmetry:

$$u_i(x, y, z) = u_i(-x, y, -z) \quad (2.3)$$

To ensure incompressibility, the projection operator  $\mathcal{P}_\perp[\mathbf{f}] = [1 - (\nabla_\perp^{-2}) \nabla_\perp (\nabla_\perp \cdot \mathbf{f})]$  in the XZ plane ( $\nabla_\perp = \{\partial_x, 0, \partial_z\}$ ), is applied to the  $x$  and  $z$  velocities. The disturbance ( $u_x, u_z$ ) here is localized at  $\mathbf{x}_1 = (x_1, 0, 0)$  and  $-\mathbf{x}_1$ ; consequently the vortex sheet  $u_y$  is stretched for the former and compressed for the latter. The parameter  $\gamma$  controls the intensity of the vortex sheet and is chosen to be 1/4 to suppress any inherent Gibbs oscillations that arise as  $\gamma \rightarrow 1$ . The vortex sheet locations are chosen with  $x_1 = \pi/2$ . We fine-tuned the extent of localization of the perturbation through  $k_\beta^{-1}$ , which, for the results presented here, was set to  $k_\beta = 4$ . Finally, the flow amplitude  $u_0 = 5$  sets the energy of the perturbation field ( $\sim 10^{-3}$  relative to that of the vortex sheet) as well as the time-scale. This perturbing flow field, with the large-scale background flow (which creates the sheet) suppressed (for clarity), is illustrated in figure 2.3(a) with the two-dimensional velocity vectors shown as green arrows superposed on the pseudo-color plot of  $\omega_z$ .

By using equations 2.2 (Fig. 2.3(a)) as initial condition, we solve the Galerkin-truncated equation with  $k_G = N/3$  ( $N = 256$ ). Given the specific configuration that we chose, the center of the left sheet (at  $-\mathbf{x}_1$ ) is compressed, whereas the right sheet (at  $\mathbf{x}_1$ ) is stretched (Fig. 2.3(b)): As the steepening velocity gradient at  $-\mathbf{x}_1$  becomes comparable to the inverse of the truncation wavenumber, we expect it to trigger the truncation waves in the dynamics, and the stretching at  $\mathbf{x}_1$  should produce no such effect. Then the question is: *how* and *where* do the

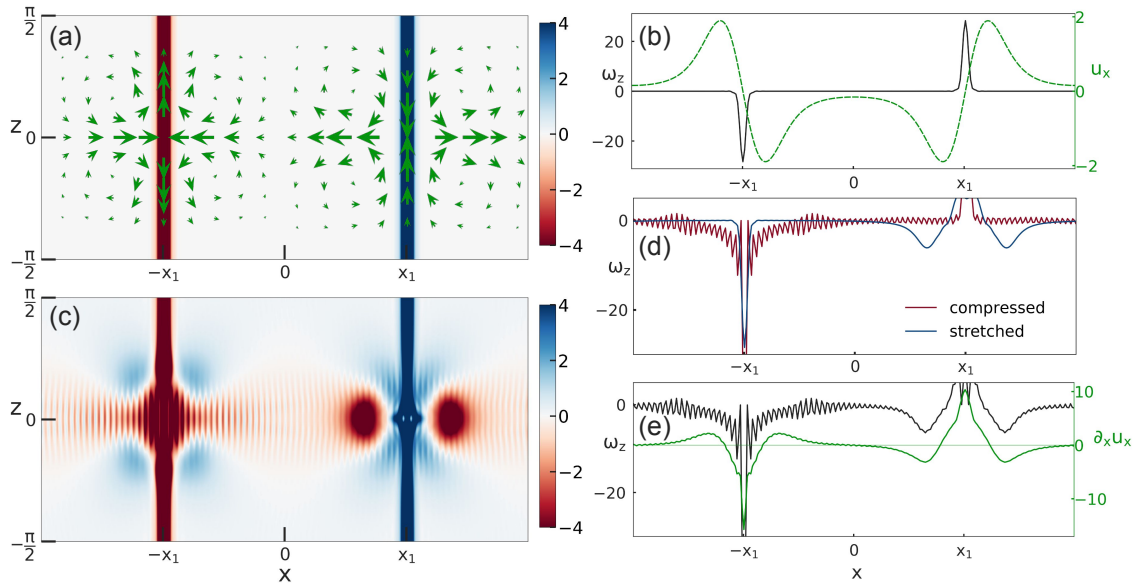


Figure 2.3: Pseudo-color plots of two-dimensional XZ plane cuts of  $\omega_z$  for the model flow (Eq. (2.2)) at (a)  $t = 0$  and (c)  $t = 0.15$  with their one-dimensional (along  $z = 0$ ) cuts (shown as black curves) in panels (b) and (e), respectively. Shown in green are the (a) instantaneous velocity vectors  $(u_x, u_z)$ , (b) instantaneous velocity component  $u_x$ , and (e) the velocity gradient  $\partial_x u_x$  fields. Panel (d) shows the line plot of  $\omega_z$  at  $t = 0.15$  when the perturbations are applied separately: Compression (*red*) at  $-\mathbf{x}_1$  and stretching (*blue*) at  $\mathbf{x}_1$ . The initial ( $t = 0$ ) profiles (panels (a) and (b)) are devoid of the  $\lambda_G$ -wavelength oscillations, which become conspicuous at later ( $t = 0.15$ ) times, as seen either (c) in the pseudocolor plots of the  $\omega_z$  field or (e) in its one-dimensional cut. Naturally, these oscillations are seen just as well in (d) for the special case of compressional perturbation applied only at  $-\mathbf{x}_1$ . (Clearly, the stretching perturbation independently does not yield any oscillations as expected.). The absence of oscillations in panel (e) near  $\mathbf{x}_1$  is subtle and discussed in the text. Ref. [160] has links to an animation of the evolution of this flow to show the onset of thermalization.

truncation waves manifest themselves in the flow?

In the analogous 1D Burgers problem, these truncation waves emerge from the region of the pre-shock and are constrained to travel along the one-dimensional velocity field, and it is straightforward to identify the location of the oscillations [39]. But for the three-dimensional flows such as ours, there are infinitely many possible directions along which these oscillations, which trigger thermalization, might emerge. Indeed, if such directions are chosen randomly by the truncated dynamics, then the problem of thermalization and, crucially, finding ways to circumvent it becomes exceptionally hard. Fortunately, as we show below, the solution to this is perhaps

simpler: assuming the evidence from such model flows holds for generic initial conditions, the essential features can be mapped to an effective one-dimensional problem.

Given that these are three-dimensional flows, it is reasonable to conjecture that since the oscillations source from these sharp structures, for short times they must be constrained to be in the same direction along which the structure is compressed. Thus, the problem of knowing where in the flow the first signs of thermalization appear may well be reduced to an effective one-dimensional problem along very specific flow lines that generate sharp structures. This conjecture is easy to check for simpler flow geometries (such as the one in Fig 2.3(a) and its one-dimensional cut along  $z = 0$  shown in panel (b)), where the argument leads to the inevitable conclusion that within a short time, oscillations of  $\omega_z$ , with wave number  $k_G$  appear along the  $z = 0$  line (compressional direction) stemming *only* from the perturbation at  $-\mathbf{x}_1$ .

In figure 2.3(c), we show the solution at time  $t = 0.15$ . Clearly and consistent with our prediction  $\omega_z$  is oscillatory with wavelength  $\lambda_G$  along the  $z = 0$  direction. Further, the perturbations at  $-\mathbf{x}_1$  and  $\mathbf{x}_1$  are applied independently, and the resulting line-plots of  $\omega_z$  along  $z = 0$  line are shown in figure 2.3(d) to stress the *necessity* of a compressive eigendirection across the structure to give birth to the truncation waves.

We now return to the solution of figure 2.3(c) where both perturbations exist. By taking a one-dimensional cut along  $z = 0$  in figure 2.3(c), we obtain  $\omega_z$ , and the velocity gradient  $S_{xx} = \partial_x u_x$ , both of which are shown in figure 2.3(e). A careful reading of this figure brings to light the basic mechanism of the onset of thermalization. The  $k_G$ -wavenumber oscillations, born from the compression, at  $-\mathbf{x}_1$  (because of the reasons mentioned above), persist along the  $z = 0$  direction and are sustained away from  $-\mathbf{x}_1$  *as long as* the velocity gradient at those points is strictly non-negative. In the regions of the flow where the gradient is negative, the oscillations are suppressed. This is illustrated, for example, in figure 2.3(e), where

there is a region between 0 and  $\mathbf{x}_1$  with a negative gradient where the oscillations are nearly absent, in contrast with what is seen in figure 2.3(d) for the compressional case since no such negative gradients exist there. This is because the squeezing effect of the negative gradient causes the wavenumbers to go beyond the truncation number  $k_G$ , resulting in their elimination through the Galerkin projector. It is important to note here that in the immediate vicinity of the source (near  $-\mathbf{x}_1$  in Fig. 2.3(e)), the negative gradient—an integral part of the compressive structure itself—cannot suppress the oscillations. As is the case for the shock in the 1D Burgers problem, the  $k_G$ -wavenumber oscillations are born continuously at  $-\mathbf{x}_1$  and are thus always present. It is worth reminding, *en passe*, that the sharp structure at  $-\mathbf{x}_1$  can also give rise to a Gibbs phenomenon—namely, the effect of summing a finite Fourier series in a region of (quasi-) discontinuity—and hence further oscillations. Lastly, even when the gradients become positive (in the narrow layer around  $\mathbf{x}_1$  in Fig. 2.3(e)), the relative suppression of oscillations is due to the negative gradient on either side of this positive gradient layer, which eliminates oscillations coming from the source.

In summary, figure 2.3 brings out the two key mechanisms responsible for the onset of thermalization in the 3D Galerkin-truncated Euler equations. Firstly, truncation waves emerge at sharply localized structures that have at least one direction of compression which squeezes them further. These play the same role as shocks do in the 1D Burgers problem [39]. Secondly, these oscillations, away from their place of birth, are sustained only when the flow gradient is non-negative. Crucially, the lack of a resonance effect ensures that (a) the oscillations are never spatially localized — in contrast to the 1D Burgers problem — at special points but proliferate everywhere, and (b) a relative suppression of oscillations in a positive-gradient region that lies ensconced within a negative-gradient insulating layer. A final, subtle point, also emerges from this figure. While imposing a negative strain along their wavevector suppresses their growth (because of the truncation constraint, see Fig. 2.3(e)), the strain from the other eigen directions can affect them subdominantly. This can be seen in the bulge in the wavepacket between  $x = -x_1$  and  $x = 0$  (Figs. 2.3(d) and (e)) caused by squeezing action from the  $u_z$

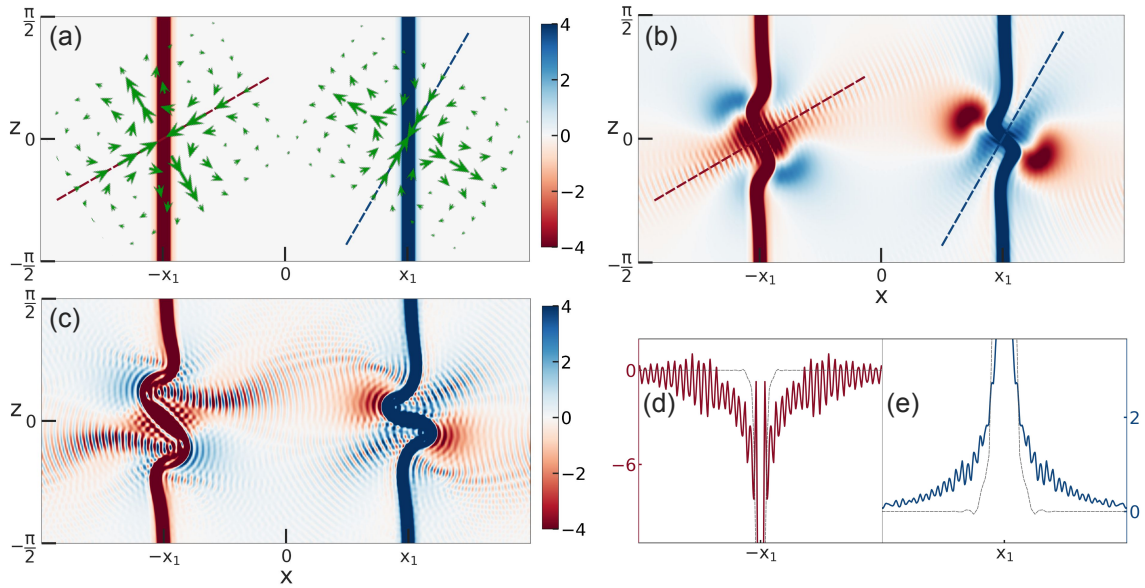


Figure 2.4: Pseudo-color plots of two-dimensional XZ plane cuts of  $\omega_z$  for the *rotated* model flow at (a)  $t = 0$  (superimposed with the velocity vectors  $(u_x, u_z)$ ), (b)  $t = 0.12$ , and (c)  $t = 0.25$ . Along the compressional directions (dashed red and blue lines in panels (a) and (b)), clear oscillations of  $\omega_z$  are seen at times  $t > 0$ . This is shown in panel (b) as well as illustrated further by their one-dimensional cuts, shown in panels (d) and (e). In panel (c), which is at a later time, the surfacing of multiple truncation wave sources and lead to a proliferated spread of oscillations in the domain. See Ref. [161] for an animation of the evolution of this flow to show the onset of thermalization.

component.

In order to test the robustness of the claim and conclusions drawn above from figure 2.3, we rotate the disturbance field in arbitrary directions to see if the early-stage oscillations in  $\omega_z$  pick out these directions every time. We choose an instance where the disturbance field  $u_x, u_z$  are rotated by  $\theta = \pi/3$  from the normal of the sheet in the XZ plane for the right half of the domain  $0 \leq x \leq \pi$  and symmetrically (following Eq. (2.3))  $\theta = \pi/6$  for the left half of the domain  $-\pi \leq x \leq 0$ . For this new configuration, the perturbations lead to a squeezing of the vortex sheet along the *new* compressional directions, which now are at an angle of  $\pi/6$  at  $-x_1$  and  $\pi/3$  at  $x_1$  away from the horizontal (indicated in figure 2.4(a) by blue and red dashed lines, respectively). We clearly see in figure 2.4(b), consistent with our predictions, that  $\omega_z$  is oscillatory in the two directions of compression for the two sheets. Thus, truncation waves are born along the compressional eigen-directions, as conjectured before. Though the compressional eigenvalues at both sheets are

the same in magnitude by construction, evidently the amplitudes are different, as seen clearly from their one-dimensional cuts along the dashed lines shown in figures 2.4(d) and (e). The reason is simply that the one-dimensional process sees a thicker (smoother) structure at  $\mathbf{x}_1$  than at  $-\mathbf{x}_1$ , or in other words, the component of compressive strain across the normal direction of the sheet differs between the two cases. While our effective one-dimensional simplified view of the thermalization onset is true *only* for arbitrarily short times and from a single source, to illustrate how multiple sources interact, we present the solution at a somewhat late time ( $t = 0.25$ ) in figure 2.4(c).

In the model flow discussed above, the parallel vortex sheets were subject to imposed perturbations. However, to make the system a bit more realistic, we now immerse the two parallel vortex sheets in a background Taylor-Green velocity field [36], given by  $u_x^{\text{TG}} = \cos x \sin y \cos z$ ,  $u_y^{\text{TG}} = -\sin x \cos y \cos z$  and evolve this system in time by using the Galerkin-truncated Euler equation. Thus, the initial condition (Fig. 2.5(a)) for a periodic domain of  $[-2\pi, 2\pi] \times [-\pi, \pi]^2$ , is of the form:

$$u_x = \varepsilon u_x^{\text{TG}} \tag{2.4a}$$

$$u_y = \varepsilon u_y^{\text{TG}} + A u_y^{\text{SH}}, \quad u_y^{\text{SH}} = 1 + \tanh[\gamma k_c (\text{sgn}(x)x - x_1)], \quad x_1 = \pi \tag{2.4b}$$

$$u_z = 0 \tag{2.4c}$$

and the parameters are chosen to be  $\gamma = 0.4$ ,  $x_1 = 3\pi/2$ . The ratio of energy between Taylor-Green flow and vortex sheet is taken to be 0.1. With total energy set to unity, this fixes  $\varepsilon$  and  $A$  in equation (2.4).

Unlike the imposed localized perturbations before (see Fig. 2.3) that compresses the sheet directly, in this case, the evolution of a large-scale background Taylor-Green flow causes the sheets to *bend* initially, leading to thinning and compression. This can be seen from the initial condition (Eq. (2.4)), where  $S_{xx} = 0$  along both sheets ( $x = \pm x_1$ ) and for  $t \geq 0$  the component  $u_x$  starts to bend the sheet, followed by the shear from the component  $u_y^{\text{SH}}$ . Hence, this compression leads to the development of sharper gradients and the eventual trigger

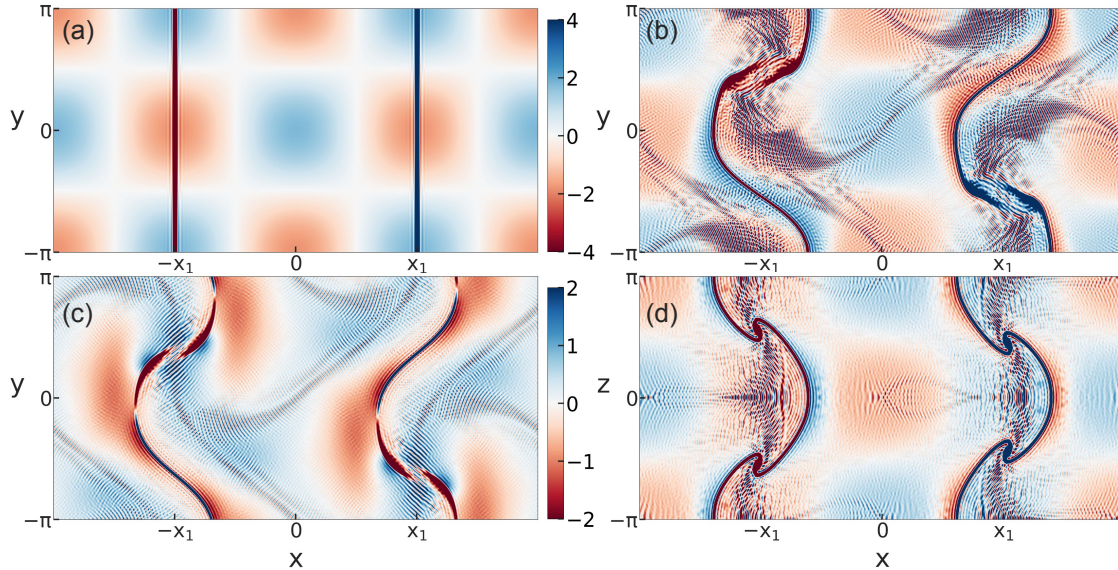


Figure 2.5: Pseudo-color plots of the two-dimensional XY cut of  $\omega_z$  for a pair of vortex sheets advected by a Taylor-Green flow (Eq. (2.4)) at (a)  $t = 0$  (along with the velocity vectors  $(u_x, u_z)$ ), (b)  $t = 0.8$ , and (d)  $t = 1.5$ . show a proliferation of oscillations in time. Shown in panel (c) is the strain component  $S_{xx}$  (at  $t = 0.8$ ). A correlation can be seen between positive strain  $S_{xx} > 0$  (*blue*) and the sustained oscillations in  $\omega_z$  by comparing panels (b) and (c). The link in Ref. [162] shows the full evolution of this flow up to the onset of thermalization.

of  $\lambda_c$ -wavelength oscillations in the vorticity field  $\omega_z$ . In figure 2.5(b), we show a representative snapshot of the  $\omega_z$  field at  $t = 0.8$ , where the bent sheets get compressed and stretched in different regions. These compressed regions become sources of truncation waves and produce streaks of oscillations in the  $\omega_z$  field.

The use of the background Taylor-Green flow validates our earlier predictions and conclusions in a more general flow configuration. Figure 2.5(c) shows the strain field  $S_{xx}$  at  $t = 0.8$ , and we observe that there is a clear correlation between regions with  $S_{xx} \geq 0$  (in *blue*) and regions with oscillations of  $\omega_z$  (see Fig. 2.5(b)). A caveat: Although the oscillations in figure 2.5(b) seem to be not oriented horizontally, our choice of the strain field  $S_{xx}$  for comparison is motivated by the fact that initially almost all of the oscillations were along the  $x$ -axis. Furthermore, the fact that the strain and vorticity fields are coupled through the evolution equations leads to faint oscillations in  $S_{xx}$  as well. Finally, as seen in figure 2.5(d), this correlation persists even for a later time ( $t = 1.5$ ), when there is further amplification of thermalization hotspots.

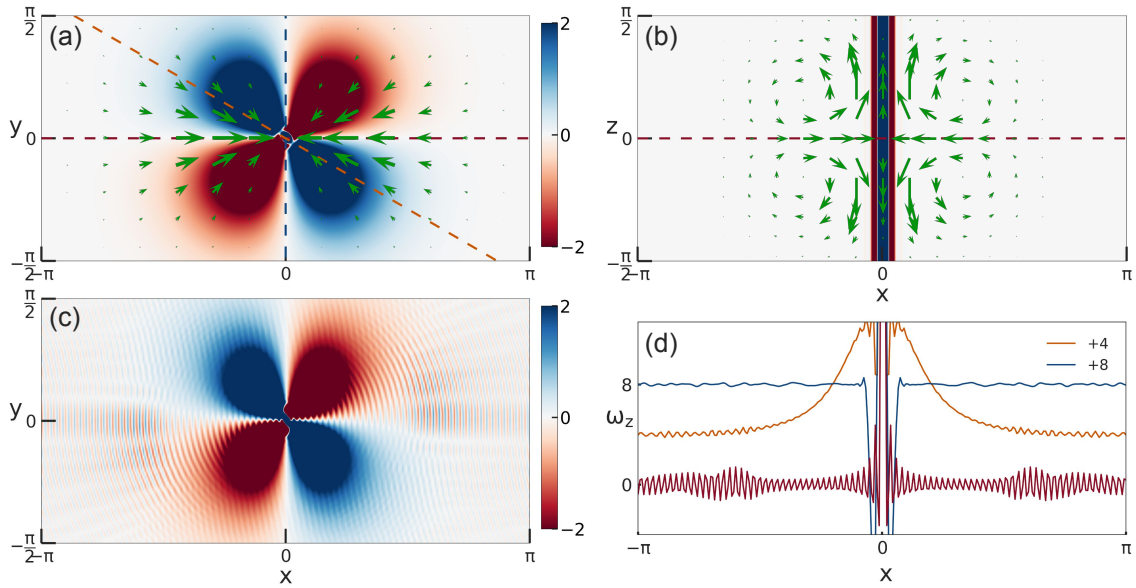


Figure 2.6: Pseudo-color plots of  $\omega_z$  at  $t = 0$  across (a) XY (b) XZ planes; the green arrows indicate the velocity components  $u_r$  and  $u_z$ , respectively. Panel (c) shows  $\omega_z$  at a later time  $t = 0.12$  with radially spreading oscillations. In panel (d), the asymmetry in the strength of the oscillations at different angles is illustrated in the line-plots of  $\omega_z$  across  $\theta = 0$  (red),  $\theta = \pi/6$  (orange), and  $\theta = \pi/2$  (blue); these directions were already indicated as dashed lines with the same color in panel (a). See Ref. [163] for an animation of the evolution of this flow to show the onset of thermalization.

As a final example featuring a different geometrical vortical structure, we simulate a vortex filament (Fig. 2.6) under the Galerkin-truncated Euler equation to illustrate the nature of the onset of thermalization in a one-dimensional intense structure. The initial condition we chose to study is a stationary vortex filament together with a locally radially compressing flow: in cylindrical coordinates

$$u_\theta(r) = \gamma k_G r \exp\left(-\frac{1}{2}(\gamma k_G r)^2\right) \quad (2.5a)$$

$$u_r(r, z, \theta) = -u_0 k_\beta r \left(\frac{1}{2} - \frac{1}{2}(k_\beta z)^2\right) \exp\left(-\frac{k_\beta^2}{2}[r^2 + z^2]\right) \cos^2 \theta \quad (2.5b)$$

$$u_z(r, z, \theta) = u_0 k_\beta z \left(1 - \frac{1}{2}(k_\beta r)^2\right) \exp\left(-\frac{k_\beta^2}{2}[r^2 + z^2]\right) \cos^2 \theta \quad (2.5c)$$

Once again, this cylindrical vortex ( $u_\theta$ ), whose thickness is determined by  $\gamma = 0.25$ , is immersed in a large-scale background flow ( $u_r, u_z$ ), that perturbs the filament within a range of  $k_\beta^{-1} = \pi/4$  and with an amplitude of  $u_0 = 10$ . Note that the presence of  $\cos^2 \theta$  in equation (2.5) induces a generic three-dimensional perturbation in an otherwise axi-symmetric flow. Hence, the radial velocity  $u_r$  compresses the

filament near  $z = 0$ , most along the  $\theta = 0$  direction ( $x$ -axis), gradually losing strength all the way to zero for  $\theta = \pi/2$ , as depicted in figure 2.6(a). Not surprising, the evolution of this initial condition (Eq. (2.5)) with the truncated Euler equations leads to oscillations that are radial with the filament at its core (Fig. 2.6(c)). The difference in the compressive eigenvalue along different radial lines (shown by red, orange, and blue lines in figure 2.6(a)) reflects in the corresponding strength of oscillations seen in the line-plot of the vorticity  $\omega_z$  along those lines in figure 2.6(d). Further, the oscillations are amplified for  $r \gtrsim \pi/2$  because of the support from the background flow.

### 2.3 The Phenomenological Picture

In all the model flows studied above, consistent with our hypothesis, the intense structures become a source of truncation waves and sustain oscillations along the compressional eigen direction. It is crucial that we emphasize two important points in our findings:

1. The compressional eigen direction of the strain field near the extreme structures need not be perpendicular to the structures themselves, but the strength of the oscillations appearing is proportional to the component of compressive strain along the normal (depicted in Figs. 2.4(d) and (e)).
2. The oscillations born along the compressional eigendirection grow in amplitude when the strain along the direction is positive. Thus, while the fluid has to be compressive (locally) only near the structure, along that compressive eigendirection, far from the structure, the positive strain is *essential* to support and sustain the growth of the oscillations and hence eventual thermalization. Indeed, a negative strain here would lead to the damping of oscillations and the suppression of the onset of thermalization.

The corresponding problem for the 1D Burgers equation is actually a special case of this phenomenon: In one-dimensional space, the flow is compressional, and hence the oscillations, trivially seen in the velocity profile, accumulate at resonance points, leading to (at early times) spatially localized structures christened *tygers* [39].

Therefore, we have now demonstrated, through numerical experiments with such specialized initial conditions, that the onset of thermalization in a *generic* three-dimensional truncated system can be seen as a superposition of processes that are essentially one-dimensional: At very short times, monochromatic oscillations arise along the compressional directions associated with fluid structures with critical velocity gradients in regions supported by fluid strain. While this was implicit for generic, large-scale initial conditions which are used to solve the Galerkin-truncated Euler equation, the use of such special flows is essential to making this phenomenon evident. In more generic flows, such extreme velocity-gradient structures proliferate the flow and emerge at different times. Hence, each of these structures can act as a sources of truncation waves. Although, as our extensive analysis of model flows suggests, these are born individually from each *source*, before long they superpose, amplify, generate other harmonics, and eventually lead to thermalization.

To summarize, the onset of thermalization requires the conspiracy of two key ingredients. Firstly, sufficiently sharp fluid structures that are compressed lead to truncation waves and hence oscillations of wavelength  $\lambda_c$ . This is perfectly analogous to the role shocks play in the well-understood problem of the 1D Burgers equation [39, 41]. Secondly, in the vicinity of these structures, the flow must have a non-negative strain to sustain such oscillations. This is essential because a negative strain would lead to squeezing and the generation of harmonics with wavenumbers in excess of  $k_c$ : Such higher harmonics would get expunged because of the truncation constraint, that allows only modes with wavenumbers  $\leq k_c$ . While there are essential points of similarity between the analogous 1D Burgers problem, there are also crucial differences. Apart from the complexity of this phenomenon in three dimensions relative to the 1D problem—and hence the need to resort to model flows—what makes the present problem unique is the lack of resonance points where oscillations

can accumulate and grow.

# Chapter 3

## Dissipative solutions from Galerkin-truncated Inviscid Hydrodynamics

In the previous Chapter ( 2), we saw the phenomena—illustrating the onset of thermalization—about *how* and *where* oscillations shows up in real space, having its support on the positive strain region, for the Galerkin-truncated solutions to the Euler equation. In this Chapter, we propose a recipe and show how the Galerkin-truncated equation can be modified mildly to obtain solutions which do not thermalize. This allows us to obtain numerically:

1. More reliable estimates of the widths of the analyticity strip.
2. Weak, but dissipative, solutions (henceforth called weak-dissipative, for convenience) of inviscid equations.

The reasons which motivates this study are of course fundamentally important for the 3D Euler equations and less so for the 1D Burgers equation. However the process and mechanisms of thermalization was best understood by

resorting to the 1D Burgers equation [39–41, 164], with an added merit that the 1D problem is solved in terms of its singularity formation and the accompanying *unique* weak solution.

This Chapter is organized as follows: In section 3.1, we present the weak solution to the inviscid Burgers equation, contrasted with the solution to the Galerkin-truncated equation. In section 3.2, we outline a novel numerical method that suppresses the thermalization, and present the numerical results portraying the success of the numerical recipe. Finally in section 3.3, we introduce a decomposition for the thermalizing solutions that serves as a useful starting point to suppress the oscillations in the 3D case.

## 3.1 Entropy *vs* Thermalizing solutions

In 1915, H. Bateman [165] introduced a partial differential equation for the field  $u$ , for the spatio-temporal domain  $(x, t) \in [0, L] \times [0, T]$

$$\frac{\partial u}{\partial t} + u \frac{\partial u}{\partial x} = \nu \frac{\partial^2 u}{\partial x^2} \quad (3.1)$$

with an initial condition  $u(x, 0) = u_0(x)$  and generalized boundary conditions  $u(0, t) = \zeta_1(t), u(L, t) = \zeta_2(t)$  for  $0 \leq t \leq T$ . Later J. M. Burgers, a Dutch scientist, used this as a one-dimensional model for pressure-less gas dynamics, [166, 167]. The idea was that such simple model having much in common with the Navier-Stokes, like the quadratic non-linearity, similar invariances and conservation laws for the ideal cases, would help significantly to the study of fluid turbulence. To honour the contributions of Burgers, this equation (3.1) is well known as Burgers equation. Later Cole [168] and Hopf [108] showed that the Burgers equation (3.1) can be integrated explicitly. Burgers equation is a fundamental partial differential equation occurring in various areas such as fluid mechanics [21, 22], statistical physics [169–171], cosmology [172] and traffic flow [173].

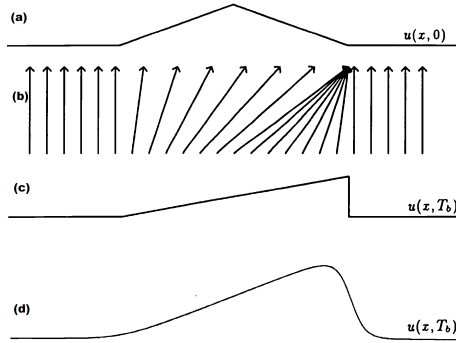


Figure 3.1: showing (a) initial profile (b) characteristics (c) formation of shock at  $t^* = T_b$ , at  $x^*$  (d) solution to viscous burgers, *Image adapted from [147]*

Here, we will focus on the nature of solutions to the inviscid case  $\nu = 0$ , starting with a *smooth* (atleast once differentiable, that is  $u_0(x) \in C^1(\mathbb{R})$ ) initial condition  $u_0(x)$ :

$$\frac{\partial u}{\partial t} + u \frac{\partial u}{\partial x} = 0 \quad (3.2)$$

The characteristic method for this hyperbolic PDE gives the solution for each particle at time  $t \geq 0$  (starting at position  $x_0$ ) as a continuous mapping of points:

$$x_0 \mapsto x = x_0 + u_0(x_0)t \quad (3.3)$$

As we can see from equation (3.3), the characteristics are straight lines with different slopes, the slope simply being the initial velocity at that point. Then for  $u_0(x) \neq \text{const}$ , two particles with different velocities can cross each other<sup>1</sup>, which is unphysical in reality and mathematically a singularity. We define *breaking time*  $t^*$  as the first time at which two neighbouring particles cross each other [147], equivalent to the vanishing of the Jacobian  $J = \frac{\partial x(t)}{\partial x_0}$ , that ceases the existence of strong solutions, is given by:

$$t^* = \min \left[ \frac{-1}{u'_0(x_0)} \right] \quad (3.4)$$

Analytical continuation into the complex domain, for time  $t < t^*$ , shows

---

<sup>1</sup>Definitely if we consider the periodic boundary conditions.

a singularity in the complex domain  $z^*(t) \in \mathbb{C}$  satisfying the equation:

$$1 + \frac{\partial u_0(z)}{\partial z} \Big|_{z^*} t = 0, \quad t \leq t^* \quad (3.5)$$

Tracking the  $z^*$  in the complex plane for the Burgers equation illustrates characteristics of the solution near the singularity [27]. For the sake of simplicity and illustration, we shall use the initial condition  $u_0(x) = -\sin(x)$  with periodic boundary conditions  $x \in [0, 2\pi]$  for the rest of this section, unless mentioned otherwise.

The breaking time is (Eq. (3.4))  $t^* = 1$  and the shock appears at  $x^* = 0 \equiv 2\pi$ . Thus for  $t \leq t^*$ , the initial position of singularity is at

$$z_0^* = \cos^{-1} \left( \frac{1}{t} \right). \quad (3.6)$$

Since  $t \leq t^* = 1$  with our initial condition, making  $z_0$  purely imaginary, that is

$$z_0^* = i\delta_0^* \quad \text{and} \quad \delta_0^* = \cosh^{-1} \left( \frac{1}{t} \right). \quad (3.7)$$

The current (*Eulerian*) position of the complex singularity at  $t$  is at

$$\delta^*(t) = \cosh^{-1} \left( \frac{1}{t} \right) - t \sinh \left( \cosh^{-1} \left( \frac{1}{t} \right) \right). \quad (3.8)$$

Thus the singularity travels along imaginary axis from  $\infty$  to 0 (see Fig. 1.1 in Chap. 1). For  $t \lesssim t^*$ , the Lagrangian  $z_0^*$  and Eulerian  $z^*$  locations of the singularity nearest to the real domain is close to the origin and can be obtained by expanding  $\sin x$  to cubic order, neglecting higher order terms.

$$z_0^* = \pm i \sqrt{\frac{2(t^* - t)}{t^*}} \quad (3.9)$$

$$z^* = \pm \frac{2\sqrt{2}}{3} i (t^* - t)^{\frac{3}{2}} \quad (3.10)$$

Similarly the velocity around the singularity points near its pre-shock location can be shown to obey,

- For  $\delta \neq 0$ ,

$$\begin{aligned} u(x, t) &\sim (x - x^*)^{\frac{1}{2}} \\ \hat{u}_k &\sim k^{-\frac{3}{2}} e^{-\delta(t)k}, \quad k \gg 1 \end{aligned} \tag{3.11}$$

- For  $\delta = 0$ , at  $t = t^*$

$$\begin{aligned} u(x, t^*) &\sim (x - x^*)^{\frac{1}{3}} \\ \hat{u}_k &\sim k^{-\frac{4}{3}}, \quad k \gg 1 \end{aligned} \tag{3.12}$$

These scaling laws are true locally near the singularity arising from an arbitrary initial condition. Now for  $t > t^*$ , the characteristic solution (Eq. (3.3)) is multi-valued, thus not physically acceptable. The only way to establish a solution after the breaking time  $t^*$  is to allow for discontinuities in  $u$  (such discontinuities are called “*shock*”) exist in a consistent manner. Such solutions are known as weak solutions and  $u$  will satisfy the integral form of the conservation law. The basic idea is to take the PDE, multiply by a smooth “*test function*” [147, 174], integrate and use integration by parts to move derivatives to the smooth test function.

Assume the shock has formed at  $t^*$  at  $x^*$  and the velocity on either end of the shock is  $u_1$  and  $u_2$ , respectively, and the velocity of the shock is, say,  $c$ . The following (*Entropy*) conditions has to be satisfied for the solution to be physically realizable, and for its uniqueness.

$$\begin{aligned} c &= \frac{1}{2}(u_1 + u_2) \\ u_1 &> u_2 \end{aligned} \tag{3.13}$$

By using the Cole-Hopf transformation [108], the viscous Burgers equation can be analytically solved, and in the vanishing viscosity limit  $\nu \rightarrow 0$ , the Entropy solutions can be obtained. The Cole-Hopf transformation from  $u(x, t)$  to a new

variable  $\phi(x, t)$  is defined as:

$$u(x) = -2\nu \frac{\partial_x \phi(x)}{\phi(x)} \quad (3.14)$$

Rewriting the Burgers equation (3.1) in terms of new variable  $\phi$ , with a bit of an algebra, we get

$$\begin{aligned} \partial_x \phi (\partial_t \phi - \nu \partial_{xx} \phi) &= \phi \partial_x (\partial_t \phi - \nu \partial_{xx} \phi) \\ \Rightarrow \partial_t \phi &= \nu \partial_{xx} \phi. \end{aligned} \quad (3.15)$$

Hence, solution to the Burgers equation (3.1) for the initial condition  $u_0(x)$  ( $\Rightarrow \phi_0(x) = \exp\left(- (2\nu)^{-1} \int_0^x dy u_0(y)\right)$ ) is

$$u(x, t) = \frac{\int dk \frac{x-k}{t} \hat{\phi}_0(k) \exp\left\{-\frac{(x-k)^2}{4\nu t}\right\}}{\int dk \hat{\phi}_0(k) \exp\left\{-\frac{(x-k)^2}{4\nu t}\right\}} \quad (3.16)$$

It is useful to introduce a velocity potential  $\psi(x, t)$  as

$$u(x, t) = -\partial_x \psi(x, t), \quad (3.17)$$

so the the solution in equation (3.16) in terms of  $\psi$  is

$$\psi(x, t) = 2\nu \ln \left[ \frac{1}{\sqrt{4\pi\nu t}} \int_0^{2\pi} dy \exp \left[ \frac{1}{2\nu} \left( \psi_0(x) - \frac{(x-y)^2}{2t} \right) \right] \right]. \quad (3.18)$$

Now in the vanishing viscosity case  $\nu \rightarrow 0$ , with a saddle point approximation on the integral in equation (3.18) leads to the limiting solution:

$$\psi(x, t) = \max_y \left[ \psi(y, 0) - \frac{(x-y)^2}{2t} \right] \quad (3.19)$$

In the  $\psi - x$  plane, the Lagrangian manifold is carved out in time by the

maps:

$$x(t) = a + tu_0(a) \quad (3.20)$$

$$\psi(x, t) = \psi_0(a) - \frac{t}{2}u_0^2(a) \quad (3.21)$$

assuming that  $a$  is the location of the evaluated maximum. Note that this solution is valid for all times, even with finite no of shocks existing throughout the domain. To show the anomalous dissipation in the entropy solution, consider the initial condition  $u_0(x) = \sin(x)$   $x \in [-\pi, \pi]$ , after the shock  $t \geq t^* = 1$ , the solution becomes

$$u(x, t) = \frac{1}{t} \left( x - \pi \tanh \left[ \frac{\pi x}{2\nu t} \right] \right), \quad (3.22)$$

then as  $\nu \rightarrow 0$ , the solution (3.22) becomes (see Fig. 3.2)

$$u = \begin{cases} \frac{1}{t}(x + \pi) & \text{for } x < 0 \\ \frac{1}{t}(x - \pi) & \text{for } x > 0 \end{cases} \quad (3.23)$$

which is just a ramp with decreasing kinetic energy  $E$  (as shown in Fig. 3.2) and with a dissipation rate  $\epsilon$  given by

$$\begin{aligned} E &= \frac{1}{2} \langle u^2 \rangle = \frac{\pi^2}{6t^2} \\ \epsilon &= -\frac{dE}{dt} = -\frac{1}{3} \frac{\pi^2}{t^3}. \end{aligned} \quad (3.24)$$

The vanishing viscosity approach is way of obtaining weak solutions to inviscid Burgers equation. Since the equation is elliptic in nature, singularities will never form for  $\nu \neq 0$ , but for the limiting case it does.

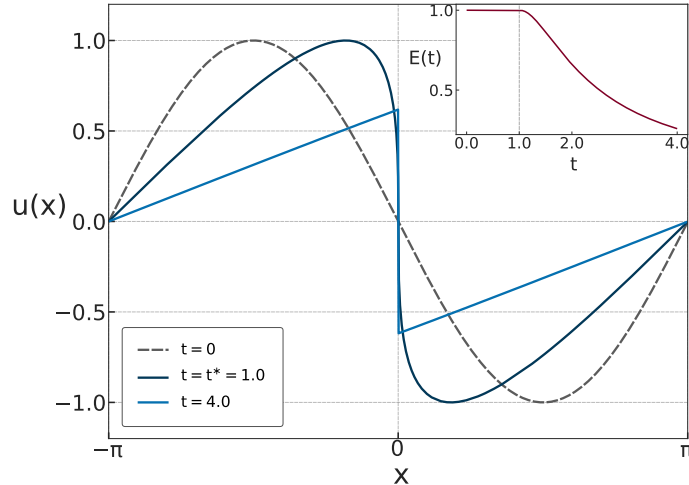


Figure 3.2: Showing the Entropy solution to the initial condition  $u_0 = \sin x$  at different times (*see legends*). Inset showing the dissipation of energy after the breaking time  $t^* = 1$ .

### 3.1.1 Galerkin-truncated Burgers equation

Now we turn to the finite-dimensional inviscid Burgers equation that is obtained via the Galerkin-truncation of the parent ODE (Eq. (3.2)) Since we work in the space of  $2\pi$  periodic solutions, we can expand the solution of equation (3.2) in a Fourier series allowing us to define the Galerkin projector  $\mathbb{P}_{k_G}$  as a low-pass filter which sets all modes with wavenumbers  $|k| > k_G$ , where  $k_G$  is a positive (large) integer, to zero via:

$$v(x) = \mathbb{P}_{k_G} u(x) = \sum_{|k| \leq k_G} e^{ikx} \hat{u}_k \quad (3.25)$$

These definitions allow us to write the Galerkin-truncated inviscid Burgers equation for the  $v(x)$  as

$$\frac{\partial v}{\partial t} + \mathbb{P}_{k_G} \frac{1}{2} \frac{\partial v^2}{\partial x} = 0 \quad (3.26)$$

and augmented with the initial conditions  $v_0 = \mathbb{P}_{k_G} u_0$  that are similarly projected onto the subspace spanned by  $k_G$ .

In the last section, we saw that the solution to the inviscid Burgers equation (3.2) show one or more shocks (determined by  $u_0(x)$ ), after an initial condition dependent finite-time  $t^*$ . Theoretically, the strong solution to the

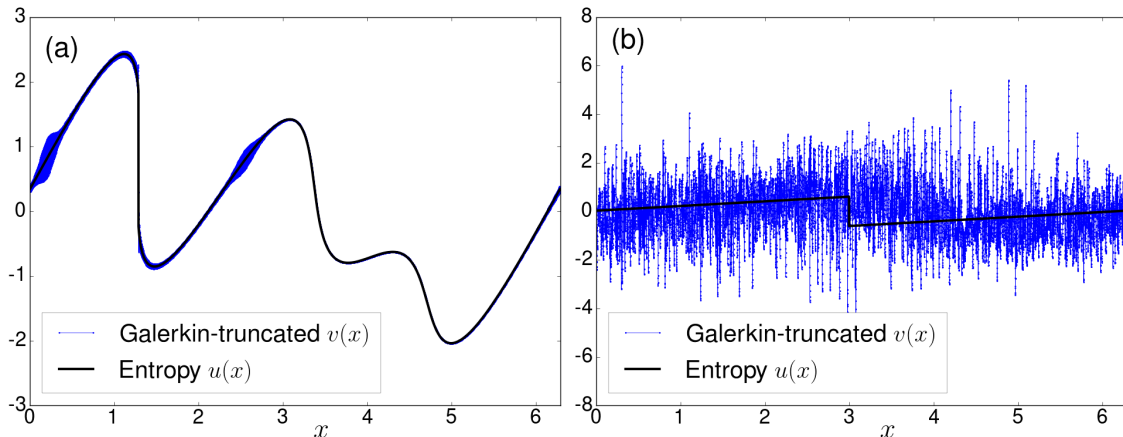


Figure 3.3: Representative plots, for  $k_G = 1000$ , of the Galerkin-truncated  $v$  (blue) and entropy  $u$  (black) solutions of the Burgers equation at (a)  $t = 0.24 \gtrsim t_*$  and (b)  $t = 5.0 \gg t_*$ . For the Galerkin-truncated solution, panel (a) shows signatures of impending thermalization through the birth of *tygers* while panel (b) shows the fully thermalized solutions. (Refer to the youtube link [175] for a movie of the time evolution of the Galerkin-truncated equation (and the entropy solution) with a single-mode initial condition for clarity.)

equation (3.2) ceases at  $t^*$ , and for  $t \geq t^*$ , the *unique* weak solution (satisfying the Entropy conditions) can be obtained by the vanishing viscosity method, that preserves the finitely many shocks in its evolution and dissipates energy through them.

In contrast, the Galerkin-truncated equation (3.26) conserves energy for all times. For initial conditions with a finite number of non-vanishing Fourier harmonic, the solution  $v$  mimics rather well that of the inviscid PDE up to time  $t \lesssim t^*$ . Indeed, for  $t \ll t^*$ , the two solutions are essentially indistinguishable. However, when the distance of the nearest (complex) singularity of the un-truncated equation (3.2) from the real domain  $\delta$  is within one Galerkin wavelength ( $\sim 2\pi/k_G$ ), at time  $t - t^* \sim k_G^{-1/3}$ , the effect of truncation becomes important. Obviously at  $t = t^*$ , no such shock profile is built in the GT solution, as the finite number of Fourier modes cannot model a discontinuity. It was originally suggested by Kraichnan and Chen that the truncated conservative can behave as dissipative ones when considering only the spatial modes which have not thermalized. The idea behind this is that high wave number thermalized modes can act as an energy sink for the low wave number modes, which will behave as in a normal turbulent flow [36].

For  $t > t^*$ , the solutions of the truncated-equation and the PDE are dramatically different: Whereas the former stays smooth, conserves energy, and start thermalizing (beginning at small scales) with an (equipartition) energy spectrum  $\langle |\hat{v}_k|^2 \rangle \sim k^0$  [40], the latter shows a monotonic decrease in its kinetic energy (dissipated through the shock(s)) and an associated scaling  $\langle |\hat{u}_k|^2 \rangle \sim k^{-2}$ . (The angular brackets  $\langle \dots \rangle$  used denotes suitable ensemble averages.) Thus thermalized solutions, inevitable in (numerical) solutions of the Galerkin-truncated inviscid equations, are fundamentally different from—and hence do not converge to—the un-truncated parent PDE.

We illustrate this phenomenon in figure 3.3 by showing the solutions of the Galerkin-truncated equation  $v$  (in blue), with  $k_c = 1000$ , and the entropy solution  $u$  (in black) for (a) an early time  $t = 0.24$  ( $\gtrsim t^*$ ) and (b) at a later time  $t = 5.0$  ( $t \gg t^*$ ); the details of such numerical simulations are given later. As discussed above, even at times very close to  $t_* \approx 0.23$  (Fig. 3.3a), the two solutions show a marked difference—*tygers*—at points which have the same velocity as the shock (and a positive fluid velocity gradient). At even later times, (Fig. 3.3b) we see clear signatures of thermalization in the truncated solution having no resemblance to the entropy solution which, as a consequence of shocks merging in time, has a saw-tooth structure with a single shock. Below we provide a brief explanation of the origin and properties on the onset of thermalization. We refer the reader to references [39–41, 148, 150, 164] for more details and the theory on the process of thermalization.

### 3.1.2 Onset of Thermalization: *Tygers*

To portray a phenomenological explanation for the Tyger phenomenon, showing the onset of thermalization, consider the projector  $\mathbb{P}_{k_c}$  that makes equation (3.26) non local in physical space. More precisely, in physical space the non-linear term  $\mathbb{P}_{k_c} \partial_x v^2$

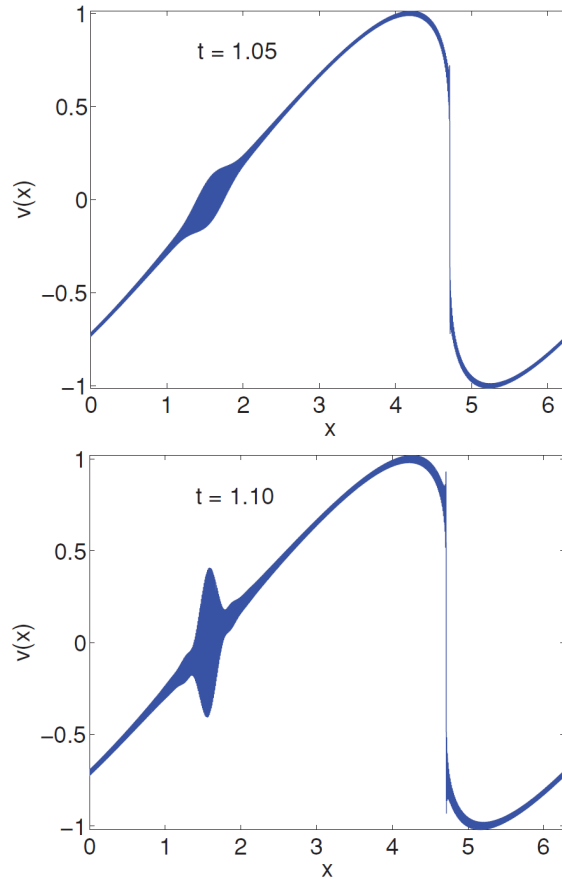


Figure 3.4: Figure showing the birth of *Tygers*, plot taken from [39]

involves a convolution with a GT delta function:

$$\mathcal{F}[\mathbb{P}_{k_G}](x) = \sum_{-k_G}^{k_G} e^{ikx} = \frac{\sin\left(k_G + \frac{1}{2}\right)x}{\sin\left(\frac{x}{2}\right)} \quad (3.27)$$

For  $k_G \gg 1$ , the GT delta function (Eq. (3.27)) is close to Dirac measure near the source, and is mostly a plane wave with a wave number close to  $k_G$  away from the shock. From a lagrangian point of view, fluid particles just move with their velocity unchanged. In the presence of truncation, those particles which happen to have a velocity equal to the phase velocity of a truncation wave  $v_{\text{shock}}$  can resonantly interact with such waves. Further, at time  $\tau$  from the pre-shock the resonant interactions are confined to particles satisfying

$$\tau|v - v_{\text{shock}}| \lesssim \lambda_{k_G} = \frac{2\pi}{k_G} \quad (3.28)$$

and with positive strain  $\partial_x v_x$  produce oscillations, which are named as *Tygers*, as

shown in figure 3.4 for the initial condition  $v_0 = -\sin x$ . Because, in the region of negative strain a wave of wave number close to  $k_G$  will be squeezed, making it to acquire wave number greater than  $k_G$ , thus disappearing beyond the truncation horizon.

Now how does the highly organized and localized tyger structure evolve into a totally random thermalized state? At first, very symmetrical bulges whose amplitude grows in time [39], because truncation wave input has accumulated, while their width decreases, as a consequence of phase mixing. This decrease in width leads to collapse of the tyger and becomes assymmetrical in nature. It is because, the Tyger's kinetic energy is constantly increasing in terms of oscillations at the Galerkin wavelength to compensate the loss of energy in the shocks. Now in (physical space) scales large compared to  $\lambda_{k_G}$  but small compared to the tyger width  $w$  (*say*), this kinetic energy gives rise to  $\tan x$  dependent Reynolds stress (due to presence of positive velocity gradient), which distorts the tyger envelop. If the envelope has a negative slope, then the tyger is pulled away from the axis and if it has positive slope then it is pulled towards the axis.

With this phenomenological understanding of the birth of tygers—illustrating the onset of thermalization—it is useful to derive scaling properties of these localized oscillations that come in handy later on when we attempt to suppress them. We have seen that tygers are born at suitable resonance points in the form of bulges made of oscillations at the Galerkin wavelength with a very symmetrical envelope. Consider a Tyger in its early onset stage with an amplitude  $a$  and width  $b$ .

As we saw in the section 3.1, when complex singularity reaches within the analyticity strip of width  $\delta$  at a *birth* time  $\tau = t - t^* \sim \mathcal{O}(k_G^{2/3})$ . With the  $u_{\text{shock}} = 0$ , the resonance is affected within the region having velocities

$$v \lesssim \frac{2\pi}{k_G k_G^{3/2}} \sim k_G^{-1/3}. \quad (3.29)$$

Since at such times, the velocity  $v$  of the truncated solution is expected to

stay close to the velocity  $u$  of the untruncated solution which varies linearly with  $x$  near the resonance point. Thus we have the width of the Tygers at  $t^*$  is of the order

$$b \sim k_G^{-\frac{1}{3}}. \quad (3.30)$$

Since untruncated solution has a cubic root singularity near the pre shock location, that is  $u(x) \sim (x - x^*)^{1/3}$ . Then the difference in energy (between the two solutions) would scale as

$$\int_0^{\lambda_G} dx x^{\frac{2}{3}} \sim k_G^{-\frac{5}{3}}. \quad (3.31)$$

Further with the GT equation conserving energy, this packet of energy is stored in the Tygers as  $a^2 b \sim k_G^{-5/3}$ . Hence the amplitude  $a$  of the Tygers is of order

$$a \sim k_G^{-\frac{2}{3}}. \quad (3.32)$$

These scaling laws found in equations (3.29),(3.30),(3.31), and (3.32) on the truncation wavenumber  $k_G$  are for the early Tygers. In the same spirit, under suitable approximations, the discrepancy between the two solutions can be studied near  $t^*$  as a linear algebra problem (see Ref. [39] for more details).

In fact, if  $u'_k = \mathbb{P}_{k_G}[\hat{v}_k - \hat{u}_k]$ , then the study has shown that the solution to  $u'$  has a clear even-odd oscillations that has a scaling representation for  $k \sim k_G$  as:

$$u'_k = \frac{i}{k_G} c_1 \exp\left\{-c_2 \frac{k_G - k}{k_G^{\frac{1}{3}}}\right\}, \quad c_1 = 0.448, \quad c_2 = 3.45 \quad (3.33)$$

## 3.2 Suppressing Thermalization in the Galerkin-truncated Burgers equation

We know that a *strong* solution to the Galerkin-truncated Burgers equation exists for all times and conserves energy. On the other hand, the actual PDE only has a weak (entropy) solution that dissipates energy through shocks. The striking

difference that these two solutions show near the (first) shock formation are in the shock formation and dissipation of energy from them.

All of this leads us to ask if we can, without resorting to viscous dissipation, actually suppress thermalization setting in in such truncated equations and obtain the entropy solution? The short answer is yes as we now report a novel approach—*tyger purging*—which, through the selective removal of a narrow, Fourier space, boundary layer near  $k_G$ , at discrete time-intervals, resulting in the suppression of thermalization. But we want the cascading energy to enter the modes near  $k_G$ , so we remove energy at regular intervals.

To summarize, the idea of the purging technique is as follows. Create a boundary layer near the truncated wavenumber from  $k_P \lesssim k_G$  to  $k_G$ . Select an appropriate purging time interval  $\tau$  such that for  $t > t^*$ , at times  $t = n\tau$ ,  $n \in \mathbb{Z}^+$ , modes in the boundary layer are set to zero, removing the energy

$$\Delta E = \sum_{k_P}^{k_G} |v_k|^2. \quad (3.34)$$

The equation of motion for the purged solution  $w(x, t)$  is, of course, the same as that of the Galerkin-truncated equation (Eq. (3.26) with the truncation wavenumber  $k_G$ )

$$\frac{\partial w}{\partial t} + \mathbb{P}_{k_G} \frac{1}{2} \frac{\partial w^2}{\partial x} = 0, \quad (3.35)$$

augmented by an additional constraint imposed at discrete times  $t_p = t^* + n\tau$  ( $n = 0, 1, 2, 3 \dots$ ):

$$\hat{w}_k = 0, \quad \forall k_P \leq |k| \leq k_G. \quad (3.36)$$

We call this truncated equation, along with the additional *purging* constraint, as in equation (3.36), as simply the purged equation. One could write them compactly in

Fourier space as

$$\frac{d\hat{w}_k}{dt} = -\frac{i}{2}k \sum_q \hat{w}_q \hat{w}_{k-q} - \Theta(k_p - k) \sum_{n=0,1,2}^{\infty} \delta(t - t^* - n\tau), \quad |k|, |q|, |k - q| \leq k_G \quad (3.37)$$

We immediately note that without the additional constraint, by definition, the solution  $w$  is the same as  $v$  obtained from the truncated equation and hence if purging is done continuously, and not discretely, in time, we would end up solving the Galerkin-truncated equation (3.26) but with a truncation wavenumber  $k_p$ .

But how do we choose  $k_p$  and  $\tau$  in a consistent manner. We now make the following *ansätze* about the inter-purging time  $\tau$  and the purging wavenumber  $k_p$ :

$$\tau = k_G^{-\alpha} \quad \text{and} \quad k_p = k_G - k_G^\beta; \quad (3.38)$$

with real, positive exponents  $\alpha$  and  $\beta$  and the immediate constraint that  $\beta < 1$ . Before we engage in a detailed numerical analysis on the purged equation, let us estimate, heuristically, optimal choices of  $\alpha$  and  $\beta$  keeping in mind that the purged solution  $w$  must converge to the entropy solution  $u$  as  $k_G \rightarrow \infty$ . For  $t > t^*$ , the entropy solution, unlike the truncated solution, is dissipative:  $\frac{dE}{dt} \leq 0$ , where  $E = \frac{1}{2} \sum_{k=0}^{\infty} |\hat{u}_k|^2$  is the total energy. Indeed, for times  $t \sim t^*$ , (when tygers are just born), the Galerkin-truncated Burgers equation remains conservative by the transfer—and subsequent accumulation—of kinetic energy  $\propto k_G^{-5/3}$  from the “shock” to the tygers [39].

By construction, however, purging technique allows for a finite energy loss  $\Delta E^P \equiv \sum_{k=k_p}^{k_G} |\hat{w}_k|^2$  at intervals of  $\tau$  resulting in a rate of loss of energy

$$\begin{aligned} \epsilon^P &= \frac{dE^P}{dt}, & E^P &= \sum_{k=1}^{k_G} |\hat{w}_k|^2 \\ &\approx \frac{\Delta E^P}{\tau}, \end{aligned} \quad (3.39)$$

where  $E^P$  total energy of the purged system. The choice of  $\alpha$  and  $\beta$  should ensure that in the limit  $k_G \rightarrow \infty$ , this rate of energy loss should be  $k_G$ -independent and converge to the rate of energy loss of the entropy solution, i.e.,  $\lim_{k_G \rightarrow \infty} \epsilon^P \rightarrow \epsilon$ .

It is hard to estimate  $\Delta E^P$  theoretically without making suitable assumptions. Since in between two consecutive purges, equation (3.35) is identical to the Galerkin-truncated equation, it is reasonable to assume that at the time of purging the solution  $\hat{w}_k$  to be a combination of the one coming from the entropy solution  $\hat{u}_k$  and a contribution from the nascent tyger. For  $k \lesssim k_G$ , the empirical form for the difference between entropy and GT solution  $\hat{u}'_k = |\hat{u}_k - \hat{v}_k|$ , for  $t \approx t^*$ , is stated in [39] and has an envelope of oscillations for  $k \gg 1$  (see Eq. (3.33)). Assuming within the inter-purging time  $\tau$ , the boundary layer modes (between  $k_p$  and  $k_G$ ) develops the similar form, then the spectral form  $\hat{w}_k$  for  $k \lesssim k_G$  can be considered as

$$\hat{w}_k = \frac{c_0}{k} e^{i\theta_1} + \frac{c_1}{k_G} e^{i\theta_2} \exp\left\{-\frac{c_2(k_G - k)}{2k_G^{\frac{1}{3}}}\right\}. \quad (3.40)$$

The energy in the boundary layer goes as:

$$\Delta E^P = \sum_{k_p}^{k_G} \left( \frac{c_0^2}{k^2} + \frac{c_1^2}{k_G^2} \exp\left\{-\frac{c_2(k_G - k)}{k_G^{\frac{1}{3}}}\right\} + \frac{c_0 c_1 \gamma}{k_G} \exp\left\{-\frac{c_2(k_G - k)}{2k_G^{\frac{1}{3}}}\right\} \right), \quad \gamma = \text{Re}(e^{i(\theta_1 - \theta_2)}) \quad (3.41)$$

Now we are interested in the leading behaviour of  $\Delta E$  on  $k_G, \beta$  as  $k_G \rightarrow \infty$ , and evaluating equation (3.41) for that will lead to

$$\Delta E^P \sim k_G^{\beta-2}. \quad (3.42)$$

The rate at which the dissipation is done through purging (from equation (3.39)) is

$$\epsilon = \frac{\Delta E^P}{\tau} \quad (3.43)$$

$$\sim k_G^{\alpha+\beta-2}. \quad (3.44)$$

The constraint derived above is useful but it still allows considerable freedom in choosing  $\alpha$  and  $\beta$ . However, since in between purgings the solution develops only

nascent *tygers*, we can estimate  $\beta$  independently by asking if an optimal choice of  $k_p$  (thence,  $\beta$ ) leads to an elimination of the boundary layer (and hence the energy content  $\delta E^P$  of the boundary layer) such that *tygers* are suppressed. In other words, since Galerkin-truncation leads to a transfer of energy  $\sim k_G^{-5/3}$  from the shock to the *tygers* resulting in an overall conservation of kinetic energy in the truncated problem, a successful purging strategy must constraint  $\delta E^P \approx k_G^{-5/3}$  thus precisely eliminating the *tygers* which trigger thermalization and hence leading to dissipative solutions. By using the functional form for the boundary layer for incipient *tygers* [39], it is easy to show that

$$\begin{aligned}
 \delta E^P &\equiv \sum_{k=k_p}^{k_G} |\hat{w}_k - \hat{u}_k|^2 \\
 &\approx \sum_{k=k_p}^{k_G} \frac{1}{k_G^2} \exp\left[-\frac{k_G - k}{k_G^{1/3}}\right] \\
 &\approx \begin{cases} k_G^{\beta-2} & \text{for } \beta < 1/3 \\ k_G^{-5/3} & \text{for } \beta > 1/3. \end{cases} \tag{3.45}
 \end{aligned}$$

Equation (3.45) leads to the inevitable conclusion that the optimal choice of the purging wavenumber is one where  $\beta \in [1/3, 1)$  and the energy loss then is actually independent of  $\beta$  and exactly the same as that which would have triggered thermalization in the absence of purging as long as  $\beta \geq 1/3$ . Thus, we obtain an independent (theoretical) bound on  $\beta \in [1/3, 1)$  for a successful purging. Before we turn to detailed numerical simulations to validate these ideas, we make one final remark. In numerical simulations,  $\delta t$  is typically set by the resolution  $k_G$  such that  $\delta t \sim \mathcal{O}(k_G^{-1})$ . As we have noted before, purging if done too frequently would be akin to solving the Galerkin-truncated Burgers equation with  $k_G = k_p$ . This implies that  $\tau/\delta t \gg 1$  which, trivially, leads to  $\alpha < 1$ . Hence, with these insights for  $\alpha$  and  $\beta$ , we revise the constraint, estimated heuristically before, to  $\alpha + \beta \lesssim 2$ .

So how effective is purging in obtaining solutions  $w$  which resemble the entropy solution  $u$ ? We answer this by resorting to extensive and detailed numerical simulation of the purged model (3.35) as well the Galerkin-truncated equation (3.26) for comparison.

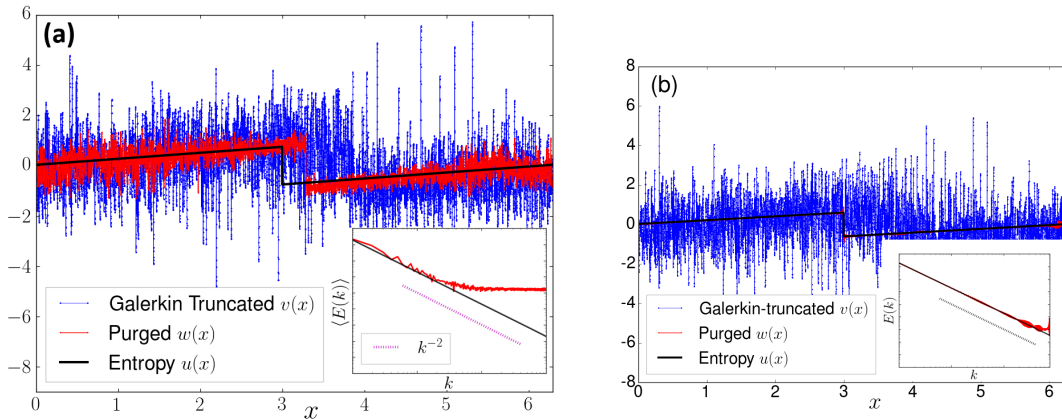


Figure 3.5: Representative plots, for  $k_G = 1000$ , of the Galerkin-truncated  $v$  (blue), the entropy  $u$  (black) and the purged  $w$  (red) solutions of the Burgers equation at  $t = 5.0$  for (a)  $\alpha = 0.6$ ,  $\beta = 0.4$  and (b)  $\alpha = \beta = 0.8$ . In panel (b), the purged and entropy solutions are quite close to being identical. (Refer to the youtube link [176] for a movie of the full evolution in time of the solutions shown in panel (b).)

For the truncated and purged equations, we perform extensive direct numerical simulations, by using a standard pseudo-spectral method and a 4<sup>th</sup> order Runge-Kutta scheme for time-marching, on a  $2\pi$ -periodic line. We use two different sets of collocation points, namely,  $N = 16384$  and  $N = 65536$  to obtain results for  $k_G = 500, 1000, 3000$  and  $5000$  (for  $N = 16384$ ) and  $k_G = 8000$ , and  $10000$  (for  $N = 65536$ ). For the purged simulations, additionally, the theoretical estimates obtained, lead us to a choice of  $\beta = 0.4, 0.6$  and  $0.8$  and for each value of  $\beta$ , the inter-purging time was obtained with  $\alpha = 0.4, 0.6, 0.8, 0.9$ , and  $1.2$ . (The simulations with  $\alpha = 0.9$  and  $1.2$  were performed to confirm that too frequent purgings lead to thermalized solutions once more with the effective truncation wavenumber  $k_p$ .)

The choice of time-steps in such simulations require some delicacy. For the truncated problem, since the maximum principle is violated, individual realisations of the velocity field can have excursions which are large (see Fig. 3.3b). Hence for the truncated simulations, as well as those where purging is ineffective in preventing thermalization, the time-step  $\delta t$  has to be kept very small. However, for the cases of *successful* purging, the maximum principle is no longer violated. Hence for these cases we are able to choose  $\delta t = 10^{-5}$  ( $N = 16384$ ) and  $\delta t = 10^{-6}$  ( $N = 65536$ ); for the analogous truncated problem (and the ones where the  $\alpha$ - $\beta$  combination fail to prevent thermalization),  $\delta t$  was taken to be at least two orders of magnitude smaller.

In numerical simulations,  $\delta t$  is typically set by the resolution  $k_G$  such that  $\delta t \sim \mathcal{O}(k_G^{-1})$ . As we have noted before, purging if done too frequently would be akin to solving the Galerkin-truncated Burgers equation with  $k_G = k_p$ . This implies that  $\tau/\delta t \gg 1$  which, trivially, leads to  $\alpha < 1$ . (We have confirmed these conjectures through several, detailed numerical simulations.)

To obtain the entropy solution  $u$ , we use the Fast Legendre transform as discussed in references [177, 178]) to solve the viscous Burgers equation in the vanishing viscosity  $\nu \rightarrow 0$  limit. In short, the fast Legendre transform uses the regularities in the equation to speed up the algorithms for finding the entropy solution. Here it is the non-decreasing nature of the Lagrangian map function  $x(t)$  (as in Eq. (3.3)) for the particles. So two particles starting at  $a_1 < a_2$  with velocities  $u_1$  and  $u_2$ , end up at time  $t$  at  $x_1$  and  $x_2$  obeying  $x_1 \leq x_2$ , with equality stating that they ended in a same shock. By implementing the standard “divide and conquer” methods, the fast Legendre transform can find the solution within  $N \log_2 N$  steps for a grid size  $N$ . We solve the equation on a  $2\pi$  line with periodic boundary conditions and choose  $N = 16384$  and  $N = 65536$  collocation points (for easy comparison with the truncated and purged solutions; see below). The velocity field is evolved keeping in mind that the velocity potential  $\psi$  (related to the velocity field via  $u = -\partial_x \psi$ , see Eq. (3.17)) obeys a maximum principle, as in equation (3.19)

Finally, we have studied the problem for several different initial conditions (all of which consist of linear combinations of trigonometric polynomials including the simplest single-mode case  $\sin(x)$ ); we have checked that our results and conclusions are consistent for all such initial conditions. In this Chapter, for brevity, we present results only for the case:

$$w_0 = v_0 = u_0 = \sin(x) + \sin(2x + 0.9) + \sin(3x) \quad (3.46)$$

In figure 3.5 we show representative plots, at  $t = 5.0$ , of the Galerkin-truncated  $v$  (in blue and thermalized), the entropy  $u$  (in black with a prominent shock) and the purged solutions  $w$  (in red) for (a)  $\alpha = 0.6$ ,  $\beta = 0.4$  and (b)  $\alpha = 0.8$ ,  $\beta = 0.8$ ; we set

the truncation wavenumber  $k_G = 1000$ . We immediately see that for  $\alpha = 0.6$  and  $\beta = 0.4$  (Fig 3.5a), the solution  $w$  approximates the entropy solution much better—in so far as picking out the ramp structure and a jump near the shock—though far from perfectly.

Remarkably, if we choose  $\alpha = \beta = 0.8$  (Fig 3.5b)—and hence much closer to satisfying the heuristic estimate  $\alpha + \beta \lesssim 2$ —the agreement between the purged and entropy solutions are near-perfect. Indeed the main point of departure between the two solutions seems to be close to the shock because of the ubiquitous Gibbs-type oscillations [179] associated with Fourier transforms of functions near discontinuities. We have checked that for  $\alpha \gtrsim 0.9$ , since  $\tau/\delta t \sim \mathcal{O}(1)$ , the purged solutions thermalize once again as we conjectured. Hence, empirically, our extensive numerical simulations show that within the range of  $\alpha$  that we study, the optimal choice is  $\alpha = 0.8$ . Furthermore, we have confirmed that our results are largely insensitive to the choice of  $\beta$  as long as its greater than  $1/3$ . Purging method can be considered as a system with scale and time dependent viscosity. For modes  $k < k_p$ , there is absolutely no viscosity, whereas for  $k \geq k_p$  it becomes infinitely viscous for a moment at purging intervals. Then how does this approach work?

Consider a finite dimensional solutions (with  $k_G$  as truncation wavenumber) to the viscous Burgers equation (3.1). At  $t = t^*(u_0)$ , a smooth shock *like* structure appears (not a mathematical shock, but a sharp structure with a width of order  $\sim \sqrt{\nu t}$ ) given  $k_G$  is large enough, that is  $k_G \gg \gg 1/\sqrt{\nu t^*}$ . For  $t > t^*$ , the modes beyond  $1/\sqrt{\nu t}$  has its dissipation term (linear) dominant over the non-linear terms, and this cutoff that separates then decreases over time. In contrast, now consider the Entropy solution, which is infinite dimensional (necessary to construct a discontinuity). Here for  $t > t^*$ ,  $\forall k \gg 1$ , there is no cutoff wavenumber, and the cascade happens till  $k \rightarrow \infty$ .

Now the purged solution, being finite dimensional, has to mimic this cascade, preserving the shock like structure for all times (unlike for a  $\nu > 0$  case) and should not thermalize. So the boundary layer created between  $k_p$  and  $k_G$  effectively

should act as a sink ( $k_{\text{cutoff}}$ ), but as an intermittent one. Since the cutoff wavenumber is fixed, the shock will not get smoothed out. Now the purging operation has to avoid thermalization which is triggered by tygers—owing to the conservation of energy. Consider the system immediately after purging, which means the boundary layer is empty. The energy from modes  $k < k_p$  sees this empty boundary layer and gushes energy into it. As the boundary layer is filled, the last mode  $k = k_c$  will saturate in some time. The purging has to happen before this, otherwise the flux will see a hard wall at  $k = k_c$  and bounce back non locally as tygers. So we have an upper bound on the purging time  $\tau$  (a lower bound on  $\alpha$ ). Suppose we purge too frequently, which implies that we keep the boundary layer mostly empty. Then effectively the flux sees a hard cutoff at  $k = k_p$  itself thus it becomes a system which is truncated at  $k_p$  rather than  $k_c$ . So the energy at  $k = k_p - 1$  gets saturated and non locally diffuses into tygers of oscillations  $\lambda_{k_p}$ . So there exists a range of purging time  $\tau$ , in which the system will converge to entropy solution without thermalization. As far as boundary layer is considered, there are no strict bounds on it as long as  $1 < \Delta k = k_c - k_p \ll k_c$  it will act as an effective sink.

The ability of the purged solution to dissipate the correct amount of energy for the right choice of  $\alpha$  is illustrated in figure 3.6, where we plot the energy in the boundary layer  $\Delta E^P$  (shown in red) against the dissipation rate of the entropy solution for the same initial conditions.

The fact that the purged and entropy solutions seem to be in agreement, visually, suggests that the purged solution is dissipative as was anticipated, by construction, earlier. However, for this solution to actually converge to the entropy solution, the rate of dissipation should be arbitrarily close to the dissipation rate  $\frac{dE}{dt}$  of the entropy solution. The most direct way to see this is to compare the total energies of the entropy  $E$  and the purged  $E^P$  solutions, as a function of time, for different values of  $\alpha$  and  $\beta$ : In figure 3.7(a) we show these results for  $k_c = 1000$ . We find, as was already suggested in figure 3.5, that for the optimal choice  $\alpha = \beta = 0.8$ , the behaviour of the total energy versus time for the purged solution is identical to the one obtained from the entropy solution. The purged solutions for other  $\alpha - \beta$

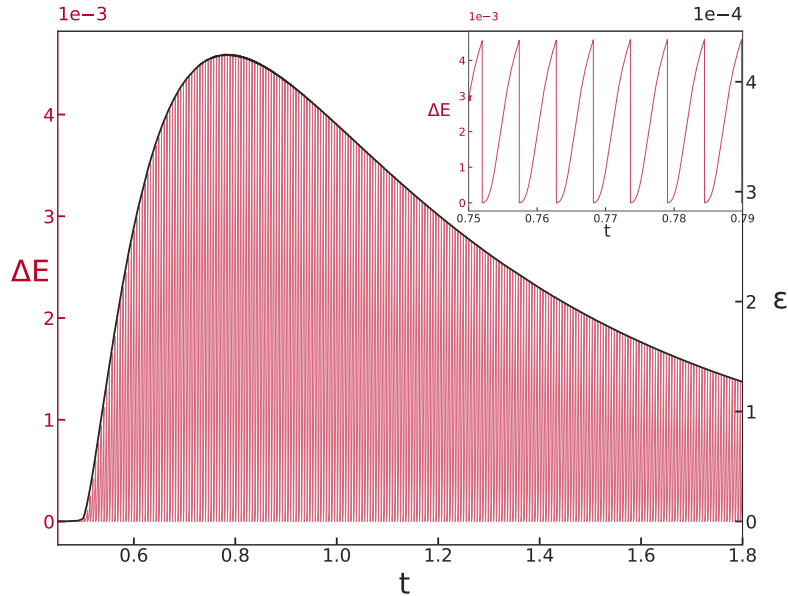


Figure 3.6: Figure showing the boundary layer energy (red)  $\Delta E$  vs  $t$  against the dissipation rate from the entropy solution (blue).

combinations are dissipative as well; however they dissipate energy at rates much slower than the entropy solution. Moreover, shock-mergers, as indicated by the vertical lines in the plot, and which lead to tiny *kinks* in the energy versus time profile, are faithfully reproduced by purged solutions for  $\alpha = \beta = 0.8$ .

A measure of how accurately the purged solution mimics the dissipation of the entropy one, is the percentage relative error  $e = \frac{E^p - E}{E} \times 100$  at  $t = 5.0$ . In the inset of figure 3.7(a), we plot  $e$  as a function of  $k_G$  for the most optimal purging choice ( $\alpha = \beta = 0.8$ ). Remarkably, this error  $e$  decreases rapidly with  $k_G$  and for  $k_G = 5000$ ,  $e \approx 0.01\%$ .

All of this leads us inevitably to the important question: For  $\alpha = \beta = 0.8$ , does the purged solution indeed converge to the entropy one as  $k_G \rightarrow \infty$ ? A precise way to answer this is to measure the percentage relative error (or the  $L_2$  norm)

$$\phi = \left( \frac{\sum_{i=1}^N [u(x_i) - w(x_i)]^2}{\sum_{i=1}^N u^2(x_i)} \right)^{1/2} \times 100 \quad (3.47)$$

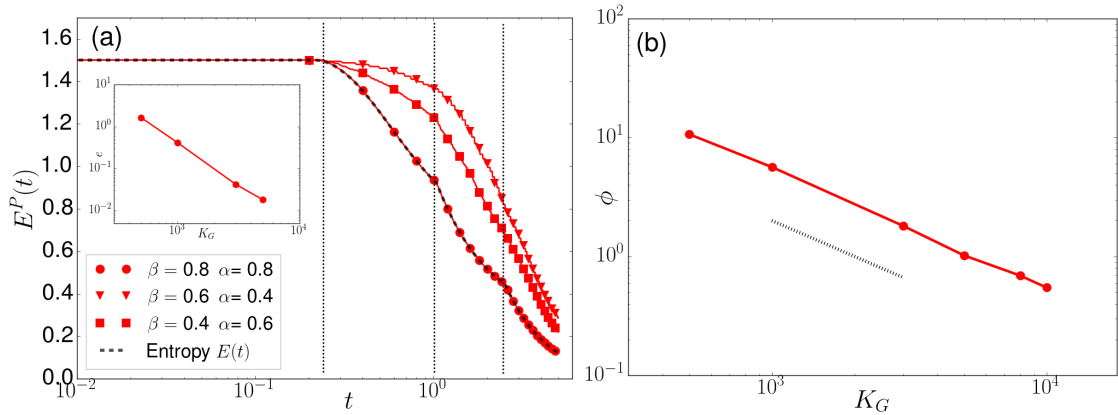


Figure 3.7: (a) A plot of the total energy  $E^P$  versus time, from our purged solutions (3.35), for different combinations of  $\alpha$  and  $\beta$  and  $k_G = 1000$ . We also show, in black, the energy versus time plot for the entropy solution for comparison. The dashed vertical lines correspond to the times at which the shocks, three in all because of the three-mode initial conditions, form. In the inset, we plot the relative percentage error  $e$  (see text) between the purged and entropy solution, for  $\alpha = \beta = 0.8$ , at  $t = 5.0$ , as a function of  $k_G$ . (b) A plot of the  $L_2$  norm of the percentage relative error  $\phi$  (see text) for  $\alpha = \beta = 0.8$  as a function of  $k_G$ ; the dashed-line shows a power-law  $k_G^{-1}$  scaling consistent with the measured error.

of the discrepancies between the solutions  $u$  and  $w$ . Given that this is a point-wise measure, unlike the global energy measurements shown in figure 3.7(a), a sharp decrease in  $\phi$  with  $k_G$  should be clinching evidence of the efficacy of our scheme. In figure 3.7(b), we show a log-log plot of  $\phi$  as a function of  $k_G$  and find a steep decrease ( $\phi \sim k_G^{-1}$  indicated by the dashed line) in the relative error as a function of  $k_G$ . For the large values of  $k_G$ , the relative error  $\phi < 1\%$ , reaching a value of  $\phi \approx 0.5\%$  for  $k_G = 10000$ . These results show that purging leads to weak-dissipative solutions which converge to the entropy solution of the parent PDE as  $k_G \rightarrow \infty$ . Importantly, the discrepancy between the two solutions is already minute for values of  $k_G$  which are easily accessible. From the point of view of numerical simulations, the  $\beta \geq 1/3$  condition is extremely helpful because it allows us to choose values of  $\beta$  small enough such that for a given  $k_G$ , the loss in resolution  $k_G - k_p$  through purging, is insignificantly small. As an example, for  $k_G = 10000$  and  $\beta = 0.4$ , fraction of resolution lost is about  $0.3\%$ .

Through the study, the main aim is to understand a way to get weak solutions in a truncated system for ideal fluid conservation laws. Here we studied

1D Burgers equation, because we can solve for the vanishing viscosity solution analytically and check the validity of the obtained weak solutions. Obviously the truncated weak solutions do not fall into the latter category. But with purging method attached to the truncating scheme is able to produce solutions arbitrarily close to the entropy solution based on selection of  $k_G$ . From the results that we have obtained through purging technique, we infer the following:

1. For the truncated system, adding a dissipation term (in spectral space) by means of purging method results in a weak solution which obeys the entropy condition and converges to the entropy solution for certain range of purging parameters.
2. The result of the purging test solely depends on the selection of purging time  $\tau$ . The purging time corresponds to the transparency level of the dissipation sink that matches behaviour with the entropy solution. Results have shown, for any arbitrary initial condition with a trigonometric polynomial (in other words, initial energy concentrated at low wavenumbers) with purging parameter  $\alpha$  in the range of 0.7 to 0.9 – the purged solution becomes a weak solution.
3. The working of purging truly corresponds to the fact that the solutions
  - Neither have expanding dissipation range
  - Nor have shrinking inertial range.

Because of this, the energy flux feels no truncated effect – rather a transparent sink near the boundary layer and outpours itself into it.

It is important to note that the purging attempts in physical space—which consists of smoothening out the *tygers* in physical space through averaging—does not result in any significant suppression of thermalization. Furthermore, such procedures lack the easy adaptability to different initial conditions, because it relies on the knowledge of the location of the shocks and resonance locations in the physical space to implement it.

Our results, if seen in isolation for the Burgers equation, are admittedly academic. This is because for the 1D Burgers equation, we have other ways to obtain weak-dissipative solutions as well as the widths of the analyticity strip  $\delta$  analytically and numerically. Also, since for the Burgers equation the effects of truncation are felt at times *very* close to  $t^*$ , the  $\delta$  obtained for the Burgers equation with and without purging, agree equally well with the theoretical estimate up to times very close to  $t^*$ . This is pathological to the Burgers equation and it is reasonable to conjecture that purging in the 3D Euler equation will yield more dividends. Furthermore, there is no analogue of the Fast-Legendre method for the 3D Euler equations.

It is in the light of the 3D Euler equations that this approach assumes special importance. To the best of our knowledge, till date there is no algorithm which allows, numerically, to obtain weak-dissipative solutions of the 3D Euler equation. This algorithm allows us to do exactly that. Numerically, our algorithm is trivial to implement in codes which solve the 3D Galerkin-truncated Euler equation. From earlier studies we know that the onset of thermalization in the 3D Galerkin-truncated Euler equation is formally similar to that in the Burgers equation. Hence, the approach outlined in this paper, should allow us to implement it for the 3D Euler equations and study, numerically, dissipative solutions as well as, and possibly most importantly, take advantage of the suppression of thermalization to finally have a firm, albeit numerical, answer for the celebrated blow-up problem. While it is true that for the 3D Euler equation, we are handicapped by a much poorer understanding of what the appropriate weak-dissipative solution ought to be, there are indeed several candidates against which our purged solutions may be benchmarked against, including the existing solutions of the incompressible Navier-Stokes equation for the largest Reynolds numbers currently attainable. We hope that our work will provide a stimulus for analogous (and important) studies of the truncated Euler equation.

Given the potential usefulness of our approach to revisit the analyticity strip method to numerically investigate the question of blow-up of the Euler equation, it might be useful to comment on recent studies of this problem. In brief,

although there is some evidence that the Euler equations could avoid singularities through the formation of vortex sheets [180–182], other results [124, 138, 183] suggests that this question is far from settled. Therefore, our work, although demonstrated here for the Burgers equation, could play a role in revisiting this issue from the point of view of the width of the analyticity strip. In this context, it may be worth recalling that the one of the earliest demonstrations of the analyticity strip method for the Galerkin-truncated inviscid hydrodynamics, was for the Burgers equation [27].

Before we conclude, it is important to ask if thermalization can be suppressed by other means (without resorting to viscosity). Purging attempts in physical space—which consists in *smoothing* out the *tygers* in physical space through local averaging—does not result in any significant suppression of thermalization and lacks easy adaptability to different initial conditions and higher dimensional equations. A second possibility is of course the use of a hyperviscous term. This however has the drawback that we would end up solving not the inviscid equation but its viscous form and for higher-orders of the hyperviscosity—which is similar in spirit to the idea of purging—the solutions thermalize [50, 52, 184]. Another approach is due to Pereira, *et al.* [150] who showed that a wavelet-based filtering technique also leads to a suppression of the resonances leading to *tygers*. However, such an approach has the limitation, as mentioned by the authors themselves, that the dual operations of filtering and truncation at every time step do not commute. Hence the weak dissipation introduced in this approach is somewhat uncontrolled. To this extent we feel that the prescription we present here is most suited for generating weak-dissipative solutions and, importantly, more easily adaptable to higher-dimensional systems such as the 3D Euler equations.

### 3.3 Suppression of Oscillations in the Galerkin-truncated Euler solution

This observation of the precise mechanism at the heart of thermalization in 3D flows is particularly important to devise numerical strategies to arrest thermalization for the reasons discussed before. Understanding how finite-dimensional equations of hydrodynamics thermalize is one aspect of this study—but perhaps the more important question relates to whether this understanding can be exploited to devise more efficient algorithms for numerical constructions of dissipative solutions of the Euler equations and indeed conjectures for finite-time blow-up through methods such as the analyticity strip [27, 137, 148].

Operationally, this would involve suppressing the oscillations that trigger the flow to thermalize—making analyticity strip approaches to singularity detection [148] impractical—and ensuring conservation of energy and thus the lack of dissipative solutions. From our DNSs, it seems that a useful starting point would be a suitable filtering of the velocity gradient field to remove the oscillatory structures.

We suggest an algorithm to be applied to the vorticity field  $\boldsymbol{\omega}$ , that reconstructs a new vorticity field  $\boldsymbol{\omega}^*$  in a self-consistent way that preserves the small-scale intense structures while discarding the oscillations. We adapt the method developed by Hamlington *et al.* [185] to decompose the strain field into local and non-local (background) contributions. This is trivially done for the vorticity field in Fourier space via

$$\hat{\omega}^{(\text{NL})}(\mathbf{k}) = f(kR)\hat{\omega}(\mathbf{k}) \quad (3.48)$$

$$\hat{\omega}^{(\text{L})}(\mathbf{k}) = \hat{\omega}(\mathbf{k}) - \hat{\omega}^{(\text{NL})}(\mathbf{k}) \quad (3.49)$$

where the *hat* denotes the Fourier space ( $k = |\mathbf{k}|$ ), the subscripts L and NL stand

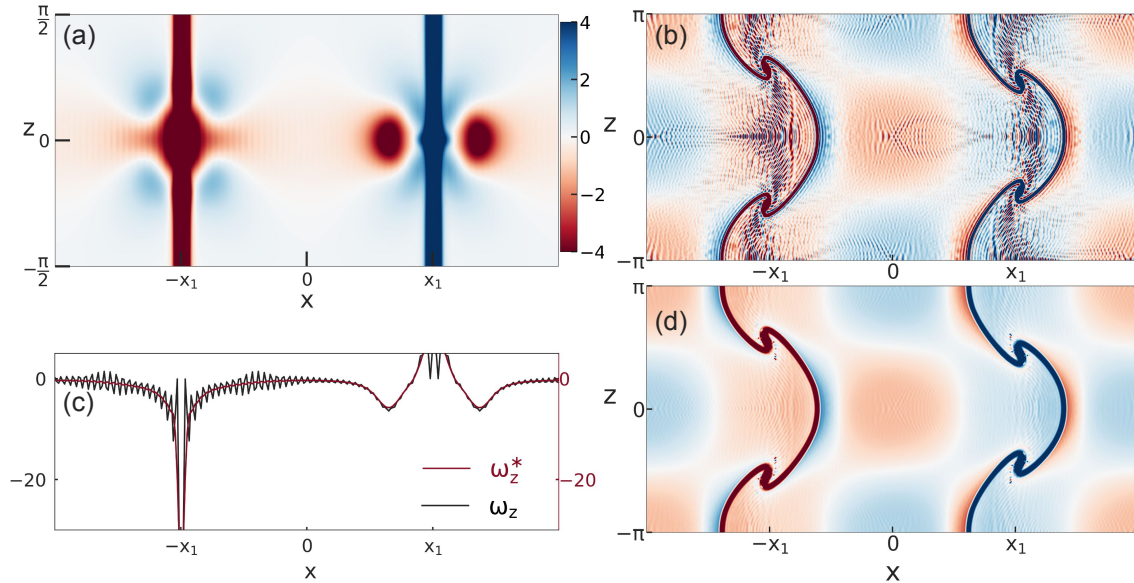


Figure 3.8: (a) Pseudo-color plot of the two-dimensional  $XZ$  plane cut of the reconstructed vorticity field  $\omega_z^*$  for the model flow (Eq. (2.2)) at  $t = 0.15$ . A comparison with the corresponding figure (Fig. 2.3(c)) for the truncated simulation shows a significant suppression of the oscillations. This is quantified in panel (c) through one-dimensional cuts (along  $z = 0$ ) of  $\omega_z$  (same as in Fig. 2.3(e)) and  $\omega_z^*$ , as a function of  $x$ . Panel (b) shows  $\omega_z$  at  $t = 1.5$  extracted from the Taylor-Green flow (Eq. (2.4)) along the  $XZ$  plane. This is contrasted with panel (d) showing the reconstructed vorticity field  $\omega_z^*$  from it, which retains the intense structures while significantly suppressing the oscillations, which would lead to thermalized solutions.

for the “local” and “non-local” contributions, respectively, and the filter

$$f(kR) = \frac{3(\sin(kR) - kR \cos(kR))}{(kR)^3} \quad (3.50)$$

is the Fourier transform of the three-dimensional complementary Heaviside function in spherical coordinates. Such a filter, by definition, ensures that the function on which it acts—namely the vorticity field in this case—is *smoothed* by averaging out over a sphere of radius  $R = \lambda_G$ . Evidently, the local contribution  $\omega^L$  alone contains all the oscillations, and hence the “reconstructed” field  $\omega^* \equiv \omega^{\text{NL}}$  with  $\omega^L$  suppressed should be free of oscillations. Hence, such a *dynamic* filtering technique, namely, solving the truncated 3D Euler by recovering  $\omega^*$  and using this field to evolve at every time step, should yield a non-thermalizing, dissipative flow.

However, such an approach has the disadvantage, that along with the oscillations, the small-scale, intense vortical structures are lost as well. We

therefore adapt this idea of decomposing the field in a way that preserves the small-scale structures as far as possible and yet suppresses the oscillatory triggers of thermalization. Thus, we propose a reconstructed field as

$$\boldsymbol{\omega}^*(\mathbf{x}) = \boldsymbol{\omega}^{(\text{NL})}(\mathbf{x}) + \Gamma_{2m}(\mathbf{x})\boldsymbol{\omega}^{(\text{L})}(\mathbf{x}) \quad (3.51)$$

$$\Gamma_{2m}(\mathbf{x}) := \text{erf} \left[ \frac{|\boldsymbol{\omega}|^{2m}}{\|\boldsymbol{\omega}\|_{2m}^{2m}} \right]. \quad (3.52)$$

where the additional regularization parameter  $\Gamma_{2m}$  allows us to capture the essential, intense local vortical regions while still filtering out the oscillations in the flow. The  $L_{2m}$  norm used in the definition of  $\Gamma_{2m}$  controls threshold level of that vortical regions we want to retain in the reconstructed field.

While this method needs to be refined and rigorously examined in future studies for generic flow fields, we provide results from preliminary tests conducted on the model flow defined by equation (2.2). In figure 3.8(a), we show the reconstructed vorticity field at  $t = 0.15$  for  $m = 4$ , corresponding to the plot shown in figure 2.3(c). Similarly, in figures 3.8(b) and (d), the vorticity field  $\omega_z$  (along the XZ plane) from the solution to the Taylor-Green initial condition (Eq. (2.4)) and its repaired field  $\omega_z^*$  are shown.

A visual comparison of the two vorticity fields shows that our reconstruction strategy indeed leads to a significant reduction in the oscillations while still preserving the intense structures, namely the vortical sheets in this case. This is quantified in figure 3.8(c) by comparing the  $z$ -component of the vorticity along the  $x$ -axis ( $z = 0$ ) in the middle of the domain for the truncated ( $\omega_z$ ) and reconstructed fields ( $\omega_z^*$ ). We clearly see that the oscillations responsible for thermalization, seen in  $\omega_z$  more or less vanish on reconstruction, as seen in the plot. Furthermore, our use of the regularization parameter  $\Gamma_{2m}$  does fully preserve the intense structure in the form of vortex sheets, as seen by the near overlap of  $\omega_z$  and  $\omega_z^*$  at  $-\mathbf{x}_1$  and  $\mathbf{x}_1$ .

While figure 3.8(c) seems to underline the success of this strategy—at least

for such a curated flow—the illustrative flow field shown in panels (a) and (d) still retains some traces of the oscillations. There are at least two reasons why this is so:

1. In our tests, we have not filtered and reconstructed the field at every time step, but, only as a proof of principle now, used this as a *static* filter and reconstruction at  $t = 0.15$  (for panel (a)) and at  $t = 1.5$  (for panel (d)). A dynamic filter, as discussed above, is essential, and perhaps the frequency—the time intervals between successive filtering—with which the filter should be applied needs further investigation. The latter may well be a delicate point as shown in reference [152] for Fourier space purging in the 1D Burgers equation.
2. Our preliminary explorations with different sharpnesses of the regularization parameter  $\Gamma_{2m}$  show that this, not surprisingly, is critically important for more effective suppression of thermalization hotspots, especially in the vicinity of flow structures with intense gradients. This will become crucial when such strategies are investigated systematically in a generic 3D flows.

Our preliminary results, albeit based on such a *static* filter for the model flow, show encouraging signs that such approaches may well diminish the precursor to small-scale thermalization and allow (a) dissipative solutions and (b) extending the analyticity strip method for singularity detection to longer times than currently possible. This approach thus complements other ongoing efforts, such as that by Fehn *et al.* [186], who use a discontinuous Galerkin discretization to obtain dissipative solutions from simulations of the finite-dimensional Euler equation.

# Chapter 4

## Many-body Chaos in Thermalized fluids

### 4.1 Fundamental Questions in Statistical Physics

Many-body chaos is the key mechanism to explain the fundamental basis—*thermalization* and *equilibration*—of statistical physics. However, we know of equally important examples in nature, such as the problem of turbulence, where chaos plays a role that is seemingly *opposite* from the *settling down* through thermalization and equilibration of several many-body systems. This contrast becomes stark if we argue in terms of the celebrated *butterfly effect* [54, 187–189]: While the amplification of the *wingbeat* results in complex dynamical macroscopic structures in driven-dissipative systems such as a turbulent fluid, the same amplification leads to a loss of memory of initial conditions, resulting in ergodic behaviour and eventual thermalization or equilibration, in Hamiltonian many-body systems. How then do we reconcile these two apparently disparate roles of many-body chaos?

An important piece of the answer lies in investigating the spatio-temporal

aspects of many-body chaos (the Lyapunov exponent  $\lambda$  and butterfly speed  $v_B$ ) in fluids to reveal its connection with macroscopic (thermodynamic) characterization of the system. This provides for concrete comparisons of length and time-scales of chaos and thermalization, on the one hand, and the non-linear dynamic structures of the fluid-velocity field on the other.

Characterizations of chaos and its connection with transport and hydrodynamics have been obtained recently in the context of both classical and quantum many-body systems such as unfrustrated and frustrated [55–57, 190] magnets, strongly correlated field theories [191–199]) and field theories of black-holes [59, 200]. A common feature responsible for the unconventional signatures of chaos in many of these systems seems to originate from a large set of strongly coupled, dynamic, low energy modes arising from competing interactions. This is not unlike the case of a turbulent fluid where the triadic interactions of velocity (Fourier) modes across several decades lead to strong couplings resulting in, example, scale-by-scale energy transfers [95, 201].

These studies have been facilitated by the development of quantum *out-of-time commutators* (OTOCs) [55, 58, 60, 198, 202–204] and their classical counterpart, the *decorrelator* [55, 56] for quantum and classical many-body chaotic Hamiltonian system respectively, that measure the spatio-temporal decorrelation in a system in the presence of a perturbation. For a elementary introduction, consider a quantum many-body Hamiltonian  $\mathcal{H}$ , and two local unitary operators  $V, W$  in Heisenberg picture. Then the squared commutator between them is defined as the OTOC:

$$C(t) = \langle [W(t), V(0)]^2 \rangle = 2 \left( 1 - \text{Re} \left\{ \langle W^\dagger(t) V^\dagger W(t) V \rangle \right\} \right) \quad (4.1)$$

The average  $\langle \cdot \rangle$  is  $\text{Tr}[\exp(-\beta\mathcal{H}) \cdot]$  with an inverse temperature  $\beta$ . Typically, for short times  $C(t)$  grows exponentially with a exponent  $\lambda_L$  [205]. As a physical picture, the operator  $W(t)$  corresponds to the growth and spread of the local perturbation under time evolution. The commutator with other operator  $V$  diagnoses the growth. By scrambling rate  $\lambda_L$ , it implies after time  $\sim \lambda_L^{-1}$  the initial state cannot be recovered via local measurements [206]. Interestingly, just

as Kolmogorov-Sinai entropy bridges dynamical instability and entropy in classical systems, the  $\lambda_L$  is interpreted as information scrambling rate, which is of great interest [207]. For a classical system, the state of a system (say  $\phi^{(b)}(\mathbf{x}, t)$ ) is perturbed infinitesimally to obtain a copy ( $\phi^{(a)}(\mathbf{x}, t)$ ) and the decorrelation between the two systems ( $a$ ) and ( $b$ )

$$\Delta(\mathbf{x}, t) = \langle \|\phi^{(a)} - \phi^{(b)}\| \rangle \quad (4.2)$$

measured with suitable norm  $\|\cdot\|$  within a thermal ensemble are termed as the decorrelators.

In particular, the classical decorrelators are an invaluable diagnostic for understanding the butterfly effect [54, 187–189] in non-integrable, chaotic, classical many-body systems through the measurement of  $\lambda$  and  $v_B$ . Since by construction, these OTOCs or decorrelators provide a unified framework to bridge thermodynamic variables (e.g., temperature  $T$ ) with the butterfly effect, they are a unique prescription to connect many-body chaos with the foundations of statistical approaches in *both* classical and quantum many-body systems. The most striking example of this is that while for quantum systems,  $\lambda \leq T/\hbar$ , limiting the rate of scrambling [60]), the analogous *conjecture* for classical systems is  $\lambda \propto \sqrt{T}$  at low temperatures [60, 208].

For classical systems, our recent understanding of spatio-temporal chaos through decorrelators stems primarily from spin systems [56, 57, 190]. However, these ideas have not been applied for the most ubiquitous of chaotic, nonlinear, many-body systems: Turbulent flows. This is because, unlike the spin-systems, turbulent flows, governed by the viscous Navier-Stokes equation, are an example of a driven-dissipative system *without* a Hamiltonian or a statistical physics description in terms of thermodynamic variables. Therefore, we look for variations of the Navier-Stokes equation which, whilst preserving the same non-linearity of the viscous Navier-Stokes equation, nevertheless has a Hamiltonian structure, resulting in a chaotic, *thermalized* fluid.

Such a prescription naturally leads us to the celebrated inviscid, three-dimensional (3D) Euler and one-dimensional (1D) Burgers equations, but retaining only a finite number of Fourier modes through a (Fourier) Galerkin-truncation [36, 38–40]. Such a projection of the inviscid, partial differential equations on to a finite-dimensional sub-space ensures not only a conservation of momentum, energy and phase space, but it guarantees chaotic solutions for the flow field which thermalize, as we saw in Chapter 1. Hence, this subtle, but significant, modification to these equations, while preserving the essential non-linearity, allows us to move away from the dissipative to thermalized solutions with an energy equipartition and Gibbs distribution of the velocity field. With mean momentum zero, and net kinetic energy as the only non-zero conserved quantity, these *fully* thermalized fluids, in  $d$ -dimensions, are characterized by an energy equipartition and velocity fields with a Gibbs distribution:

$$\mathcal{P}[\mathbf{v}] d\mathbf{v} = \left(\frac{\beta}{4\pi}\right)^{d/2} \exp\left(-\frac{\beta|\mathbf{v}|^2}{2}\right) d\mathbf{v} \quad (4.3)$$

Refer to figure 4.2 for an illustration of the PDF . Here  $\beta$  is the inverse temperature of the system, in the thermodynamic limit<sup>1</sup>, related to conserved energy  $E$  as:

$$E = \frac{1}{V} \int_{\mathcal{D}} d\mathbf{x} \frac{1}{2} |\mathbf{v}(\mathbf{x})|^2 \quad (4.4)$$

$$= \frac{1}{2} \langle |\mathbf{u}|^2 \rangle = \frac{d}{2\beta} \quad (4.5)$$

Hence, different thermalized configurations are realizations from a thermodynamical canonical ensemble with a prescribed temperature  $T$ . Thus for an ideal Galerkin-truncated hydrodynamical system in the asymptotic thermalized state, the energy spectrum will behave as:

$$E(k) = \sum_{k-1/2 \leq |\mathbf{k}| < k+1/2} |\mathbf{v}(\mathbf{k})|^2 \sim k^{d-1} \quad (4.6)$$

In the thermalized state, there is no clear cascade of energy, hence, no inertial range, unlike the driven-dissipative turbulent flows. The dynamics in a

---

<sup>1</sup>Pertaining to large, but, finite degrees of freedom in the thermalized fluid

thermalized fluid hardly resembles anything to actual hydro-dynamical behaviour. The Galerkin-truncated system cannot characterize any structure smaller than the size  $\sim 1/k_G$  in real space. Nevertheless, the dynamics shares similarity with the governing PDE. Furthermore, the equilibrium statistics of such systems are well-known, and as a dynamical system with large degrees of freedom, the thermal dependence of the *largest* Lyapunov exponent is what we are after in this study.

Consider the 3D case, in a completely thermalized state, the statistics (taken over ensemble of such systems) becomes *stationary* in time that is  $d\langle\cdot\rangle/dt = 0$ . In addition, the statistics is *homogeneous* and *isotropic* allowing the two-point correlation  $D_{ij}(\mathbf{x}, \mathbf{r}) = \langle u_i(\mathbf{x}) \cdot u_j(\mathbf{x} + \mathbf{r}) \rangle$  to be written as:

$$D_{ij}(\mathbf{r}) = \sum_{\mathbf{k}} e^{i\mathbf{k}\cdot\mathbf{r}} \langle v_i(-\mathbf{k})v_j(\mathbf{k}) \rangle \quad (4.7)$$

In a thermalized system, all the degrees of freedom  $\{v_i(\mathbf{k})\}$  are uncorrelated in the statistical sense.

$$\langle v_i(-\mathbf{k})v_j(\mathbf{k}) \rangle = \frac{1}{2}P_{ij}(\mathbf{k}) \langle |\mathbf{v}(\mathbf{k})|^2 \rangle \quad (4.8)$$

By means of equipartition, every degree of freedom  $|\mathbf{v}(\mathbf{k})|^2$  has a variance independent of  $\mathbf{k}$ . In the thermodynamic limit of  $N \rightarrow \infty$ ,

$$D_{ij}(\mathbf{r}) = \frac{1}{2} \sum_{\mathbf{k}} e^{i\mathbf{k}\cdot\mathbf{r}} P_{ij}(\mathbf{k}) \langle |\mathbf{v}(\mathbf{k})|^2 \rangle \quad (4.9)$$

$$= \frac{1}{3}N_G^3\delta_{ij}\boldsymbol{\delta}(\mathbf{r}) \langle |\mathbf{v}(\mathbf{k})|^2 \rangle = \frac{2E}{3}\delta_{ij}\boldsymbol{\delta}(\mathbf{r}) \quad (4.10)$$

where  $N_G^3$  is the total no of Fourier modes in the summation, hence degrees of freedom. Thus even the neighbouring points are uncorelated and the system becomes *delta corelated* (in this sense) in space in the thermodynamic limit of a fully thermalized regime, and hence termed to have no structure in it. So a thermalized fluid is thus not dissimilar to that of correlated many-body condensed matter systems (e.g., frustrated magnets) where the microscopic memory does not dictate the dynamical correlations.

In this Chapter, by using this fascinatingly rich model of *thermalized fluids*, we derive  $\lambda \propto \sqrt{T}$  and demonstrate a possible universality of the nature of many-body chaos without an apparent (weakly interacting) quasi-particle description, and hence a Kinetic Theory. Equally interestingly, we show how decorrelators *sense* the emergent dynamical structures of the fluid velocity field which provides an elegant way to bridge the ideas of many-body chaos with the foundational principles of statistical physics: Thermalization, equilibration and ergodicity.

Now we formally define the thermalized fluids used in this study. Within the space of  $2\pi$  periodic solutions to the Euler equations, an expansion of the solution in an infinite Fourier series allows us to define the Galerkin projection as a low-pass filter  $\mathbb{P}_{k_G}$  which sets all modes with wave vectors  $|\mathbf{k}| > k_G$ , where  $k_G$  is a positive (large) integer, to zero via  $\mathbb{P}_{k_G} \mathbf{u}(\mathbf{x}) = \sum_{|\mathbf{k}| \leq k_G} e^{i\mathbf{k}\cdot\mathbf{x}} \mathbf{v}(\mathbf{k})$ . The truncation wavenumber  $k_G$  sets the number of Fourier modes  $\sim N_G^3$  kept and is a measure of the effective number of degree of freedom as well as providing a microscopic (ultraviolet) cut-off for the system. These definitions, without the loss of incompressibility, lead to the Galerkin-truncated Euler equation for the truncated field, written, most conveniently, component-wise in Fourier space:

$$3\text{D: } \frac{dv_i(\mathbf{k}, t)}{dt} = ik_l \mathbb{P}_{k_G} \left[ P_{ij}(\mathbf{k}) \sum_{\mathbf{p}+\mathbf{q}=\mathbf{k}} v_l(\mathbf{q}, t) v_j(\mathbf{p}, t) \right] \quad (4.11)$$

Equation (4.11) is naturally augmented with the initial conditions  $\mathbf{u}(\mathbf{x}, 0) = \mathbf{u}_0$ ,  $\nabla \cdot \mathbf{u}_0 = 0$  and the truncation constraints  $|\mathbf{q}|, |\mathbf{p}|, |\mathbf{k}| \leq k_G$ .

The same definitions of Galerkin-truncation can be extended *mutatis mutandis* to one dimension, without the additional constraints of incompressibility or pressure gradients, to similarly project the 1D inviscid,  $2\pi$ -periodic Burgers equation onto the subspace spanned by  $k_G$ :

$$1\text{D: } \frac{dv(k, t)}{dt} = ik \mathbb{P}_{k_G} \left[ \sum_{p+q=k} v(q, t) v(p, t) \right] \quad (4.12)$$

With initial conditions  $u(x, 0) = u_0(x)$ , the Galerkin-truncated Burgers equation also imposes the constraint  $|q|, |p|, |k| \leq k_G$  from the truncation.

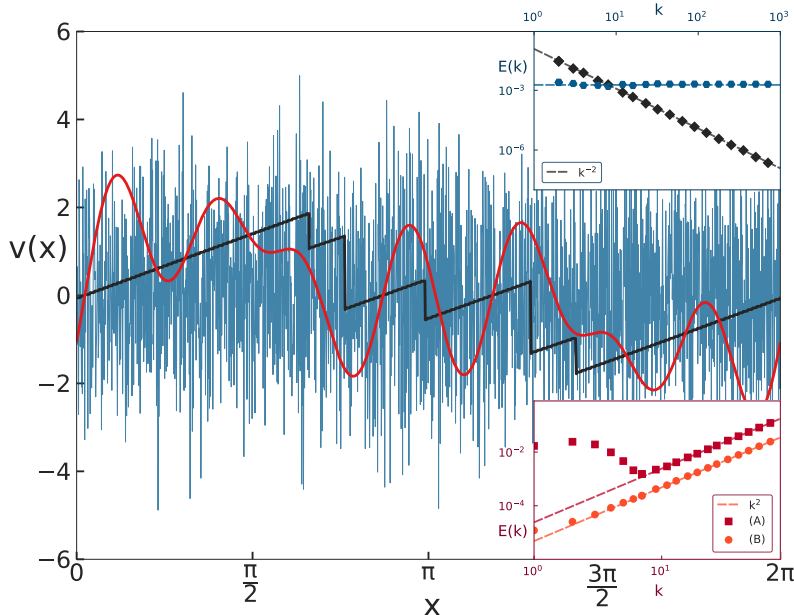


Figure 4.1: Velocity plots of the Galerkin-truncated Burgers equation (blue) and the entropy solution  $u$  (black) at time  $t = 10.0$  for an initial condition (red). (Upper Inset) Log-log plots of energy spectrum for the truncated (blue circles) and un-truncated (black squares) equations showing  $E(k) \sim k^0$  and  $k^{-2}$  scaling respectively. (Lower Inset) The kinetic energy spectrum of a partially (A) and fully (B) thermalized 3D fluid obtained from the Galerkin-truncated Euler equation, with the  $k^2$  scaling is indicative of energy equipartition.

## 4.2 Decorrelators in Thermalized fluid

We perform direct numerical simulations (DNSs) of these Galerkin-truncated 3D Euler and the 1D Burgers equations by using a standard pseudo-spectral method with a fourth order Runge-Kutta algorithm for time marching. These equations are solved on a  $2\pi$  periodic domain with  $N^3$  (for the 3D) and  $N$  resolution points (for the 1D), with a truncation wavenumber  $k_G$  which results in  $N_G^3 < N^3$  (or, in 1D,  $N_G < N$ ) number of degrees of freedom. In our numerical simulations, we have explicitly checked that the kinetic energy is conserved and within a finite time energy equipartition is reached.

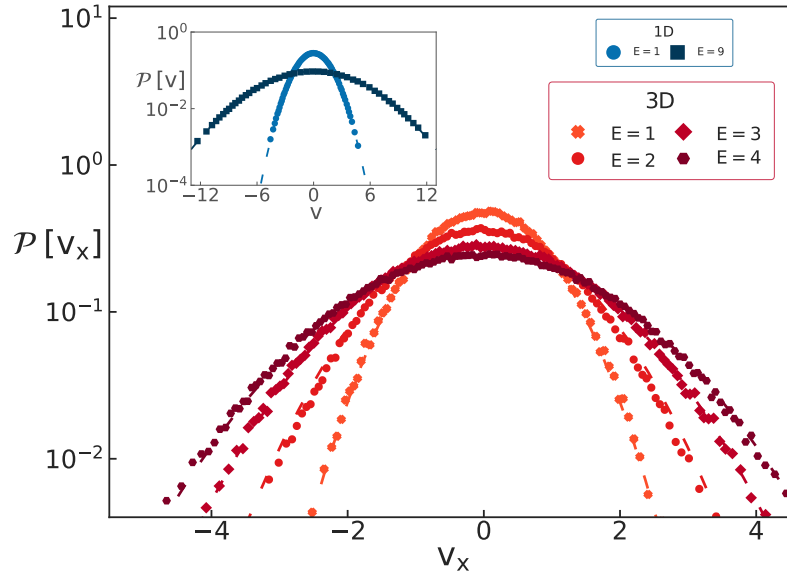


Figure 4.2: Probability distribution functions of the  $x$ -component of the thermalized velocity field, obtained from simulations of the Galerkin-truncated 3D Euler equation, and (inset) the 1D Burgers equation for different energies. The dashed lines denote a fit to the corresponding Gibbs distribution.

The inviscid Euler equation in 3D, with any prototypical large scale initial condition depicting actual fluid will allow cascade of energy to smaller and smaller scales, corresponding to higher wavenumbers in spectral space. In a truncated system, the cascade is soon interrupted by the absence of higher wavenumbers than  $k_G$ . Heuristically, this leads to accommodation of energy near the boundary  $|\mathbf{k}| \lesssim k_G$ , creating a fictitious batch. Acting like a *two-fluid* model [38], partially thermalized modes near  $k_G$  and fluid-like modes interact, resulting in a net transfer of energy from the latter to the former [36]. In the limit of  $t \rightarrow \infty$ , the whole system is thermalized.

Although the exact form of initial condition doesn't play any role in our study. Nevertheless, the direct numerical experiments on the thermalized states described in this Chapter are generated from an exponentially decaying initial condition in spectral space, having a energy spectrum of the form,

$$E(k) = A_0 k^s \exp\left[-\frac{k^2}{k_0^s}\right] \quad (4.13)$$

with  $s = 2$  or  $4$ . Changing the numerical value of the factor  $A_0$  allows us to

generate thermalized fluid with different energies  $E$  and hence different temperatures  $T$  in the range  $0.125 \leq T \leq 4$ . In our simulations, we use different resolutions  $N^3 = 96^3, 128^3, 160^3, 196^3, 224^3$  and  $256^3$  to generate different values of the  $N_G$ . Our time-step for integration, depending on  $k_G$  and  $E$ , varies as  $\Delta t \lesssim \sqrt{\frac{3}{2E}} \frac{2\pi}{N}$  with a CFL (Courant-Friedrichs-Levy) number <sup>2</sup> greater than 10 and the truncated equations were integrated up to a time  $t \approx 10$  to generate fully thermalized solution  $\mathbf{v}^{\text{th}}$  which provides the starting point to generate systems  $\mathbf{a}$  and  $\mathbf{b}$  used in our calculations of the decorrelator  $\Phi(t)$ .

A fully thermalized solution would imply that the energy spectrum to behave as  $E(k) \sim k^2$ . Although it takes infinite time to obtain such a fully thermalized state, it is sufficient if most of the modes are thermalized for carrying out the numerical studies with it. The large scale structures (small modes), has large *turn-over* time scales and so they tend to be more stable in the time scale of thermalized modes. This can be associated with the *permanence of large eddies*.. These small unthermalized modes, superimpose a large scale flow over the thermalized noise. A degree of thermalization can be quantified by defining  $\gamma = E_{\text{th}}/E \ll 1$ , where  $E_{\text{th}}$  is the energy is the thermalized modes, and in the limit of  $\gamma \simeq 1$  the system can be considered to be fairly thermalized. The study of many-body chaos is done in systems with such thermalized initial conditions obtained in this method, below shown in figure 4.1 is one instance.

For the 1D truncated Burgers problem, we choose an initial condition  $v_0 = A_0[\sin x + \sin(2x - 0.2) + \sin(5x - 0.4) + \sin(7x - 0.5)]$ ; the precise functional form of the initial conditions is immaterial with the total conserved momentum  $\int_0^{2\pi} v_0 dx = 0$ . Further (as in the 3D problem), changing the numerical constant  $A_0$ , allows us to change the energy  $E = \frac{1}{2\pi} \int_0^{2\pi} v_0^2 dx = 2A_0^2$  of our system and thence the temperature  $2 \leq T \leq 18$ . Given the lower computational cost for solving the 1D system, we were able use a much larger number of collocation points  $N = 2^{14}$  to generate systems with larger values of  $k_G = 1000$  ( $\delta t = 10^{-5}$ ) and  $5000$  ( $\delta t = 10^{-6}$ ) leading to values of  $N_G$  much larger than those accessible to 3D simulations.

---

<sup>2</sup>CFL number is the ratio of numerical time step and time required for a particle to cross a computational grid.

These thermalized fluids sets the platform for addressing the primary question of the growth of perturbations in a classical, chaotic system. To do this, an arbitrary realisation of the thermalized solution  $\mathbf{v}_0^{\mathbf{a}} = \mathbf{v}^{\text{th}}$  is taken and a second copy is generated added with a perturbation in velocity field. For the 3D case, the perturbation is chosen as

$$\mathbf{v}_0^{\mathbf{b}}(\mathbf{x}) = \mathbf{v}_0^{\mathbf{a}}(\mathbf{x}) + \delta\mathbf{v}_0(\mathbf{x}) \quad (4.14)$$

$$\mathbf{v}_0(\mathbf{x}) = \nabla \times \mathbf{A}, \quad A_i = \epsilon\sqrt{E}r_0 \exp\left(-\frac{r^2}{2r_0^2}\right)\hat{e}_i \quad (4.15)$$

characterized with  $\epsilon \ll 1$  and centered at the origin, that falls off rapidly with distance  $r$  (within the reference scale  $r_0 \ll 2\pi$ ) making it *spatially localized*. To underline the universality of our results, the perturbation is seeded entirely in Fourier space for the 1D Burgers case. As before, from the thermalized solution (in Fourier space)  $\hat{v}^{\text{th}}$ , defining a control field  $\hat{v}_0^{\mathbf{a}} = \hat{v}^{\text{th}}$  and a perturbed field,

$$\hat{v}_0^{\mathbf{b}} = \hat{v}_0^{\mathbf{a}}(1 + \epsilon \delta_{k,k_p}) \quad (4.16)$$

with large values of the perturbation wave-number  $k_p$  to generate de-localized small-scale perturbations in the systems. It is important to stress that given the seed perturbation is localized in Fourier space in 1D (and hence de-localized in physical space), the spatial spread of perturbations, which is relevant and studied for 3D fluids in this Chapter, remains outside the scope of analysis here.

To perturb the system  $\mathbf{a}$ , we introduce, for the 3D fluid, a perturbation of strength  $\epsilon = 10^{-6}$ ; in the 1D problem, we use  $\epsilon = 10^{-5}$  and  $10^{-4}$ . Furthermore, since the perturbation, for the 1D problem, is introduced at wavenumber  $k_p$  in the Fourier space, we choose different values of  $k_p = 500, 900, 2500$  and  $4000$  to demonstrate the insensitivity of our results to the precise (small) scales of perturbation (and  $\epsilon$ ). Now we have to quantify the decorrelators for both 3D and 1D systems, from which the Lyapunov exponents can be extracted and studied. Evolving the Galerkin-truncated Euler equation (4.11), *independently* for the two copies, with initial conditions  $\mathbf{v}_0^{\mathbf{a}}$  and  $\mathbf{v}_0^{\mathbf{b}}$  to obtain (thermalized) solutions  $\mathbf{v}^{\mathbf{a}}(\mathbf{x}, t)$  and  $\mathbf{v}^{\mathbf{b}}(\mathbf{x}, t)$

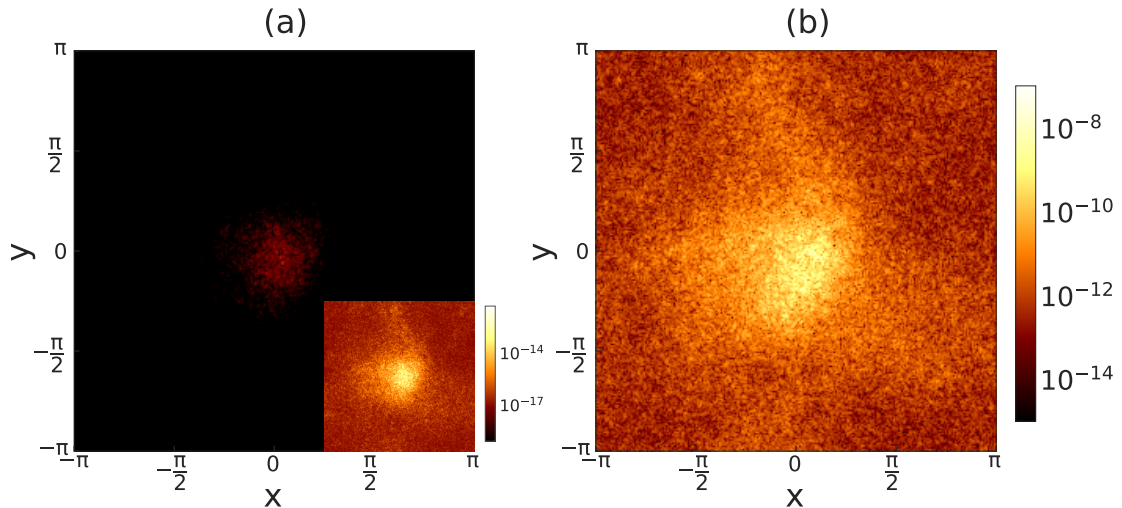


Figure 4.3: Representative plots of the difference field  $|\delta\mathbf{v}(\mathbf{x}, t)|^2$ , along the  $z = 0$  plane of a 3D thermalized fluid (with energy  $E = 2.0$  and a perturbation amplitude  $\epsilon = 10^{-6}$  at (a) early ( $t = 0.4$ ) and (b) later ( $t = 0.7$ ) times. The inset of panel (a) shows the same early time data, with a magnified scale, to reveal a somewhat *self-similar* spatial structure that arises from non-local interactions [209].

and thence obtaining the *difference field*

$$\delta\mathbf{v}(\mathbf{x}, t) = \mathbf{v}^{\mathbf{b}}(\mathbf{x}, t) - \mathbf{v}^{\mathbf{a}}(\mathbf{x}, t) \quad (4.17)$$

Since initially this difference field  $\delta\mathbf{v}(\mathbf{x}, 0) \equiv \delta\mathbf{v}_0$  was spatially localized and vanishingly small, its subsequent spatio-temporal evolution reflects how the butterfly effect manifests itself in such nonlinear, many-body chaotic systems. Fundamentally, this is of course a question of how systems  $\mathbf{a}$  and  $\mathbf{b}$  decorrelate and one that is intimately connected with questions of ergodicity and thermalization. A rigorous assessment would be to construct the spatially resolved decorrelator of the form

$$\Delta^2(\mathbf{x}, t) = \left\langle \frac{1}{2} |\delta\mathbf{v}(\mathbf{x}, t)|^2 \right\rangle \quad (4.18)$$

where  $\langle \cdot \rangle$  would denote averaging over the configurations taken from the thermalized ensemble and the point  $\mathbf{x}$  measured from the origin where the perturbation is seeded at  $t = 0$ . In figure 4.3 we show the spatial profile (in the  $z = 0$  plane) of  $|\delta\mathbf{v}(\mathbf{x}, t)|^2$  for a particular initial realisation of systems  $\mathbf{a}$  and  $\mathbf{b}$  at two different instants of time. While at very early times  $t = 0^+$ , in panel (a),  $|\delta\mathbf{v}(\mathbf{x}, t)|^2$  remains small but diffuses *instantly* and *arbitrarily*, a more striking behaviour is seen at later times

(panel (b)) when the spatial spread is controlled by the strain in the velocity field as we shall see below. It is likely that that the initial, instantaneous spread is a result of the non-locality (in space) of the 3D fluid because of the pressure term; however since the Galerkin-truncation also introduces an additional non-locality, the precise mechanism for the initial spread is hard to pin down.

Furthermore before proceeding further, performing an ensemble average over several realization is an exceptionally difficult task for a three-dimensional system owing to the limited computational power available to us. But, since the thermalized fluid is *statistically* isotropic, the decorrelator  $\Delta(\mathbf{x}, t)$  remains a function of  $r = |\mathbf{x}|$ . Hence exploiting this to our advantage, we construct a more tractable angular-averaged decorrelator

$$\phi(r, t) = \frac{1}{4\pi r^2} \int_{|\mathbf{x}|=r} d\mathbf{x} |\delta\mathbf{v}(\mathbf{x}, t)|^2 \quad (4.19)$$

It is vital to note that given the non-locality of the 3D Euler equation owing from the pressure, these systems differ crucially from spin systems in the absence of pilot waves and a distinct velocity scale  $v_B$  akin to a butterfly speed [55, 56]. The lack of a sharp wave-front and self-similarity is evident from figure 4.3. Therefore to track the temporal evolution of the decorrelator we find it convenient to introduce the space-averaged global decorrelator

$$\Phi(t) = \frac{1}{V} \int d\mathbf{x} |\delta\mathbf{v}(\mathbf{x}, t)|^2 \quad (4.20)$$

which then serve as an excellent diagnostic to focus purely on the temporal aspects of this problem. For the case of 1D Burgers equation, similar to the 3D case, the two systems,  $\hat{v}_k^{\mathbf{a}}$  and  $\hat{v}_k^{\mathbf{b}}$ , are evolved independently and the relevant Fourier space decorrelator  $|\hat{\Delta}_k|^2$  is defined as

$$|\hat{\Delta}_k|^2 = \left\langle |\hat{v}_k^{\mathbf{a}} - \hat{v}_k^{\mathbf{b}}|^2 \right\rangle \quad (4.21)$$

measuring the mode-by-mode spread of the perturbation as a function of time.

### 4.3 Thermal Bound of Lyapunov exponents

Although we are dealing with non-linear equations for hydrodynamics which do not yield easily to an analytical treatment, it is tempting to theoretically estimate the functional dependence of  $\lambda$  on  $T$  and  $N_G$ . In order to do so, it is essential to study the the growth of these decorrelators, given that we know the statistics of the thermalized solutions. Starting with the 3D case, since solutions  $\mathbf{a}$  and  $\mathbf{b}$  both satisfy the Galerkin-truncated, three-dimensional (3D) Euler equation. Therefore the evolution equation for the *difference field*  $\delta\mathbf{v}(\mathbf{x}, t) = \mathbf{v}^{\mathbf{b}} - \mathbf{v}^{\mathbf{a}}$ , component-wise is given by:

$$\partial_t \delta v_i(\mathbf{x}, t) = -\partial_j \left[ v_i^{\mathbf{a}} \delta v_j + v_j^{\mathbf{a}} \delta v_i + \delta v_i \delta v_j \right] + \partial_{ijl}^3 \int_{\mathcal{D}} d\mathbf{x}' G(\mathbf{x}, \mathbf{x}') \left[ v_j^{\mathbf{a}} \delta v_l + v_l^{\mathbf{a}} \delta v_j + \delta v_j \delta v_l \right]'; \quad (4.22)$$

with an initial conditions  $\delta\mathbf{v}(\mathbf{x}, 0) = \delta\mathbf{v}_0$  and a Green's function satisfying  $\nabla^2 G(\mathbf{x}, \mathbf{x}') = \delta(\mathbf{x} - \mathbf{x}')$ . The non-local and convective terms in this equation clearly suggest that a localized, initial difference  $\delta\mathbf{v}(\mathbf{x}, 0) = \delta\mathbf{v}_0$ , introduced through the perturbation in  $\mathbf{b}$ :  $\mathbf{v}_0^{\mathbf{b}} = \mathbf{v}_0^{\mathbf{a}} + \delta\mathbf{v}_0$  will de-localize with a spatio-temporal spreading. However, given the nonlinear nature of this equation, estimating how this happens, or more specifically, the temporal growth of the decorrelator  $\Phi(t)$  and thence the Lyapunov exponent, is a challenge. Since the main question which concerns us has to do with the *short* time growth of these decorrelators, when nonlinear terms  $\mathcal{O}(\delta v^2)$  can be ignored, a reasonable assumption which can be validated against the data from our Direct Numerical Simulations (DNSs), we *linearize* the equation (4.22):

$$\frac{\partial \delta v_i^{\text{lin}}}{\partial t} \approx -v_j^{\mathbf{a}} \frac{\partial \delta v_i^{\text{lin}}}{\partial x_j} - \delta v_j^{\text{lin}} \frac{\partial v_i^{\mathbf{a}}}{\partial x_j} + \frac{\partial T}{\partial x_i}; \quad (4.23)$$

where,  $T = 2\delta_{ij}^2 \int d\mathbf{y} G(|\mathbf{x} - \mathbf{y}|) \delta v_j^{\text{lin}}(\mathbf{y}) v_k^{(a)}(\mathbf{x})$  is the non-local (linear) contribution from the pressure term. It is worth stressing that although we linearize the equation, it still allows for the spatio-temporal spread of the difference field because of its non-local nature. The error between the linearized solution  $\delta\mathbf{v}^{\text{lin}}$  and  $\delta\mathbf{v}$  is quantified

by defining a global relative error:

$$\Gamma(t) = \frac{\frac{1}{V} \int_{\mathcal{D}} d\mathbf{x} \frac{1}{2} |\delta\mathbf{v} - \delta\mathbf{v}^{\text{lin}}|^2}{\Phi(t)} \quad (4.24)$$

where  $\mathcal{D}$  is the domain and  $V$  the volume of space. The error function  $\Gamma(t)$  will eventually become  $\mathcal{O}(1)$  at large times, when the  $|\delta\mathbf{v}| \sim |\mathbf{v}|$ . Nevertheless, starting with the equation (4.22) and taking dot products with  $\delta\mathbf{v}(\mathbf{x}, t)$  followed by a spatial integration, we eventually obtain:

$$\dot{\Phi}(t) = -\langle \delta v_i S_{ij} \delta v_j \rangle + \langle \partial_j W_j \rangle \quad (4.25)$$

$$W_j = -\frac{1}{2} v_j^{\mathbf{b}} |\delta\mathbf{v}|^2 + \delta v_j \partial_{il}^2 \int_{\mathcal{D}} d\mathbf{x}' (v_i^{\mathbf{a}} \delta v_l + \delta v_i v_l^{\mathbf{b}})' G_{\mathbf{x}, \mathbf{x}'} \quad (4.26)$$

and  $S_{ij}$  the familiar rate-of-strain tensor  $2S_{ij} = \partial_i v_j^{\mathbf{a}} + \partial_j v_i^{\mathbf{a}}$  for the thermalized fluid. The second, divergence term in equation (4.26) vanishes however because of periodic boundary conditions leading to a compact form:

$$\dot{\Phi}(t) = -\langle \delta\mathbf{v} \cdot \mathbf{S} \cdot \delta\mathbf{v} \rangle \quad (4.27)$$

At the early times, expecting an exponential growth of the  $\Phi(t)$ , equation (4.28) should lead us to a Lyapunov exponent  $\lambda_S$ :

$$\lambda_S(t) = -\langle \delta\mathbf{v} \cdot \mathbf{S} \cdot \delta\mathbf{v} \rangle / \Phi(t) \quad (4.28)$$

Further, since the rate-of-strain tensor is diagonalisable in its eigenbasis with eigenvalues  $\{\gamma_i\}$  (satisfying the incompressibility constraint  $\sum_i \gamma_i = 0$  with extensional  $\gamma_1 > 0$  and compressional  $\gamma_3 < 0$  eigen-directions) we decompose  $\delta\mathbf{v}$  in the eigenbasis of  $\mathbf{S}$  with (undetermined) components  $\alpha_i$  along each eigenvector and re-write the equation (4.27) as

$$\begin{aligned} \dot{\Phi}(t) &= -\sum_{i=1}^3 \langle \alpha_i^2 \gamma_i \rangle \\ &= -\sum_{i=1}^3 \langle \hat{\alpha}_i^2 \gamma_i |\delta\mathbf{v}|^2 \rangle, \end{aligned} \quad (4.29)$$

where the  $\{\hat{\alpha}_i\}$  are the direction cosines of  $\delta\mathbf{v}$  along the three eigen-directions. Equation (4.29), which formally resembles the enstrophy production term for the Euler equation [210, 211], is an important result that *connects* the decorrelator with the dynamical structures of the velocity field. Keeping in mind that the thermalized fluid is incompressible, with  $\gamma_3 < 0$  always, and  $\dot{\Phi}(t)$  being positive at short times, it seems likely that there *must* be a preferential alignment of  $\delta\mathbf{v}$  with the compressional eigenvector. This allows us to simplify the equation of motion of the decorrelator, upto scaling constants

$$\dot{\Phi}(t) \sim -\langle \alpha_3^2 \gamma_3 \rangle \sim -\bar{\gamma}_3 \Phi \quad (4.30)$$

with  $\bar{\gamma}_3$  the average (negative) eigenvalue along the compressional direction. The linear theory developed above is not just as useful to predict the nature of decorrelators at early times, but they are indispensable to estimate the Lyapunov exponents and their dependence on both temperature  $T$  and degrees of freedom of the system  $N_G$ .

For the 3D thermalized fluid, the linearized theory as summarized in equation (4.30) leads to the following bound on the growth of the decorrelator:

$$\begin{aligned} \left\langle -\sum_{i=1}^3 \gamma_i \alpha_i^2 \right\rangle &\leq \langle -\gamma_2 \alpha_2^2 \rangle + \langle -\gamma_3 \alpha_3^2 \rangle \\ &< \langle -\gamma_3 (\alpha_2^2 + \alpha_3^2) \rangle, \quad \text{as } -\gamma_2 < -\gamma_3 \\ &< \langle -\gamma_3 |\delta\mathbf{v}|^2 \rangle \\ &< -2\bar{\gamma}_3 \Phi \end{aligned} \quad (4.31)$$

Hence the Lyapunov exponent is bound from above by  $\lambda < -2\bar{\gamma}_3$ . In order to uncover the exact dependence of  $\lambda$  on  $T$  and  $N_G$ , we exploit the fact that the linear theory helps us to associate the Lyapunov exponent with the eigenvalues of the strain tensor. Hence, the statistics of this tensor, which depends only on the properties of the velocity field of the thermalized fluid, determines the functional form of  $\lambda$ . The average  $\bar{\gamma}_3$  can be computed if the joint probability distribution of  $\{\gamma_i\}$  is known. Since  $\text{Tr}[\mathbf{S}] = 0$ , the second invariant would be  $\text{Tr}[\mathbf{S}^2]$  hence

$$\overline{\gamma_3} \sim \sqrt{\langle \text{Tr} [\mathbf{S}^2] \rangle}.$$

$$\begin{aligned} \langle \text{Tr} [\mathbf{S}^2] \rangle &= \langle S_{ij} S_{ij} \rangle \\ &\approx \sum_{\mathbf{k}, \mathbf{k}'} -k_i k'_j \langle \hat{v}_i(\mathbf{k}) \hat{v}_j(\mathbf{k}') \rangle \\ &\approx \frac{E}{N_G^3} \sum_{\mathbf{k}} k^2 \approx E N_G^2 \end{aligned} \quad (4.32)$$

leading to  $\lambda \sim N_G \sqrt{T}$ . Given the relative analytical simplicity of the 1D system, we construct the equation of motion of  $|\hat{\Delta}_k|^2$  and derive an exponential growth of the decorrelator associated with a Lyapunov exponent  $\lambda$ . The theoretical calculations for the 1D model are not only consistent with the more complex 3D system but also provide, as we see below, a more rigorous insight into how the Lyapunov exponent scales with the thermodynamic variable of temperature  $T$  and the degrees of freedom  $N_G$  of our system. Since both fields  $\mathbf{a}$  and  $\mathbf{b}$  satisfy the Galerkin-truncated Burgers equation, we can write down the evolution equation:

$$\frac{\partial \Delta}{\partial t} + \mathbb{P}_{k_G} \left[ \frac{\partial \Delta v^{\text{th}}}{\partial x} + \frac{1}{2} \frac{\partial \Delta^2}{\partial x} \right] = 0; \quad (4.33)$$

with initial conditions, most conveniently defined in Fourier space, as  $\hat{\Delta}_k(t=0) = \epsilon_0 \hat{v}_0^{\text{th}} \delta_{k, k_p}$  and the projector  $\mathbb{P}_{k_G}$  constraining the dynamics on a finite dimensional subspace with a maximum wavenumber  $k_G$  and  $N_G$  degrees of freedom. At *short* times, we linearize (for the same reasons as outlined for the 3D thermalized fluid) by dropping the quadratic non-linearity of  $\Delta$  and obtain estimates, made precise in the next section, of an exponential,  $k$ -independent growth of  $|\hat{\Delta}_k|^2$  consistent with our findings for the Euler equation. For the 1D problem, a similar estimate for the Lyapunov exponent on the energy and degrees of freedom  $N_G$  is obtained by simpler manipulations of the linearized evolution equation for the decorrelator  $|\hat{\Delta}_k|^2$ :

$$\frac{\partial |\hat{\Delta}_k|^2}{\partial t} - \frac{\sqrt{T}}{N_G} \sum_{q=1}^{N_G} q \left[ \hat{\Delta}_q \hat{\Delta}_{-k} + \hat{\Delta}_{-k} \hat{\Delta}_{-k-q} \right] = 0. \quad (4.34)$$

Assuming that at short times  $\hat{\Delta}_q \hat{\Delta}_k$  remains spectrally flat (later confirmed numerically), i.e.,  $\hat{\Delta}_q \hat{\Delta}_k \propto |\Delta_k|^2$ , up to some undetermined numerical constant. Hence, and by using the identity  $\sum_{q=1}^{N_G} q \approx N_G^2$  (for large  $N_G$ ), we obtain (where  $C$

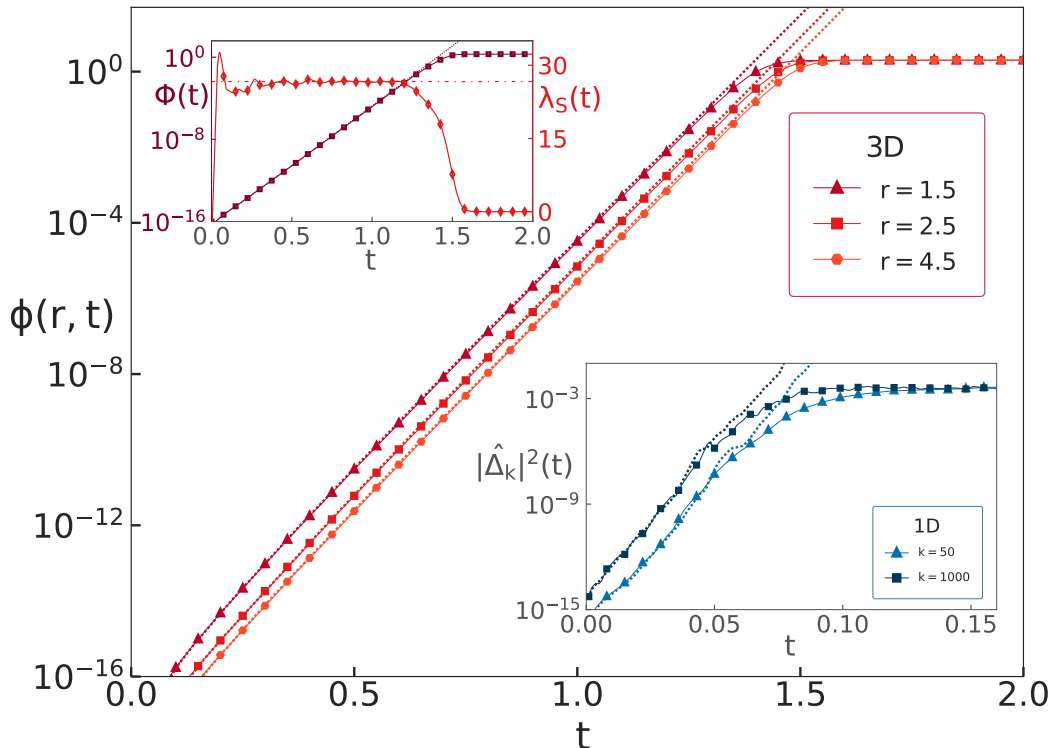


Figure 4.4: Semi-log plots of the decorrelators  $\phi(r, t)$  (for  $E = 1.0$ ) and (lower inset)  $|\hat{\Delta}_k|^2$  (for  $E = 2.0$ ) for a 3D and (lower inset) 1D thermalized fluid, respectively showing an initial exponential growth and eventual saturation. The dashed lines, which do not saturate, are from the linearized theory are in excellent agreement with data from our DNSs at early times. (Upper inset) Semi-log (left y-axis) plot of the averaged decorrelator  $\Phi(t)$  (for the 3D thermalized fluid) along with results from our linearized theory (dashed line). The Lyapunov exponent  $\lambda$ , extracted from  $\Phi(t)$ , shown as dash-dot horizontal line, agrees well with the one  $\lambda_S$  predicted from our linearized theory (right y-axis).

is a numerical constant)  $|\Delta_k|^2 \propto e^{CN_G\sqrt{T}t}$  and thus, just like for the 3D thermalized fluid,  $\lambda \sim N_G\sqrt{T}$ .

With these theoretical insights presented in the above section for both the 1D and 3D systems, we test them against the results from our numerical simulations.

In the figure 4.4 we show representative results for the decorrelators  $\phi(r, t)$  (and  $\Phi$  in the upper inset) in 3D Euler and  $|\hat{\Delta}_k|^2$  for the 1D Burgers (lower inset) as a function of time on a semi-log scale. The symbols (for different values of  $r$  and  $k$ ) are results from the full nonlinear DNSs while the dashed lines correspond to the decorrelators obtained from the effective linearized equations for the difference fields. Consistent with our theoretical estimates described above, the decorrelators from the full, nonlinear DNSs (shown by symbols) grow exponentially, signifying a positive Lyapunov exponent, before

eventually saturating (as the two systems decorrelate) to a value set by the energy of the system. In the figure 4.4 (inset) shows plots of the decorrelator obtained from our linearized model (Eqs. (4.23) and (4.34)), shown as dashed lines; the agreement in the exponential growth phase with the decorrelator obtained from the full DNSs at the early-time is remarkable. However the approximations which go into the linear theory—dropping of the quadratic term—fails at later times. Hence, while the actual decorrelator measured from simulations of the full nonlinear system saturates, with the  $\Phi$  and  $|\hat{\Delta}_k|^2$  to a value equal to  $2E$  and  $2E/N_G$  respectively, the one obtained from the linear theory continue to grow exponentially, as they are insensitive to the role of non-linearities in the system. The error in the linearized decorrelator, for the 3D case, defined in the equation (4.24) is shown in the figure 4.6, the exponential growth regime  $\Gamma \sim 10^{-4}$  and reaches  $\mathcal{O}(1)$  at times when the  $\Phi(t)$  (or  $\phi(r, t)$ ) obtained from DNSs start to saturate. The linear theory of course fails in this saturation region as the approximations leading upto it no longer holds as  $\langle \mathbf{v}^a \cdot \mathbf{v}^b \rangle = 0$  and  $|\delta \mathbf{v}|$  is of the same order as the root-mean-squared velocity  $\sim \sqrt{E}$  of the thermalized fluid. We will soon return to the question of time-scales which determine this saturation.

Our direct numerical simulations (DNSs) of the truncated 3D Euler equation show strong evidence that the difference fields preferentially grow, at *short* times, along the compressional eigen-direction ( $i = 3$ ) of the thermalized fluid, establishing a validity of the simplification in equation (4.30). Theoretically, this claim of preferential alignment is hard to prove exactly. However, we are able to construct from our numerical data the probability distributions of the  $\alpha_i$ , and shown in the figure 4.5 for all three eigen-directions and find that the conjectured preferential alignment, namely that the sum in the right hand side of equation (4.28) is dominated by  $\gamma_3 < 0$  leading to  $\dot{\Phi} > 0$ , holds.

Finally, we confirm the validity of the equation (4.27) by showing in the upper inset of figure 4.4, where the agreement between  $\lambda_S(t)$  (defined in equation (4.28)) and the Lyapunov exponent  $\lambda$  extracted from the exponential growth of decorrelator  $\Phi(t)$  measured. The agreement between the two is almost

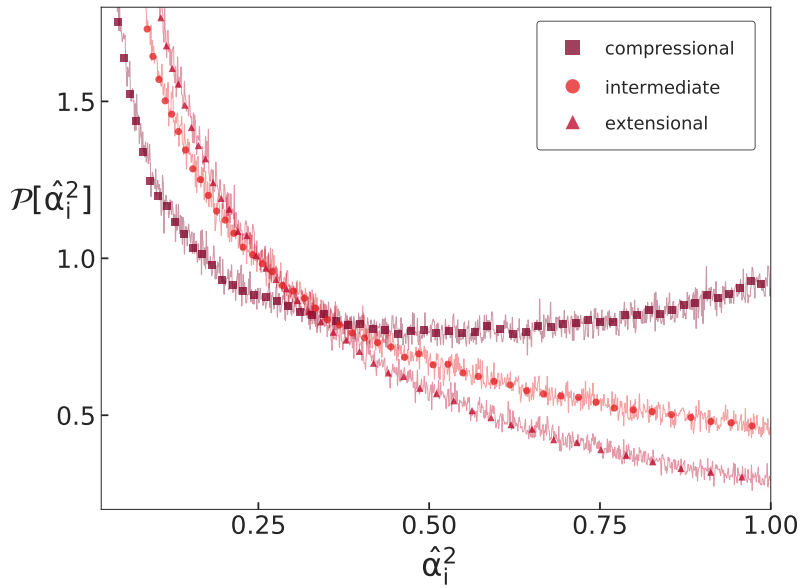


Figure 4.5: The probability distribution of the components  $\hat{\alpha}_i^2$  for the three eigen-directions, clearly suggests the preferential alignment along the direction of compression.

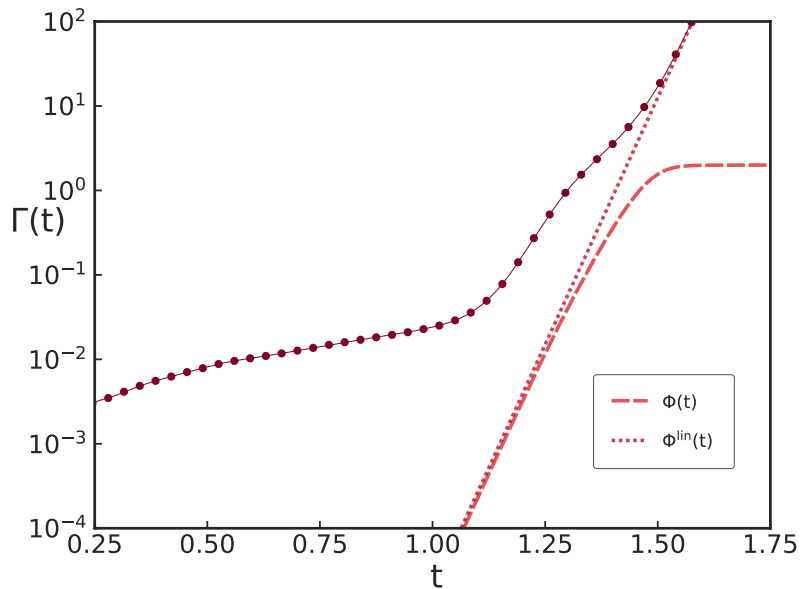


Figure 4.6: Error between the non-linear decorrelator and the linearized decorrelator for the 3D thermalized fluid.

perfect at short times before  $\lambda_S(t)$  decays to zero as the decorrelator saturates. This inevitably leads us to central question of this work: How fast do perturbations grow in a classical, chaotic system and how does it depend on the temperature  $T$  as well as the number of modes,  $N_G$ ? Furthermore is the scaling behaviour of  $\lambda$  really

universal?

Although we are dealing with non-linear equations for hydrodynamics which do not yield easily to an analytical treatment, an extensive analysis of the linearized equations (4.23) and (4.34) for both sets of the decorrelators— $\Phi(t)$  and  $|\hat{\Delta}_k|^2$ —show that under very reasonable approximations, the Lyapunov exponents  $\lambda \propto N_G \sqrt{T}$ . Whereas for the Euler fluid this scaling is a direct result of the statistics of the strain-rate-tensor which determines the behaviour of  $\Phi(t)$ , the analogous result for the 1D system is arrived at by straightforward algebraic manipulations, factoring in the statistical fluctuations, of the equation governing the evolution of  $|\hat{\Delta}_k|^2$ .

This theoretical prediction is easily tested from measurements of the Lyapunov exponent from DNSs of the full non-linear 3D Euler and 1D Burgers equations. From plots such as those shown in figure 4.4 we extract the mean Lyapunov exponent  $\lambda$  and its (statistical) error-bar, and examine its dependence on temperature  $T$  (and  $N_G$ ) by changing the magnitude of the initial conditions and hence the initial energy or temperature. Surprisingly,  $\lambda$  measured through such decorrelators are independent of  $r$  or  $k$ , as was already suggested in figure 4.4. In figure 4.7, we show a unified, with data from 3D Euler and 1D Burgers simulations, log-log plot of all the rescaled Lyapunov exponent  $\lambda/N_G$  measured—for different strengths and scales of perturbations and resolutions  $N_G$ —as a function of temperature  $T$ . The collapse of the data on the dotted lines, denoting a  $\sqrt{T}$  scaling, shows, beyond any doubt, that the many-body chaos of such thermalized fluids *is* characterized by the behaviour  $\lambda \propto N_G \sqrt{T}$ . It is worth stressing that these DNS results for the 3D Euler equations makes the theoretical bound sharp. Also in the figure 4.10 (inset), results from our DNSs confirming the bound derived in equation (4.31) and the scaling relation in equation (4.30), as we find  $\lambda \approx -0.62\bar{\gamma}_3$ . This concretely connects the straining of the flow-field with the Lyapunov exponent. While we do understand why and at what time scales  $t_{\text{sat}}$  the decorrelators of thermalized fluids saturate, as in figure 4.4, it still remains to be understood how they approach the saturated value. To understand this for the 3D thermalized fluid, for simplicity, we define a normalized decorrelator  $\bar{\Phi}(t) = \frac{\Phi(t)}{2E}$ . Given that the only

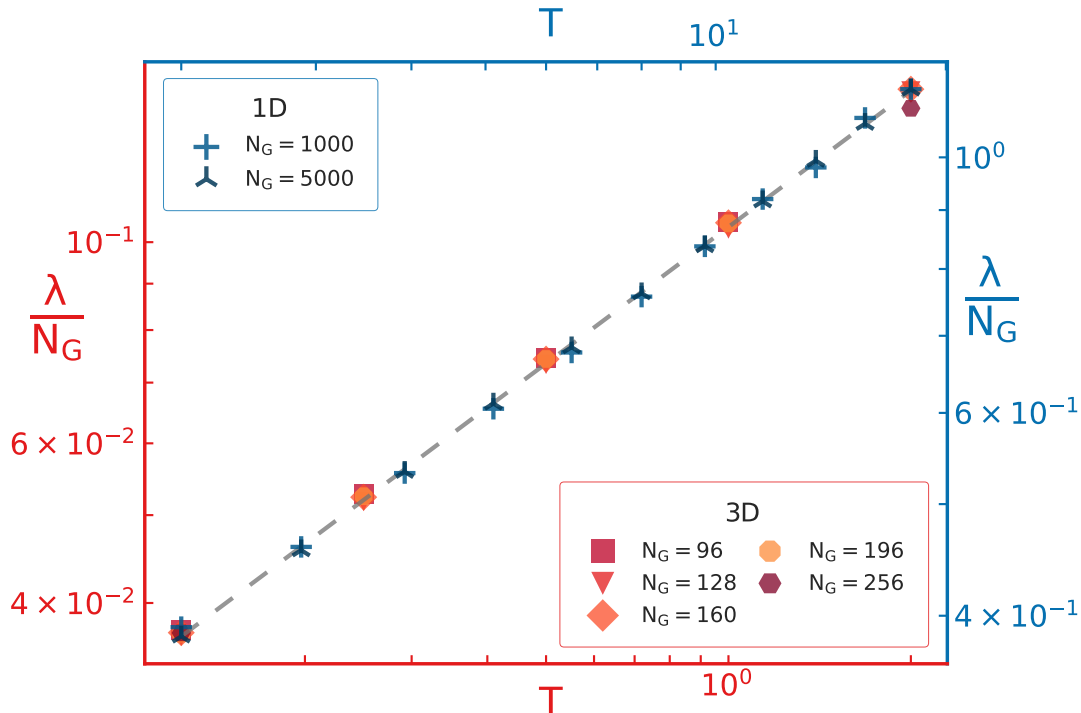


Figure 4.7: Log-log plot of the rescaled Lyapunov exponents  $\lambda/N_G$  versus the temperature  $T$  for the 3D (axes in red) and 1D (axes in blue) thermalized fluids corresponding to different values of  $\epsilon$ ,  $N_G$  and, for the 1D fluid,  $k_p$ . The dashed line with a  $\sqrt{T}$  scaling confirms our theoretical prediction.

time scale in the problem is the inverse of the Lyapunov exponent, we construct the following empirical form for  $\bar{\Phi}$

$$\bar{\Phi}^{\text{emp}}(t) = (1 + \exp[-\lambda(t - t_{\text{sat}})])^{-1} \quad (4.35)$$

with a saturation time-scale  $t_{\text{sat}} \sim 1/\lambda$ , but found more precisely by fitting the data from our simulations. In figure. 4.8 we show a representative plot illustrating how the empirical form approximately fits the data. While the functional form of the decorrelator  $\bar{\Phi}(t)$  defined above is purely heuristic it does serve to underline the fact that the nature of many-body chaos is determined solely by the Lyapunov exponent. *Non-locality* is inherent in 3D thermalized flows due to the pressure term as well as Galerkin-truncation. Hence it allows the perturbation seeded locally at  $t = 0$  to affect the evolution of thermalized velocity everywhere. This is already seen in equation (4.22) which shows that at  $t = 0^+$ , at spatial points far from the center of perturbation, the growth of  $\delta\mathbf{v}(\mathbf{x})$  is essentially triggered by the *non-local* integral

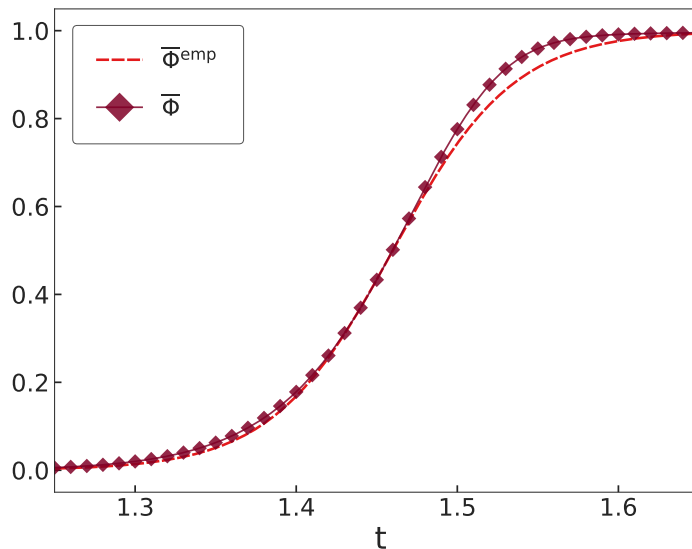


Figure 4.8: A representative plot of the decorrelator  $\bar{\Phi}(t)$  for a 3D thermalized flow ( $E = 1$ ) and the empirical form  $\bar{\Phi}^{\text{emp}}(t)$  illustrating the approximate agreement between the two.

term. The subsequent growth of the difference field is then through its coupling with the rate-of-strain tensor.

All of this suggest that the spatially resolved decorrelator  $\phi(r, t)$  will not have a *wavefront* which propagates (radially) with a finite *butterfly* speed. On the contrary, as was also suggested in the inset of the figure 4.3(a), one should expect a self-similar spatial profile for decorrelator, i.e.,  $\phi(r, t) \sim r^{-\alpha}$ .

In figure 4.9, we see clear evidence of  $\phi(r, t) \sim r^{-\alpha}$ , with  $\alpha \cong 4$ , for in the range  $0 \ll r \ll \pi$  (where  $\pi$  is half the system size since the perturbation is seeded in the middle of a  $2\pi^3$  cubic box). A further consequence of this (as seen in Fig. 4.9, inset) is that the isocontours of the decorrelator (measured through a suitable threshold value  $\phi_0$ ) are spread in space-time as  $t \sim \ln r$ . While we do not have a way of obtaining the exponent  $\alpha \cong 4$  analytically, the constraint that  $\Phi(t) = \int_0^L dr r^2 \phi(r, t)$  must be bounded (from above) suggests that  $\alpha > 3$  which is consistent with what we measure in our data. This, to the best of our knowledge, is the first reported result, and confirmation of what has been conjectured earlier [60, 208] and demonstrated for classical spin systems [56], that  $\lambda \propto \sqrt{T}$  in a chaotic and

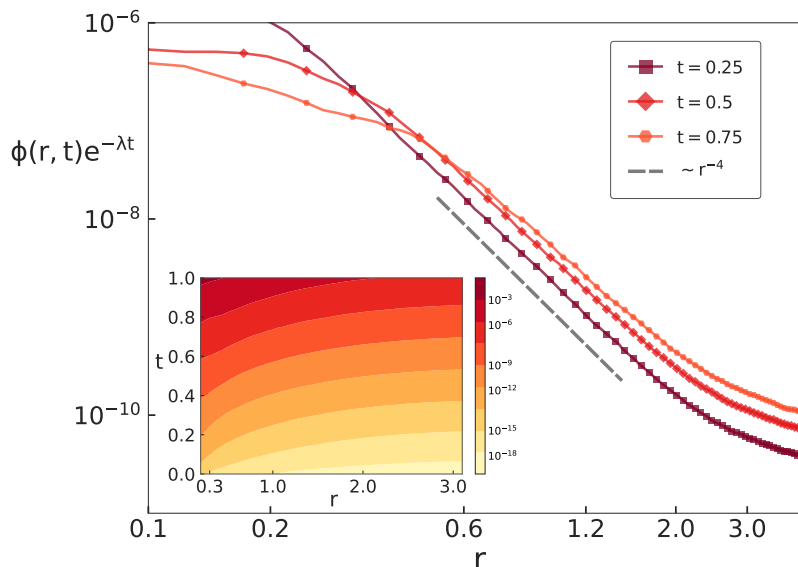


Figure 4.9: The compensated decorrelator  $\phi(r, t) \exp(-\lambda t)$  for different values of  $t$  ( $E = 1$ ); the grey dashed line shows a scaling  $r^{-4}$  is an illustration of the self-similar nature of the spatial spread of the decorrelations. This is confirmed (inset) in the space-time plot of the isocontours of the decorrelator which suggests a spread of the form  $t \sim \ln r$ .

non-linear, many-body classical system obeying the equations of hydrodynamics. Remarkably, we also find strong evidence that the Lyapunov exponent scales linearly with the degrees of freedom  $N_G$  in such extended systems and is truly independent of both the spatial dimension and compressibility of the flow.

Given the association of many-body chaos with issues of ergodicity and equilibration in classical statistical physics, how well do these measurements of  $\lambda$  relate to the (inverse) time-scales associated with the loss of *memory*? The simplest measure of how fast a system *forgets* is to define the ensemble-averaged normalized autocorrelation function:

$$C(t) = \frac{1}{2E} \langle \mathbf{v}^{\text{th}}(t) \cdot \mathbf{v}^{\text{th}} \rangle \quad (4.36)$$

Analytically for short times  $t \lll 1$ , by Taylor expansion upto  $\mathcal{O}(t^2)$

$$\begin{aligned} C(t) &= \left( 1 + \frac{1}{\langle \mathbf{v}^2 \rangle} \frac{d}{dt} \langle \mathbf{v}^2 \rangle + \frac{1}{2} t^2 \frac{\langle \mathbf{v}(0) \cdot \partial_t^2 \mathbf{v} \rangle}{\langle \mathbf{v}^2 \rangle} \right) \\ &= 1 - \frac{t^2}{2\tau^2}, \quad \tau^2 = \frac{\langle (\partial_t \mathbf{v})^2 \rangle}{\langle \mathbf{v}^2 \rangle} \end{aligned} \quad (4.37)$$

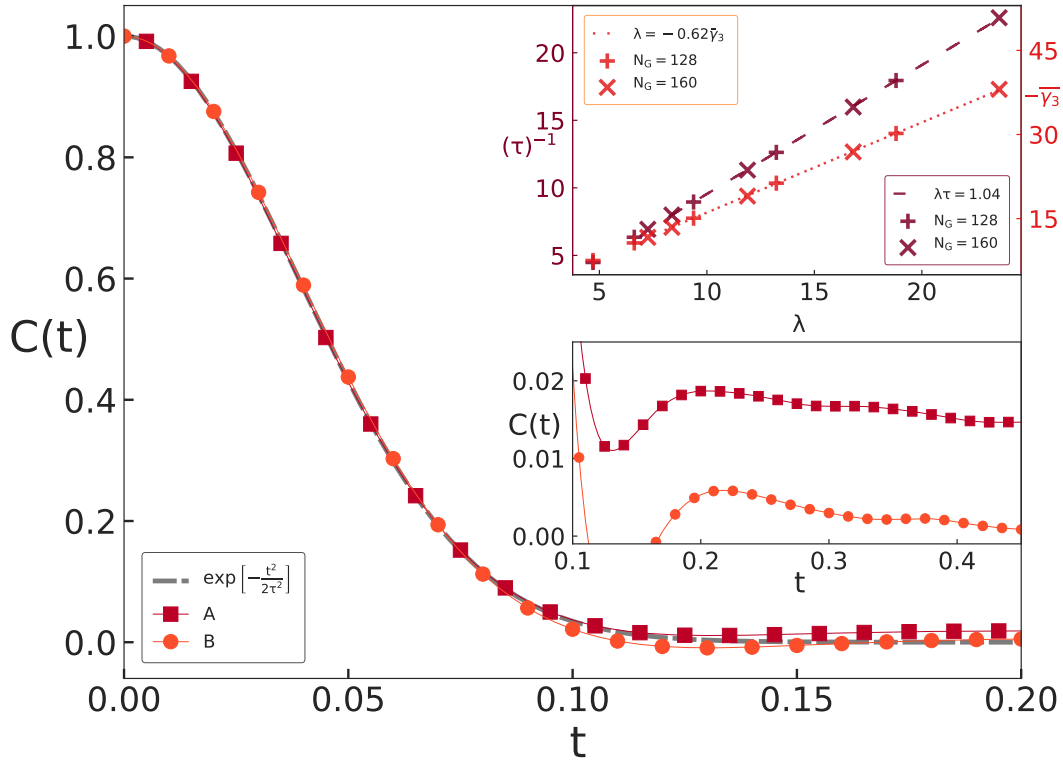


Figure 4.10: A representative plot of the autocorrelation function for a (A) *nearly* and (B) *completely* thermalized 3D fluid along with the theoretical Gaussian prediction. (Lower inset) A magnified view of the same shows that for a fluid which is not completely thermalized,  $C(t)$  falls off to zero much more slowly. (Upper inset) Representative plots of the decorrelation time  $\tau$  and the average (negative) eigen-value corresponding to the compressional direction versus  $\lambda$ .

to extract a autocorrelation time  $\tau$ . Since the velocity can be considered as a time signal with a power spectral density of a white noise with a ultraviolet cutoff  $\tau^{-1}$  in the frequency domain, then by Wiener-Khincin theorem, the auto-correlation function becomes a Gaussian with a timescale  $\tau$ .

$$C(t) = \exp\left(-\frac{t^2}{2\tau^2}\right) \quad (4.38)$$

The linear relation  $\tau \sim 1/\lambda$  is clearly shown from our measurements in the upper inset of figure 4.10. This association of the time scales of the dynamic correlator with the Lyapunov exponent provides a firm foundation to interpret the salient features of classical many-body chaos in terms of principles of statistical physics: Ergodicity and thermalization.

The relative generality of the OTOCs and cross-correlators naturally lead to questions of connecting the macroscopic variables with the scales of chaos in the most canonical of chaotic systems: Those described by non-linear equations of hydrodynamics. Here we provide the first evidence of the temperature dependence of the Lyapunov exponent in (continuum) classical non-linear hydrodynamic systems and show its robustness with respect to spatial dimensions and compressibility effects. It is important to underline that the many-body chaos and the estimate  $\lambda \sim N_G \sqrt{T}$  is really an emergent feature of a fluid which *is* thermalized. We checked this explicitly by measuring the decorrelators in the flow *before* it thermalizes and found, despite the conservation laws still holding, no associated exponential growth and spread of the difference field. It is also worth stressing that the  $\lambda$  that we measure should be identified with the largest Lyapunov exponent of the system and that the time scales at which the decorrelators saturate is a useful estimate of the time taken to thermalize and equilibration.

Before we conclude, we note that that the temperature-dependence of  $\lambda$  is consistent with recent results for classical spin liquids without quasi-particles [56, 57, 190, 212] as well as more general dimensional arguments based on phase-space dynamics [208] of classical many-body systems. In this regard we note that in classical spin-systems [57], the existence of low energy quasi-particles seems to *reduce* the chaotic behaviour of the system ( $\lambda \propto T^a$ ,  $a > 0.5$ ). While more detailed and theoretical investigation of these features, as well as, how far these ideas are relevant for the more spontaneously stochastic Navier-Stokes turbulence are naturally interesting future directions, this behaviour of a *butterfly effect* for classical, non-linear, hydrodynamic systems seems to be a robust and generic feature.

While it is probably true that the exact nature of the dependence of the Lyapunov exponent on the temperature (or the energy density) and number of degrees of freedom should vary from system to system, the concrete evidence we provide of their inter-dependence opens new avenues and questions for the community. In particular, these studies serve to demonstrate the dependence of signatures of spatio-temporal chaos on the thermodynamic variables as well its

relation with the transport properties.

# Chapter 5

## Local Nature of Multifractality in Turbulence

A central scaffold for interpreting and describing out-of-equilibrium pattern forming processes [213–216], multifractality has inevitably woven itself into turbulence theory [91, 217, 218], phenomenology [219] and data analysis [220]. The Frisch-Parisi multifractal model [67, 221] indeed remains the most powerful theoretical justification for the statistical properties of turbulence like the anomalous scaling of correlation functions of velocity differences [67, 222–226], strongly non-Gaussian distributions of velocity gradients [227–229] and fluid accelerations [230]. Constructed on the premise of an intermittent, infinite Reynolds number flow with a form of *local* scale-invariance under the transformations  $r \rightarrow \lambda r$ ,  $u \rightarrow \lambda^h u$  and  $t \rightarrow \lambda^{1-h} t$  [231], it provides corrections to the Kolmogorov *mean field* theory in a way which is consistent with measurements made in experiments and direct numerical simulations (DNSs). The key ingredient in the construction of such theories is the assumption that intermittency effects lead to a range of Hölder exponents  $h \in [h_{\min}, h_{\max}]$  for the (turbulent) velocity field  $\mathbf{u}(\mathbf{x})$ . The simplest interpretation for these exponents relate to the (inertial range) scale-invariance in turbulence of the longitudinal velocity difference  $\delta u_r \equiv \langle \mathbf{u}(\mathbf{x} + \mathbf{r}) - \mathbf{u}(\mathbf{x}) \rangle \sim r^h$  [67].

These ideas, when applied to the intermittent energy dissipation field  $\epsilon(\mathbf{x})$ , leads to the remarkable result that the total dissipation in  $d$ -dimensional “boxes” of size  $r$ , denoted  $\mathcal{E}_r$ , scales as a *fractal* power-law with a variable scaling exponent  $\alpha$  as  $\mathcal{E}_r \sim r^{\alpha-1+d}$  [67, 232–234]. This is a direct consequence of the multifractal interpretation that despite the three-dimensional embedding dimension, the energy dissipation—which is a culmination of the energy cascading process—accumulates in different, entangled fractal subsets with unique dimensions. It is then possible to associate the fractal dimension  $f_\alpha$  of these subsets with exponents lying between  $\alpha$  and  $\alpha + d\alpha$  yielding the well-known singularity or multifractal spectrum  $f_\alpha - \alpha$ .

The framework of these ideas are a powerful tool bridging the conceptual picture of the energy cascade with intermittency of the dissipation field. Indeed, it is easy to show that  $\alpha = 3h$  is exactly the same (arbitrary) scaling exponent which leaves the Navier-Stokes equations invariant under its rescaling transformations [67]. Furthermore, within the Kolmogorov non-intermittent phenomenology, there is a single exponent  $h = 1/3$  (i.e.  $\alpha = 1$ ) [86, 231] which leads to the familiar  $2/3$  and  $5/3$  laws of turbulence. However, obtaining the measured exponents and the corrections to the Kolmogorov prediction from the Navier-Stokes equation still remains elusive.

This singularity spectrum though remains a central pillar in modern statistical theories of fully developed turbulence. Beginning with the earliest measurements of Meneveau and Sreenivasan [232–234], the robustness of the multifractal nature of the kinetic energy dissipation field has never been in question. And yet, all these measurements pertain to the statistics of the *entire* field (or signal). This is somewhat surprising because implicit in the ideas of multifractality is the spatial *fluctuation* of the scaling exponents over the flow field.

We arrive here at an impasse. The global analysis tends to suppress an unremarked symptom of its construction: Even if a measure is multifractal *only* in small localized patches, one is *bound* to find a broad  $f_\alpha$  curve representing the entire data. In Appendix A.1 we give a brief discussion on how local multifractal nature dominates the global results. Is it possible then to actually probe the

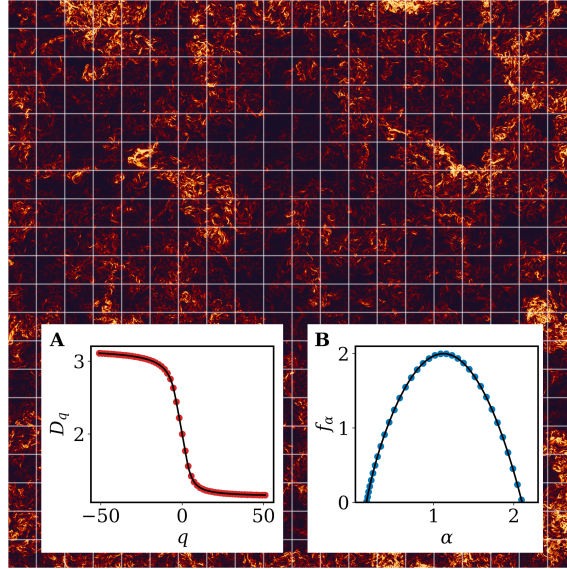


Figure 5.1: Pseudo-color plot of dissipation  $\epsilon$  at a representative cross-section from the Johns Hopkins isotropic 4096<sup>3</sup> data. Superimposed on this is a regular tiling as a pictorial guide to show how the local multifractal properties are calculated (made with Processing [239, 240]). (Insets) **(A)** Generalized dimensions  $D_q$  and **(B)** the singularity spectrum  $f_\alpha - \alpha$  calculated over the full 2D cross-section shows the essential multifractal nature of the dissipation field, consistent with earlier measurements.

multifractal nature of turbulence in a local way, that is, to have estimates of the spatial dependence of the generalized dimensions  $D_q(\mathbf{x})$ , the singularity spectrum  $f_{\alpha(\mathbf{x})} - \alpha(\mathbf{x})$  and thence of course the distribution of the Hölder exponents  $h(\mathbf{x})$ ? The closest, so far, have been recent attempts [235–238] using wavelet techniques and local energy transfer concepts to characterize fields similar to the intractable  $h(\mathbf{x})$ . While characterizing Hölder exponents point-wise may indeed be difficult, a local multifractal analysis, keeping the robustness of the Frisch-Parisi formalism, opens up a way to reveal the crucial underlying variation in multifractality, which has so far remained uncharted.

## 5.1 Coarse-grained Local Measurement

In this Chapter, we show how a locally adapted construction of multifractal measures of turbulence dissipation fields throws up surprises. In particular, we find that *most* of the flow is essentially monofractal with an almost delta function for

$f_\alpha$  at  $\alpha \approx 1$  which corresponds to the Kolmogorov mean field exponent  $h = 1/3$ . The few patches of multifractal behaviour (with broad  $f_\alpha(\mathbf{x})$  vs.  $\alpha(\mathbf{x})$  curves) are directly correlated with spatial regions of enhanced dissipation and, by extension, intermittency. Indeed, a more accurate description of fully developed turbulence would be intermittent, multifractal islands on a vast and calm *Kolmogorovean* sea.

Our analysis is based on kinetic energy dissipation fields  $\epsilon(\mathbf{x}) \equiv 2\nu S_{ij}S_{ij}$ , where  $S_{ij}$  is the symmetric part of the velocity gradient tensor, obtained from 3 different direct numerical simulations, with very different (Taylor-scale based) Reynolds numbers  $Re_\lambda$ , of the three-dimensional (3D), triply-periodic, incompressible Navier-Stokes equation. For the smallest  $Re_\lambda \approx 200$ , we use our own fully de-aliased pseudospectral code with  $N = 512^3$  collocation points and a constant energy-injection rate on the first 2 shells. For higher Reynolds numbers, we use publicly available data from the Johns Hopkins Turbulence Database (JHTD) [241–243] with  $N = 1024^3$  ( $Re_\lambda \approx 433$ ) and  $4096^3$  ( $Re_\lambda \approx 610$ ). Our results are consistent across this wide range of Reynolds numbers and independent of simulations; in what follows, we present converged results, using a  $4096^2 \times 192$  subset of the  $4096^3$  dataset.

Let us first recall how the classical multifractal spectrum for a  $d$ -dimensional dissipation field is constructed. Denoting the average dissipation on a scale  $r$  by  $\epsilon_r$ , we construct  $N_r$  number of (space-filling)  $d$ -dimensional boxes of size  $r$  in the full domain. This allows us to estimate the total dissipation  $\mathcal{E}_r \sim \epsilon_r r^d \sim r^{\alpha-1+d}$  within each box. By taking the  $q$ -th moment of this and summing over all  $N_r$  boxes one obtains the *partition function*  $Z_q \equiv \sum_{N_r} \mathcal{E}_r^q \sim r^{(q-1)D_q}$ , where  $D_q$  is the generalized dimension and the following relation holds:  $\sum_{N_r} r^{(\alpha-1+d)q} \sim r^{(q-1)D_q}$ . Further analysis [67, 232] yields the exact relations for the singularity spectrum:

$$\alpha = \frac{d}{dq} [(q-1)(D_q - d + 1)] \quad (5.1)$$

$$f_\alpha = \alpha q - (q-1)(D_q - d + 1) + d - 1 \quad (5.2)$$

Clearly, within the mean field, monofractal Kolmogorov ideas for 3D turbulence,

$D_q = d = 3$  leading to  $\alpha = 1$  ( $h = 1/3$ ) and  $f_\alpha = d = 3$  and thence a  $\delta$ -function like  $f_\alpha - \alpha$  curve.

In figure 5.1, we show a representative plot of a 2D ( $d = 2$ ) slice of the  $\epsilon$  field constructed from the 4096<sup>3</sup> JHTD data; the insets show the generalized dimensions  $D_q$  and the singularity spectrum  $f_\alpha - \alpha$  for this slice of data, which is consistent with results reported earlier [67, 232]: The broad  $f_\alpha$  curve is the most precise indicator that turbulence admits a range of scaling exponents and not just the mean field Kolmogorov exponent  $\alpha = 1$ .

However, as is well known—and illustrated in figure 5.1—the dissipation field is strongly intermittent. It is not immediately obvious, therefore, whether the fractal sets on which  $\epsilon(\mathbf{x})$  is distributed are themselves uniform in space. There might, in fact, be an equally strong variation in multifractality over  $\mathbf{x}$ , which would be revealed if it were possible to measure the generalized dimensions  $D_q(\mathbf{x})$  and  $f_\alpha(\mathbf{x}) - \alpha(\mathbf{x})$  locally. These variations would not only help connect the ideas of the cascade with multifractality but also provide important insights in the detection of (possible) singular  $h \leq 1/3$  regions with anomalous dissipation [17, 244]. Important and enticing as this question is, the very nature of the multifractal calculation precludes any possibility of a *single* point  $\mathbf{x}$  measurement of such quantities. This is because at a practical level the partition function  $Z_q(\mathbf{x})$  must be measured over a range of scales to extract the generalized dimensions  $D_q(\mathbf{x})$  from which follows the (local) singularity spectrum and scaling exponents.

To circumvent this problem, we develop a tiling approach to allow us to self-consistently measure the spatial variation in the multifractality of the field. This is illustrated in figure 5.1 where a (exaggerated) white grid is superimposed on the 2D slice of the dissipation field, leading to square data-tiles with edge  $\mathcal{L}_T$  (or cubical divisions used for 3D analysis). We then treat each of these tiles, centered at  $\mathbf{x}$ , independently and calculate the multifractal measures in them as one would ordinarily for the full domain. The size of these tiles was tested in the range between  $2\eta < \mathcal{L}_T < 16\eta$ , where  $\eta$  is the Kolmogorov dissipation scale. Larger tiles, which

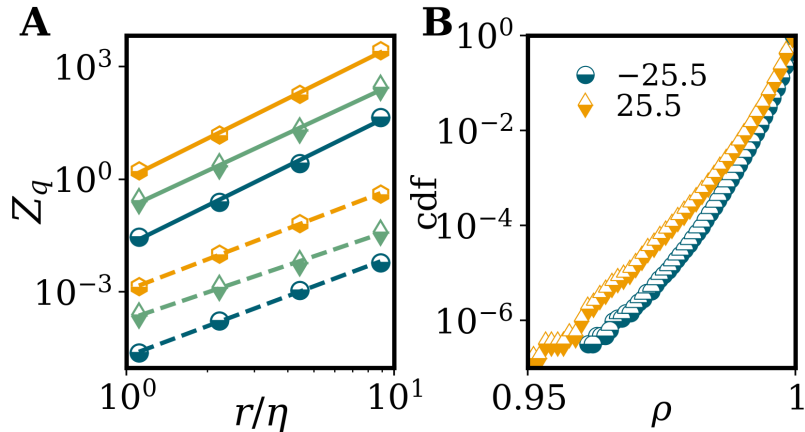


Figure 5.2: **(A)** Loglog plots of the partition function  $Z_q(\mathbf{x})$  vs  $r$  for  $q = -25.5$  (solid lines) and  $q = 25.5$  (dashed lines), vertically shifted for clarity, calculated in randomly chosen spatial locations in data-tiles of size  $\approx 10\eta$ . **(B)** Cumulative distribution function of the Pearson correlation coefficient  $\rho$  for the linear-regression fits used to obtain  $D_q$ , for  $q = -25.5$  and  $q = 25.5$ , over all tiles.

are still smaller than the inertial range, give a wider range of  $r$  values over which to construct  $Z_q(\mathbf{x})$  while, for an ideal local measure, we would like the tiles to be as small as possible. However, the lower end of  $\mathcal{L}_T$  is dictated by the constraint that we need *enough* points to measure the scaling of  $Z_q(\mathbf{x})$  unambiguously. At an operational level, this is not obvious since, unlike the full domain, we have fewer points within individual tiles on which the measurement can be made.

Calculating the local variation of  $D_q(\mathbf{x})$  with  $q$ , requires obtaining a clean scaling of the partition function  $Z_q(\mathbf{x})$  now measured within the tiles. Thus, in figure 5.2(A), we begin by showing representative plots of the partition function for  $q = -25.5$  (solid lines) and  $q = 25.5$  (dashed lines), calculated in three-dimensional tiles with  $\mathcal{L}_T \approx 10\eta$ , at randomly chosen  $\mathbf{x}$  locations. While this plot already suggests that a  $Z_q$  vs  $r$  scaling can be reliably obtained, we test the overall accuracy of doing so in figure 5.2(B) by calculating the cumulative distribution of the Pearson correlation coefficient  $\rho$  for linear-regression fits used to obtain  $D_q$ , over all tiles. The distribution shows a high degree of confidence, with more than 99.98% of tiles with  $\rho > 0.98$ , for both  $q$  values.

Clearly, these plots show that a local  $D_q(\mathbf{x})$  can be meaningfully extracted by using the prescription we propose. We found our results to be insensitive to the

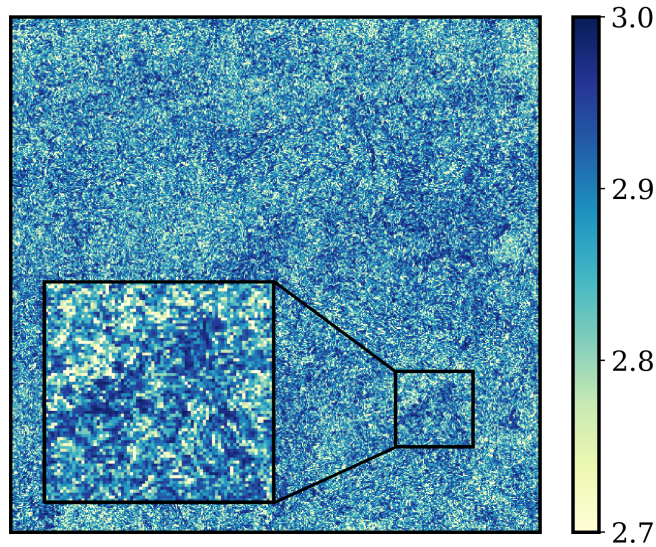


Figure 5.3: We show a cross-section of the  $D_2$  field, also known as the correlation dimension. Our analysis coarsens a  $4096 \times 4096 \times 8$  data-slice to  $512 \times 512$  tiles. This reveals a stark variation in  $D_2$  over space, which remained hitherto unseen. Coherent patches of similarly valued regions of  $D_2$  are found nestling in a fluctuating (and non-random) field.

chosen  $\mathcal{L}_T$ , indicating the consistency and convergence of our approach. In what follows, we report results from a tiling of  $\mathcal{L}_T \approx 10\eta$  and carry out the analysis in three dimensions. Before stepping into spatially varying multifractal spectra, we pause to look at the special case of  $D_q$  for  $q = 2$ , also known as the correlation dimension, that provides a measure of inhomogeneity in a fractal set [92, 245], or simply  $D_2$ . Figure 5.3 shows a planar cross-section of the  $D_2(\mathbf{x})$  field, starkly varying in space, with sizeable pockets of coherent regions of similarly valued correlation dimensions. This also shows that the field is far from random, and at some level this is reflective of the structures in the dissipation field. We wish to underline that our method allows, perhaps for the first time, to visualize this field, which further opens up directions to study the structure of these intrinsic, and as yet elusive, features of turbulence.

The dissipation field of course varies within these tiles, and we find it useful to keep track, for each tile, of the maximum  $\epsilon_{\max}(\mathbf{x})$ , the minimum  $\epsilon_{\min}(\mathbf{x})$  and mean  $\bar{\epsilon}(\mathbf{x})$  dissipation as well as use  $\Delta\epsilon(\mathbf{x}) \equiv \epsilon_{\max}(\mathbf{x}) - \epsilon_{\min}(\mathbf{x})$  as a measure of the fluctuation of the field; while all these values are presented as multiples of the global mean dissipation  $\langle\epsilon\rangle$ . We are now equipped to calculate *local* measures of

multifractality— $D_q(\mathbf{x})$  and  $f_\alpha(\mathbf{x}) - \alpha(\mathbf{x})$ —and estimate conclusively how uniformly (or not) multifractal turbulence really is. We construct a precise estimate of this through  $\Phi(\mathbf{x}) \equiv \text{std}(\alpha(\mathbf{x})) = \sqrt{\langle \alpha^2 \rangle - \langle \alpha \rangle^2}$ , where  $\langle \dots \rangle$  denotes an average over all values of  $\alpha$ . This provides a quantitative measure, using the spread of singularity strengths, of the degree of local multifractality in the flow. We know that these multifractal measures, even locally, should satisfy bounds such as  $\alpha \geq \alpha_{\min} = -2$ ,  $f_\alpha \leq \alpha + 2$ , and  $f_\alpha \geq 0$  (see Ref. [218]). If the  $f_\alpha$  spectrum has a peak  $f_\alpha^*$  corresponding to some  $\alpha = \alpha^*$ , then we have  $f_\alpha^* \lesssim 3$  (where  $\alpha^* = 1$  and  $f_\alpha^* = 3$  in the Kolmogorov framework). While there is no bound for  $\alpha_{\max}$ , it is reasonable to assume  $\alpha_{\max} \approx 3$  for a region with no singular structures. Such monofractal regions can be expected to show  $\Phi \approx 0$ . However, the largest values of  $\Phi$ , corresponding to highly multifractal regions, is estimated as  $\Phi \approx \sqrt{\langle \alpha^2 \rangle - \langle \alpha \rangle^2} \approx 1.7 \sim \mathcal{O}(1)$  for  $\alpha$  uniformly ranging from  $-2$  to  $3$ . Hence, on such theoretical grounds we expect  $0 \lesssim \Phi(\mathbf{x}) \lesssim 1.7$ , with the lower and upper bound corresponding to mono and multifractal statistics, respectively.

## 5.2 Correlation with Dissipation

In figure 5.4(A), we show  $D_q(\mathbf{x})$  vs  $q$  curves measured at different spatial positions, corresponding to different values of  $\bar{\epsilon}$ . Clearly, while the shape of each curve is similar to the global statistics (Fig. 5.1, Inset A), a very strong spatial dependence on where we measure the generalized dimensions is unmissable. Furthermore, the spread in  $D_q(\mathbf{x})$  is not trivially related to the mean dissipation around  $\mathbf{x}$ ; the secret to this variation, as we shall demonstrate, lies in how locally fluctuating (within each tile) the dissipation field is.

The measurement of the generalized dimension  $D_q(\mathbf{x})$  allows us now to calculate local singularity spectra. In figure 5.4(B), we show representative plots of  $f_\alpha(\mathbf{x}) - \alpha(\mathbf{x})$  for the same locations (see legend in panel A) for which the generalized dimensions were calculated. Quite clearly—and contrary to what one

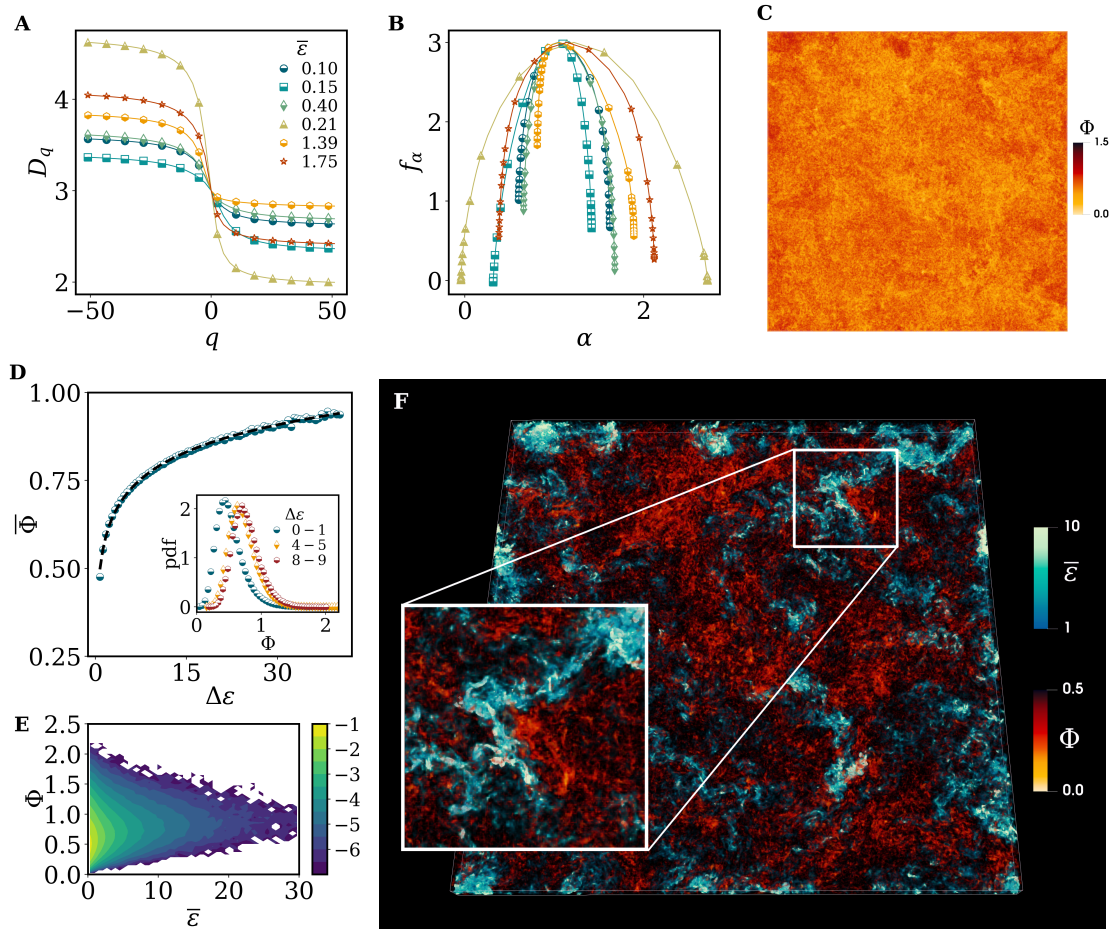


Figure 5.4: (A) Generalized dimensions  $D_q$  vs  $q$ , calculated locally for randomly sampled tiles, together with (B) the corresponding  $f_\alpha - \alpha$  spectra of singularity strengths, show a strong variation in the multifractal properties between different spatial regions. (C) The resultant  $\Phi$  field shows large regions of the flow are actually almost monofractal with  $\Phi \approx 0$ , with pockets of  $\Phi \sim \mathcal{O}(1)$  with its pdf [(D)(inset)] shifting towards higher  $\Phi$  when sampled in regions of higher  $\Delta\epsilon = \epsilon_{\max} - \epsilon_{\min}$ . (D) The mean value of  $\Phi$  is shown to grow as the logarithm of  $\Delta\epsilon$ . (E) The full joint-distribution of  $\Phi$  and the mean dissipation  $\bar{\epsilon}$  in each tile. While lower  $\bar{\epsilon}$  corresponds most likely to low values of  $\Phi$ , an increase in  $\bar{\epsilon}$  makes larger  $\Phi$  equally likely, while also increasing the smallest admissible  $\Phi$  value. (F) A volume-rendering of  $\bar{\epsilon} \geq 1$  is superimposed with the  $\Phi \leq 0.5$  field, which being spatially-exclusive, gives a clear message that the most *monofractal* flow regions are coincident with mild dissipation.

sees in the conventional global measurements of the singularity spectrum (see Refs. [67, 232] and Fig. 5.1, inset)—there are several regions where the flow is essentially monofractal (the  $f_\alpha$  spectrum being very narrow) and fully consistent with the ideas of Kolmogorov, while other highly multifractal regions lead to broad  $f_\alpha$  curves. These results already hint that multifractality can be considered as a *local* property of the field.

In figure 5.4(C), we show a pseudo-color plot of  $\Phi$ . Quite remarkably, much of the flow is Kolmogorov-like with  $\Phi \ll 1$ ; the highly multifractal regions— $\Phi(\mathbf{x}) \sim \mathcal{O}(1)$ —are isolated patches which, as we shall see, correlate completely with the extreme (singular) regions of energy dissipation. This result is remarkable. It illustrates that, surprisingly, turbulent flows are *not* uniformly multifractal; indeed on the contrary, much of the turbulent flow seems to respect, locally, Kolmogorov’s ideas of an exact, self-similar cascade. We also note that the range of  $\Phi(\mathbf{x})$  is well bounded by the theoretical range that we have discussed above.

What determines the magnitude and variation of  $\Phi(\mathbf{x})$ ? Measurements of the generalized dimensions and singularity spectra suggest that the strength of the local dissipation  $\bar{\epsilon}$  is not where the answer lies. We find that the probability distribution function (pdf) of  $\Phi$ , conditioned on  $\Delta\epsilon(\mathbf{x})$ , is revealing. In the inset of figure 5.4 (D) we show this pdf for three different values of  $\Delta\epsilon$ . Clearly, as evident from the previous measurements, the distribution is sharply peaked at values of  $\Phi \gtrsim 0$  with an (likely) exponential tail for  $\Phi \sim \mathcal{O}(1)$ . We also find that the probability of having a higher degree of multifractality increases, albeit marginally, when there is a greater variation of  $\epsilon(\mathbf{x})$  within a tile. The mean value  $\bar{\Phi}$ , for a given  $\Delta\epsilon$  (sampled in windows of  $\Delta\epsilon \pm 0.25$ ), in fact grows logarithmically, as seen clearly in figure 5.4(D).

What then is the role of the average dissipation  $\bar{\epsilon}(\mathbf{x})$  in determining the spatial non-uniformity of multifractality  $\Phi(\mathbf{x})$ ? A joint-distribution (Fig. 5.4 (E)) shows that the answer is fairly non-trivial. Clearly, for low values of  $\bar{\epsilon}(\mathbf{x})$  it is far more likely to have  $\Phi(\mathbf{x}) \ll 1$ ; although, surprisingly, the less-likely extreme values of  $\Phi(\mathbf{x})$  also coincide with regions of low  $\bar{\epsilon}(\mathbf{x})$ . This reflects that it is not the mean dissipation in a region, but the *variation* of dissipation, that manifests multifractality (as shown in Fig. 5.4 (D)). At higher  $\bar{\epsilon}(\mathbf{x})$ , the smallest values of  $\Phi(\mathbf{x})$  admissible slightly increases with  $\bar{\epsilon}(\mathbf{x})$ , while the largest values of  $\Phi(\mathbf{x})$  also dip. While this result might appear contrary to our notion that extreme dissipation *alone* begets multifractality, it finds parallel in an equally intriguing finding from a recent study showing local Hölder exponents, measured by proxy, also do not trivially

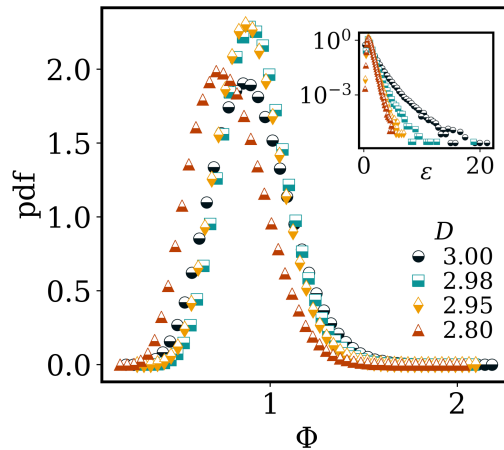


Figure 5.5: Local multifractal statistics from decimated flow simulations. The inset shows that increasing decimation leads to a significant narrowing of the tails of the  $\bar{\epsilon}$  pdfs. This is accompanied by the pdf of  $\Phi$  itself shifting to lower values, reflecting reduced local multifractality corresponding to a reduction in intermittency.

correlate with inertial dissipation [237]. In fact, experiments have shown that the *most* dissipative structures locally resemble Burgers vortices [246]. While these intense spots make the entire field highly intermittent and contribute to broadening the global multifractal spectrum, the *local* multifractal picture can be different.

We finally cement these results with a visual illustration of where the Kolmogorov-like regions are embedded. We look at a snapshot (with volume-rendering) in figure 5.4 (F) of the 3D dissipation field, restricted to large values of  $\bar{\epsilon}(\mathbf{x}) \geq 1$ . Superimposed on this is the local measure of  $\Phi(\mathbf{x}) \leq 0.5$ . Unlike the sparsely populated high  $\bar{\epsilon}(\mathbf{x})$  regions, the more frequent low  $\bar{\epsilon}(\mathbf{x})$  regions (hidden from view here) remain largely occupied by low  $\Phi(\mathbf{x})$  (these regions are also coincident with mild to low kinetic energy). Clearly, then, the regions of monofractal flow are *strongly correlated* to the more populous regions of mild dissipation, showing that the Kolmogorov-like regions locally dissipate less than the multifractal regions.

We have, so far, shown compelling evidence which suggests that multifractality in turbulent flow is not as spatially uniform as one might have suspected. In the absence of a robust theory to explain this singular feature of turbulence, we make a final test of these ideas in a Navier-Stokes-like flow which

is *guaranteed* to be non-intermittent. An obvious choice for this is the so-called decimated turbulence model which was introduced by Frisch *et al.* [35]. The basic principle lies in (numerically) solving the Navier-Stokes equation on a Fourier lattice with a quenched disorder—namely the absence of a pre-chosen set of modes either randomly or fractally—by ensuring both the initial conditions and the non-linearity are projected on this sub-set of remaining Fourier modes. Subsequent to the introduction of this model, we now know [45, 47–49, 164, 247] that such surgical removal of modes lead to a *turbulence* which is non-intermittent.

We take advantage of such a flow to repeat the local multifractal analysis performed on regular turbulence. A confirmation of the conclusions drawn from our results would mean that the decimated flow ought to show lower values of  $\Phi(\mathbf{x})$  than what is measured in fully developed turbulence. Indeed, this is what we find in figure 5.5, showing measurements of the pdf of  $\Phi(\mathbf{x})$  for several different levels of fractal decimation (which leads to decreasing intermittency as seen from the pdfs of  $\bar{\epsilon}$  in the inset). The  $\Phi$  distributions consistently shift toward lower values. Joint-distributions of  $\Phi$  and  $\bar{\epsilon}$  were also found to show a simultaneous reduction in their spreads. This confirms a strong link between intermittency and local multifractality.

In conclusion, we wish to highlight two equally important contributions of this Chapter. First is the finding that turbulence fields are not *uniformly* multifractal, but instead manifest strong multifractality in localized pockets of intermittency in a quiescent Kolmogorovean background of mild dissipation. This paints over a lacuna in our understanding of turbulence where, owing to the very construction of the classical multifractal analysis, the notion of a spatially varying multifractality remained inconcievable. Secondly, our local analysis framework opens up a completely novel avenue for studying both the structure and dynamics of flow singularities and generalized dimension fields, in tandem with turbulence structures like intense vorticity worms [248–250], non-locally induced velocity jets [251], or precursors to singular dissipation [236, 246]. This projects multifractality out of its role of simply being a statistically reductive tool unrevealing of spatio-temporal

minutiae, as noted before [252], to possible applications in prediction and diagnostics of flows. Moreover, this localized analysis begs to be applied to data from across disciplines, where multifractality has been found emergent including in the areas of physics and chemistry [213], medicine [253], geophysics [254], climate [255] and finance [256], and is likely to be revealing, as we demonstrate for the long standing picture of turbulence, in unpredictable ways.

# Chapter 6

## Dynamo Problem in the EDQNM -MHD Closure Model

### 6.1 Introduction to the Dynamo Problem

Large magnetic fields are at the heart of almost every observation in astrophysics [103, 104, 257–260]. Indeed, they play a pivotal role in, as well as shape the consequence of, the dynamics of phenomena ranging from star formation, the interstellar medium to the underpinnings of the solar wind [261, 262]. And yet questions remain how such sustained magnetic fields arise—the *dynamo* problem—in the first place. Since astrophysical flows are also, typically, notoriously turbulent, it is natural to look for answers to such questions within the framework of magnetohydrodynamic (MHD) turbulence [2, 258, 259, 263].

While a theory for the dynamo problem rooted in the full set of equations for MHD is desirable, there are formidable challenges to this for reasons somewhat similar to the situation in fluid turbulence. Even, from the point of view direct numerical simulations (DNSs) of such systems, the parameter space accessible to modern simulations are quite far from what is realisable in either astrophysical

systems or liquid-metal experiments [264]. For example, the Prandtl number, defined as the ratio of the kinetic viscosity to the magnetic diffusivity  $\text{Pm} \equiv \nu/\xi$ , range from values as large as  $10^{14}$  (interstellar medium) to those as small as  $10^{-5}$  (liquid sodium experiments). Such a range of numbers are prohibitively expensive for DNSs; thus more often than not, theoretical approaches based on reasonable assumptions provide additional insights and a fresh perspective in understanding the nuances of the dynamo problem.

An excellent example of such theoretical approaches, and the deep insights they provide, is the Kazantsev model [265] (see also Refs. [103, 104, 260, 266]). In this stochastic model, the velocity field is Gaussian and statistically homogenous, isotropic, and parity invariant. In addition, the correlation time is assumed to be zero—probably the strongest simplification in this model. By varying the features of the spatial correlations of the velocity field, it is possible to study the magnetic growth as function of the degree of compressibility of the flow, its spatial regularity, the space dimension, as well as the Prandtl and magnetic Reynolds numbers. In particular, the Kazantsev model has provided the first evidence of the existence of a maximum critical dimension for the dynamo effect beyond which the random flow becomes unable to amplify a magnetic field [267, 268]. The range of dimensions where there is dynamo shrinks as the velocity becomes less and less regular in space, until it vanishes when the Hölder exponent of the velocity falls below  $1/2$  [269]. Compressibility, however, has the effect of widening the range of dimensions over which the dynamo is possible [270]. Interestingly, dimension three is the one where the least flow regularity is required for the dynamo effect to take place, independently of the degree of compressibility.

While it is easy to appreciate why theoretical models with variable roughness (of the velocity field) and compressibility have a direct bearing on understanding *real* dynamos, the role of dimensions  $d$  (beyond the obvious  $d = 2$  no-dynamo theorem) in the dynamo—no-dynamo transition has been completely ignored. This is somewhat surprising because several aspects of MHD turbulence, and the dynamo problem in particular, have parallels with critical phenomena

and phase transitions. Taking this point of view and recalling the fundamental discoveries—such as dimensional regularization or the  $4 - \epsilon$  expansion [271]—made possible by going beyond the physically obvious  $d = 2$  or  $3$  dimensions, it is not unreasonable to ask if there is an analogue of a *lower* and *upper critical dimension* below and beyond which, respectively, dynamo action ceases to be. Indeed, such a point of view, of going beyond physically realisable integer dimensions of two and three, has been exploited to investigate fundamental questions of intermittency and energy cascades in classical fluid turbulence [35, 44, 49, 63, 64]. In this Chapter, we simply ask if there are lower  $d_L$  and upper  $d_U$  *critical* dimension within which dynamo action is confined?

While desirable, it is difficult to answer this question directly by using DNSs in arbitrary dimension  $d$ . Hence, as we show below, we construct and use a closure model—the well-known Eddy-Damped Quasi-Normal Markovian (EDQNM) [29, 63, 95, 96, 272] approach—for the MHD equations. The problem is approached in  $d$ -dimensions and final model obtained is used to test the *dynamo* effect in various spatial dimensions, including non-integer ones. In particular, we find that for a given magnetic and kinetic Reynolds number (Rm and Re), the dynamo action is constrained between  $d_L$  and  $d_U$ , that is dynamo action occurs for  $d_L \leq d \leq d_U$ . Surprisingly,  $d_L$  is slightly larger than the two dimensional constraint from the no-dynamo theorems and there exists a finite upper dimension  $d_U < \infty$ , beyond which dynamo fails to a different reason.

Theoretically, the full magnetohydrodynamic (MHD) equations suffer from the same closure problems—and hence analytical progress—as the Navier-Stokes equation for fluid turbulence [30]. We recall that in fluid turbulence theoretical progress in understanding the two-point correlation function stems first from a Quasi-Normal approximation which allows a rewriting of fourth-order moments as sums of products of different second-order moments and then successive use of an (phenomenological) eddy-damping rate and *Markovianization* leads to a closed form equation for the kinetic energy spectrum  $E^u(k)$  in the EDQNM model. See Fig. 6.1 for multiple interconnected routes leading to various closure models.

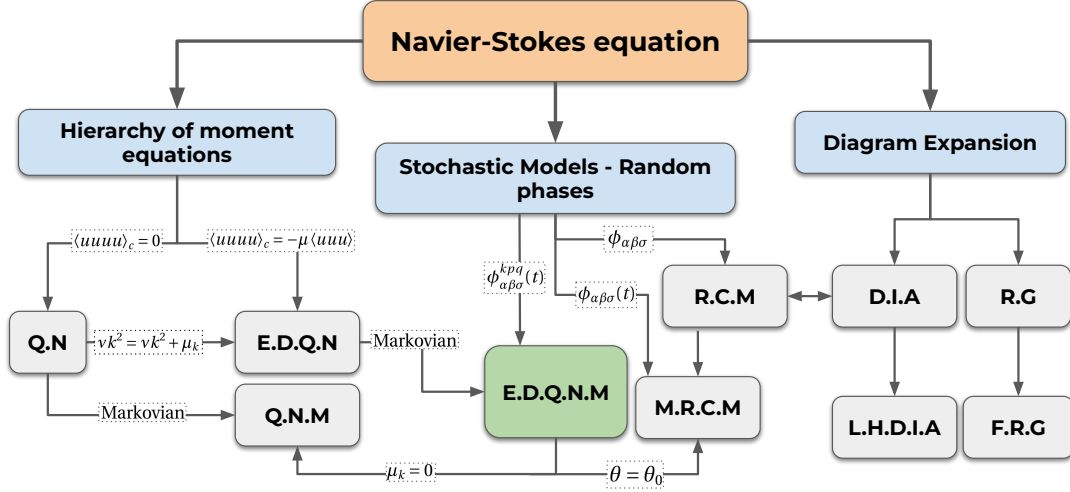


Figure 6.1: Showing various closure models stemming from the parent—Navier-Stokes equation—and the interconnecting routes. Figure adapted from an illustration in Ref. [30].

## 6.2 EDQNM-MHD Closure model

In this section, we outline the Eddy-Damped Quasi-Normal Markovian closure procedure and extend the approach to develop a generalized  $d$ -dimensional closure model for the magnetohydrodynamic turbulence. The governing MHD equations for the incompressible velocity  $\mathbf{U}$  and magnetic  $\mathbf{B}$  fields, for the unit density fluid, are (see Refs. [103, 104] for derivation)

$$\partial_t \mathbf{U}(\mathbf{x}, t) = -\nabla P - (\mathbf{U} \cdot \nabla) \mathbf{U} + (\mathbf{B} \cdot \nabla) \mathbf{B} + \nu \nabla^2 \mathbf{U}, \quad \nabla \cdot \mathbf{U} = 0 \quad (6.1a)$$

$$\partial_t \mathbf{B}(\mathbf{x}, t) = \nabla \times (\mathbf{U} \times \mathbf{B}) + \xi \nabla^2 \mathbf{B}, \quad \nabla \cdot \mathbf{B} = 0 \quad (6.1b)$$

In this study, the kinetic helicity  $h_k = \mathbf{U} \cdot \boldsymbol{\omega}$ , magnetic helicity  $h = \mathbf{A} \cdot \mathbf{B}$  ( $\mathbf{A}$  is the magnetic potential,  $\mathbf{B} = \nabla \times \mathbf{A}$ ) and cross helicity  $h_c = \mathbf{U} \cdot \mathbf{B}$  are assumed to be zero for all times.

In Fourier space, equations (6.1) can be written component-wise <sup>1</sup> as:

$$\left[ \frac{d}{dt} + \nu k^2 \right] u_\alpha(\mathbf{k}, t) = \mathcal{P}_{\alpha\rho\gamma}^{(k)} \int d\mathbf{q} \int d\mathbf{p} [u_\rho(\mathbf{q})u_\gamma(\mathbf{p}) - b_\rho(\mathbf{q})b_\gamma(\mathbf{p})] \delta(\mathbf{p} + \mathbf{q} - \mathbf{k}) \quad (6.2a)$$

$$\left[ \frac{d}{dt} + \xi k^2 \right] b_\alpha(\mathbf{k}, t) = \mathcal{C}_{\alpha\rho\gamma}^{(k)} \int d\mathbf{q} \int d\mathbf{p} [b_\rho(\mathbf{q})u_\gamma(\mathbf{p}) + b_\rho(\mathbf{p})u_\gamma(\mathbf{q})] \delta(\mathbf{p} + \mathbf{q} - \mathbf{k}) \quad (6.2b)$$

Note that for the magnetic field  $\mathbf{b}$ , the equation (6.2b) is deliberately expressed symmetrically between the modes  $\mathbf{p}$  and  $\mathbf{q}$ , for convenience. The incompressibility condition implies in spectral space,  $\mathbf{k} \cdot \mathbf{u}(\mathbf{k}) = 0$  &  $\mathbf{k} \cdot \mathbf{b}(\mathbf{k}) = 0$  respectively, and if the initial condition satisfies it, the evolution equations (6.2) retains it for all times. The projection  $\mathcal{P}^{(k)}$  and transport  $\mathcal{C}^{(k)}$  tensors defined in equations (6.2) are

$$\mathcal{P}_{\alpha\rho\gamma}^{(k)} = -\frac{l}{2} (\mathbb{P}_{\alpha\rho}^{(k)} k_\gamma + \mathbb{P}_{\alpha\gamma}^{(k)} k_\rho), \quad \mathbb{P}_{\alpha\beta}^{(k)} = \delta_{\alpha\beta} - \frac{k_\alpha k_\beta}{k^2} \quad (6.3a)$$

$$\mathcal{C}_{\alpha\rho\gamma}^{(k)} = -\frac{l}{2} (\delta_{\alpha\rho} k_\gamma - \delta_{\alpha\gamma} k_\rho) \quad (6.3b)$$

For homogeneous systems, the generalized  $n^{\text{th}}$  order spectral moment will be a function of  $n - 1$  wavevectors:

$$\mathcal{S}_{\alpha_1\alpha_2\cdots\alpha_n}^{X^{(1)}X^{(2)}\cdots X^{(n)}}(k_1, k_2, \cdots, k_{n-1}) = \left\langle X_{\alpha_1}^{(1)}(k_1) X_{\alpha_2}^{(2)}(k_2) \cdots X_{\alpha_{n-1}}^{(n-1)}(k_{n-1}) X_{\alpha_n}^{(n)} \left( -\sum_{i=1}^{n-1} k_i \right) \right\rangle \quad (6.4)$$

where the field  $X^{(i)}(k)$  can be  $u(k)$  or  $b(k)$ . For example, one of the third moment can be written as  $\mathcal{S}_{\alpha\rho\gamma}^{ubb}(k, -q) = \langle u_\alpha(k) b_\rho(-q) b_\gamma(-p) \rangle$  with  $p = k - q$ .

Using equation (6.2), we can obtain the evolution equations for the second

---

<sup>1</sup>Einstein summation convention is opted, and all indices are written in Greek to avoid confusion from Latin.

moments  $\mathcal{S}^{uu}$  and  $\mathcal{S}^{bb}$  as follows: <sup>2</sup>

$$\left[ \frac{d}{dt} + 2\nu k^2 \right] \mathcal{S}_{\alpha\beta}^{uu}(k) = \int_{\Delta_{\mathbf{k}}} \mathcal{P}_{\beta\rho\gamma}^{(-k)} \left[ \mathcal{S}_{\alpha\rho\gamma}^{uuu}(k, -q) - \mathcal{S}_{\alpha\rho\gamma}^{ubb}(k, -q) \right] + \text{c} \cdot \text{c} \Big|_{\alpha \leftrightarrow \beta} \quad (6.5a)$$

$$\left[ \frac{d}{dt} + 2\xi k^2 \right] \mathcal{S}_{\alpha\beta}^{bb}(k) = \int_{\Delta_{\mathbf{k}}} \mathcal{C}_{\beta\rho\gamma}^{(-k)} \left[ \mathcal{S}_{\alpha\rho\gamma}^{bbu}(k, -q) + \mathcal{S}_{\alpha\rho\gamma}^{bbu}(k, -p) \right] + \text{c} \cdot \text{c} \Big|_{\alpha \leftrightarrow \beta} \quad (6.5b)$$

Similarly, for the third moments, the evolution equations for  $\mathcal{S}^{uuu}$ ,  $\mathcal{S}^{ubb}$ , and  $\mathcal{S}^{bbu}$  are as follows:

$$\begin{aligned} \left[ \frac{d}{dt} + \nu(k^2 + q^2 + p^2) \right] \mathcal{S}_{\alpha\rho\gamma}^{uuu}(k, -q) &= \int d\mathbf{r} \mathcal{P}_{\alpha\mu\sigma}^{(k)} \left[ \mathcal{S}_{\rho\gamma\mu\sigma}^{uuuu}(-q, -p, r) - \mathcal{S}_{\rho\gamma\mu\sigma}^{uubb}(-q, -p, r) \right] \\ &+ \int d\mathbf{r} \mathcal{P}_{\rho\mu\sigma}^{(-q)} \left[ \mathcal{S}_{\alpha\gamma\mu\sigma}^{uuuu}(k, -p, r) - \mathcal{S}_{\alpha\gamma\mu\sigma}^{uubb}(k, -p, r) \right] \\ &+ \int d\mathbf{r} \mathcal{P}_{\gamma\mu\sigma}^{(-p)} \left[ \mathcal{S}_{\alpha\rho\mu\sigma}^{uuuu}(k, -q, r) - \mathcal{S}_{\alpha\rho\mu\sigma}^{uubb}(k, -q, r) \right] \end{aligned} \quad (6.6a)$$

$$\begin{aligned} \left[ \frac{d}{dt} + \nu k^2 + \xi(q^2 + p^2) \right] \mathcal{S}_{\alpha\rho\gamma}^{ubb}(k, -q) &= \int d\mathbf{r} \mathcal{P}_{\alpha\mu\sigma}^{(k)} \left[ \mathcal{S}_{\rho\gamma\mu\sigma}^{bbuu}(-q, -p, r) - \mathcal{S}_{\rho\gamma\mu\sigma}^{bbbb}(-q, -p, r) \right] \\ &+ 2 \int d\mathbf{r} \left[ \mathcal{C}_{\rho\mu\sigma}^{(-q)} \mathcal{S}_{\gamma\mu\alpha\sigma}^{bbuu}(-p, r, k) + \mathcal{C}_{\gamma\mu\sigma}^{(-p)} \mathcal{S}_{\rho\mu\alpha\sigma}^{bbuu}(-q, r, k) \right] \end{aligned} \quad (6.6b)$$

$$\begin{aligned} \left[ \frac{d}{dt} + \nu p^2 + \xi(k^2 + q^2) \right] \mathcal{S}_{\alpha\rho\gamma}^{bbu}(k, -q) &= \int d\mathbf{r} \mathcal{P}_{\gamma\mu\sigma}^{(-p)} \left[ \mathcal{S}_{\alpha\rho\mu\sigma}^{bbuu}(k, -q, r) - \mathcal{S}_{\alpha\rho\mu\sigma}^{bbbb}(k, -q, r) \right] \\ &+ 2 \int d\mathbf{r} \left[ \mathcal{C}_{\alpha\mu\sigma}^{(k)} \mathcal{S}_{\rho\mu\gamma\sigma}^{bbuu}(-q, r, -p) + \mathcal{C}_{\rho\mu\sigma}^{(-q)} \mathcal{S}_{\alpha\mu\gamma\sigma}^{bbuu}(k, r, -p) \right] \end{aligned} \quad (6.6c)$$

$$\begin{aligned} \left[ \frac{d}{dt} + \nu q^2 + \xi(k^2 + p^2) \right] \mathcal{S}_{\alpha\rho\gamma}^{bbu}(k, -p) &= \int d\mathbf{r} \mathcal{P}_{\gamma\mu\sigma}^{(-q)} \left[ \mathcal{S}_{\alpha\rho\mu\sigma}^{bbuu}(k, -p, r) - \mathcal{S}_{\alpha\rho\mu\sigma}^{bbbb}(k, -p, r) \right] \\ &+ 2 \int d\mathbf{r} \left[ \mathcal{C}_{\alpha\mu\sigma}^{(k)} \mathcal{S}_{\rho\mu\gamma\sigma}^{bbuu}(-p, r, -q) + \mathcal{C}_{\rho\mu\sigma}^{(-p)} \mathcal{S}_{\alpha\mu\gamma\sigma}^{bbuu}(k, r, -q) \right] \end{aligned} \quad (6.6d)$$

The second moments depend on the third moments (Eq.(6.5)), the

---

<sup>2</sup>Here  $\int_{\Delta_{\mathbf{k}}} \equiv \int d\mathbf{q} \int d\mathbf{q} \delta(\mathbf{q} + \mathbf{p} - \mathbf{k})$  and  $\text{c} \cdot \text{c}$  means *complex conjugate* and  $\alpha \leftrightarrow \beta$  implies the exchange of indices.

evolution of a third order moment depends on a fourth order moment (Eq.(6.6)). The  $n^{\text{th}}$  moment will depend on the  $(n + 1)^{\text{th}}$  moment and there is an infinite hierarchy. This is the closure problem originating in the MHD equations. In general, to tackle it, at certain level some physically acceptable assumptions have to be included in these set of equations and close down the hierarchy.

### 6.2.1 Quasi-Normality

The Quasi-Normal (QN) assumption is that the fourth order moment of the field is Gaussian in nature, or to say the fourth cumulant of the velocity moment vanishes. This would close the hierarchy of equations at the fourth moment. So the fourth-order moment in the QN approximation would bread down as:

$$\begin{aligned} \mathcal{S}_{\alpha\beta\rho\gamma}^{X^{(1)}X^{(2)}X^{(3)}X^{(4)}}(k_1, k_2, k_3) &= \mathcal{S}_{\alpha\beta}^{X^{(1)}X^{(2)}}(k_1)\mathcal{S}_{\rho\gamma}^{X^{(3)}X^{(4)}}(k_3)\delta(k_1 + k_2) + \mathcal{S}_{\alpha\rho}^{X^{(1)}X^{(3)}}(k_1)\mathcal{S}_{\beta\gamma}^{X^{(2)}X^{(4)}}(k_2)\delta(k_1 + k_3) \\ &+ \mathcal{S}_{\alpha\gamma}^{X^{(1)}X^{(4)}}(k_1)\mathcal{S}_{\beta\rho}^{X^{(2)}X^{(3)}}(k_2)\delta(k_2 + k_3) \end{aligned} \quad (6.7)$$

Note that, in this closure model the cross-correlated second moment between velocity and magnetic field is assumed to be zero:

$$\langle u_\alpha(k_1)b_\beta(k_2) \rangle = 0, \quad \forall k_1, k_2 \quad (6.8)$$

Using the QN approximation, equations (6.6) reduce to:

$$\left[ \frac{d}{dt} + \nu(k^2 + p^2 + q^2) \right] \mathcal{S}_{\alpha\rho\gamma}^{uuu}(k, -q) = 2 \left[ \mathcal{P}_{\alpha\mu\sigma}^{(k)} \mathcal{S}_{\rho\mu}^{uu}(-q) \mathcal{S}_{\gamma\sigma}^{uu}(-p) + \mathcal{P}_{\rho\mu\sigma}^{(-q)} \mathcal{S}_{\alpha\sigma}^{uu}(k) \mathcal{S}_{\gamma\mu}^{uu}(-p) \right. \\ \left. + \mathcal{P}_{\gamma\mu\sigma}^{(-p)} \mathcal{S}_{\alpha\mu}^{uu}(k) \mathcal{S}_{\rho\sigma}^{uu}(-q) \right] \quad (6.9a)$$

$$\left[ \frac{d}{dt} + \nu k^2 + \xi(q^2 + p^2) \right] \mathcal{S}_{\alpha\rho\gamma}^{bbb}(k, -q) = 2 \left[ \mathcal{C}_{\rho\mu\sigma}^{(-q)} \mathcal{S}_{\gamma\mu}^{bb}(-p) \mathcal{S}_{\alpha\sigma}^{uu}(k) + \mathcal{C}_{\gamma\mu\sigma}^{(-p)} \mathcal{S}_{\rho\mu}^{bb}(-q) \mathcal{S}_{\alpha\sigma}^{uu}(k) \right. \\ \left. - \mathcal{P}_{\alpha\mu\sigma}^{(k)} \mathcal{S}_{\rho\mu}^{bb}(-q) \mathcal{S}_{\gamma\sigma}^{bb}(-p) \right] \quad (6.9b)$$

$$\left[ \frac{d}{dt} + \nu p^2 + \xi(k^2 + q^2) \right] \mathcal{S}_{\alpha\rho\gamma}^{bbu}(k, -q) = 2 \left[ \mathcal{C}_{\alpha\mu\sigma}^{(k)} \mathcal{S}_{\rho\mu}^{bb}(-q) \mathcal{S}_{\gamma\sigma}^{uu}(-p) + \mathcal{C}_{\rho\mu\sigma}^{(-q)} \mathcal{S}_{\alpha\mu}^{bb}(k) \mathcal{S}_{\gamma\sigma}^{uu}(-p) \right. \\ \left. - \mathcal{P}_{\gamma\mu\sigma}^{(-p)} \mathcal{S}_{\alpha\mu}^{bb}(k) \mathcal{S}_{\rho\sigma}^{bb}(-q) \right] \quad (6.9c)$$

$$\left[ \frac{d}{dt} + \nu q^2 + \xi(k^2 + p^2) \right] \mathcal{S}_{\alpha\rho\gamma}^{bbu}(k, -p) = 2 \left[ \mathcal{C}_{\alpha\mu\sigma}^{(k)} \mathcal{S}_{\rho\mu}^{bb}(-p) \mathcal{S}_{\gamma\sigma}^{uu}(-q) + \mathcal{C}_{\rho\mu\sigma}^{(-p)} \mathcal{S}_{\alpha\mu}^{bb}(k) \mathcal{S}_{\gamma\sigma}^{uu}(-q) \right. \\ \left. - \mathcal{P}_{\gamma\mu\sigma}^{(-q)} \mathcal{S}_{\alpha\mu}^{bb}(k) \mathcal{S}_{\rho\sigma}^{bb}(-p) \right] \quad (6.9d)$$

Let us define the inverse of the linear operator:

$$\left[ \frac{d}{dt} + \omega \right]^{-1} = \hat{\theta}(\omega) \cdot = \int_0^t ds \cdot e^{-(t-s)\omega} \quad (6.10)$$

Now inverting the equations (6.9) and substituting it into equations (6.5) yields a closed equations for the second moment.

$$\left[ \frac{d}{dt} + 2\nu k^2 \right] \mathcal{S}_{\alpha\beta}^{uu}(k) = \int_{\Delta_k} 2\hat{\theta}(\omega_{kpq}^u) \mathcal{P}_{\beta\rho\gamma}^{(-k)} \left[ \mathcal{P}_{\alpha\mu\sigma}^{(k)} \mathcal{S}_{\rho\mu}^{uu}(-q) \mathcal{S}_{\gamma\sigma}^{uu}(-p) + \mathcal{P}_{\rho\mu\sigma}^{(-q)} \mathcal{S}_{\alpha\sigma}^{uu}(k) \mathcal{S}_{\gamma\mu}^{uu}(-p) \right. \\ \left. + \mathcal{P}_{\gamma\mu\sigma}^{(-p)} \mathcal{S}_{\alpha\mu}^{uu}(k) \mathcal{S}_{\rho\sigma}^{uu}(-q) \right] + c \cdot c \Big|_{\alpha \leftrightarrow \beta} \\ - \int_{\Delta_k} 2\hat{\theta}(\omega_{kpq}^b) \mathcal{P}_{\beta\rho\gamma}^{(-k)} \left[ \mathcal{C}_{\rho\mu\sigma}^{(-q)} \mathcal{S}_{\alpha\sigma}^{uu}(k) \mathcal{S}_{\gamma\mu}^{bb}(-p) + \mathcal{C}_{\gamma\mu\sigma}^{(-p)} \mathcal{S}_{\alpha\sigma}^{uu}(k) \mathcal{S}_{\rho\mu}^{bb}(-q) \right. \\ \left. - \mathcal{P}_{\alpha\mu\sigma}^{(k)} \mathcal{S}_{\rho\mu}^{bb}(-q) \mathcal{S}_{\gamma\sigma}^{bb}(-p) \right] + c \cdot c \Big|_{\alpha \leftrightarrow \beta} \quad (6.11a)$$

$$\left[ \frac{d}{dt} + 2\xi k^2 \right] \mathcal{S}_{\alpha\beta}^{bb}(k) = \int_{\Delta_k} 2\hat{\theta}(\omega_{pkq}^b) \mathcal{C}_{\beta\rho\gamma}^{(-k)} \left[ \mathcal{C}_{\alpha\mu\sigma}^{(k)} \mathcal{S}_{\rho\mu}^{bb}(-q) \mathcal{S}_{\gamma\sigma}^{uu}(-p) + \mathcal{C}_{\rho\mu\sigma}^{(-q)} \mathcal{S}_{\alpha\mu}^{bb}(k) \mathcal{S}_{\gamma\sigma}^{uu}(-p) \right. \\ \left. - \mathcal{P}_{\gamma\mu\sigma}^{(-p)} \mathcal{S}_{\alpha\mu}^{bb}(k) \mathcal{S}_{\rho\sigma}^{bb}(-q) \right] \\ + \int_{\Delta_k} 2\hat{\theta}(\omega_{qkp}^b) \mathcal{C}_{\beta\rho\gamma}^{(-k)} \left[ \mathcal{C}_{\alpha\mu\sigma}^{(k)} \mathcal{S}_{\rho\mu}^{bb}(-p) \mathcal{S}_{\gamma\sigma}^{uu}(-q) + \mathcal{C}_{\rho\mu\sigma}^{(-p)} \mathcal{S}_{\alpha\mu}^{bb}(k) \mathcal{S}_{\gamma\sigma}^{uu}(-q) \right. \\ \left. - \mathcal{P}_{\gamma\mu\sigma}^{(-q)} \mathcal{S}_{\alpha\mu}^{bb}(k) \mathcal{S}_{\rho\sigma}^{bb}(-p) \right] + c \cdot c \Big|_{\alpha \leftrightarrow \beta} \quad (6.11b)$$

The frequencies defined in the operators  $\hat{\theta}$  in equations (6.11) are:

$$\begin{aligned}\omega_{kpq}^u &= \omega_k^u + \omega_p^u + \omega_q^u, & \omega_k^u &= \nu k^2 \\ \omega_{kpq}^b &= \omega_k^u + \omega_p^b + \omega_q^b, & \omega_k^b &= \xi k^2\end{aligned}\quad (6.12)$$

Equations (6.11) are the closure equations for the second moments  $\mathcal{S}^{uu}, \mathcal{S}^{bb}$  obtained from the QN approximation. Under the assumption of isotropy, the second moment  $\mathcal{S}^{XX}(k)$  becomes directly proportional to the energy of the the mode  $\mathcal{U}^X(k) = \langle X(k)X(-k) \rangle$

$$\mathcal{S}_{\alpha\beta}^{XX}(k) = \frac{1}{(d-1)} \mathbb{P}_{\alpha\beta}^{(k)} \mathcal{U}^X(k) \quad (6.13)$$

The Quasi-Normal closure equations (6.11) under isotropy, in terms of  $\mathcal{U}^X(k)$  can be written as (Refer to Appendix B.1 for detailed derivation)

$$\begin{aligned}\left[ \frac{d}{dt} + 2\nu k^2 \right] \mathcal{U}^u(k) &= \frac{4}{(d-1)^2} \int_{\Delta_{\mathbf{k}}} \hat{\theta}(\omega_{kpq}^u) \mathcal{P}_{\alpha\rho\gamma}^{(k)} \left[ -\mathcal{P}_{\alpha\mu\sigma}^{(k)} \mathbb{P}_{\rho\mu}^{(q)} \mathbb{P}_{\gamma\sigma}^{(p)} \mathcal{U}^u(q) \mathcal{U}^u(p) \right. \\ &\quad \left. + \mathcal{P}_{\rho\mu\sigma}^{(q)} \mathbb{P}_{\alpha\sigma}^{(k)} \mathbb{P}_{\gamma\mu}^{(p)} \mathcal{U}^u(k) \mathcal{U}^u(p) + \mathcal{P}_{\gamma\mu\sigma}^{(p)} \mathbb{P}_{\alpha\mu}^{(k)} \mathbb{P}_{\rho\sigma}^{(q)} \mathcal{U}^u(k) \mathcal{U}^u(q) \right] \\ &- \frac{4}{(d-1)^2} \int_{\Delta_{\mathbf{k}}} \hat{\theta}(\omega_{kpq}^b) \mathcal{P}_{\alpha\rho\gamma}^{(k)} \left[ \mathcal{P}_{\alpha\mu\sigma}^{(k)} \mathbb{P}_{\rho\mu}^{(q)} \mathbb{P}_{\gamma\sigma}^{(p)} \mathcal{U}^b(q) \mathcal{U}^b(p) \right. \\ &\quad \left. + \mathcal{C}_{\rho\mu\sigma}^{(q)} \mathbb{P}_{\alpha\sigma}^{(k)} \mathbb{P}_{\gamma\mu}^{(p)} \mathcal{U}^u(k) \mathcal{U}^b(p) + \mathcal{C}_{\gamma\mu\sigma}^{(p)} \mathbb{P}_{\alpha\mu}^{(k)} \mathbb{P}_{\rho\sigma}^{(q)} \mathcal{U}^u(k) \mathcal{U}^b(q) \right]\end{aligned}\quad (6.14a)$$

$$\begin{aligned}\left[ \frac{d}{dt} + 2\xi k^2 \right] \mathcal{U}^b(k) &= \frac{4}{(d-1)^2} \int_{\Delta_{\mathbf{k}}} \hat{\theta}(\omega_{pqk}^b) \mathcal{C}_{\alpha\rho\gamma}^{(k)} \left[ -\mathcal{P}_{\gamma\mu\sigma}^{(p)} \mathbb{P}_{\alpha\mu}^{(k)} \mathbb{P}_{\rho\sigma}^{(q)} \mathcal{U}^b(k) \mathcal{U}^b(q) \right. \\ &\quad \left. - \mathcal{C}_{\alpha\mu\sigma}^{(k)} \mathbb{P}_{\rho\mu}^{(q)} \mathbb{P}_{\gamma\sigma}^{(p)} \mathcal{U}^b(q) \mathcal{U}^u(p) + \mathcal{C}_{\rho\mu\sigma}^{(q)} \mathbb{P}_{\alpha\mu}^{(k)} \mathbb{P}_{\gamma\sigma}^{(p)} \mathcal{U}^b(k) \mathcal{U}^u(p) \right] \\ &+ \frac{4}{(d-1)^2} \int_{\Delta_{\mathbf{k}}} \hat{\theta}(\omega_{qkp}^b) \mathcal{C}_{\alpha\rho\gamma}^{(k)} \left[ -\mathcal{P}_{\gamma\mu\sigma}^{(q)} \mathbb{P}_{\alpha\mu}^{(k)} \mathbb{P}_{\rho\sigma}^{(p)} \mathcal{U}^b(k) \mathcal{U}^b(p) \right. \\ &\quad \left. - \mathcal{C}_{\alpha\mu\sigma}^{(k)} \mathbb{P}_{\rho\mu}^{(p)} \mathbb{P}_{\gamma\sigma}^{(q)} \mathcal{U}^b(p) \mathcal{U}^u(q) + \mathcal{C}_{\rho\mu\sigma}^{(p)} \mathbb{P}_{\alpha\mu}^{(k)} \mathbb{P}_{\gamma\sigma}^{(q)} \mathcal{U}^b(k) \mathcal{U}^u(q) \right]\end{aligned}\quad (6.14b)$$

Now this tedious expression in the equations (6.14) can be simplified by

defining geometric coefficients:

$$a_{kqp} = a_{kpq} = -\frac{1}{k^2} \mathcal{P}_{\alpha\rho\gamma}^{(k)} \mathcal{P}_{\alpha\mu\sigma}^{(k)} \mathbb{P}_{\rho\mu}^{(q)} \mathbb{P}_{\gamma\sigma}^{(p)} \quad (6.15a)$$

$$b_{kpq} = -\frac{2}{k^2} \mathcal{P}_{\mu\rho\gamma}^{(k)} \mathcal{P}_{\gamma\mu\sigma}^{(p)} \mathbb{P}_{\rho\sigma}^{(q)} \quad (6.15b)$$

$$c_{kpq} = \frac{2}{k^2} \mathcal{P}_{\mu\rho\gamma}^{(k)} \mathcal{C}_{\gamma\mu\sigma}^{(p)} \mathbb{P}_{\rho\sigma}^{(q)} \quad (6.15c)$$

$$g_{kqp} = g_{kpq} = -\frac{2}{k^2} \mathcal{C}_{\alpha\rho\gamma}^{(k)} \mathcal{C}_{\alpha\mu\sigma}^{(k)} \mathbb{P}_{\rho\mu}^{(q)} \mathbb{P}_{\gamma\sigma}^{(p)} \quad (6.15d)$$

$$h_{kpq} = -\frac{2}{k^2} \mathcal{C}_{\mu\rho\gamma}^{(k)} \mathcal{C}_{\rho\mu\sigma}^{(p)} \mathbb{P}_{\gamma\sigma}^{(q)} \quad (6.15e)$$

With the use of the geometric coefficients defined above in equations (6.15), we can write express the equations (6.14) as:

$$\begin{aligned} \left[ \frac{d}{dt} + 2\nu k^2 \right] \mathcal{U}^u(k) &= \frac{2k^2}{(d-1)^2} \int_{\Delta_{\mathbf{k}}} \left( \hat{\theta}(\omega_{kpq}^u) \left[ 2a_{kqp} \mathcal{U}^u(p) \mathcal{U}^u(q) - (b_{kqp} \mathcal{U}^u(p) + b_{kpq} \mathcal{U}^u(q)) \mathcal{U}^u(k) \right] \right. \\ &\quad \left. + \hat{\theta}(\omega_{kpq}^b) \left[ 2a_{kqp} \mathcal{U}^b(p) \mathcal{U}^b(q) - (c_{kqp} \mathcal{U}^b(p) + c_{kpq} \mathcal{U}^b(q)) \mathcal{U}^u(k) \right] \right) \end{aligned} \quad (6.16a)$$

$$\begin{aligned} \left[ \frac{d}{dt} + 2\xi k^2 \right] \mathcal{U}^b(k) &= \frac{2k^2}{(d-1)^2} \int_{\Delta_{\mathbf{k}}} \left( \hat{\theta}(\omega_{pqk}^b) \left[ -\frac{p^2}{k^2} c_{pkq} \mathcal{U}^b(k) \mathcal{U}^b(q) + (g_{kqp} \mathcal{U}^b(q) - h_{kqp} \mathcal{U}^b(k)) \mathcal{U}^u(p) \right] \right. \\ &\quad \left. + \hat{\theta}(\omega_{qkp}^b) \left[ -\frac{q^2}{k^2} c_{qkp} \mathcal{U}^b(k) \mathcal{U}^b(p) + (g_{kpq} \mathcal{U}^b(p) - h_{kpq} \mathcal{U}^b(k)) \mathcal{U}^u(q) \right] \right) \end{aligned} \quad (6.16b)$$

These geometric coefficients purely depend on the angle of triangle formed by  $\mathbf{k}, \mathbf{p}, \mathbf{q}$ , and can be expressed in terms of the cosines of angles formed in the triangle. The notation we follow is same as in [99, 101, 272]. For the triangle formed by the sides of length  $k, p, q$  the angles opposite to their sides are  $\alpha, \beta, \gamma$  and

their cosines are  $x, y, z$  respectively.

$$x^2 + y^2 + z^2 = 1 - 2xyz$$

$$a_{kpq} = \frac{1}{2} \left( 1 - 2y^2z^2 - xyz + \frac{(d-3)}{2} [2 - y^2 - z^2] \right) \quad (6.17a)$$

$$b_{kpq} = \frac{p}{k} \left( z^3 + xy + \frac{(d-3)}{2} [z + xy] \right) \quad (6.17b)$$

$$c_{kpq} = \frac{p}{k} \left( z[1 - y^2] + \frac{(d-3)}{2} [z + xy] \right) \quad (6.17c)$$

$$g_{kpq} = 1 + xyz + \frac{(d-3)}{2} [2 - y^2 - z^2] \quad (6.17d)$$

$$h_{kpq} = \frac{p}{2k} ((d-1)[z + xy]) \quad (6.17e)$$

Denoting the evolution equation (6.16) for spectral energies as

$$\left[ \frac{d}{dt} + 2\nu k^2 \right] \mathcal{U}^X = \int_{\Delta_{\mathbf{k}}} \mathcal{T}^X(\Delta_k) \quad (6.18)$$

where  $\mathcal{T}^X(\Delta_k)$  is the transfer integrand for the field  $X$  arising from a particular triad  $\mathbf{k}, \mathbf{p}, \mathbf{q}$ . The constructed integrand depends only the geometry of the triad, neither the absolute position nor its orientation, hence allowing us to integrate out all the extra degrees of freedom in such integral  $\int_{\Delta_{\mathbf{k}}}$  (Refer to Appendix B.2 for a detailed derivation).

$$\left[ \frac{d}{dt} + 2\nu k^2 \right] \mathcal{U}^X = S_{d-2} \int_{\Delta_k} dq dp \left( \frac{pq}{k} \right)^{d-2} (1 - x^2)^{\frac{(d-3)}{2}} \mathcal{T}^X(\Delta_k) \quad (6.19)$$

Here  $S_d$  is the solid angle of a  $d$ -dimensional sphere. Now we have to integrate equation (6.19) over the  $p - q$  plane that can form a triangle with a side of length  $k = |\mathbf{k}|$ . By Triangle inequality, the region would involve  $p + q < k < |p - q|$ , as shown in figure 6.2, for every  $k$ . Isotropy implies that the energy spectrum and spectral energy are related by

$$\mathcal{U}^X(k) = \frac{2E^X(k)}{k^{d-1}S_{d-1}} \quad (6.20)$$

Now equation (6.16) in terms of  $E^u(k), E^b(k)$  using the reduced integral in

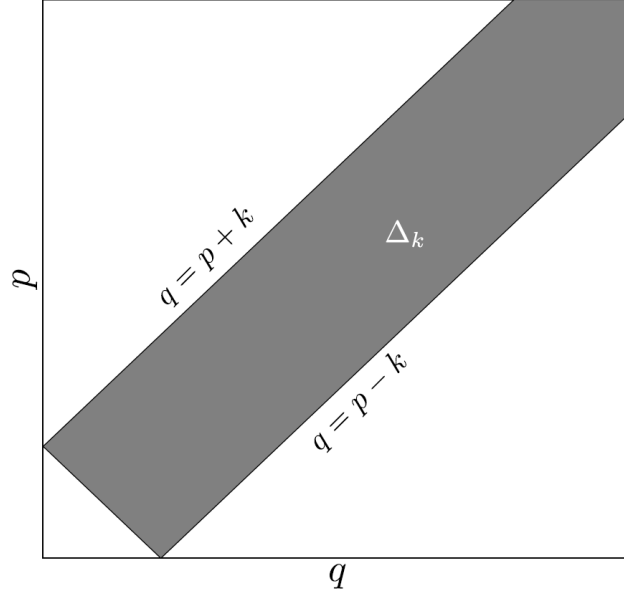


Figure 6.2: Showing the area of integration in the  $p - q$  plane, for a given  $k$ , that satisfies the triangle inequality for the sides  $k, p, q$ , hence contributing to the integral in the transfer term  $\mathcal{T}^X$

equation (6.19) becomes

$$\left[ \frac{d}{dt} + 2\nu k^2 \right] E^u(k) = 8K_d \int_{\Delta_k} dq dp \left[ \mathcal{T}_u^{uu}(\Delta_k) + \mathcal{T}_u^{bb}(\Delta_k) + \mathcal{T}_u^{ub}(\Delta_k) \right] W_d(\Delta_k) \quad (6.21a)$$

$$\mathcal{T}_u^{uu}(\Delta_k) = \hat{\theta}(\omega_{kpq}^u) \frac{k}{pq} \left[ a_{kpq} k^{d-1} E^u(p) E^u(q) - \frac{1}{2} (b_{kpq} p^{d-1} E^u(q) + b_{kqp} q^{d-1} E^u(p)) E^u(k) \right] \quad (6.21b)$$

$$\mathcal{T}_u^{bb}(\Delta_k) = \hat{\theta}(\omega_{kpq}^b) \frac{k}{pq} a_{kpq} k^{d-1} E^b(p) E^b(q) \quad (6.21c)$$

$$\mathcal{T}_u^{ub}(\Delta_k) = -\frac{1}{2} \hat{\theta}(\omega_{kpq}^b) \frac{k}{pq} (c_{kpq} p^{d-1} E^b(q) + c_{kqp} q^{d-1} E^b(p)) E^u(k) \quad (6.21d)$$

$$\left[ \frac{d}{dt} + 2\xi k^2 \right] E^b(k) = 8K_d \int_{\Delta_k} dq dp \left[ \mathcal{T}_b^{ub}(\Delta_k) + \mathcal{T}_b^{bb}(\Delta_k) \right] W_d(\Delta_k) \quad (6.22a)$$

$$\begin{aligned} \mathcal{T}_b^{ub}(\Delta_k) &= \frac{1}{2} \hat{\theta}(\omega_{pqk}^b) \frac{k}{pq} \left[ g_{kqp} k^{d-1} E^b(q) - h_{kqp} q^{d-1} E^b(k) \right] E^u(p) \\ &+ \frac{1}{2} \hat{\theta}(\omega_{qkp}^b) \frac{k}{pq} \left[ g_{kqp} k^{d-1} E^b(p) - h_{kqp} p^{d-1} E^b(k) \right] E^u(q) \end{aligned} \quad (6.22b)$$

$$\mathcal{T}_b^{bb}(\Delta_k) = -\frac{1}{2} \frac{k}{pq} \left[ \hat{\theta}(\omega_{pqk}^b) \frac{p^2}{k^2} c_{pkq} p^{d-1} E^b(k) E^b(q) + \hat{\theta}(\omega_{qkp}^b) \frac{q^2}{k^2} c_{qkp} q^{d-1} E^b(k) E^b(p) \right] \quad (6.22c)$$

The dimensional pre-factor  $K_d$ , and the triad weightage term  $W_d(\Delta_k)$  in equations (6.21) & (6.22) are,

$$K_d = \frac{1}{(d-1)^2} \frac{S_{d-2}}{S_{d-1}}, \quad S_{d-1} = \frac{2\pi^{d/2}}{\Gamma(d-1)} \quad (6.23a)$$

$$W_d(\Delta_k) = \left( \frac{(1-x^2)}{k^2} \right)^{(d-3)/2} = \left( \frac{\sin^2 x}{k^2} \right)^{(d-3)/2} \quad (6.23b)$$

All the coefficients are not independent of each other, the following identities are trivial to prove.

$$2a_{kpq} = b_{kpq} + b_{kqp} \quad (6.24a)$$

$$2a_{kpq} = c_{kpq} + c_{kqp} \quad (6.24b)$$

$$k^2 b_{kpq} = p^2 b_{pkq} \quad (6.24c)$$

$$k^2 h_{kpq} = p^2 h_{pkq} \quad (6.24d)$$

$$g_{kpq} = h_{kpq} + \frac{q^2}{k^2} c_{qkp} \quad (6.24e)$$

$$q^4 c_{qkp}^{(3)} = k^4 c_{kqp}^{(3)} \quad (6.24f)$$

$$\left( p^2 c_{kqp} + q^2 c_{kpq} \right) = \left( p^2 h_{kqp} + q^2 h_{kpq} \right) \frac{(d-2)}{(d-1)} \quad (6.24g)$$

$$k^2 a_{kpq}^{(2)} = p^2 b_{kpq}^{(2)} + q^2 b_{kqp}^{(2)} \quad (6.24h)$$

$$k^2 c_{kqp}^{(2)} = q^2 \left( h_{pqk}^{(2)} - h_{qpq}^{(2)} \right) \quad (6.24i)$$

Here the superscripts (2), (3) denote the particular dimension. Using the relations in equations (6.24), we can rewrite  $a_{kpq}$  and  $g_{kpq}$  in the transfer integrands

in equation (6.21) and (6.22) in terms of  $b_{kpq}$ ,  $c_{kpq}$  &  $h_{kpq}$ . Further the transfer integrands for the triad  $\Delta_k$  can then be shown with the symmetry between the contributions from  $p$  and  $q$ .

$$\begin{aligned}
 \mathcal{T}_u^{uu}(\Delta_k) &= \frac{1}{2} \hat{\theta}(\omega_{kpq}^u) \frac{k}{pq} b_{kpq} [k^{d-1} E^u(p) - p^{d-1} E^u(k)] E^u(q) + p \leftrightarrow q \\
 \mathcal{T}_u^{bb}(\Delta_k) &= \frac{1}{2} \hat{\theta}(\omega_{kpq}^b) \frac{k}{pq} c_{kpq} k^{d-1} E^b(p) E^b(q) + p \leftrightarrow q \\
 \mathcal{T}_u^{ub}(\Delta_k) &= -\frac{1}{2} \hat{\theta}(\omega_{kpq}^b) \frac{k}{pq} c_{kpq} p^{d-1} E^u(k) E^b(q) + p \leftrightarrow q \\
 \mathcal{T}_b^{ub}(\Delta_k) &= \frac{1}{2} \hat{\theta}(\omega_{qkp}^b) \frac{k}{pq} h_{kpq} [k^{d-1} E^b(p) - p^{d-1} E^b(k)] E^u(q) \\
 &\quad + \frac{1}{2} \hat{\theta}(\omega_{pqk}^b) \frac{p}{kq} c_{pkq} k^{d-1} E^u(p) E^b(q) + p \leftrightarrow q \\
 \mathcal{T}_b^{bb}(\Delta_k) &= -\frac{1}{2} \hat{\theta}(\omega_{pqk}^b) \frac{p}{kq} c_{pkq} p^{d-1} E^b(k) E^b(q) + p \leftrightarrow q
 \end{aligned} \tag{6.25}$$

In equations (6.25), the  $p \leftrightarrow q$  implies a repetition of the previous expression with the exchange of the  $p$  and  $q$  in the arguments. If we denote the triad  $\Delta_k$  as  $k, p, q$  and  $\Delta_k^{(c)}$  as  $k, q, p$  the complementary triad, then clearly  $\mathcal{T}_{X_1}^{X_2 X_3}(\Delta_k) = \mathcal{T}_{X_1}^{X_2 X_3}(\Delta_k^{(c)})$ . Hence, we can define an asymmetric transfer integrand  $\mathbb{T}_{X_1}^{X_2 X_3}(k, p, q)$  that satisfies

$$\mathcal{T}_{X_1}^{X_2 X_3}(\Delta_k) = \frac{1}{2} \mathbb{T}_{X_1}^{X_2 X_3}(k, p, q) + \frac{1}{2} \mathbb{T}_{X_1}^{X_2 X_3}(k, q, p) \tag{6.26}$$

and replace the transfer integrand as  $\mathbb{T}_{X_1}^{X_2 X_3}(k, p, q)$  in equations (6.25). The  $d$ -dimensional Quasi-Normal closure model for the magnetohydrodynamics

equations are

$$\left[ \frac{d}{dt} + 2\nu k^2 \right] E^u(k, t) = 8K_d \int_{\Delta_k} dq dp \left[ \mathbb{T}_u^{uu}(k, p, q) + \mathbb{T}_u^{bb}(k, p, q) + \mathbb{T}_u^{ub}(k, p, q) \right] W_d(\Delta_k) \quad (6.27a)$$

$$\left[ \frac{d}{dt} + 2\xi k^2 \right] E^b(k, t) = 8K_d \int_{\Delta_k} dq dp \left[ \mathbb{T}_b^{ub}(k, p, q) + \mathbb{T}_b^{bb}(k, p, q) \right] W_d(\Delta_k) \quad (6.27b)$$

$$\mathbb{T}_u^{uu}(k, p, q) = \hat{\boldsymbol{\theta}}(\omega_{kpq}^u) \frac{k}{pq} b_{kpq} \left[ k^{d-1} E^u(p) - p^{d-1} E^u(k) \right] E^u(q) \quad (6.27c)$$

$$\mathbb{T}_u^{bb}(k, p, q) = \hat{\boldsymbol{\theta}}(\omega_{kpq}^b) \frac{k}{pq} c_{kpq} k^{d-1} E^b(p) E^b(q) \quad (6.27d)$$

$$\mathbb{T}_u^{ub}(k, p, q) = -\hat{\boldsymbol{\theta}}(\omega_{kpq}^b) \frac{k}{pq} c_{kpq} p^{d-1} E^u(k) E^b(q) \quad (6.27e)$$

$$\begin{aligned} \mathbb{T}_b^{ub}(k, p, q) &= \hat{\boldsymbol{\theta}}(\omega_{qkp}^b) \frac{k}{pq} h_{kpq} \left[ k^{d-1} E^b(p) - p^{d-1} E^b(k) \right] E^u(q) \\ &\quad + \hat{\boldsymbol{\theta}}(\omega_{pqk}^b) \frac{p}{kq} c_{pkq} k^{d-1} E^u(p) E^b(q) \end{aligned} \quad (6.27f)$$

$$\mathbb{T}_b^{bb}(k, p, q) = -\hat{\boldsymbol{\theta}}(\omega_{pqk}^b) \frac{p}{kq} c_{pkq} p^{d-1} E^b(k) E^b(q) \quad (6.27g)$$

This is a closed set of integro-differential equations, that can be solved numerically. Note that the operators  $\hat{\boldsymbol{\theta}}(\omega_{kpq}^u)$ ,  $\hat{\boldsymbol{\theta}}(\omega_{kpq}^b)$  involve time integrals, as defined in equation (6.10). This QN model (Eqs.(6.27)) respects the conservation laws that the original PDE has. The sum of kinetic and magnetic energy is conserved for the ideal fluid, that is  $\nu = \xi = 0$ . Particularly, in two-dimensions, the net magnetic potential is conserved and for a pure kinetic model ( $\mathbf{B} = 0$ ) the enstrophy remains conserved. Refer Appendix B.3 for the detailed proof.

## 6.2.2 Eddy-Damping

In this subsection, we would describe two further approximations that were made in the original EDQNM model [10, 30, 94, 95] called addition of a damping time-scale for the third moment–eddy damping rate and the Markovianization of the third-order moments. Later, we would extend it to the MHD formulation as well. Although the Quasi-Normal closure model is an approximated version of the Navier-Stokes equation, assuming Gaussian moments at the fourth order,

it fails to capture the turbulent behaviour for the spectrum obeying K41 theory. Rather earlier numerical simulations suggested the possibility of negative energy spectra, which is physically unrealizable. Orszag identified that the reason for this anomalous behaviour of the Quasi-Normal model is the high build-up for the third-order moments. To rectify it, a damping action is to be given to saturate the behaviour of the third-order moments.

Defining an inverse time-scale  $\mu_{kpq}$  for the triad  $k, p, q$  for the third moments:

$$\left[ \frac{d}{dt} + \nu(k^2 + p^2 + q^2) + \mu_{kpq} \right] \langle uuu \rangle = \langle uu \rangle \langle uu \rangle$$

$$\mu_{kpq} = \mu_k + \mu_p + \mu_q \quad (6.28)$$

The damping time-scale must originate purely from the spectrum, thus from dimensional grounds we can formulate:

$$\mu_k \approx \left[ k^3 E^u(k) \right]^{\frac{1}{2}} \quad (6.29)$$

But this definition provides a decreasing function of  $k$ , thus for high wavenumbers there is essentially no-damping. Later Frisch and Pouquet [97] suggested the modification as follows,

$$\mu_k = \alpha_d \left[ \int_0^k dp p^2 E^u(p) \right]^{\frac{1}{2}} \quad (6.30)$$

which is an increasing function of  $k$  and represents the average deformation rate of eddies of size  $k^{-1}$  by larger eddies. There is a free parameter  $\alpha_d$  in this definition of the eddy-damping rate  $\mu_k$ , which can be fixed to get the correct Kolmogorov constant  $C_d$ , in  $d$ -dimensions, for the kinetic energy spectrum  $E(k) = C_d k^{-5/3} \epsilon^{2/3}$ .

In the same spirit, for the EDQNM-MHD model, one can define an eddy-damping timescale from the magnetic spectrum

$$\mu_k = \alpha_d \left[ \int_0^k dp p^2 E^b(p) \right]^{\frac{1}{2}} \quad (6.31)$$

While damping rates given in equations (6.30) and (6.31) models for the nonlinear scrambling of the flow. The magnetic field equations have an additional timescale originating from the Alfvén waves [263]. Hence, introducing another term for the magnetic eddy-damping timescale to include the effect of Alfvén waves, results in

$$\mu_k = \alpha_d \left[ \int_0^k dp p^2 E^b(p) \right]^{\frac{1}{2}} + \sqrt{\frac{2}{3}} \left( \int_0^k dp E^b(p) \right)^{\frac{1}{2}} \quad (6.32)$$

The coefficient  $\sqrt{2/3}$  in equation (6.32) comes from an explicit calculation of Alfvén timescale for the Gaussian large-scale magnetic fields [99]. It is checked that the omission of the Alfvén wave term would affect the model dynamics severely.

So, the final timescales that act linearly on the third order moments for the kinetic and magnetic cases, for the wavenumber  $k$  are:

$$\begin{aligned} \omega_k^u &= \nu k^2 + \alpha_d \left[ \int_0^k dp p^2 E^V(p) \right]^{\frac{1}{2}} \\ \omega_k^b &= \xi k^2 + \alpha_d \left[ \int_0^k dp p^2 E^b(p) \right]^{\frac{1}{2}} + \sqrt{\frac{2}{3}} \left( \int_0^k dp E^b(p) \right)^{\frac{1}{2}} \end{aligned} \quad (6.33)$$

### 6.2.3 Markovianization

Even after adding this eddy-damping timescale to the third order moment, the system of EDQN equations does not guarantee a positive energy spectrum always. Orszag suggested a further modification [95], called the *Markovianization*, which assumes that the third-order moments to be slowly varying as compared to the timescale in  $\hat{\theta}(\omega_{kpq}^u)$ . This allows the time integral in  $\hat{\theta}(\omega_{kpq}^u)$  to be computed explicitly, leading to the simplification:

$$\hat{\theta}(\omega_{kpq}^u) = \int_0^t ds \exp(-\omega_{kpq}^u(t-s)) = \frac{1 - \exp(-\omega_{kpq}^u t)}{\omega_{kpq}^u} \quad (6.34)$$

Further in the large  $t$  limit, it becomes  $\hat{\theta}(\omega_{kpq}^u) = 1/\omega_{kpq}^u \equiv \theta_{kpq}^u$  and  $\hat{\theta}(\omega_{kpq}^b) = 1/\omega_{kpq}^b \equiv \theta_{kpq}^b$ . This establishes an instantaneous relationship between third and

second order moments, by forgetting the history, hence Markovian.

Now the final set of equations for our EDQNM-MHD model are given below. Since the entire evolution equation is large and tedious, we present it in parts, with sub-sequent definitions for more clarity. The evolution of the energy spectrum (both kinetic and magnetic case) depends on a linear damping term (determined by the viscosity  $\nu$  and diffusivity  $\xi$  respectively) and a non-linear transfer term.

$$\frac{d}{dt} E^u(k, t) = \mathbb{T}^u(k, t) - 2\nu k^2 E^u(k, t) \quad (6.35a)$$

$$\frac{d}{dt} E^b(k, t) = \mathbb{T}^b(k, t) - 2\xi k^2 E^b(k, t) \quad (6.35b)$$

It is extremely useful to study how the kinetic energy and magnetic energy spectrum interacts in the transfer terms. In order to do that, divide the contributions to the transfer terms as *self* and *coupled*.

$$\mathbb{T}^u(k) = \mathbb{T}_{(s)}^u(k) + \mathbb{T}_{(c)}^u(k) \quad (6.36a)$$

$$\mathbb{T}^b(k) = \mathbb{T}_{(s)}^b(k) + \mathbb{T}_{(c)}^b(k) \quad (6.36b)$$

Here the subscripts (s) and (c) stands for self and coupled. The self and coupling transfer terms are defined as:

$$\mathbb{T}_{(s)}^u(k) = 8K_d \int_{\Delta_k} dq dp W_d(\Delta_k) \theta_{kpq}^u \frac{k}{pq} b_{kpq} \left[ k^{d-1} E^u(p) - p^{d-1} E^u(k) \right] E^u(q) \quad (6.37a)$$

$$\mathbb{T}_{(c)}^u(k) = 8K_d \int_{\Delta_k} dq dp W_d(\Delta_k) \theta_{kpq}^b \frac{k}{pq} c_{kpq} \left[ k^{d-1} E^b(p) - p^{d-1} E^u(k) \right] E^b(q) \quad (6.37b)$$

$$\mathbb{T}_{(s)}^b(k) = 8K_d \int_{\Delta_k} dq dp W_d(\Delta_k) \theta_{qkp}^b \frac{k}{pq} h_{kpq} \left[ k^{d-1} E^b(p) - p^{d-1} E^b(k) \right] E^u(q) \quad (6.37c)$$

$$\mathbb{T}_{(c)}^b(k) = 8K_d \int_{\Delta_k} dq dp W_d(\Delta_k) \theta_{pqk}^b \frac{p}{kq} c_{pkq} \left[ k^{d-1} E^u(p) - p^{d-1} E^b(k) \right] E^b(q) \quad (6.37d)$$

Basically, the  $\mathbb{T}_{(s)}^u(k)$  exchanges kinetic energy from other wavenumbers into  $k$ , and in net it keeps the total kinetic energy constant, that is  $\int_0^\infty dk \mathbb{T}_{(s)}^u(k) = 0$ . Similarly, self transfer term for the magnetic spectrum exchanges magnetic energy between various modes obeying  $\int_0^\infty dk \mathbb{T}_{(s)}^b(k) = 0$ . But it has a weight

from the kinetic spectrum, with  $E^u = 0$ , this self transfer would vanish. These follows directly from the properties in equations (6.24c) and (6.24d) of the geometric coefficients  $b$  and  $h$  respectively. The coupling terms  $\mathbb{T}_{(c)}^b, \mathbb{T}_{(c)}^u$  transfer energy between the kinetic and magnetic spectrum, but keeping the net energy constant, that is  $\int_0^\infty dk (\mathbb{T}_{(c)}^u + \mathbb{T}_{(c)}^b) = 0$ .

In the context of the dynamo problem, we can further divide the magnetic interaction terms into linear and non-linear terms as follows,

$$\mathbb{T}_{(c)}^b(k) = \mathbb{T}_{(c,NL)}^b(k) + \mathbb{T}_{(c,L)}^b(k)$$

$$\mathbb{T}_{(c,NL)}^b(k) = -8K_d \int_{\Delta_k} dq dp W_d(\Delta_k) \theta_{pqk}^b \frac{p}{kq} c_{pkq} p^{d-1} E^b(k) E^b(q) \quad (6.38a)$$

$$\mathbb{T}_{(c,L)}^b(k) = 8K_d \int_{\Delta_k} dq dp W_d(\Delta_k) \theta_{pqk}^b \frac{p}{kq} c_{pkq} k^{d-1} E^u(p) E^b(q) \quad (6.38b)$$

so that at the initial time of studying the dynamo effect where  $E^b(k) \lll E^u(k)$  the non-linear (quadratic) term can be neglected.

Coming to the other terms defined in the equation (6.37). The transfer terms are associated with the set of timescales  $\theta_{kpq}^u, \theta_{kpq}^b$ , for every triad  $(k, p, q)$ , emerging from the eddy-damping approximation and Markovian assumption. The timescales are inverse of sum of frequencies from each wavenumber in the triad:

$$\theta_{kpq}^u = \frac{1}{\omega_k^u(k) + \omega_p^u(p) + \omega_q^u(q)} \quad (6.39a)$$

$$\theta_{kpq}^b = \frac{1}{\omega_k^b(k) + \omega_p^b(p) + \omega_q^b(q)} \quad (6.39b)$$

The  $\omega_k^u$  and  $\omega_k^b$  are defined in the equation (6.33). As for the free parameter  $\alpha_d$  defined in them is considered, it affects the triadic interactions quantitatively not qualitatively. In  $d = 3$  dimensions, if the pure EDQNM spectrum must match with results from the direct numerical simulations or experiments, then to get the same Kolmogorov constant, that is  $C_3 = 1.72$ , we have to choose a value of  $\alpha_3 = 0.49$ . One can show that  $C_3 \approx 2.75\alpha_3^{2/3}$ , or even a general result for  $d$ -dimensions. From the study of  $d$ -dimensional EDQNM model in the reference. [272], the constant

$C_d$  values and the  $\alpha_d(C_d)$  relations for different dimensions are provided. Finally, the dimensional prefactor  $K_d$ , and the triad weightage term  $W_d(\Delta_k)$  are given in equation (6.23).

### 6.2.4 Special cases

In the  $d = 3$  case, the EDQNM-MHD model described above reduces to the ones studied in the references [101]. Note the special symmetry in equation (6.24) for  $d = 3$  along with  $K_3 = 1/8$  and  $W_3 = 1$  that simplifies the equation. Similarly, for  $d = 2$  case, which was modeled and studied in reference [100] agrees with our general case on substituting  $d = 2$ . To obtain the pure kinetic EDQNM model in  $d$ -dimensions, as presented in the reference [272], one has to substitute  $E^b(k) = 0, \forall k$  in our model. Although in references [99–101] (where  $d = 2, 3$  are studied), the eddy-damping time scale is chosen uniformly for both kinetic and magnetic case:

$$\omega_k^u = \omega_k^b = (\nu + \xi)k^2 + \alpha \left[ \int_0^k dp p^2 (E^u(p) + E^b(p)) \right]^{\frac{1}{2}} + \sqrt{\frac{2}{3}} \left( \int_0^k dp E^b(p) \right)^{\frac{1}{2}} \quad (6.40)$$

## 6.3 Dynamo Problem in the EDQNM-MHD Framework

Since the dynamo problem corresponds to the question of excitation and sustainment of magnetic field in an electrically conducting fluids in turbulence. In the EDQNM-MHD framework, the dynamo action can be considered as the stable growth of the net magnetic energy of the system, injected arbitrarily small initially, and ability to maintain it steadily with the aid from the kinetic energy.

Denoting the net kinetic and magnetic energy is denoted as:

$$\mathcal{E}^u = \int_0^\infty dk E^u(k) \quad (6.41)$$

$$\mathcal{E}^b = \int_0^\infty dk E^b(k) \quad (6.42)$$

Theoretically one can define the growth rate of the net magnetic energy, for initial times (in the  $E^b \ll E^u$  limit), from the coupling interaction from the kinetic energy as

$$\begin{aligned} \frac{d\mathcal{E}^b}{dt} &\approx \int_0^\infty dk \mathbb{T}_{(c,L)}^b(k) - 2\xi \int_0^\infty dk k^2 E^b(k) \\ &= \int_0^\infty dk (\lambda(k) - 2\xi k^2) E^b(k) \\ \lambda(k) &= 8K_d \int_{\Delta_k} dq dp W_d(\Delta_k) \theta_{pkq} \frac{p}{kq} c_{pqk} q^{d-1} E^u(p) \end{aligned} \quad (6.43)$$

where we have neglected the non-linear contribution from quadratic terms  $\mathcal{O}(E^b E^b)$  in the  $\mathbb{T}_{(c,NL)}^b$  (see Eq. (6.38)) in the early times. The spectral dynamo timescale  $\lambda(k)$  depends only on the kinetic spectrum and the dimension of the system.

If the net growth of the magnetic energy of the system follows an exponential behaviour  $\mathcal{E}^b(t) \sim \exp(\bar{\lambda}t)$ , then the growth exponent  $\bar{\lambda}(t)$  is given by

$$\bar{\lambda}(t) = \frac{\int_0^\infty dk (\lambda(k) - 2\xi k^2) E^b(k)}{\int_0^\infty dk E^b(k)} \quad (6.44)$$

For a system that supports the dynamo growth, the  $\bar{\lambda}$  will be non-zero for all times. Whereas, for the system where the dynamo is not possible, it might be positive for a finite time, before eventually becoming negative at long times.

In the case of ideal magnetic fluid  $\nu = \xi = 0$ , in the truncated EDQNM-MHD model, global equipartition is expected as the fixed point for the system, that is  $E^u(k) = E^b(k) \sim k^{d-1}$ . Consider two separately equipartitioned

fields,  $E^u(k) = A_u k^{d-1}$  and  $E^B(k) = A_b k^{d-1}$ . This would imply that the self-transfer terms  $\mathbb{T}_{(s)}^b, \mathbb{T}_{(s)}^u$  are zero. But for  $A_u \ll A_b$ , there will be a non-zero interaction term driving the system. For such a state, the eddy-damping time scale can be approximated as:

$$\mu_k = \alpha_d \left( A_u \frac{k^{d+2}}{d+2} \right)^{1/2} \quad (6.45)$$

Since we assumed that  $A_b \ll A_u$ , allowing to calculate the rate of change of net magnetic energy, for initial times as

$$\frac{d\mathcal{E}^b}{dt} \approx 8K_d \frac{A_u A_b}{\alpha} \sqrt{\frac{d+2}{A_V}} \int dq dp dk W_d(\Delta_k) p^{\frac{(d-2)}{2}} k^{d-2} q^{d-2} c_{pkq} \quad (6.46)$$

Upto a cut-off wavenumber, say  $k_G$ , the integral in equation (6.46) can be computed directly, say in *Mathematica*.

Here,  $d = 2$  is a special case, the conservation of magnetic potential

$$\frac{d}{dt} \mathcal{A} = \frac{d}{dt} \int_0^\infty dk \frac{E^b(k)}{k^2} = 0 \quad (6.47)$$

strictly disallows the model to reach a global equipartition. We have numerically verified that for all dimensions  $d > 2$ , the growth rate is different based on the dimension, but the system reaches the global fixed point. So, for example, with  $\mathcal{E}^u(0) = 0.99, \mathcal{E}^b(0) = 0.01$ , asymptotically it becomes  $\mathcal{E}^b = \mathcal{E}^u = 0.5$ . For  $d = 2$ , the conservation of magnetic potential retains the system in  $\mathcal{E}^b \ll \mathcal{E}^u$  state, for all times.

For the real case, with  $\nu, \xi \neq 0$ , the no-dynamo scenario can arise if the non-zero magnetic diffusion overcomes the pumping of energy from the kinetic case. From the anti-dynamo theorems [103, 273], for  $d = 2$  there will be no dynamo effect in either case. This is a necessary condition that the EDQNM-MHD model should satisfy.

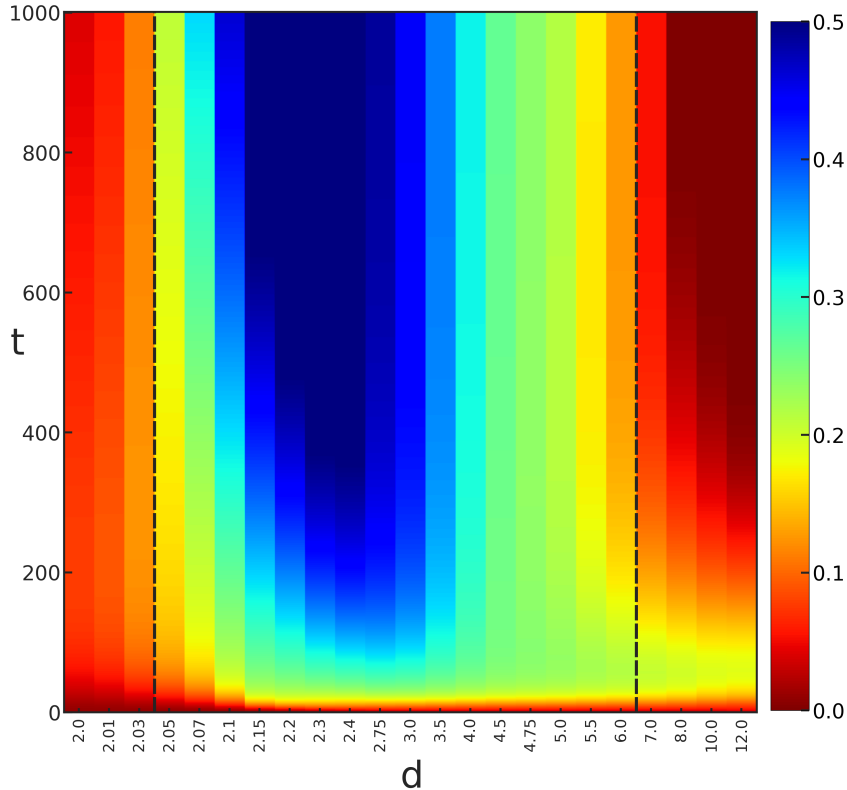


Figure 6.3: A *space-time* color plot of the fraction  $R(t)$  of magnetic to fluid energy. The dynamo phase (with colors ranging from light green to dark blue at large times) are indicated by thick, black vertical lines suggesting lower  $d_L \approx 2.03$  and upper  $d_U \approx 6.0$  *critical* dimensions for dynamo action, for the  $\nu = 5 \times 10^{-4}$  case.

### 6.3.1 Numerical study

We perform detailed numerical simulation of the MHD-EDQNM model (Eqs. (6.35)–(6.37)) in dimensions  $2 \leq d \leq 12$  with  $\nu = \xi = 5 \times 10^{-4}$ , corresponding to Prandtl number  $\text{Pr}$  unity, a well-resolved inertial range with the minimum and maximum wavenumbers  $k_{\min} = 2^{-3}$  and  $k_{\max} = 2^{10}$ , respectively and time-stepping  $\delta t = 2 \times 10^{-5}$ . See Appendix B.4 for details of discrete wavenumbers used in this numerical study.

In order to study the dynamo problem, first, we develop a stationary steady state for the pure kinetic EDQNM model with forcing at large scales (small  $k$ ).

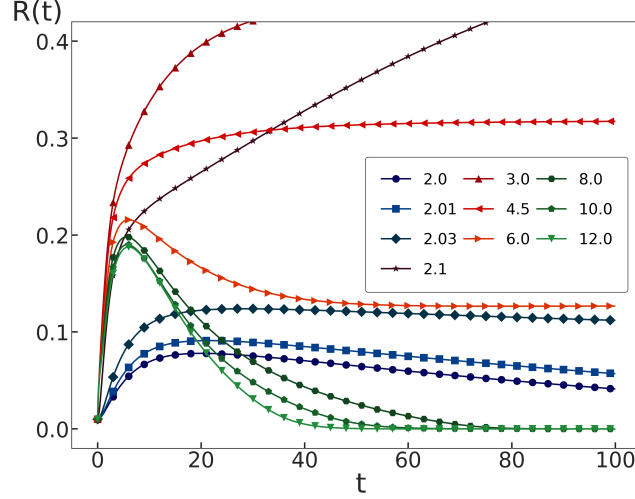


Figure 6.4: A plot of  $R(t)$  vs  $t$  for several dimensions; clearly the magnetic energy and thence dynamo action is sustained for  $d_L \lesssim d \lesssim d_U$  (red plots). For dimensions outside this range (blue and green plots), the magnetic energy, after a peaking, decays showing the unsustainable growth of the magnetic field and hence the no-dynamo phase.

Forcing term is included in the evolution of the kinetic spectrum as:

$$\frac{d}{dt} E^u(k, t) = T_{(s)}^u(k) - 2\nu k^2 E^u(k) + F(k) \quad (6.48)$$

Forcing spectrum  $F(k)$  is chosen to be concentrated at large scales,  $F(k) \sim k^2 \exp(-k^2/2k_l^2)$ . The injection of energy through forcing is matched with the net viscous dissipation rate

$$\int_0^\infty dk F(k) = \epsilon^u = \int_0^\infty dk 2\nu k^2 E^u(k) \quad (6.49)$$

keeping the net kinetic energy constant, at  $\mathcal{E}^u = 1.0$ .

Once a steady state is reached  $dE^u(k)/dt = 0$ , with a robust Kolmogorov spectrum  $E^u(k) \sim k^{-5/3}$  (albeit with an ever-pronounced bottleneck effect as the dimension exceeds  $d = 3$  [272]), the magnetic spectrum interaction is switched on with a initial seed of magnetic energy with  $\mathcal{E}^b = 10^{-2}$ . With the interaction on, the

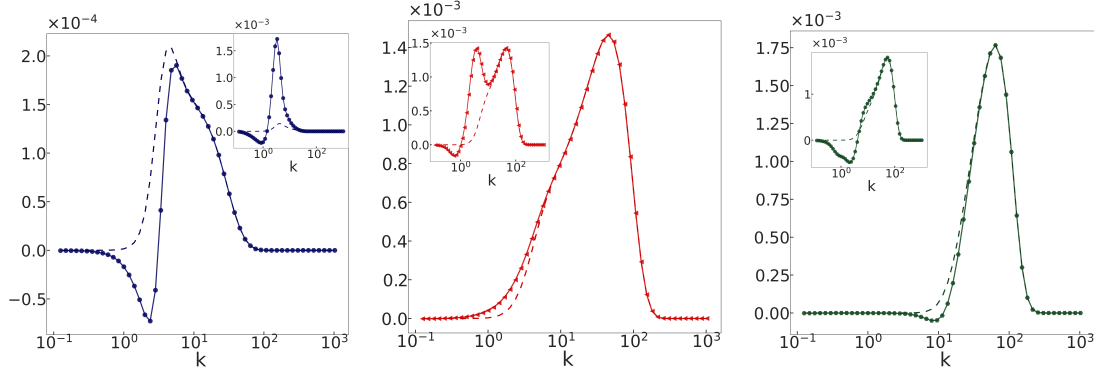


Figure 6.5: Plots of the combined transfer terms  $T_b^{(s)}(k) + T_b^{(c)}(k)$  (symbols) and the effective magnetic diffusive term  $2\xi k^2 E^b$  (dashed lines) for (a)  $d_L \gtrsim d = 2.0$  (b)  $d_L \lesssim d = 4.0 \lesssim d_U$  and (c)  $d_U \lesssim d = 8.0$  at short  $t = 5$  (inset) and long  $t = 30$  times.

forcing is adjusted to match the net dissipation rate:

$$\int_0^\infty dk F(k) = \epsilon^u + \epsilon^b \quad (6.50)$$

Allowing the coupled set of equations in the full EDQNM-MHD model to evolve with this initial seed of magnetic energy, the characteristic growth of the magnetic energy determines the dynamo or no-dynamo. We choose this as the  $t = 0$  state in what follows.

Dynamo action in the subsequent dynamics of the model can be simply defined as follows. Let us define the ratio of the magnetic and kinetic energy as

$$R(t) = \frac{\mathcal{E}^b(t)}{\mathcal{E}^u(t)} \quad (6.51)$$

which of course evolves in time. By choosing the initial ratio  $R(0) = 10^{-2}$  to be small, a dynamo (or no dynamo) happens if  $R(t) \rightarrow 1$  (or  $R(t) \rightarrow 0$ ) at large times. In figure 6.4 we show representative plots of  $R$  vs  $t$ , for a few spatial dimensions  $d$ . As a consistency check, clearly for  $d = 2$  there is no dynamo whereas for three dimensions  $R \rightarrow 0.5$  indicating a robust dynamo with energy equipartition between the magnetic and fluid fields. However, surprisingly and as already anticipated in figure 6.3, the no-dynamo phase boundary extends beyond  $d = 2.0$  upto  $d_L = 2.03$ .

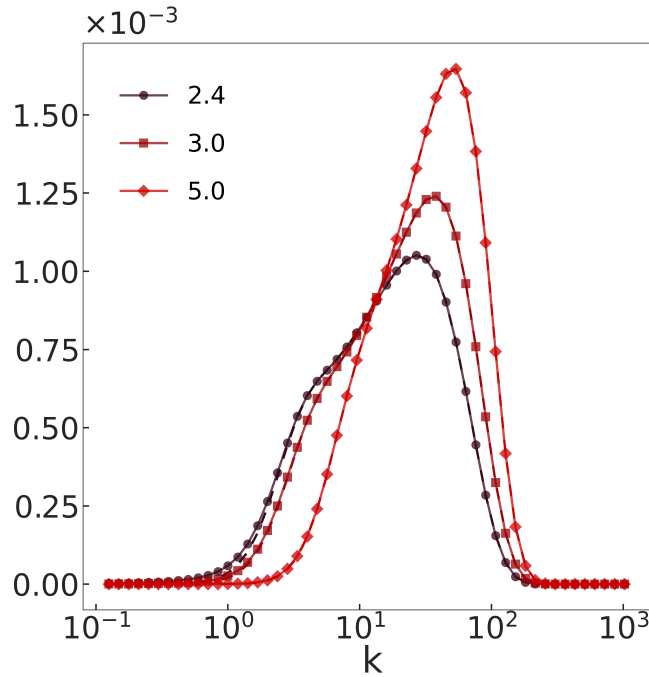


Figure 6.6: The transfer terms (in symbols) and the magnetic diffusion term (in dashed) line for different dimensions at time  $t = 100$ . In this dynamo phase where the magnetic energy saturates to a finite value there is an exact compensation of the two contributions as discussed in the text.

Equally interestingly, the dynamo phase disappears at higher dimension  $d > d_U \approx 7$  (Fig. 6.3).

Is it possible to have a theoretical explanation, starting from the equations of motion, which suggests such a phase diagram? While the short answer is, unfortunately, no, a scrutiny of the EDQNM-MHD model suggests that in the coupled set of equations, dynamo action is likely to happen when the interaction terms are such that the energy transfer is predominantly from  $\mathbf{u} \rightarrow \mathbf{b}$ . Thus, the  $\mathcal{T}^b(c)(k)$  acts, effectively, like a forcing on the magnetic field. Thus it seems reasonable to assume that for  $d_L \leq d \leq d_U$ , this preferential transfer of energy (at scales larger than those where the diffusive damping becomes strong) from the fluid to the magnetic field would lead an increasing magnetic energy  $\mathcal{E}_b$  with an eventual saturation which is a consequence of both the nonlinearities (negligible at short times) and damping. A similar line of argument would also suggest that for  $d < d_L$  or  $d > d_U$  the energy transfer at large scales (where the damping term is negligible) ought to be, preferentially, from  $\mathbf{b} \rightarrow \mathbf{u}$  even if there is a net  $\mathbf{u} \rightarrow \mathbf{b}$

transfer at smaller scales. This is because at small scales the dissipate term acts as a counter to the net *pumping* from the fluid field.

While the argument outlined above stems from the observation in figure 6.3 it is admittedly heuristic. To make this somewhat concrete, we must analyse the spectral properties of the interaction terms in equation (6.37). In figure 6.5 we plot  $\mathbf{T}_{(s)}^b(k) + \mathbf{T}_{(c)}^b(k)$  in Fourier space superimposed with the magnetic diffusion term  $2\xi k^2 E^b$  at (inset) short ( $t = 5$ ) and long ( $t = 30$ ) times for  $d = 2.03 < d_L$ ,  $d_L \leq d = 4.0 \leq d_U$  and  $d = 10 > d_U$ . As conjectured, at short times the transfer terms are strictly *forcing* for all  $d$  and, being consistently above the damping term  $2\xi k^2 E^b$ , dominates leading to an initial growth of the total magnetic energy (Fig. 6.4). However at long times while for  $d_L \leq d \leq d_U$  the net transfer is strictly positive—hence the dynamo action—for other dimensions at small wavenumbers the net transfer is strictly from  $\mathbf{b} \rightarrow \mathbf{u}$ , at small wavenumbers (where the diffusive damping term is small), indicating an effective depletion of the magnetic energy at these scales. At larger wavenumbers—reason is quite different—there is however an effective  $\mathbf{u} \rightarrow \mathbf{b}$  transfer; however, as seen in figure 6.5 these wavenumbers are typically much higher than those for  $d_L \leq d \leq d_U$  and consequently damped out by the magnetic diffusivity. Therefore the term-by-term analysis clearly indicates that a no-dynamo phase not only for dimensions around 2 but also for higher dimensions  $d > d_U$ .

For dimensions  $d_L \leq d \leq d_U$ , the relatively small scales of the pumping prevents compensation by the diffusion term which allows dynamo action to take place. Indeed, in such dimensions at long times there is a miraculous cancellation of the pumping and damping, when integrated over all wavenumbers leading to the saturation of magnetic energies with a finite  $R$  and thence the dynamo action. An example of this effect is shown in figure 6.6 for  $d = 4.0$ . We note that the critical dimensions  $d_L$  and  $d_U$  are, hence, strictly dependent on the diffusive scales present in the system.

Further evidence of this is implicit in the nature of the magnetic energy

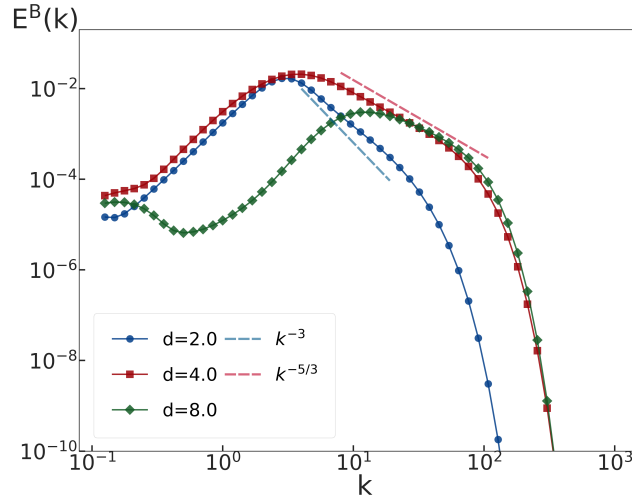


Figure 6.7: Log-log plots of the magnetic energy spectrum  $E^b$  vs  $k$  for different dimensions. The forcing scale from the fluid-magnetic interactions show up at intermediate scales which become larger for  $d \gtrsim d_U$ . The scaling exponent switches from  $-3$  ( $d \lesssim d_L$ ) to  $-5/3$  ( $d \gtrsim d_L$ ) as indicated by the dashed lines indicating power-laws as a guide to the eye.

spectrum for different dimensions. In figure 6.7 we show log-log plots of the magnetic spectrum for several dimensions, both in the dynamo and no-dynamo phase. We measure the spectra at time  $t \gtrsim t^*$ , where  $t^*$  is the peak in  $R(t)$ . We find a transition in the spectral exponent on either side of the lower *critical dimension*: For  $d \lesssim d_L$ ,  $E^b \sim k^{-3}$  and for  $d \gtrsim d_L$ ,  $E^b \sim k^{-5/3}$ . While this is related to the inverse cascade etc etc Furthermore, the peak in the spectrum corresponds to wavenumbers where the pumping via the transfer terms peak lending further evidence of the interpretation of the dynamo—no-dynamo phase transition outlined above.

In this Chapter, we have focussed on showing the existence of a dynamo—no-dynamo phase boundary, for a given point in the magnetic Reynolds number and Prandtl number landscape, by using the remarkably robust  $d$ -dimensional MHD-EDQNM model (Eqs. (6.35) – (6.37)). However, this model can be used to further investigate effects of compressibility and a wide range of Prandtl and magnetic Reynolds numbers which are currently difficult in full MHD direct numerical simulation. We hope that this model will trigger further interest in tackling the important questions of dynamo from a firmer theoretical standpoint.

# Chapter 7

## Conclusion

This Thesis is an intensive, analytically-assisted numerical exploration of some of the fundamental problems in turbulence and statistical physics. The topic of the thermalization of classical systems with many degrees of freedom is a profoundly important one in statistical physics. There are various instances of such systems, with intentionally broken integrability, that thermalize. This Thesis primarily focuses on the finite-dimensional (Galerkin-truncated) equations of ideal hydrodynamics. Although their long-term solutions being thermalized can be understood by virtue of them being a many-body chaotic Hamiltonian system—conserving phase space and energy—the precise mechanisms that genesis the thermalization for the three-dimensional Euler equations are still not completely understood and have remained an open question. Numerical spectral simulations of inviscid equations of hydrodynamics are practically always solving the Galerkin-truncated problem by definition. There are two key consequences of this. Firstly, a numerical strategy to anticipate the finite-time blow-up of the Euler equation fails as the small scales thermalize. Secondly, *weak* (dissipative) solutions of the Euler equation are diligently hard to realize numerically.

By uncovering the mechanisms at the heart of the thermalization in the Galerkin-truncated three-dimensional Euler equations in Chapter 2, the study

showed how certain types of fluid structures, which are nearly always present, lead to hotspots of small-scale thermalization, which eventually trigger a global Gibbs distribution in the velocity field. Further, it describes the phenomenon reduced to the point of view of a one-dimensional problem, thus rendering comparisons with the well-researched Burger's equation [39] viable. The work sheds light on various elements of the genesis of thermalization, such as its non-local character, dependency on compressional eigenvectors near critically evolved structures, and conditions that proliferate the process.

Consequently, this understanding paved the way for constructing numerical prescriptions (as in Chap. 3) that may well avoid thermalization without resorting to viscous damping, thereby opening up the prospect of developing weak solutions to the Euler equation. We contemplate that, in the future, with additional refinement from others with expertise in the area, a sub-grid-size model might be built that would considerably solve the longstanding difficulties of the Euler equation. Our work on Tyger purging serves as a hope and witness to the formulation of such numerical formulas that reliably prevent thermalization at the early stages. The only catch is the absence of an equivalent entropy solution for the former.

If studies of the truncated system with the goal of understanding the origins of, and then suppressing, thermalized solutions are fundamental questions in the area of turbulence, then the application of such thermalized solutions for investigating other statistical and condensed matter problems is also vital to address. This is due to the fact that statistical physics is based on the concepts of thermalization and equilibration, which are facilitated by the many-body chaos inherent in such systems. We reconciled these two seemingly disparate roles and radically different fallouts of chaos in Chapter 4 by studying the decorrelators in the non-linear equations of hydrodynamics such as the 1D Burgers and the 3D Euler equations, which result in chaotic but thermalized flows. With the use of numerical simulations and analytical calculations, the chapter shows that the Lyapunov exponent grows as the square root of temperature and linearly with the degrees of freedom. This calculation underlined the universal aspects of many-body chaos and its fundamental connection

to equilibrium properties of the system.

While these three chapters in the Thesis above dealt with the instance of inviscid hydrodynamics, Chapter 5 deals with an intriguing inquiry connected to the multifractal rationalization of the fully formed turbulence. Statistics and measures are produced on the entire dissipation field of the flow to provide a global multifractal measure, without any local fluctuations accounting for. It is evident that there are patches with very little activity and areas with abnormally large dissipation. Given such variance, it appears obvious what one needs is a measure of local, space-dependent multifractality to understand turbulence better and not the global statistics that we were accustomed to. This Thesis highlights progress by creating a local measure  $\Phi(\mathbf{x})$  of the local multifractality in the flow such that  $\Phi(\mathbf{x}) \lll 1$  indicates local monofractality and  $\Phi(\mathbf{x}) \sim \mathcal{O}(1)$  indicates highly multifractal. In addition, we provide a map of the turbulence field showing the areas that are and are not monofractal. This highlights the notion that turbulence may be characterized as intermittent, multifractal islands on the vast and calm Kolmogorov Sea. One may now make the connection between the two fundamental phenomenological foundations of turbulence—the problem of energy cascades and its ultimate culmination in dissipative structures—thanks to this innovative and new approach to local multifractal statistics.

The final part of the Thesis, Chapter 6 focuses on the Eddy-Damped Quasi-Normal Markovian (EDQNM) Closure Model used to comprehend the dynamo problem associated with magnetohydrodynamic (MHD) turbulence in arbitrarily high dimensions. We have calculated a ‘d’-dimensional EDQNM-MHD equation for the first time and demonstrated the presence of critical dimensions beyond which the dynamo ceases to exist, partially compatible with findings from other prior models [265]. Most crucially, this platform supports the compatibility of other essential effects in the image, such as the compressibility, smoothness of the turbulent field, Prandtl and magnetic Reynolds numbers, and lets to investigate and quantify the dynamo effect.

# Appendix A

## Multifractal analysis of Curdling model

### A.1 Localized Multifractality Dominating the Global Analysis

A caveat of the multifractal analysis, that has gone largely unremarked and hence unaccounted, is that the global analysis gets biased in favour of a broad singularity spectrum (reflecting a high degree of multifractality) even if the underlying measure field is *only* multifractal (fluctuating) in localized patches. We demonstrate this using a simple measure conserving curdling (multiplicative cascade) model [233, 234, 274]. It is easiest to spell out the construction algorithmically. We start with a unit initial measure  $\rho(0) \equiv \{\rho_0\} \equiv \{1\}$ , over a length 1. In the first generation, the measure is split into two parts, generating  $\rho(1) \equiv \{\rho_1, \rho_2\} \equiv \{\rho_0 f_0, \rho_0(1 - f_0)\}$  over lengths  $1/2$  each, with  $f_i$  a random variable drawn uniformly from the interval  $[0.5 - \sigma, 0.5 + \sigma]$  and  $0 \leq \sigma < 0.5$ . In the second generation, the same process is repeated on  $\rho_1$  and  $\rho_2$  independently, with new realizations of the random variable  $f_i$  for each splitting, hence for instance  $\rho_1$  is split into  $\{\rho_{11}, \rho_{12}\} \equiv$

$\{\rho_1 f_1, \rho_1(1 - f_1)\}$  and  $\rho_2$  is split into  $\{\rho_{21}, \rho_{22}\} \equiv \{\rho_2 f_2, \rho_2(1 - f_2)\}$ . This gives the second generation measure  $\rho(2) \equiv \{\rho_{11}, \rho_{12}, \rho_{21}, \rho_{22}\}$ , over lengths  $1/4$  each. Intuitively, after  $n$ -generations, we have a measure  $\rho(n)$  consisting of  $2^n$  parts, each of length  $1/2^n$ , hence preserving the integral of the original measure to 1. The choice of  $\sigma$  allows controlling the degree of multifractality, with  $\sigma \approx 0$  giving a uniform, monofractal measure (i.e. with a single scaling exponent) and  $\sigma \approx 0.5$  giving a highly fluctuating, multifractal measure (with multiscaling).

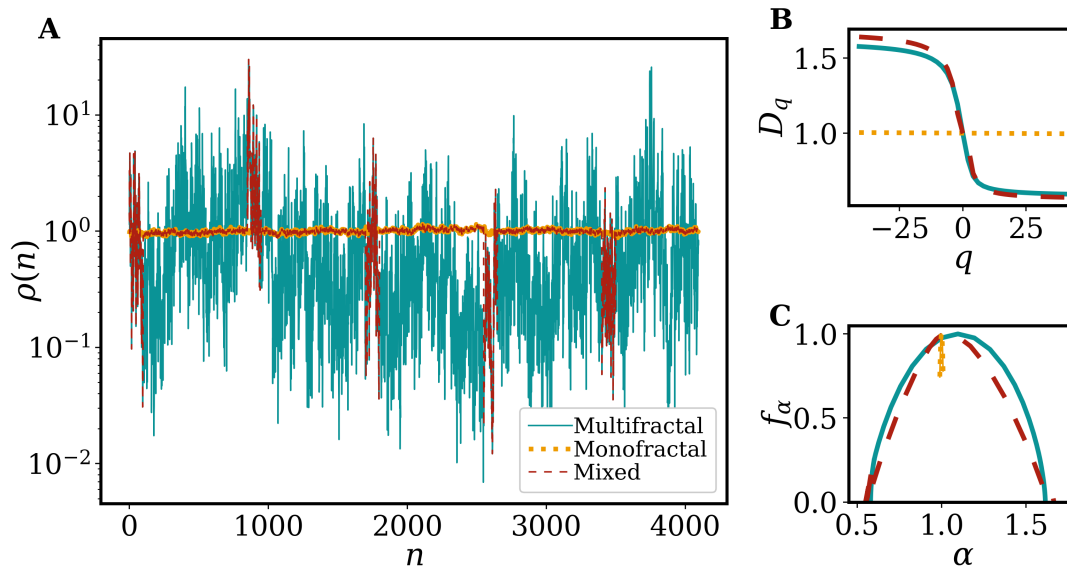


Figure A.1: **(A)** A multifractal and a monofractal measure, constructed using a random curdling model over 12 generations (4096 divisions) using  $\sigma = 0.3$  (strongly multifractal) and  $\sigma = 0.01$  (essentially monofractal, with a single scaling exponent). A third “mixed” measure is created identical everywhere to the monofractal measure, except in five localized regions (of  $\Delta n = 100$  points each) where it is identical to multifractal measure. **(B)**  $D_q$  vs  $q$  and **(C)**  $f_\alpha$  vs  $\alpha$  for all three measures shows that the multifractal measure yields a broad singularity spectrum (multiscaling behaviour), while the monofractal measure is essentially a Dirac-delta as expected for a single scaling exponent. Crucially, the “mixed” measure, despite being  $\approx 90\%$  monofractal, yields an equally broad singularity spectrum as the uniformly multifractal measure, showing how even small regions of local multifractality (fluctuations) can completely dominate the global analysis.

Figure A.1(A) shows a multifractal measure (with  $\sigma = 0.3$  and  $n = 12$ ) and an essentially monofractal measure (with  $\sigma = 0.01$  and  $n = 12$ ), where the final measure  $\rho(n)$  has been normalized by the mean of  $\rho(n)$ , for both cases (the normalization helps prevent numerical issues that arise when calculating higher moments of the partition function, for measures created with higher values of  $\sigma$ ). Figure A.1(B) shows the  $D_q$  vs  $q$  curves, where the monofractal measure has a

flat profile while the multifractal measure has a broad  $D_q$  distribution, leading in figure A.1(C) to the Dirac-delta and broad singularity spectra, respectively, as is readily expected. We then construct a third, “*mixed*” measure, which is identical to the monofractal measure everywhere, except at five localized regions of  $\Delta n = 100$ , where it is identical to the multifractal measure. Therefore, this measure is  $\approx 90\%$  monofractal, with only 10% of the regions having multifractal fluctuations (mimicking the qualitative behaviour of turbulent dissipation). The global multifractal analysis, unfortunately, gets completely dominated by these localized multifractal spots, and the mixed measure yields  $D_q$  vs  $q$  and  $f_\alpha$  vs  $\alpha$  that are as broad as those for the uniformly multifractal measure.

This shows the need for reconsidering multifractality as a *local* flow property, which can be used to distinguish multifractal and monofractal regions of a given measure field. This would allow separating local spatial regions with multiscaling and intermittency from the more quiescent and calm regions.

# Appendix B

## EDQNM-MHD model

### B.1 Isotropic Quasi-Normal equations

The only rotationally invariant second rank tensors are  $\delta_{\alpha\beta}$  and  $\hat{k}_\alpha, \hat{k}_\beta$ . Thus writing the second-moment in terms of these tensors:

$$\mathcal{S}_{\alpha\beta}^{XX}(k) = (c_1\delta_{\alpha\beta} + c_2\hat{k}_\alpha\hat{k}_\beta)\mathcal{U}^X(k) \quad (\text{B.1})$$

Since  $\mathcal{S}_{\alpha\alpha}^{XX}(k) = \mathcal{U}^X(k)$ ,  $k_\alpha\mathcal{S}_{\alpha\beta}^{XX}(k) = 0$ , (from incompressibility) which yields  $c_1 =$

$\frac{1}{d-1} = -c_2$ , and thus equation (6.13).

$$\begin{aligned}
 \frac{1}{(d-1)} \mathbb{P}_{\alpha\beta}^{(k)} \left[ \frac{d}{dt} + 2\nu k^2 \right] \mathcal{U}^u(k) &= \frac{1}{(d-1)^2} \int_{\Delta_{\mathbf{k}}} 2\hat{\theta}(\omega_0) \mathcal{P}_{\beta\rho\gamma}^{(k)} \left[ -\mathcal{P}_{\alpha\mu\sigma}^{(k)} \mathbb{P}_{\rho\mu}^{(q)} \mathbb{P}_{\gamma\sigma}^{(p)} \mathcal{U}^u(q) \mathcal{U}^u(p) \right. \\
 &\quad \left. + \mathcal{P}_{\rho\mu\sigma}^{(q)} \mathbb{P}_{\alpha\sigma}^{(k)} \mathbb{P}_{\gamma\mu}^{(p)} \mathcal{U}^u(k) \mathcal{U}^u(p) \right. \\
 &\quad \left. + \mathcal{P}_{\gamma\mu\sigma}^{(p)} \mathbb{P}_{\alpha\mu}^{(k)} \mathbb{P}_{\rho\sigma}^{(q)} \mathcal{U}^u(k) \mathcal{U}^u(q) \right] + c \cdot c \Big|_{\alpha\leftrightarrow\beta} \\
 - \frac{1}{(d-1)^2} \int_{\Delta_{\mathbf{k}}} 2\hat{\theta}(\omega_k) \mathcal{P}_{\beta\rho\gamma}^{(k)} \left[ \mathcal{C}_{\rho\mu\sigma}^{(q)} \mathbb{P}_{\alpha\sigma}^{(k)} \mathbb{P}_{\gamma\mu}^{(p)} \mathcal{U}^u(k) \mathcal{U}^b(p) \right. \\
 &\quad \left. + \mathcal{C}_{\gamma\mu\sigma}^{(p)} \mathbb{P}_{\alpha\sigma}^{(k)} \mathbb{P}_{\rho\mu}^{(q)} \mathcal{U}^u(k) \mathcal{U}^b(q) \right. \\
 &\quad \left. + \mathcal{P}_{\alpha\mu\sigma}^{(k)} \mathbb{P}_{\rho\mu}^{(q)} \mathbb{P}_{\gamma\sigma}^{(p)} \mathcal{U}^b(q) \mathcal{U}^b(p) \right] + c \cdot c \Big|_{\alpha\leftrightarrow\beta}
 \end{aligned} \tag{B.2}$$

$$\begin{aligned}
 \frac{1}{(d-1)} \mathbb{P}_{\alpha\beta}^{(k)} \left[ \frac{d}{dt} + 2\zeta k^2 \right] \mathcal{U}^k(k) &= \frac{1}{(d-1)^2} \int_{\Delta_{\mathbf{k}}} 2\hat{\theta}(\omega_p) \mathcal{C}_{\beta\rho\gamma}^{(k)} \left[ -\mathcal{C}_{\alpha\mu\sigma}^{(k)} \mathbb{P}_{\rho\mu}^{(q)} \mathbb{P}_{\gamma\sigma}^{(p)} \mathcal{U}^b(q) \mathcal{U}^u(p) \right. \\
 &\quad \left. + \mathcal{C}_{\rho\mu\sigma}^{(q)} \mathbb{P}_{\alpha\mu}^{(k)} \mathbb{P}_{\gamma\sigma}^{(p)} \mathcal{U}^b(k) \mathcal{U}^u(p) \right. \\
 &\quad \left. - \mathcal{P}_{\gamma\mu\sigma}^{(p)} \mathbb{P}_{\alpha\mu}^{(k)} \mathbb{P}_{\rho\sigma}^{(q)} \mathcal{U}^b(k) \mathcal{U}^b(q) \right] \\
 + \frac{1}{(d-1)^2} \int_{\Delta_{\mathbf{k}}} 2\hat{\theta}(\omega_q) \mathcal{C}_{\beta\rho\gamma}^{(k)} \left[ -\mathcal{C}_{\alpha\mu\sigma}^{(k)} \mathbb{P}_{\rho\mu}^{(p)} \mathbb{P}_{\gamma\sigma}^{(q)} \mathcal{U}^b(p) \mathcal{U}^u(q) \right. \\
 &\quad \left. + \mathcal{C}_{\rho\mu\sigma}^{(p)} \mathbb{P}_{\alpha\mu}^{(k)} \mathbb{P}_{\gamma\sigma}^{(q)} \mathcal{U}^b(k) \mathcal{U}^u(q) \right. \\
 &\quad \left. - \mathcal{P}_{\gamma\mu\sigma}^{(q)} \mathbb{P}_{\alpha\mu}^{(k)} \mathbb{P}_{\rho\sigma}^{(p)} \mathcal{U}^b(k) \mathcal{U}^b(p) \right] + c \cdot c \Big|_{\alpha\leftrightarrow\beta}
 \end{aligned} \tag{B.3}$$

Substituting the form of equation (6.13) in equation (6.11), noting that  $\mathcal{S}^{XX}(k)$  becomes real and  $\mathcal{S}^{XX}(-k) = \mathcal{S}^{XX}(k)$  in the isotropic field. In that every term on the R.H.S of the equations (B.2), (B.3) becomes real after this substitution of (6.13). Thus the complex conjugate is the same as the first term adding a net factor to each term. Useful properties of our tensors:

$$\begin{aligned}
 \mathbb{P}_{\alpha\beta}^{(k)} \mathbb{P}_{\alpha\rho}^{(k)} &= \mathbb{P}_{\beta\rho}^{(k)} \quad ; \quad \mathbb{P}_{\alpha\beta}^{(k)} \mathbb{P}_{\alpha\beta}^{(k)} = d-1 \\
 \mathcal{P}_{\alpha\rho\gamma}^{(k)} &= \mathcal{P}_{\alpha\gamma\rho}^{(k)} \quad ; \quad \mathcal{C}_{\alpha\rho\gamma}^{(k)} = -\mathcal{C}_{\alpha\gamma\rho}^{(k)} \\
 \mathbb{P}_{\alpha\beta}^{(k)} \mathcal{P}_{\beta\rho\gamma}^{(k)} &= \mathcal{P}_{\alpha\rho\gamma}^{(k)} \quad ; \quad \mathbb{P}_{\alpha\beta}^{(k)} \mathcal{C}_{\beta\rho\gamma}^{(k)} = \mathcal{C}_{\alpha\rho\gamma}^{(k)}
 \end{aligned} \tag{B.4}$$

Then multiplying the equations (B.2), (B.3) by  $\mathbb{P}_{\alpha\beta}^{(k)}$  using the identity in (B.4) results in equations (6.14a), and (6.14b).

## B.2 $d$ -dimensional Integral

For a given  $\mathbf{k}$  and  $\mathbf{q}$ , only the angle between them and the magnitudes of them are relevant in the transfer term. Thus we can pull off a factor by integrating the remaining angles in  $d$ -dimensions. In  $d$ -dimensional spherical co-ordinates, the cartesian co-ordinates are related to the spherical angles  $\phi_1, \phi_2, \dots, \phi_{n-1}$  and radius  $r$  by

$$\begin{aligned}
 x_1 &= r \cos(\phi_1) \\
 x_2 &= r \sin(\phi_1) \cos(\phi_2) \\
 &\vdots \\
 x_{n-1} &= r \sin(\phi_1) \cdots \sin(\phi_{n-2}) \cos(\phi_{n-1}) \\
 x_n &= r \sin(\phi_1) \cdots \sin(\phi_{n-2}) \sin(\phi_{n-1})
 \end{aligned} \tag{B.5}$$

By orienting the axis such that  $\mathbf{k}$  is along  $x_1$  direction, then  $\mathbf{q}$  subtends an angle of  $\phi_1 = \beta$  from the figure. Thus we can integrate the remaining angles  $\phi_2, \dots, \phi_{n-1}$  which form a  $d - 2$  dimensional sphere .

$$\begin{aligned}
 d^{d-1}\Omega &= \sin^{d-2}(\phi_1) \sin^{d-3}(\phi_2) \cdots \sin(\phi_{d-2}) d\phi_1 d\phi_2 \cdots d\phi_{d-1} \\
 \int d^{d-1}\Omega &= S_{d-1} = \frac{2\pi^{d/2}}{\Gamma(\frac{d}{2})}
 \end{aligned} \tag{B.6}$$

Denoting the evolution equations (6.16a), and (6.16b) for spectral energies

as

$$\begin{aligned}
 \left[ \frac{d}{dt} + 2\nu k^2 \right] \mathcal{U}^X &= \int_{\Delta_k} \mathcal{T}^X(\Delta_k) \\
 &= \int d\mathbf{q} d\mathbf{p} \delta(\mathbf{p} + \mathbf{q} - \mathbf{k}) \mathcal{T}^X(\Delta_k) \\
 &= \int d^d q \mathcal{T}^X(\Delta_k) = \int dq q^{d-1} d^{d-1} \Omega \mathcal{T}^X(\Delta_k) \\
 &= \int_{q=0}^{\infty} dq q^{d-1} \int_{\beta=0}^{\pi} d\beta \sin^{d-2}(\beta) \mathcal{T}^X(\Delta_k) \int d^{d-2} \Omega \\
 &= \int_{q=0}^{\infty} dq q^{d-1} \int_{y=-1}^{y=1} dy \sin^{d-3}(\beta) \mathcal{T}^X(\Delta_k) S_{d-2} \quad (\text{B.7})
 \end{aligned}$$

To further simplify (B.7), we use sine law of triangle and change of variables.

$$\begin{aligned}
 \frac{\sin(\alpha)}{k} &= \frac{\sin(\beta)}{p} \\
 \int_0^{\infty} dq \int_0^1 dy &= \mathbf{J} \left[ \frac{\partial(q(q,p), y(q,p))}{\partial(q,p)} \right] \int_0^{\infty} dq \int_{|k-q|}^{|k+q|} dp \\
 &= \left( \frac{p}{kq} \right) \int_{\Delta_k} dq dp \quad (\text{B.8})
 \end{aligned}$$

where  $\mathbf{J} \left[ \frac{\partial(q(q,p), y(q,p))}{\partial(q,p)} \right]$  is the Jacobian for change of variables, and  $\int_{\Delta_k} dq dp = \int_0^{\infty} dq \int_{|k-q|}^{|k+q|} dp$ . Using the relation (B.8) in equation (B.7) finally gives the equation (6.19).

### B.3 Conserved quantities in the Quasi-Normal model

To see that this model respects the *trivial* conserved quantities in the ideal case  $\nu = 0$ ,  $\xi = 0$ ; the sum of net kinetic and magnetic energy has to be constant. To show this for a finite dimensional variant, consider any arbitrary triad,  $k, p, q$ , the net transfer of energy (both kinetic and magnetic) between the modes has to be zero. Then the net energy is conserved for any finite number of triads. Let  $\mathcal{E}$  be the

net energy of the system consisting of one triad.

$$\begin{aligned}\frac{d\mathcal{E}}{dt} &= \frac{d}{dt} \left[ E^u(k, t) + E^u(p, t) + E^u(q, t) + E^b(k, t) + E^b(p, t) + E^b(q, t) \right] \\ &= \sum_{s=k,p,q} \left[ \mathcal{T}_u^{uu}(\Delta_s) + \mathcal{T}_u^{bb}(\Delta_s) + \mathcal{T}_u^{ub}(\Delta_s) + \mathcal{T}_b^{ub}(\Delta_s) + \mathcal{T}_b^{bb}(\Delta_s) \right] \quad (\text{B.9})\end{aligned}$$

In equation (B.9) on substituting the transfer integrands as in equation (6.25) it is easy to note that there are 3 types of spectral terms, quadratic in nature, for every pair of wavenumbers. Since energy conservation has to be independent of the current state of the system, each of these three coefficients must vanish simultaneously and does so as shown below,

1. For terms of type  $E^u(p)E^u(q)$ :

$$\begin{aligned}&= \hat{\theta}(\omega_{kpq}^u) k^{d-1} \left[ \frac{k}{pq} b_{kpq} + \frac{k}{pq} b_{kqp} - \frac{p}{kq} b_{pkq} - \frac{q}{kp} b_{qkp} \right] \\ &= \hat{\theta}(\omega_{kpq}^u) k^{d-1} \frac{k}{pq} \left[ b_{kpq} - \frac{p^2}{k^2} b_{pkq} + b_{kqp} - \frac{q^2}{k^2} b_{qkp} \right] \\ &= 0 \quad (\text{B.10})\end{aligned}$$

which vanishes on the identity (6.24c). This is exchange of energy between kinetic spectrum  $E^u(k)$ , implying the conservation of kinetic energy in the non-magnetic case

2. For terms of type  $E^b(p)E^b(q)$ :

$$\begin{aligned}&= \hat{\theta}(\omega_{kpq}^b) \frac{k}{pq} k^{d-1} [c_{kpq} + c_{kqp} - c_{kpq} - c_{kqp}] \\ &= 0 \quad (\text{B.11})\end{aligned}$$

which vanishes trivially (since we have used certain identities already). These terms represent a non-linear transfer term between kinetic and magnetic spectrum composed only from magnetic spectrum.

3. For terms of type  $E^b(p)E^u(k)$ : The contribution from the coefficients  $c_{kpq}$  from  $\mathbb{T}_u^{ub}(\Delta_k|p)$  and  $\mathbb{T}_b^{ub}(\Delta_p|k)$  directly cancels each other. For the terms with

the coefficient  $h$ ,

$$\begin{aligned}
 &= \hat{\boldsymbol{\theta}}(\omega_{pqk}^b) k^{d-1} \left[ \frac{k}{pq} h_{kqp} - \frac{q}{kp} h_{kqp} \right] \\
 &= \hat{\boldsymbol{\theta}}(\omega_{pqk}^b) k^{d-1} \frac{k}{pq} \left[ h_{kqp} - \frac{q^2}{k^2} h_{qkp} \right] \\
 &= 0
 \end{aligned} \tag{B.12}$$

which vanishes on the identity (6.24d). These terms represent a linear transfer term between kinetic and magnetic spectrum.

Hence, the conservation of net energy is valid, in any dimension. For the special case of  $d = 2$ , we have additional conserved quantities. The MHD equations in two-dimensions can be written in terms of two scalars, the  $z$ -component of the vorticity field  $\omega = \partial_x U_y - \partial_y U_x$  and the magnetic potential  $\mathbf{B} = \nabla \times A \hat{e}_z$ .

$$\frac{\partial \omega}{\partial t} = -\mathbf{U} \cdot \nabla \omega + \mathbf{B} \cdot \nabla (\nabla \times \mathbf{B}) + \nu \nabla^2 \omega \tag{B.13a}$$

$$\frac{\partial A}{\partial t} = -\mathbf{U} \cdot \nabla A + \xi \nabla^2 A \tag{B.13b}$$

In the ideal, pure kinetic EDQNM model ( $\nu = 0, \mathbf{B} = 0$ ), the net enstrophy  $\int d\mathbf{x} |\omega|^2$  is conserved. The equivalent in the QN spectral model is  $\sum_k k^2 E^u(k)$ . For a single triad  $(k, p, q)$  the conservation of enstrophy implies,

$$\begin{aligned}
 \frac{d}{dt} (k^2 E^u(k, t) + p^2 E^u(p, t) + q^2 E^u(q, t)) &= 0 \\
 &= \sum_{s=k,p,q} s^2 \mathcal{T}_u^{uu}(\Delta_s)
 \end{aligned} \tag{B.14}$$

Similar to the above proof, the coefficient of terms of type  $E^u(p)E^u(q)$  is

$$\begin{aligned}
 &= \hat{\boldsymbol{\theta}}(\omega_{kpq}^u) \left[ \frac{k^4}{pq} (b_{kpq}^{(2)} + b_{kqp}^{(2)}) - \frac{p^3}{q} b_{pkq}^{(2)} - \frac{q^3}{p} b_{qkp}^{(2)} \right] \\
 &= \hat{\boldsymbol{\theta}}(\omega_{kpq}^u) \frac{k^2}{pq} [k^2 a_{kpq}^{(2)} - p^2 b_{kpq}^{(2)} - q^2 b_{kqp}^{(2)}] \\
 &= 0
 \end{aligned} \tag{B.15}$$

which vanishes on the identity (6.24h). Now for the ideal magnetic fluid in two-dimensions, the net magnetic potential  $\int d\mathbf{x} |A|^2$  is conserved. In the presence of a non-zero resistivity  $\xi > 0$ , the net magnetic potential can only decay, hence its derivative, the magnetic energy cannot be contained stably forever and has to start decrease. This is the main argument of Zeldovich in the reference [273]. Again in the QN spectral model, this corresponds to  $\sum_k \frac{E^b(k)}{k^2}$ . For a single triad  $(k, p, q)$  the conservation of magnetic potential implies

$$\begin{aligned} \frac{d}{dt} \left( \frac{E^b(k, t)}{k^2} + \frac{E^b(p, t)}{p^2} + \frac{E^b(q, t)}{q^2} \right) &= 0 \\ &= \sum_{s=k,p,q} \frac{1}{s^2} \left( \mathcal{T}_b^{ub}(\Delta_s) + \mathcal{T}_b^{bb}(\Delta_s) \right) \end{aligned} \quad (\text{B.16})$$

1. For terms of type  $E^b(p)E^b(q)$ , the coefficient is

$$\begin{aligned} &= -\hat{\theta}(\omega_{kpq}^b) \left( \frac{1}{q^2} \frac{k}{qp} c_{kqp}^{(2)} k + \frac{1}{p^2} \frac{k}{pq} c_{kpq}^{(2)} k \right) \\ &= -\hat{\theta}(\omega_{kpq}^b) \frac{k^2}{q^3 p^3} \left( p^2 c_{kqp}^{(2)} + q^2 c_{kpq}^{(2)} \right) \\ &= 0 \end{aligned} \quad (\text{B.17})$$

which vanishes on the identity (6.24g) with  $d = 2$ .

2. For terms of type  $E^b(p)E^u(k)$ , the coefficient is

$$\begin{aligned} &= \hat{\theta}(\omega_{kpq}^b) \left( \frac{1}{q^2} \frac{k}{qp} q c_{kqp}^{(2)} - \frac{1}{p^2} \frac{p}{kq} q h_{pqk}^{(2)} + \frac{1}{q^2} \frac{q}{kp} q h_{qp k}^{(2)} \right) \\ &= \hat{\theta}(\omega_{kpq}^b) \frac{1}{pq^2 k} \left( k^2 c_{kqp}^{(2)} - q^2 \left( h_{pqk}^{(2)} - h_{qp k}^{(2)} \right) \right) \end{aligned} \quad (\text{B.18})$$

which vanishes on the identity (6.24i).

## B.4 Numerical Simulation of EDQNM-MHD

The original EDQNM-MHD equations given has infinite degrees of

freedom, to numerically study them we have to discretise the wavenumber space, say  $\mathcal{D}$ . Since we are expecting a power law behaviour for energy spectrum in the inertial range, and want to achieve high Reynolds number (both kinetic and magnetic) in the simulation, it is easier if we discretise the  $N$  wavenumbers  $\{k_i\}$  in a geometric sequence as follows:

$$\mathcal{D} \equiv \{k_i = k_1 \lambda^{i-1}\}, \quad i = 1, 2, \dots, N \quad (\text{B.19})$$

The wavenumber bands are chosen as  $\Delta k_i = k_i \ln \lambda$ . Suppose we denote the upper  $k_i^+$  and lower  $k_i^-$  limits of the  $i^{\text{th}}$  band by

$$k_i^+ = k_i + \Delta k_i^+ \quad (\text{B.20a})$$

$$k_i^- = k_i - \Delta k_i^- \quad (\text{B.20b})$$

$$\Delta k_i^+ + \Delta k_i^- = \Delta k_i \quad (\text{B.20c})$$

Since we wish to cover the whole of wavenumber space till  $k_N$  without any gaps or over lap, for this to happen the lower limit of  $i + 1^{\text{th}}$  band should coincide with the upper limit of  $i^{\text{th}}$  band.

$$k_i + \Delta k_i^+ = k_{i+1} - \Delta k_{i+1}^- \quad (\text{B.21a})$$

$$\Delta k_{i+1}^- = \Delta k_i^- + k_{i+1} \left(1 - \frac{1}{\lambda} - \frac{\ln \lambda}{\lambda}\right) \quad (\text{B.21b})$$

$$= \Delta k_i^- + k_1 \left(1 - \frac{1}{\lambda} - \frac{\ln \lambda}{\lambda}\right) \frac{\lambda^i - \lambda}{\lambda - 1} \quad (\text{B.21c})$$

$$k_i^+ = \frac{\Delta k_i}{\lambda - 1} + \frac{k_1}{\lambda - 1} (\lambda - 1 - \ln \lambda) - \Delta k_1^- \quad (\text{B.21d})$$

$$k_i^- = \frac{\Delta k_{i-1}}{\lambda - 1} + \frac{k_1}{\lambda - 1} (\lambda - 1 - \ln \lambda) - \Delta k_1^- \quad (\text{B.21e})$$

Now without loss of generality, choose  $\Delta k_1^- = k_1 \frac{(\lambda - 1 - \ln \lambda)}{\lambda - 1}$ :

$$k_i^- = \frac{\Delta k_i}{\lambda - 1} \quad (\text{B.22a})$$

$$k_i^+ = \frac{\Delta k_{i+1}}{\lambda - 1} \quad (\text{B.22b})$$

In this frame work of discrete wavenumber bands, the integral in the

transfer terms becomes:

$$\int_{\Delta_k} dq dp \Big|_{k=k_i} \equiv \sum_{j=1}^N \sum_{l=l_{\min}}^{l_{\max}} \quad (\text{B.23a})$$

$$l_{\min}(i, j) = [\text{Log}_\lambda (|k_i - k_j|)]_> + 1 \quad (\text{B.23b})$$

$$l_{\max}(i, j) = \text{Max} \left\{ N, [\text{Log}_\lambda (k_i + k_j)]_< + 1 \right\} \quad (\text{B.23c})$$

The integration limits are chosen such that  $k_i, k_j, k_l \in \mathcal{D}$  can form a triangle.  $[x]_<, [x]_>$  corresponds to lowest and greatest integer function.

# Bibliography

- [1] M. Lesieur, A. Yaglom, and F. David, eds., *New trends in Turbulence: nouveaux aspects*, Vol. 74 (Springer, 2001).
- [2] E. Falgarone and T. Passot, *Turbulence and Magnetic Fields in Astrophysics*, 1st ed. (Springer, 2013).
- [3] G. Mathis, A. Marcowith, and J.-P. Zahn, *Astrophysical Turbulence and Instabilities*, 1st ed. (Springer, 2021).
- [4] P. A. Davidson, *Turbulence in Rotating, Stratified and Electrically Conducting Fluids* (Cambridge University Press, 2013).
- [5] H. A. Panofsky and J. A. Dutton, *Atmospheric turbulence : models and methods for engineering applications* (Wiley, 1984).
- [6] R. Govindarajan, S. Ravichandran, J. Picardo, S. Ray, S. Prasath, and V. Vasani, “Raindrops and turbulence in a cloud,” *The International Conference on Computational & Experimental Engineering and Sciences* **22**, 194–194 (2019).
- [7] G. T. Csanady, *Turbulent Diffusion in the Environment* (Springer Netherlands, 1973).
- [8] S. A. Thorpe, *An Introduction to Ocean Turbulence* (Cambridge University Press, 2007).
- [9] H. Tennekes and J. L. Lumley, *A First Course in Turbulence* (MIT Press, 1972).

- [10] P. Sagaut and C. Cambon, *Homogeneous Turbulence Dynamics* (Springer International Publishing, 2018).
- [11] J. Cardy, G. Falkovich, and K. Gawedzki, *Non-equilibrium Statistical Mechanics and Turbulence* (Cambridge University Press, 2008).
- [12] L. Euler, “Principia motus fluidorum,” *Novi Commentarii academiae scientiarum Petropolitanae*, 271–311 (1761).
- [13] P. Constantin, “On the Euler equations of incompressible fluids,” *Bulletin of the American Mathematical Society* **44**, 603–622 (2007).
- [14] R. Temam, “On the Euler equations of incompressible perfect fluids,” *Journal of Functional Analysis* **20**, 32–43 (1975).
- [15] A. J. Majda and A. L. Bertozzi, *Vorticity and Incompressible Flow* (Cambridge University Press, 2001).
- [16] G. L. Eyink, “Dissipative anomalies in singular Euler flows,” *Physica D: Nonlinear Phenomena Euler Equations: 250 Years On*, **237**, 1956–1968 (2008).
- [17] L. Onsager, “Statistical hydrodynamics,” *Nuovo Cim* **6**, 279–287 (1949).
- [18] P. Constantin, E. Weinan, and E. S. Titi, “Onsager’s conjecture on the energy conservation for solutions of Euler’s equation,” *Communications In Mathematical Physics* **165**, 207–209 (1994).
- [19] G. L. Eyink, “Energy dissipation without viscosity in ideal hydrodynamics I. Fourier analysis and local energy transfer,” *Physica D: Nonlinear Phenomena* **78**, 222–240 (1994).
- [20] R. Shvydkoy, “Lectures on the Onsager conjecture,” *Discrete and Continuous Dynamical Systems - Series S* **3**, 473–496 (2010).
- [21] J. Bec and K. Khanin, “Burgers turbulence,” *Physics Reports* **447**, 1 – 66 (2007).
- [22] U. Frisch and J. Bec, “Burgulence,” in *Les Houches - Ecole d’Ete de Physique Theorique*, Vol. 74 (Springer Berlin Heidelberg, 2001) pp. 341–383.

- [23] J. T. Beale, T. Kato, and A. Majda, “Remarks on the breakdown of smooth solutions for the 3-D Euler equations,” [Communications in Mathematical Physics](#) **94**, 61–66 (1984).
- [24] G. Ponce, “Remarks on a paper by J. T. Beale, T. Kato, and A. Majda,” [Communications in Mathematical Physics](#) **98**, 349–353 (1985).
- [25] J. Leray, “Sur le mouvement d’un liquide visqueux emplissant l’espace,” [Acta Mathematica](#) **63**, 193–248 (1934).
- [26] J. Leray and R. Terrell, “On the motion of a viscous liquid filling space,” [ArXiv e-prints](#) (2016), 10.48550/arXiv.1604.02484.
- [27] C. Sulem, P. L. Sulem, and H. Frisch, “Tracing Complex Singularities with Spectral Methods,” [Journal of Computational Physics](#) **50**, 138–161 (1983).
- [28] G. Carrier, M. Krook, and C. Pearson, [Functions of a Complex Variable: Theory and Technique](#) (Society for Industrial and Applied Mathematics, 2005).
- [29] Rose, H.A. and Sulem, P.L., “Fully developed turbulence and statistical mechanics,” [Journal de Physique](#) **39**, 441–484 (1978).
- [30] M. Lesieur, [Turbulence in fluids](#) (Springer Netherlands, 2008).
- [31] R. K. Pathria, [Statistical Mechanics](#) (Elsevier Science & Technology Books, 1972).
- [32] E. Hopf, “Statistical Hydromechanics and Functional Calculus,” [Journal of Rational Mechanics and Analysis](#) **1**, 87–123 (1952).
- [33] T. D. Lee, “On some statistical properties of hydrodynamical and magneto-hydrodynamical fields,” [Quarterly of Applied Mathematics](#) **10**, 69–74 (1952).
- [34] R. H. Kraichnan, “On the Statistical Mechanics of an Adiabatically Compressible Fluid,” [The Journal of the Acoustical Society of America](#) **27**, 438–441 (1955).

- [35] U. Frisch, A. Pomyalov, I. Procaccia, and S. S. Ray, “Turbulence in Noninteger Dimensions by Fractal Fourier Decimation,” [Physical Review Letters](#) **108**, 074501 (2012).
- [36] C. Cichowlas, P. Bonaïti, F. Debbasch, and M. Brachet, “Effective Dissipation and Turbulence in Spectrally Truncated Euler Flows,” [Physical Review Letters](#) **95**, 264502 (2005).
- [37] W. J. T. Bos and J.-P. Bertoglio, “Dynamics of spectrally truncated inviscid turbulence,” [Physics of Fluids](#) **18**, 071701 (2006).
- [38] G. Krstulovic and M.-E. Brachet, “Two-fluid model of the Truncated Euler’s Equations,” [Physica D: Nonlinear Phenomena](#) **237**, 2015–2019 (2007).
- [39] S. S. Ray, U. Frisch, S. Nazarenko, and T. Matsumoto, “Resonance phenomenon for the Galerkin-truncated Burgers and Euler equations,” [Physical Review E](#) **84**, 016301 (2011).
- [40] A. J. Majda and I. Timofeyev, “Remarkable statistical behavior for truncated Burgers–Hopf dynamics,” [Proceedings of the National Academy of Sciences](#) **97**, 12413–12417 (2000).
- [41] D. Venkataraman and S. Sankar Ray, “The onset of thermalization in finite-dimensional equations of hydrodynamics: insights from the Burgers equation,” [Proceedings of the Royal Society A: Mathematical, Physical and Engineering Sciences](#) **473**, 20160585 (2017).
- [42] P. Clark di Leoni, P. Mininni, and M.-E. Brachet, “Dynamics of partially thermalized solutions of the Burgers equation,” [Physical Review Fluids](#) **3** (2018), 10.1103/physrevfluids.3.014603.
- [43] C. Rampf, U. Frisch, and O. Hahn, “Eye of the tyger: Early-time resonances and singularities in the inviscid Burgers equation,” [Physical Review Fluids](#) **7**, 104610 (2022).
- [44] V. S. L’vov, A. Pomyalov, and I. Procaccia, “Quasi-gaussian statistics of hydrodynamic turbulence in  $\frac{4}{3} + \epsilon$  dimensions,” [Physical Review Letters](#) **89**, 064501 (2002).

- [45] A. S. Lanotte, R. Benzi, S. K. Malapaka, F. Toschi, and L. Biferale, “Turbulence on a Fractal Fourier Set,” [Physical Review Letters](#) **115**, 264502 (2015).
- [46] A. S. Lanotte, S. K. Malapaka, and L. Biferale, “On the vortex dynamics in fractal Fourier turbulence,” [European Physical Journal E: Soft Matter](#) **39**, 49 (2016).
- [47] M. Buzzicotti, L. Biferale, U. Frisch, and S. S. Ray, “Intermittency in fractal Fourier hydrodynamics: Lessons from the Burgers equation,” [Physical Review E](#) **93**, 033109 (2016).
- [48] M. Buzzicotti, A. Bhatnagar, L. Biferale, A. S. Lanotte, and S. S. Ray, “Lagrangian statistics for Navier–Stokes turbulence under Fourier-mode reduction: fractal and homogeneous decimations,” [New Journal of Physics](#) **18**, 113047 (2016).
- [49] S. S. Ray, “Non-intermittent turbulence: Lagrangian chaos and irreversibility,” [Physical Review Fluids](#) **3**, 072601 (2018).
- [50] U. Frisch, S. Kurien, R. Pandit, W. Pauls, S. S. Ray, A. Wirth, and J.-Z. Zhu, “Hyperviscosity, Galerkin Truncation, and Bottlenecks in Turbulence,” [Physical Review Letters](#) **101**, 144501 (2008).
- [51] U. Frisch, S. S. Ray, G. Sahoo, D. Banerjee, and R. Pandit, “Real-Space Manifestations of Bottlenecks in Turbulence Spectra,” [Physical Review Letters](#) **110**, 064501 (2013).
- [52] D. Banerjee and S. S. Ray, “Transition from dissipative to conservative dynamics in equations of hydrodynamics,” [Physical Review E](#) **90**, 041001 (2014).
- [53] E. Lorenz, “The Butterfly Effect,” in *The Chaos Avant-Garde*, Vol. Volume 39 (WORLD SCIENTIFIC, 2001) pp. 91–94.
- [54] E. N. Lorenz, *The essence of chaos* (University of Washington Press, 1993).

- [55] A. Das, S. Chakrabarty, A. Dhar, A. Kundu, D. A. Huse, R. Moessner, S. S. Ray, and S. Bhattacharjee, “Light-cone spreading of perturbations and the butterfly effect in a classical spin chain,” [Physical Review Letters](#) **121**, 024101 (2018).
- [56] T. Bilitewski, S. Bhattacharjee, and R. Moessner, “Temperature dependence of the butterfly effect in a classical many-body system,” [Physical Review Letters](#) **121**, 250602 (2018).
- [57] T. Bilitewski, S. Bhattacharjee, and R. Moessner, “Classical many-body chaos with and without quasiparticles,” [Physical Review B](#) **103**, 174302 (2021).
- [58] A. I. Larkin and Y. N. Ovchinnikov, “Quasiclassical method in the theory of superconductivity,” [Soviet Journal of Experimental and Theoretical Physics](#) **28**, 1200 (1969).
- [59] S. H. Shenker and D. Stanford, “Black holes and the butterfly effect,” [Journal of High Energy Physics](#) **2014**, 67 (2014).
- [60] J. Maldacena, S. H. Shenker, and D. Stanford, “A bound on chaos,” [Journal of High Energy Physics](#) **2016**, 106 (2016).
- [61] S. D. Murugan, D. Kumar, S. Bhattacharjee, and S. S. Ray, “Many-Body Chaos in Thermalized Fluids,” [Physical Review Letters](#) **127**, 124501 (2021).
- [62] D. Bandak, N. Goldenfeld, A. A. Mailybaev, and G. Eyink, “Dissipation-range fluid turbulence and thermal noise,” [Physical Review E](#) **105**, 065113 (2022).
- [63] J.-D. Fournier and U. Frisch, “d-dimensional turbulence,” [Physical Review A](#) **17**, 747–762 (1978).
- [64] A. Celani, S. Musacchio, and D. Vincenzi, “Turbulence in More than Two and Less than Three Dimensions,” [Physical Review Letters](#) **104**, 184506 (2010).
- [65] O. Reynolds, “An Experimental Investigation of the Circumstances Which Determine Whether the Motion of Water Shall Be Direct or Sinuous, and of the Law of Resistance in Parallel Channels,” [Proceedings of the Royal Society of London Series I](#) **35**, 84–99 (1883).

- [66] C. Fefferman, “Existence and smoothness of the Navier-Stokes equation,” [The Millennium Prize Problems](#) (2006), 10.2139/ssrn.4473471.
- [67] U. Frisch, *Turbulence: The Legacy of A. N. Kolmogorov* (Cambridge University Press, 1995).
- [68] W. D. McComb, *The Physics of Fluid Turbulence* (Clarendon Press, 1990).
- [69] L. F. Richardson, *Weather Prediction by Numerical Process* (Cambridge University Press, 1922).
- [70] A. N. Kolmogorov, “Equations of turbulent motion in an incompressible fluid,” [Doklady Akademii Nauk SSSR](#) **30**, 299–303 (1941).
- [71] Y. Narita, *Plasma Turbulence in the Solar System* (Springer, 2012).
- [72] K. R. Sreenivasan and R. A. Antonia, “The Phenomenology of Small-Scale Turbulence,” [Annual Review of Fluid Mechanics](#) **29**, 435–472 (1997).
- [73] U. Frisch and R. Morf, “Intermittency in nonlinear dynamics and singularities at complex times,” [Physical Review A](#) **23**, 2673–2705 (1981).
- [74] F. Anselmet, Y. Gagne, E. J. Hopfinger, and R. A. Antonia, “High-order velocity structure functions in turbulent shear flows,” [Journal of Fluid Mechanics](#) **140**, 63–89 (1984).
- [75] D. Buaria, A. Pumir, E. Bodenschatz, and P. K. Yeung, “Extreme velocity gradients in turbulent flows,” [New Journal of Physics](#) **21**, 043004 (2019).
- [76] G. I. Taylor, “Statistical Theory of Turbulence,” [Proceedings of the Royal Society of London. Series A, Mathematical and Physical Sciences](#) **151**, 421–444 (1935).
- [77] G. I. Taylor, “Diffusion by Continuous Movements,” [Proceedings of the London Mathematical Society](#) **s2-20**, 196–212 (1922).
- [78] A. N. Kolmogorov, “Local structure of turbulence in an incompressible viscous fluid at very large Reynolds numbers,” [Doklady Akademii Nauk SSSR](#) **30**, 299–301 (1941).

- [79] A. N. Kolmogorov, “On the degeneration of isotropic turbulence in an incompressible viscous fluid,” [Doklady Akademii Nauk SSSR](#) **31**, 319–323 (1941).
- [80] A. N. Kolmogorov, “Dissipation of energy in isotropic turbulence,” [Doklady Akademii Nauk SSSR](#) **32**, 325–327 (1941).
- [81] J. C. R. Hunt and J. C. Vassilicos, “Kolmogorovs Contributions to the Physical and Geometrical Understanding of Small-Scale Turbulence and Recent Developments,” [Proceedings of the Royal Society of London. Series A: Mathematical and Physical Sciences](#) **434**, 183–210 (1991).
- [82] J. Jiménez, “The Contributions of A. N. Kolmogorov to the theory of turbulence,” [Arbor CLXXVIII](#) **704**, 589–606 (2004).
- [83] R. Benzi, S. Ciliberto, R. Tripicciono, C. Baudet, F. Massaioli, and S. Succi, “Extended self-similarity in turbulent flows,” [Physical Review E](#) **48**, R29–R32 (1993).
- [84] A. Kolmogorov, “A refinement of previous hypotheses concerning the local structure of turbulence in a viscous incompressible fluid at high Reynolds number,” [Journal of Fluid Mechanics](#) **13**, 82–85 (1962).
- [85] Z.-S. She and E. Leveque, “Universal scaling laws in fully developed turbulence,” [Physical Review Letters](#) **72**, 336–339 (1994).
- [86] R. Benzi, G. Paladin, G. Parisi, and A. Vulpiani, “On the multifractal nature of fully developed turbulence and chaotic systems,” [Journal of Physics A: Mathematical and General](#) **17**, 3521–3531 (1984).
- [87] G. Parisi and U. Frisch, “On the singularity structure of fully developed turbulence in Turbulence and predictability in geophysical fluid dynamics and climate dynamics,” [NTurbulence and Predictability of Geophysical Flows and Climate Dynamics](#) **88** (1985).
- [88] D. R. Chapman, “Computational Aerodynamics Development and Outlook,” [AIAA Journal](#) **17**, 1293–1313 (1979).

- [89] S. G. Saddoughi and S. V. Veeravalli, “Local isotropy in turbulent boundary layers at high Reynolds number,” *Journal of Fluid Mechanics* **268**, 333–372 (1994).
- [90] N. D. Katopodes, “Chapter 8 - Turbulent Flow,” in *Free-Surface Flow*, edited by N. D. Katopodes (Butterworth-Heinemann, 2019) pp. 566–650.
- [91] G. Boffetta, A. Mazzino, and A. Vulpiani, “Twenty-five years of multifractals in fully developed turbulence: a tribute to Giovanni Paladin,” *Journal of Physics A: Mathematical and Theoretical* **41**, 363001 (2008).
- [92] G. Paladin and A. Vulpiani, “Anomalous scaling laws in multifractal objects,” *Physics Reports* **156**, 147–225 (1987).
- [93] S. Pope, *Turbulent Flows* (Cambridge University Press, 2000).
- [94] P. Sagaut, “EDQNM Modeling,” in *Large Eddy Simulation for Incompressible Flows: An Introduction*, edited by P. Sagaut (Springer, 2002) pp. 391–395.
- [95] S. A. Orszag, “Analytical theories of turbulence,” *Journal of Fluid Mechanics* **41**, 363–386 (1970).
- [96] R. H. Kraichnan, “Inertial Ranges in Two-Dimensional Turbulence,” *The Physics of Fluids* **10**, 1417–1423 (1967).
- [97] A. Fouquet, M. Lesieur, J. C. André, and C. Basdevant, “Evolution of high Reynolds number two-dimensional turbulence,” *Journal of Fluid Mechanics* **72**, 305–319 (1975).
- [98] R. H. Kraichnan, “Helical turbulence and absolute equilibrium,” *Journal of Fluid Mechanics* **59**, 745–752 (1973).
- [99] A. Pouquet, U. Frisch, and J. Leorat, “Strong MHD helical turbulence and the nonlinear dynamo effect,” *Journal of Fluid Mechanics* **77**, 321–354 (1976).
- [100] A. Pouquet, “On two-dimensional magnetohydrodynamic turbulence,” *Journal of Fluid Mechanics* **88**, 1–16 (1978).

- [101] O. Schilling and Y. Zhou, “Triadic energy transfers in non-helical magnetohydrodynamic turbulence,” *Journal of Plasma Physics* **68**, 389–406 (2002).
- [102] U. Frisch, A. Pouquet, J. LÉOrat, and A. Mazure, “Possibility of an inverse cascade of magnetic helicity in magnetohydrodynamic turbulence,” *Journal of Fluid Mechanics* **68**, 769–778 (1975).
- [103] S. M. Tobias, “The turbulent dynamo,” *Journal of Fluid Mechanics* **912**, P1 (2021).
- [104] F. Rincon, “Dynamo theories,” *Journal of Plasma Physics* **85**, 205850401 (2019).
- [105] E. Levich, “The Hamiltonian formulation of the Euler equation and subsequent constraints on the properties of randomly stirred fluids,” *Physics Letters A* **86**, 165–168 (1981).
- [106] T. D. Lee and C. N. Yang, “Statistical Theory of Equations of State and Phase Transitions. II. Lattice Gas and Ising Model,” *Physical Review* **87**, 410–419 (1952).
- [107] C. Cichowlas and M.-E. Brachet, “Evolution of complex singularities in Kida–Pelz and Taylor–Green inviscid flows,” *Fluid Dynamics Research* **36**, 239–248 (2005).
- [108] E. Hopf, “The partial differential equation  $ut + uux = \mu xx$ ,” *Communications on Pure and Applied Mathematics* **3**, 201–230 (1950).
- [109] R. H. Kraichnan, “The structure of isotropic turbulence at very high Reynolds numbers,” *Journal of Fluid Mechanics* **5**, 497–543 (1959).
- [110] A. N. Kolmogorov, V. Levin, J. C. R. Hunt, O. M. Phillips, and D. Williams, “The local structure of turbulence in incompressible viscous fluid for very large Reynolds numbers,” *Proceedings of the Royal Society of London. Series A: Mathematical and Physical Sciences* **434**, 9–13 (1991).

- [111] T. Buckmaster, C. D. Lellis, L. Székelyhidi, and V. Vicol, “Onsager’s Conjecture for Admissible Weak Solutions,” *Communications on Pure and Applied Mathematics* **72**, 229–274 (2019).
- [112] J. D. Gibbon, “The three-dimensional Euler equations: Where do we stand?” *Physica D: Nonlinear Phenomena Euler Equations: 250 Years On*, **237**, 1894–1904 (2008).
- [113] J. D. Gibbon, M. Bustamante, and R. M. Kerr, “The three-dimensional Euler equations: singular or non-singular?” *Nonlinearity* **21**, T123–T129 (2008).
- [114] U. Frisch, T. Matsumoto, and J. Bec, “Singularities of Euler Flow? Not Out of the Blue!” *Journal of Statistical Physics* **113**, 761–781 (2002).
- [115] M. E. Brachet, D. I. Meiron, S. A. Orszag, B. G. Nickel, R. H. Morf, and U. Frisch, “Small-scale structure of the Taylor–Green vortex,” *Journal of Fluid Mechanics* **130**, 411–452 (1983).
- [116] M. E. Brachet, M. Meneguzzi, A. Vincent, H. Politano, and P. L. Sulem, “Numerical evidence of smooth self similar dynamics and possibility of subsequent collapse for three dimensional ideal flows,” *Physics of Fluids A: Fluid Dynamics* **4**, 2845–2854 (1992).
- [117] O. N. Boratav, R. B. Pelz, and N. J. Zabusky, “Reconnection in orthogonally interacting vortex tubes: Direct numerical simulations and quantifications,” *Physics of Fluids A: Fluid Dynamics* **4**, 581–605 (1992).
- [118] R. M. Kerr, “Evidence for a singularity of the three-dimensional, incompressible Euler equations,” *Physics of Fluids A: Fluid Dynamics* **5**, 1725–1746 (1993).
- [119] M. J. Shelley, D. I. Meiron, and S. A. Orszag, “Dynamical aspects of vortex reconnection of perturbed anti-parallel vortex tubes,” *Journal of Fluid Mechanics* **246**, 613–652 (1993).
- [120] O. N. Boratav and R. B. Pelz, “Direct numerical simulation of transition to turbulence from a high-symmetry initial condition,” *Physics of Fluids* **6**, 2757–2784 (1994).

- [121] R. M. Kerr, “Velocity and scaling of collapsing Euler vortices,” [Physics of Fluids](#) **17**, 075103 (2005).
- [122] R. Pelz and K. Ohkitani, “Linearly strained flows with and without boundaries - The regularizing effect of the pressure term,” [Fluid Dynamics Research](#) **36**, 193–210 (2005).
- [123] T. Y. Hou and R. Li, “Dynamic Depletion of Vortex Stretching and Non-Blowup of the 3-D Incompressible Euler Equations,” [Journal of Nonlinear Science](#) **16**, 639–664 (2006).
- [124] G. Luo and T. Y. Hou, “Potentially singular solutions of the 3D axisymmetric Euler equations,” [Proceedings of the National Academy of Sciences](#) **111**, 12968–12973 (2014).
- [125] D. W. Moore, “The Spontaneous Appearance of a Singularity in the Shape of an Evolving Vortex Sheet,” [Proceedings of the Royal Society of London. Series A, Mathematical and Physical Sciences](#) **365**, 105–119 (1979).
- [126] R. H. Morf, S. A. Orszag, and U. Frisch, “Spontaneous Singularity in Three-Dimensional Inviscid, Incompressible Flow,” [Physical Review Letters](#) **44**, 572–575 (1980).
- [127] R. B. Pelz and Y. Gulak, “Evidence for a Real-Time Singularity in Hydrodynamics from Time Series Analysis,” [Physical Review Letters](#) **79**, 4998–5001 (1997).
- [128] Y. Gulak and R. B. Pelz, “High-symmetry Kida flow: Time series analysis and resummation,” [Fluid Dynamics Research](#) **36**, 211 (2005).
- [129] A. J. Chorin, “The evolution of a turbulent vortex,” [Communications in Mathematical Physics](#) **83**, 517–535 (1982).
- [130] E. D. Siggia, “Collapse and amplification of a vortex filament,” [The Physics of Fluids](#) **28**, 794–805 (1985).
- [131] A. Pumir and E. Siggia, “Collapsing solutions to the 3-D Euler equations,” [Physics of Fluids A: Fluid Dynamics](#) **2**, 220–241 (1990).

- [132] J. B. Bell and D. L. Marcus, “Vorticity intensification and transition to turbulence in three-dimensional Euler equations,” [Communications in Mathematical Physics](#) **147**, 371–394 (1992).
- [133] R. B. Pelz, “Locally self-similar, finite-time collapse in a high-symmetry vortex filament model,” [Physical Review E](#) **55**, 1617–1626 (1997).
- [134] R. Grauer and T. C. Sideris, “Numerical computation of 3D incompressible ideal fluids with swirl,” [Physical Review Letters](#) **67**, 3511–3514 (1991).
- [135] R. Grauer, C. Marliani, and K. Germaschewski, “Adaptive Mesh Refinement for Singular Solutions of the Incompressible Euler Equations,” [Physical Review Letters](#) **80**, 4177–4180 (1998).
- [136] P. Orlandi and G. F. Carnevale, “Nonlinear amplification of vorticity in inviscid interaction of orthogonal Lamb dipoles,” [Physics of Fluids](#) **19**, 057106 (2007).
- [137] S. S. V. Kolluru, P. Sharma, and R. Pandit, “Insights from a pseudospectral study of a potentially singular solution of the three-dimensional axisymmetric incompressible Euler equation,” [Physical Review E](#) **105**, 065107 (2022).
- [138] C. S. Campolina and A. A. Mailybaev, “Chaotic Blowup in the 3D Incompressible Euler Equations on a Logarithmic Lattice,” [Physical Review Letters](#) **121**, 064501 (2018).
- [139] A. Larios, M. R. Petersen, E. S. Titi, and B. Wingate, “A computational investigation of the finite-time blow-up of the 3D incompressible Euler equations based on the Voigt regularization,” [Theoretical and Computational Fluid Dynamics](#) **32**, 23–34 (2018).
- [140] P. Constantin, C. Fefferman, and A. J. Majda, “Geometric constraints on potentially singular solutions for the 3-D Euler equations,” [Communications in Partial Differential Equations](#) **21**, 559–571 (1996).
- [141] P. Constantin, “Singular, weak and absent: Solutions of the Euler equations,” [Physica D: Nonlinear Phenomena](#) **237**, 1926–1931 (2008).

- [142] D. Chae, “On the finite-time singularities of the 3D incompressible Euler equations,” [Communications on Pure and Applied Mathematics](#) **60**, 597–617 (2007).
- [143] J. DENG, T. Y. Hou, and X. YU, “Geometric Properties and Nonblowup of 3D Incompressible Euler Flow,” [Communications in Partial Differential Equations](#) **30**, 225–243 (2005).
- [144] J. Deng, T. Y. Hou, and X. Yu, “Improved Geometric Conditions for Non-Blowup of the 3D Incompressible Euler Equation,” [Communications in Partial Differential Equations](#) **31**, 293–306 (2006).
- [145] T. Y. Hou and R. Li, “Blowup or no blowup? The interplay between theory and numerics,” [Physica D: Nonlinear Phenomena Euler Equations: 250 Years On](#), **237**, 1937–1944 (2008).
- [146] C. Canuto, M. Y. Hussaini, A. Quarteroni, and T. A. Zang, Jr, [Spectral Methods in Fluid Dynamics](#) (Springer Science & Business Media, 2012).
- [147] R. J. LeVeque, [Numerical Methods for Conservation Laws](#) (Birkhäuser Basel, 1992).
- [148] M. Bustamante and M.-E. Brachet, “Interplay between the Beale-Kato-Majda theorem and the analyticity-strip method to investigate numerically the incompressible Euler singularity problem,” [Physical Review E](#) **86**, 066302 (2012).
- [149] T. D. Drivas and H. Q. Nguyen, “Remarks on the Emergence of Weak Euler Solutions in the Vanishing Viscosity Limit,” [Journal of NonLinear Science](#) **29**, 709–721 (2019).
- [150] R. M. Pereira, R. Nguyen van yen, M. Farge, and K. Schneider, “Wavelet methods to eliminate resonances in the Galerkin-truncated Burgers and Euler equations,” [Physical Review E](#) **87**, 033017 (2013).
- [151] M. Farge, N. Okamoto, K. Schneider, and K. Yoshimatsu, “Wavelet-based regularization of the Galerkin truncated three-dimensional incompressible Euler flows,” [Physical Review E](#) **96**, 063119 (2017).

- [152] S. D. Murugan, U. Frisch, S. Nazarenko, N. Besse, and S. S. Ray, “Suppressing thermalization and constructing weak solutions in truncated inviscid equations of hydrodynamics: Lessons from the Burgers equation,” [Physical Review Research](#) **2**, 033202 (2020).
- [153] R. M. Pereira, N. N. van yen, K. Schneider, and M. Farge, “Adaptive solution of initial value problems by a dynamical Galerkin scheme,” [Multiscale Modeling and Simulation](#) **20**, 1147–1166 (2022).
- [154] G. Krstulovic, P. D. Mininni, M. E. Brachet, and A. Pouquet, “Cascades, thermalization, and eddy viscosity in helical Galerkin truncated Euler flows,” [Physical Review E](#) **79**, 056304 (2009).
- [155] M. K. Verma, “Boltzmann equation and hydrodynamic equations: their equilibrium and non-equilibrium behaviour,” [Philosophical Transactions of the Royal Society A: Mathematical, Physical and Engineering Sciences](#) **378**, 20190470 (2020).
- [156] M. K. Verma, S. Bhattacharya, and S. Chatterjee, “Euler turbulence and thermodynamic equilibrium,” [ArXiv e-prints](#) (2020), 10.48550/arXiv.2004.09053.
- [157] S. D. Murugan, “[Strain field from Galerkin-truncated Euler equation.](#)” (2022).
- [158] S. D. Murugan, “[Vorticity isosurfaces from Galerkin-truncated Euler equation.](#)” (2022).
- [159] A. J. Chorin, “Turbulence and vortex stretching on a lattice,” [Communications on Pure and Applied Mathematics](#) **39**, S47–S65 (1986).
- [160] S. D. Murugan, “[Perturbed vortex sheets showing onset of thermalization,](#)” (2022).
- [161] S. D. Murugan, “[Perturbed vortex sheets showing onset of thermalization,](#)” (2022).
- [162] S. D. Murugan, “[Vortex sheets disturbed by Taylor-Green flow, showing onset of thermalization,](#)” (2023).

- [163] S. D. Murugan, “Perturbed vortex filament showing onset of thermalization,” (2023).
- [164] S. S. Ray, “Thermalized solutions, statistical mechanics and turbulence: An overview of some recent results,” *Pramana* **84**, 395–407 (2015).
- [165] M. P. Bonkile, A. Awasthi, C. Lakshmi, V. Mukundan, and V. S. Aswin, “A systematic literature review of Burgers equation with recent advances,” *Pramana* **90**, 69 (2018).
- [166] J. M. Burgers, “Hydrodynamics — On the application of statistical mechanics to the theory of turbulent fluid motion. IV,” in *Selected Papers of J. M. Burgers*, edited by F. T. M. Nieuwstadt and J. A. Steketee (Springer Netherlands, 1995) pp. 143–180.
- [167] J. Burgers, “A Mathematical Model Illustrating the Theory of Turbulence,” in *Advances in Applied Mechanics*, Vol. 1 (Elsevier, 1948) pp. 171–199.
- [168] J. D. Cole, “On a quasi-linear parabolic equation occurring in aerodynamics,” *Quarterly of Applied Mathematics* **9**, 225–236 (1951).
- [169] M. Kardar, G. Parisi, and Y.-C. Zhang, “Dynamic Scaling of Growing Interfaces,” *Physical Review Letters* **56**, 889–892 (1986).
- [170] M. Kardar and Y.-C. Zhang, “Scaling of Directed Polymers in Random Media,” *Physical Review Letters* **58**, 2087–2090 (1987).
- [171] J. P. Bouchaud, M. Mézard, and G. Parisi, “Scaling and intermittency in Burgers turbulence,” *Physical Review E* **52**, 3656–3674 (1995).
- [172] Y. B. Zel’dovich, “Gravitational instability: An approximate theory for large density perturbations.” *Astronomy and Astrophysics* **5**, 84–89 (1970).
- [173] D. Chowdhury, L. Santen, and A. Schadschneider, “Statistical physics of vehicular traffic and some related systems,” *Physics Reports* **329**, 199–329 (2000).
- [174] S. S. Shen, *A Course on Nonlinear Waves* (Springer Netherlands, 1993).

- [175] S. S. Ray, “Galerkin-truncated, inviscid equations of hydrodynamics: Tygers and Thermalisation,” (2019).
- [176] S. S. Ray, “Weak, dissipative solutions from truncated, inviscid equations of hydrodynamics: Tyger Purging,” (2019).
- [177] A. Noullez and M. Vergassola, “A fast legendre transform algorithm and applications to the adhesion model,” *Journal of Scientific Computing* **9**, 259–281 (1994).
- [178] D. Mitra, J. Bec, R. Pandit, and U. Frisch, “Is Multiscaling an Artifact in the Stochastically Forced Burgers Equation?” *Physical Review Letters* **94**, 194501 (2005).
- [179] W. H. Press, S. A. Teukolsky, W. T. Vetterling, and B. P. Flannery, *Numerical Recipes in Fortran 77* (Cambridge University Press, 1992).
- [180] R. M. Kerr, “Bounds for Euler from vorticity moments and line divergence,” *Journal of Fluid Mechanics* **729**, R2 (2013).
- [181] J. Yao and F. Hussain, “On singularity formation via viscous vortex reconnection,” *Journal of Fluid Mechanics* **888**, R2 (2020).
- [182] J. Yao and F. Hussain, “A physical model of turbulence cascade via vortex reconnection sequence and avalanche,” *Journal of Fluid Mechanics* **883**, A51 (2020).
- [183] T. M. Elgindi, “Finite-time singularity formation for  $c^{1,\alpha}$  solutions to the incompressible euler equations on  $\mathcal{R}^3$ ,” *ArXiv e-prints* (2019), 10.48550/arXiv.1904.04795.
- [184] R. Agrawal, A. Alexakis, M. E. Brachet, and L. S. Tuckerman, “Turbulent cascade, bottleneck, and thermalized spectrum in hyperviscous flows,” *Physical Review Fluids* **5**, 024601 (2020).
- [185] P. E. Hamlington, J. Schumacher, and W. J. A. Dahm, “Direct assessment of vorticity alignment with local and nonlocal strain rates in turbulent flows,” *Physics of Fluids* **20**, 111703 (2008).

- [186] N. Fehn, M. Kronbichler, P. Munch, and W. A. Wall, “Numerical evidence of anomalous energy dissipation in incompressible Euler flows,” *Journal of Fluid Mechanics* **932** (2022), [10.1017/jfm.2021.1003](https://doi.org/10.1017/jfm.2021.1003).
- [187] E. N. Lorenz, “Deterministic nonperiodic flow,” *Journal of the atmospheric sciences* **20**, 130–141 (1963).
- [188] E. Lorenz, “The butterfly effect,” *World Scientific Series on Nonlinear Science Series A* **39**, 91–94 (2000).
- [189] R. C. Hilborn, “Sea gulls, butterflies, and grasshoppers: A brief history of the butterfly effect in nonlinear dynamics,” *American Journal of Physics* **72**, 425–427 (2004).
- [190] S. Ruidas and S. Banerjee, “Many-body chaos and anomalous diffusion across thermal phase transitions in two dimensions,” *SciPost Phys.* **11**, 087 (2021).
- [191] M. Blake, “Universal charge diffusion and the butterfly effect in holographic theories,” *Physical Review Letters* **117**, 091601 (2016).
- [192] M. Blake, R. A. Davison, and S. Sachdev, “Thermal diffusivity and chaos in metals without quasiparticles,” *Physical Review D* **96**, 106008 (2017).
- [193] Y. Gu, A. Lucas, and X.-L. Qi, “Energy diffusion and the butterfly effect in inhomogeneous Sachdev-Ye-Kitaev chains,” *SciPost Physics* **2**, 018 (2017).
- [194] A. Lucas, “Constraints on hydrodynamics from many-body quantum chaos,” *ArXiv e-prints* (2017), [10.48550/arXiv.1710.01005](https://arxiv.org/abs/10.48550/arXiv.1710.01005).
- [195] Y. Werman, S. A. Kivelson, and E. Berg, “Quantum chaos in an electron-phonon bad metal,” *ArXiv e-prints* (2017), [10.48550/arXiv.1705.07895](https://arxiv.org/abs/10.48550/arXiv.1705.07895).
- [196] A. A. Patel, D. Chowdhury, S. Sachdev, and B. Swingle, “Quantum butterfly effect in weakly interacting diffusive metals,” *Physical Review X* **7**, 031047 (2017).
- [197] A. A. Patel and S. Sachdev, “Quantum chaos on a critical fermi surface,” *Proceedings of the National Academy of Sciences* **114**, 1844–1849 (2017).

- [198] A. Kitaev, “[KITP Program: Entanglement in Strongly-Correlated Quantum Matter](#),” .
- [199] S. Banerjee and E. Altman, “Solvable model for a dynamical quantum phase transition from fast to slow scrambling,” [Physical Review B](#) **95**, 134302 (2017).
- [200] J. S. Cotler, G. Gur-Ari, M. Hanada, J. Polchinski, P. Saad, S. H. Shenker, D. Stanford, A. Streicher, and M. Tezuka, “Black holes and random matrices,” [Journal of High Energy Physics](#) **2017**, 118 (2017).
- [201] R. H. Kraichnan, “Inertial-range transfer in two and three-dimensional turbulence,” [Journal of Fluid Mechanics](#) **47**, 525–535 (1971).
- [202] D. A. Roberts and D. Stanford, “Diagnosing chaos using four-point functions in two-dimensional conformal field theory,” [Physical Review Letters](#) **115**, 131603 (2015).
- [203] B. Dóra and R. Moessner, “Out-of-time-ordered density correlators in luttinger liquids,” [Physical Review Letters](#) **119**, 026802 (2017).
- [204] I. L. Aleiner, L. Faoro, and L. B. Ioffe, “Microscopic model of quantum butterfly effect: Out-of-time-order correlators and traveling combustion waves,” [Annals of Physics](#) **375**, 378–406 (2016).
- [205] Y. Chen, “Universal Logarithmic Scrambling in Many Body Localization,” [ArXiv e-prints](#) (2016), 10.48550/arXiv.1608.02765.
- [206] M. J. Klug, M. S. Scheurer, and J. Schmalian, “Hierarchy of information scrambling, thermalization, and hydrodynamic flow in graphene,” [Physical Review B](#) **98**, 045102 (2018).
- [207] S. Sachdev and J. Ye, “Gapless spin-fluid ground state in a random quantum heisenberg magnet,” [Physical Review Letters](#) **70**, 3339–3342 (1993).
- [208] J. Kurchan, “Quantum bound to chaos and the semiclassical limit,” [Journal of Statistical Physics](#) **171**, 965–979 (2018).
- [209] S. D. Murugan, “[Decorrelator Spread - Chaos in a thermalized fluid](#),” (2021).

- [210] W. T. Ashurst, A. R. Kerstein, R. M. Kerr, and C. H. Gibson, “Alignment of vorticity and scalar gradient with strain rate in simulated Navier–Stokes turbulence,” *The Physics of Fluids* **30:8**, 2343–2353 (1987).
- [211] B. Galanti, J. D. Gibbon, and M. Heritage, “Vorticity alignment results for the three-dimensional Euler and Navier - Stokes equations,” *Nonlinearity* **10**, 1675 (1997).
- [212] T. Scaffidi and E. Altman, “Chaos in a classical limit of the sachdev-ye-kitaev model,” *Physical Review B* **100**, 155128 (2019).
- [213] H. E. Stanley and P. Meakin, “Multifractal phenomena in physics and chemistry,” *Nature* **335**, 405–409 (1988).
- [214] I. Procaccia, “Universal properties of dynamically complex systems: the organization of chaos,” *Nature* **333**, 618–623 (1988).
- [215] M. C. Cross and P. C. Hohenberg, “Pattern formation outside of equilibrium,” *Reviews of modern physics* **65**, 851 (1993).
- [216] M. F. Shlesinger, G. M. Zaslavsky, and J. Klafter, “Strange kinetics,” *Nature* **363**, 31–37 (1993).
- [217] K. R. Sreenivasan, “Fractals and Multifractals in Fluid Turbulence,” *Annual Review of Fluid Mechanics* **23**, 539–604 (1991).
- [218] B. Dubrulle and J. D. Gibbon, “A correspondence between the multifractal model of turbulence and the Navier–Stokes equations,” *Philosophical Transactions of the Royal Society A: Mathematical, Physical and Engineering Sciences* **380**, 20210092 (2022).
- [219] F. Argoul, A. Arneodo, G. Grasseau, Y. Gagne, E. J. Hopfinger, and U. Frisch, “Wavelet analysis of turbulence reveals the multifractal nature of the Richardson cascade,” *Nature* **338**, 51–53 (1989).
- [220] J.-F. Muzy, E. Bacry, and A. Arneodo, “Wavelets and multifractal formalism for singular signals: Application to turbulence data,” *Physical Review Letters* **67**, 3515 (1991).

- [221] U. Frisch and G. Parisi, “Turbulence and Predictability of Geophysical Fluid Dynamics and Climate Dynamics,” [Proceedings of the International School of Physics Enrico Fermi, Varenna, 1985](#) **85** (1985).
- [222] D. Mitra and R. Pandit, “Varieties of Dynamic Multiscaling in Fluid Turbulence,” [Physical Review Letters](#) **93**, 024501 (2004).
- [223] D. Mitra and R. Pandit, “Dynamics of Passive-Scalar Turbulence,” [Physical Review Letters](#) **95**, 144501 (2005).
- [224] S. S. Ray, D. Mitra, and R. Pandit, “The universality of dynamic multiscaling in homogeneous, isotropic Navier–Stokes and passive-scalar turbulence,” [New Journal of Physics](#) **10**, 033003 (2008).
- [225] S. S. Ray, D. Mitra, P. Perlekar, and R. Pandit, “Dynamic Multiscaling in Two-Dimensional Fluid Turbulence,” [Physical Review Letters](#) **107**, 184503 (2011).
- [226] S. K. Rathor, S. Chakraborty, and S. S. Ray, “Dynamic scaling in rotating turbulence: A shell model study,” [Physical Review E](#) **105**, L063102 (2022).
- [227] M. Nelkin, “Multifractal scaling of velocity derivatives in turbulence,” [Physical Review A](#) **42**, 7226–7229 (1990).
- [228] P. Kailasnath, K. R. Sreenivasan, and G. Stolovitzky, “Probability density of velocity increments in turbulent flows,” [Physical Review Letters](#) **68**, 2766–2769 (1992).
- [229] R. Benzi and L. Biferale, “Fully Developed Turbulence and the Multifractal Conjecture,” [Journal of Statistical Physics](#) **135**, 977–990 (2009).
- [230] A. La Porta, G. A. Voth, A. M. Crawford, J. Alexander, and E. Bodenschatz, “Fluid particle accelerations in fully developed turbulence,” [Nature](#) **409**, 1017–1019 (2001).
- [231] U. Frisch, “From global scaling, à la Kolmogorov, to local multifractal scaling in fully developed turbulence,” [Proceedings of the Royal Society of London. Series A: Mathematical and Physical Sciences](#) **434**, 89–99 (1991).

- [232] C. Meneveau and K. R. Sreenivasan, “The multifractal spectrum of the dissipation field in turbulent flows,” *Nuclear Physics B - Proceedings Supplements* **2**, 49–76 (1987).
- [233] C. Meneveau and K. R. Sreenivasan, “Simple multifractal cascade model for fully developed turbulence,” *Physical Review Letters* **59**, 1424–1427 (1987).
- [234] C. Meneveau and K. R. Sreenivasan, “The multifractal nature of turbulent energy dissipation,” *Journal of Fluid Mechanics* **224**, 429–484 (1991).
- [235] D. Kuzzay, E.-W. Saw, F. J. W. A. Martins, D. Faranda, J.-M. Foucaut, F. Daviaud, and B. Dubrulle, “New method for detecting singularities in experimental incompressible flows,” *Nonlinearity* **30**, 2381 (2017).
- [236] F. Nguyen, J.-P. Laval, P. Kestener, A. Cheskidov, R. Shvydkoy, and B. Dubrulle, “Local estimates of Hölder exponents in turbulent vector fields,” *Physical Review E* **99**, 053114 (2019).
- [237] B. Dubrulle, “Beyond Kolmogorov cascades,” *Journal of Fluid Mechanics* **867**, P1 (2019).
- [238] F. Nguyen, J.-P. Laval, and B. Dubrulle, “Characterizing most irregular small-scale structures in turbulence using local Hölder exponents,” *Physical Review E* **102**, 063105 (2020).
- [239] C. Reas and B. Fry, *Processing: a programming handbook for visual designers and artists* (MIT Press, 2007).
- [240] M. Pearson, *Generative art: a practical guide using processing* (Simon and Schuster, 2011).
- [241] E. Perlman, R. Burns, Y. Li, and C. Meneveau, “Data exploration of turbulence simulations using a database cluster,” in *Proceedings of the 2007 ACM/IEEE Conference on Supercomputing* (2007) pp. 1–11.
- [242] Y. Li, E. Perlman, M. Wan, Y. Yang, C. Meneveau, R. Burns, S. Chen, A. Szalay, and G. Eyink, “A public turbulence database cluster and

- applications to study Lagrangian evolution of velocity increments in turbulence,” [Journal of Turbulence](#) **9**, N31 (2008).
- [243] P. Yeung, D. Donzis, and K. Sreenivasan, “Dissipation, enstrophy and pressure statistics in turbulence simulations at high Reynolds numbers,” [Journal of Fluid Mechanics](#) **700**, 5–15 (2012).
- [244] G. L. Eyink and K. R. Sreenivasan, “Onsager and the theory of hydrodynamic turbulence,” [Reviews of Modern Physics](#) **78**, 87–135 (2006).
- [245] P. Grassberger and I. Procaccia, “Characterization of Strange Attractors,” [Physical Review Letters](#) **50**, 346–349 (1983).
- [246] P. Debue, V. Valori, C. Cuvier, F. Daviaud, J.-M. Foucaut, J.-P. Laval, C. Wiertel, V. Padilla, and B. Dubrulle, “Three-dimensional analysis of precursors to non-viscous dissipation in an experimental turbulent flow,” [Journal of Fluid Mechanics](#) **914**, A9 (2021).
- [247] J. R. Picardo, A. Bhatnagar, and S. S. Ray, “Lagrangian irreversibility and Eulerian dissipation in fully developed turbulence,” [Physical Review Fluids](#) **5**, 042601 (2020).
- [248] Z.-S. She, E. Jackson, and S. A. Orszag, “Intermittent vortex structures in homogeneous isotropic turbulence,” [Nature](#) **344**, 226–228 (1990).
- [249] J. Jiménez, A. A. Wray, P. G. Saffman, and R. S. Rogallo, “The structure of intense vorticity in isotropic turbulence,” [Journal of Fluid Mechanics](#) **255**, 65–90 (1993).
- [250] F. Moisy and J. Jiménez, “Geometry and clustering of intense structures in isotropic turbulence,” [Journal of Fluid Mechanics](#) **513**, 111–133 (2004).
- [251] S. Mukherjee, M. Mascini, and L. M. Portela, “Correlation and decomposition concepts for identifying and disentangling flow structures: Framework and insights into turbulence organization,” [Physics of Fluids](#) **34**, 015119 (2022).
- [252] E.-W. Saw, D. Kuzzay, D. Faranda, A. Guittonneau, F. Daviaud, C. Wiertel-Gasquet, V. Padilla, and B. Dubrulle, “Experimental

- characterization of extreme events of inertial dissipation in a turbulent swirling flow,” *Nature communications* **7**, 12466 (2016).
- [253] R. Lopes and N. Betrouni, “Fractal and multifractal analysis: a review,” *Medical image analysis* **13**, 634–649 (2009).
- [254] B. B. Mandelbrot, “Multifractal measures, especially for the geophysicist,” in *Fractals in Geophysics* (Birkhäuser Basel, 1989) pp. 5–42.
- [255] S. Lovejoy and D. Schertzer, *The weather and climate: emergent laws and multifractal cascades* (Cambridge University Press, 2018).
- [256] Z.-Q. Jiang, W.-J. Xie, W.-X. Zhou, and D. Sornette, “Multifractal analysis of financial markets: a review,” *Reports on Progress in Physics* **82**, 125901 (2019).
- [257] D. Biskamp, *Nonlinear Magnetohydrodynamics* (Cambridge University Press, 1993).
- [258] D. Biskamp, *Magnetohydrodynamic Turbulence* (Cambridge University Press, 2003).
- [259] A. R. Choudhuri, *The Physics of Fluids and Plasmas: An Introduction for Astrophysicists* (Cambridge University Press, 1998).
- [260] A. Brandenburg, “Advances in mean-field dynamo theory and applications to astrophysical turbulence,” *Journal of Plasma Physics* **84**, 735840404 (2018).
- [261] Schleicher, D. R. G., Banerjee, R., Sur, S., Arshakian, T. G., Klessen, R. S., Beck, R., and Spaans, M., “Small-scale dynamo action during the formation of the first stars and galaxies - i. the ideal mhd limit,” *Astronomy and Astrophysics* **522**, A115 (2010).
- [262] R. M. Kulsrud, “A critical review of galactic dynamos,” *Annual Review of Astronomy and Astrophysics* **37**, 37–64 (1999).
- [263] P. A. Davidson, *An Introduction to Magnetohydrodynamics* (Cambridge University Press, 2001).

- [264] R. Monchaux, M. Berhanu, M. Bourgoïn, M. Moulin, P. Odier, J.-F. Pinton, R. Volk, S. Fauve, N. Mordant, F. Pétrélis, A. Chiffaudel, F. Daviaud, B. Dubrulle, C. Gasquet, L. Marié, and F. Ravelet, “Generation of a magnetic field by dynamo action in a turbulent flow of liquid sodium,” [Physical Review Letters](#) **98**, 044502 (2007).
- [265] A. P. Kazantsev, “Enhancement of a Magnetic Field by a Conducting Fluid,” [Soviet Journal of Experimental and Theoretical Physics](#) **26**, 1031 (1968).
- [266] G. Falkovich, K. Gawędzki, and M. Vergassola, “Particles and fields in fluid turbulence,” [Reviews of Modern Physics](#) **73**, 913–975 (2001).
- [267] A. Gruzinov, S. Cowley, and R. Sudan, “Small-Scale-Field Dynamo,” [Physical Review Letters](#) **77**, 4342–4345 (1996).
- [268] A. A. Schekochihin, S. A. Boldyrev, and R. M. Kulsrud, “Spectra and Growth Rates of Fluctuating Magnetic Fields in the Kinematic Dynamo Theory with Large Magnetic Prandtl Numbers,” [The Astrophysical Journal](#) **567**, 828 (2002).
- [269] H. Arponen and P. Horvai, “Dynamo Effect in the Kraichnan Magnetohydrodynamic Turbulence,” [Journal of Statistical Physics](#) **129**, 205–239 (2007).
- [270] M. Martins Afonso, D. Mitra, and D. Vincenzi, “Kazantsev dynamo in turbulent compressible flows,” [Proceedings of the Royal Society A: Mathematical, Physical and Engineering Sciences](#) **475**, 20180591 (2019).
- [271] K. G. Wilson and M. E. Fisher, “Critical exponents in 3.99 dimensions,” [Physical Review Letters](#) **28**, 240–243 (1972).
- [272] D. Clark, R. D. J. G. Ho, and A. Berera, “Effect of spatial dimension on a model of fluid turbulence,” [Journal of Fluid Mechanics](#) **912**, A40 (2021).
- [273] I. B. Zeldovich and A. A. Ruzmaikin, “Magnetic field of a conducting fluid in two-dimensional motion,” in [Selected Works of Yakov Borisovich Zeldovich, Volume I](#), Vol. 78 (Princeton University Press, 1980) pp. 980–986.

- [274] L. Pietronero and A. Siebesma, “Self-similarity of fluctuations in random multiplicative processes,” *Physical Review Letters* **57**, 1098 (1986).